eman ta zabal zazu

Universidad del País Vasco
Euskal Herriko Unibertsitatea

Concentration Fluctuations and Broadening of the Glass Transition in Dynamically Asymmetric Mixtures

PhD Thesis Submitted by

Numera Shafqat

to the

University of the Basque Country

Thesis Supervisors:

Prof. Arantxa Arbe Mendez

Prof. Angel Alegría Loinaz

Donostia – San Sebastián, 2023

(cc)2022 NUMERA SHAFQAT (cc by-nc 4.0)

Institutions

UPV/EHU

San Sebastián - Spain

Materials Physics Center

San Sebastián - Spain

Consejo Superior de Investigaciones Científicas

San Sebastián - Spain

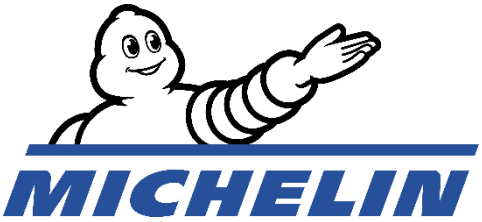

Campus RDI - Michelin

Ladoux - France

List of Abbreviations

AC	Alternative Current
ADSC	Alternating Differential Scanning Calorimetry
BDS	Broadband Dielectric Spectroscopy
BG	Background
BS	Backscattering Spectrometer
BuLi	Butyllithium
CC	Cole– Cole
CD	Cole–Davidson
CRG	Collaborating Research Group
CRR	Cooperatively Rearranging Regions
DSC	Differential Scanning Calorimetry
EFWS	Elastic Fixed Window Scans
G-T	Gordon-Taylor
HN	Havriliak and Negami
ICTAC	International Confederation for Thermal Analysis and Calorimetry
ILL	Institut Laue-Langevin
KWW	Kohlraush-Williams-Watts
LCST	Lower Critical Solution Temperature
LNCS	Liquid Nitrogen Cooling System
NMR	Nuclear Magnetic Resonance
MDSC	Modulated Differential Scanning Calorimetry
MPC	Material Physic Centre
MSD	Mean-Squared Displacement
MSF	Mean-Squared Fluctuation
MTDSC	Modulated-Temperature Differential Scanning Calorimetry
ODSC	Oscillating Differential Scanning Calorimetry
OZ	Ornstein-Zernike
PB	Polybutadiene
PDI	Polydispersity Index
PEO	Poly(ethylene oxide)

PET	Polyethylene Terephthalate
PI	Polyisoprene
PMMA	Poly(Methyl Methacrylate)
PS	Polystyrene
PSD	Position Sensitive Detector
PtBS	Poly(*Tert*-Butylstyrene)
PVE	Poly(Vinyl Ethylene)
PVME	Poly(Vinyl Methyl Ether)
RPA	Random Phase Approximation
RT	Room Temperature
SANS	Small-Angle Neutron Scattering
SAXS	Small-Angle X-Ray Scattering
SBR	Styrene-Butadiene Rubber
SC	Self-Concentration
SEC	Size Exclusion Chromatography
SF	Spin-Flip
SSD	Sample-Detector Distances
TCF	Thermally Driven Concentration Fluctuations
THF	Tetrahydrofuran
UCST	Upper Critical Solution Temperature
V	Specific Volume
VFT	Vogel-Fulcher-Tammann
M_n	Number Molecular Weight
M_w	Weight Molar Mass
T_g	Glass Transition Temperature
T_m	Melting Temperature
τ_R	Resolution Time
ΔG	Gibb Free Energy
ΔH	Enthalpy
ΔS	Entropy

Contents

Fluctuaciones de concentración y ensanchamiento de la transición vítrea en mezclas dinámicamente asimétricas

Las propiedades dinámicas de los elastómeros en régimen lineal son una de las líneas de investigación centrales de la industria basada en estos materiales. Por ejemplo. la comprensión del efecto del plastificante en la dependencia con la temperatura de la relajación mecánica es un punto clave para mejorar el rendimiento de un neumático, en particular aumentar la adherencia durante el frenado y la disminución de la resistencia a la rodadura. De hecho, durante su período de uso, el neumático debe disipar la mayor cantidad de energía posible durante el frenado, sin embargo, debemos minimizar este proceso durante el rodamiento regular. Variar la temperatura de transición vítrea (T_g) del sistema permite modificar el dominio de la frecuencia y la temperatura en el que el material disipa la energía.

La transición vítrea es un concepto clave en el estudio de los polímeros y sus aplicaciones. Los polímeros generalmente están formados por una estructura de cadena larga y tienen una alta viscosidad en estado líquido. Cuando se realiza un enfriamiento, los movimientos moleculares se vuelven más lentos. A veces las estructuras químicas no son compatibles con la formación de una fase cristalina. De este modo, el polímero mantiene una conformación desordenada como un líquido, aunque la viscosidad es tan alta que el polímero podría verse como un sólido. La estructura de no equilibrio resultante se conoce como estado vítreo y la pérdida del equilibrio que conduce al estado vítreo se conoce como transición vítrea. En general, los valores de T_g de interés están muy por debajo de la temperatura ambiente y definen el dominio de los elastómeros, ya que debido al enmarañamiento de las cadenas largas se produce una respuesta elástica importante, a pesar de ser materiales relativamente blandos. Aquellos polímeros con valores de T_g por encima de la temperatura ambiente definen polímeros rígidos. Los polímeros amorfos exhiben diferentes procesos de relajación. A bajas temperaturas se produce la relajación secundaria (β), que se atribuye a la aparición de

movimientos locales de pequeña amplitud. Calentando por encima de T_g, observamos la aparición de la relajación principal (α), que corresponde a una caída del módulo mecánico de varias décadas desde valores de unos pocos GPa (típicos de un sólido), y se atribuye a reordenamientos de varias unidades monoméricas que están bloqueadas por debajo de T_g.

La temperatura de transición vítrea de un polímero se ve fuertemente afectada al agregar un plastificante. Un plastificante suele ser una molécula pequeña que se inserta entre las cadenas de polímero y las espacia entre sí. Este proceso aumenta el volumen libre y por lo tanto, las cadenas de polímero pueden deslizarse unas sobre otras más fácilmente y moverse de forma diferente a como lo harían sin el plastificante. Este segundo componente hace posible lograr mejores características de procesamiento de compuestos, al tiempo que proporciona flexibilidad en el producto de uso final. Sin embargo, también es posible usar, como en nuestro caso, como "plastificantes" una cantidad de cadenas poliméricas de otro tipo que las de la matriz polimérica. En ese caso, la palabra utilizada "plastificante" podría no ser apropiada porque, dependiendo del tipo de polímero usado como "plastificante", la temperatura de transición vítrea de la matriz del polímero puede aumentar, con respecto a la del polímero inicial. En cualquier caso, estos sistemas pertenecen a la categoría de mezclas de polímeros miscibles.

Las mezclas de polímeros miscibles son en general tecnológicamente interesantes porque pueden conducir a nuevos materiales sin los gastos de tiempo y económicos requeridos para realizar nuevas síntesis. La capacidad de comprender el comportamiento de las mezclas de polímeros miscibles, basado en el comportamiento de los polímeros puros que forman la mezcla, es un punto clave para diseñar mezclas de polímeros con las propiedades apropiadas. La dinámica y el comportamiento de relajación de las mezclas de polímeros son particularmente complicados de predecir. De hecho, los estudios de calorimetría típicamente revelan una única transición de vítrea ancha. Sin embargo, las sondas de dinámica segmental, como la espectroscopia dieléctrica de banda ancha (BDS), resonancia magnética nuclear y la dispersion cuasielástica (QENS) por ejemplo, revelan que cada componente de la mezcla puede

mostrar una dinámica distinta. Se han propuesto modelos teóricos basados en conceptos tales como las fluctuaciones espontaneas de concentración y la auto-concentración para explicar el comportamiento dinámico de la mezcla y sus componentes. Cuando una mezcla de polímeros en la región monofásica se acerca al límite de estabilidad de fase, se producen variaciones de la concentración al rededor del valor promedio, que se define como fluctuaciones de la concentración. Por otro lado, en una mezcla de polímeros miscible, debido a la conectividad de la cadena, el entorno local de un monómero de tipo A será, en promedio, rico en A en comparación con la composición en masa, y de manera similar para B. Este efecto se ha llamado como auto-concentración.

El efecto de la mezcla en la dinámica del polímero se ha estudiado para numerosos sistemas. Nuestro estudio se centrará en la mezcla SBR/PS, un sistema industrial simplificado. Los cauchos de estireno butadieno (SBR) son los cauchos sintéticos más prevalentes que se derivan de la copolimerización de estireno y butadieno. Estos materiales tienen una buena resistencia a la abrasión y una buena estabilidad al envejecimiento cuando están protegidos por aditivos. Alrededor del 50% de los neumáticos de automóviles están hechos de diferentes tipos de SBR. La relación estireno / butadieno tiene un fuerte efecto sobre las propiedades del polímero. Un oligómero de poliestireno, como aditivo de mayor T_g que SBR, será el segundo componente de las mezclas de polímeros dinámicamente asimétricas binarias que estudiaremos en este trabajo.

En este trabajo, hemos combinado la difracción de rayos X y de neutrones, la dispersión de neutrones de ángulo pequeño (SANS), los barridos con ventana fija elástica de neutrones (EFWS) y la calorimetría de barrido diferencial (DSC) para investigar mezclas poliméricas compuestas por oligómeros de SBR y PS usando materiales con distinta composición isotópica (deuterados o protonados). La calorimetría diferencial de barrido (DSC) es probablemente la técnica más utilizada para corroborar la miscibilidad en mezclas de polímeros, ya que el criterio tradicional más extendido para la miscibilidad es la observación de una única temperatura de transición vítrea T_g en la curva calorimétrica. La espectroscopia dieléctrica de banda ancha (BDS)

es un método poderoso para el estudio de movimientos moleculares de materia blanda en un amplio intervalo de frecuencias (1mHz - 1GHz) y amplio rango de temperatura. Los experimentos de difracción, es decir, la exploración de escalas locales, del orden de las distancias intermoleculares típicas, informan sobre el orden de corto alcance del material. Los experimentos de dispersión de ángulo pequeño permiten la observación directa de TCF en mezclas, revelando su amplitud y la longitud de correlación de estas fluctuaciones. Los experimentos de dispersión cuasielástica de neutrones permiten obtener información dinámica. En el caso de las mezclas, existe la posibilidad de 'marcar' un componente determinado y seguir selectivamente su dinámica microscópica a escalas de longitud locales, en particular, los movimientos propios de sus hidrógenos, deuterando el otro componente. El objetivo general de este trabajo de tesis es: establecer una conexión cuantitativa entre el proceso de transición vítrea, y en particular el ensanchamiento de la región de transición, con las fluctuaciones espontaneas térmicas de concentración en mezclas miscibles.

Para lograr este objetivo utilizamos un enfoque que se basa en dos pasos:

i) Primero contrastar las TCF según se observan mediante SANS con la dinámica segmental de la mezcla en equilibrio (por encima de T_g), según se caracterizan mediante espectroscopía dieléctrica de banda ancha y utilizando en su análisis un modelo simple desarrollado previamente.

ii) Establecer una relación unívoca entre la dinámica segmental de la mezcla en equilibrio y el proceso de transición vítrea de las mezclas observado por DSC, lo que proporciona la manifestación de cómo se pierde el equilibrio termodinámico al disminuir la temperatura por debajo de T_g en estos sistemas binarios miscibles.

Más allá de este objetivo principal, también se aborda la comparación entre los fenómenos de transición vítrea asociados a cada componente de la mezcla tal como se determinan del análisis de las medidas macroscópicas de DSC y las manifestaciones microscópicas del proceso de vitrificación al que se accede por dispersión de neutrones, en escalas de tiempo cercanas a "100 ps".

La presentación de esta tesis doctoral está organizada de la siguiente manera:

En el capítulo 1 se presenta una descripción general de los polímeros. Se describen los aspectos físicos y moleculares de los polímeros: forma y tamaño molecular, características distintivas, comportamiento conformacional y configuracional, características estructurales, morfología, fenómenos de transición térmica y propiedades de relajación. Finalmente, se dan las nociones básicas de la termodinámica y la fenomenología de las mezclas de polímeros miscibles.

En el capítulo 2 se presentan las muestras utilizadas a lo largo de este trabajo. Además, se proporciona una descripción detallada sobre el conjunto de las diferentes técnicas y las condiciones utilizadas para la caracterización de las muestras.

En el capítulo 3 se aplican los distintos métodos experimentales a la investigación de la dinámica de los componentes puros de un sistema industrial simplificado, en particular elastómeros de estireno-butadieno (SBR) y oligómeros de poliestireno (PS). Como técnicas experimentales, en este capítulo se utilizaron DSC, BDS, SANS y la dispersión de neutrones cuasielástica (medidas de barrido con ventana fija elástica).

En el capítulo 4 se presentan los resultados experimentales obtenidos por DSC, BDS y SANS en mezclas SBR/PS para tres sistemas diferentes. Los resultados de DSC y BDS se describen desde un punto de vista fenomenológico, mientras que los resultados de dispersión se analizan en detalle para obtener información sobre las TCF y determinar el diagrama de fase de las mezclas.

En el capítulo 5 se establece una conexión cuantitativa entre las TCF en las mezclas investigadas, tal como se han caracterizado previamente por SANS, y el comportamiento dinámico en la región de transición vítrea, particularmente la anchura de la región de transición vítrea determinada mediante DSC. Para este fin, primero se incluyen los efectos de las TFC en el modelado de los datos de relajación dieléctrica. A continuación, se propone una conexión directa entre este modelado y el comportamiento de las curvas DSC, lo que permite conectar la dinámica segmental de los componentes en la mezcla por encima de la temperatura de transición vítrea (en equilibrio) y la forma en que se pierde el equilibrio al enfriar la mezcla hasta alcanzar el estado vítreo. El modelo desarrollado para este propósito, basado en los conceptos de autoconcentración y fluctuaciones térmicas espontaneas de concentración se describe en detalle. Este

modelo permite extraer las dos contribuciones 'macroscópicas' a la curva calorimétrica, es decir, determinar la 'T_g efectiva' de cada componente en las mezclas.

En el capítulo 6, las transiciones vítreas efectivas 'macroscópicas' de los componentes se comparan con las contrapartidas 'microscópicas', determinadas por los desplazamientos atómicos de los hidrógenos, en escalas de tiempo de algunas decenas de "ps", tal como se observan en los experimentos de EFWS, los cuales son sensibles al inicio de movimientos similares a los líquidos a través del transición vítrea calorimétrica. Estas temperaturas de transición vítrea efectivas "microscópicas" son accesibles para los componentes individuales gracias a la selectividad de dispersión de neutrones cuando se combina con el etiquetado isotópico. Además, se han determinado las diferentes escalas de longitudes relevantes desde el punto de vista estructural, termodinámico y dinámico en estas mezclas complejas y se discuten sus posibles interacciones.

Finalmente, en el capítulo 7 se resumen las principales conclusiones e implicaciones de esta tesis.

Chapter 1

1 Introduction

1.1 Polymers

The word *polymer* is derived from Ancient Greek words *poly* meaning 'many' and *meros* meaning 'parts'. A polymer is a material composed of long molecular chains called *macromolecules*. A macromolecule is formed by a large number of *repeating units* (between 100 and 10000 approximately) linked by covalent bonds. The repeat unit is called *monomer* and the number of monomers in a polymer chain determines the degree of polymerization.[1] The process that converts a monomer to a polymer is called *polymerization*. A molecule with only few repeating units (between 5 and 100 approximately) is called an *oligomer*.

Polymers can be found in nature (e.g. proteins, cellulose…) or produced by synthesis (e.g. polystyrene, polyethylene…). When a polymer is synthesized by using one type of monomer, is called *homo-polymer*. When two or more different types of monomers are used, the polymer is called *copolymer*, and it can lead to different structures depending on the relative position of the monomers. When two monomers are arranged in alternated positions (-A-B-A-B-A-B-A-B-) it is called *alternating copolymer*. In a *random copolymer* the two monomers do not follow a particular order (-A-A-B-A-A-B-B-A-), whereas *block copolymers* have homopolymer subunits (-A-A-A-A-B-B-B-B-).

In addition to the type, number, and sequential arrangements of monomers along the backbone chain, the spatial arrangement of substituent groups, R, is also important in determining properties. When all the R groups lie on the same side of the polymer chain, such polymers are termed *isotactic*; if the substituents groups regularly alternate from one side to the other, the polymer is called *syndiotactic* and polymers with no preferred order are *atactic*.

Polymers exhibit two types of morphology: *amorphous* and *semi-crystalline*. In an amorphous polymer the molecules are oriented randomly and are intertwined; while in semi-crystalline polymers, the molecules pack together in ordered regions called crystallites surrounded by a region of amorphous polymer as shown in figure 1.1.

A polymer cannot be 100% crystalline. In this study only amorphous polymers are considered.

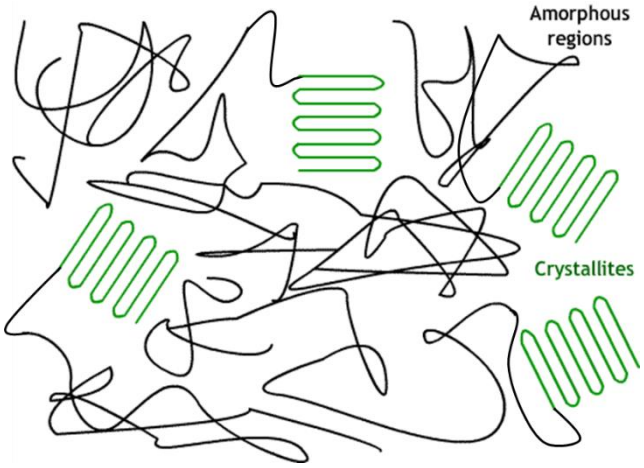

Figure 1.1: Schematic of semi-crystalline morphology.

Polymers do not have a fixed number of repeat units per chain due to polymerization conditions and as different chains have usually different length, they have different molar masses. The most common statistical magnitude to characterize the molar mass distribution are the number average molecular weight and the weight average method molecular weight.[1] The number-average molecular weight $\bar{M}_n$ is the arithmetic mean of the molar mass and is obtained by diving the total mass by the number of chains:

$$\bar{M}_n = \frac{\sum_i N_i M_i}{\sum_i N_i} \tag{1.1}$$

where M_i is the mass of the chain i and N_i the number of chains of mass M_i.

The weight average molar mass $\bar{M}_w$ represents an average over weight of the polymer and is defined as:

$$\bar{M}_w = \frac{\sum_i N_i {M_i}^2}{\sum_i N_i M_i} \tag{1.2}$$

with $\bar{M}_w > \bar{M}_n$ always and the ratio $\bar{M}_w/\bar{M}_n \geq 1$ is called *polydispersity index* (PDI), that characterize the width of the molecular weight distribution. A polymer is called

polydisperse when there is as a variation of molecular weight of the chain over a wide range ($\bar{M}_w \neq \bar{M}_n$, $\bar{M}_w/\bar{M}_n > 1$) and monodisperse when the molecular weight is not distributed ($\bar{M}_w = \bar{M}_n$, $\bar{M}_w/\bar{M}_n = 1$).

1.2 Polymer Dynamics

The main characteristic dynamical process in polymers are vibrations, side-groups motions, secondary relaxation, segmental dynamics, Rouse dynamics, reptation and terminal relaxations. These processes involve different scales, from the atomic bond involved in the vibrations up to the whole chain involved in the terminal relaxation.

The Glass Transition

In many polymer crystallizations cannot occur or occur partially, because of the long-entangled chain and the irregular polymer microstructures. This is why most polymers show an amorphous behavior instead of a crystalline one. The glass transition or vitrification phenomena is not an exclusive of polymer, but it is exhibited by glass forming systems in general, including also low molecular systems.

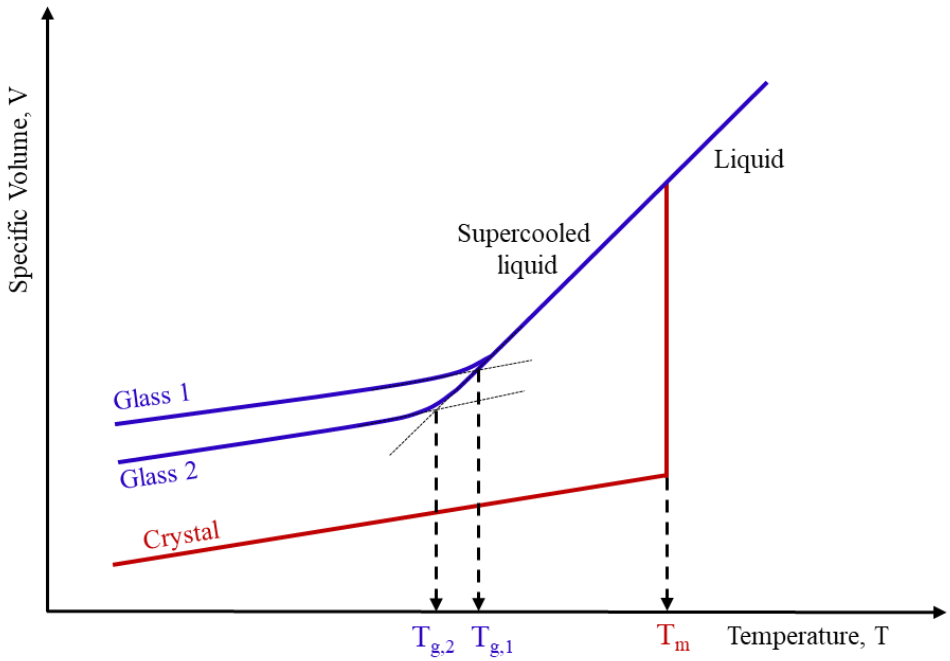

Figure 1.2: Temperature dependence of the specific volume, V.

Figure 1.2 shows the evolution of the specific volume (V) in function of the temperature. A typical liquid, upon cooling from high temperatures, may crystallize at T_m. A liquid that manages to get below the melting temperature without crystallizing is called a supercooled liquid. If the temperature decreases, the so-called *glass transition* T_g *temperature* is reached, which refers to the temperature where the material goes from a rubbery/viscous-liquid state to a glassy state and the volume with temperature deviates from equilibrium and thus exhibits a sudden change of slope.[2] In the glassy state, the high viscosity prevents the molecules to rearrangements necessary to reach thermodynamic equilibrium. It is possible to detect a glass transition in the amorphous regions of a semi-crystalline polymer.

When considering the mechanical properties of polymers, the glass transition temperature, T_g, does not occur suddenly, but rather over a range of temperatures and is strongly related to the cooling rate; the slower the cooling rate, the longer the molecules can rearrange and the lower is the glass transition temperature (see 'glass 2' of Fig.1.2). It is important to emphasize that the glassy state is a non-equilibrium one and that the glass transition is not a phase transition. Indeed, it is a kinetic phenomenon which depends upon the crossing of an experimental time scale and the time scales for molecular rearrangements. As indicated by figure 1.2, there is not a single glassy state; the thermodynamic (and dynamic) properties of a glass depend upon how it was formed.

There are five regions of viscoelastic behavior for a linear amorphous polymer shown in figure 1.3:

- in region I ($T < T_g$) or the *glassy region*, the polymer is brittle. The molecular motions are localized and largely restricted to vibrations and short-range rotational motions. The modulus is high and approximately constant.
- in region II ($T \approx T_g$) or the *glass transition region*, polymers exhibit tough leather-like behavior. The molecular motions occur at segmental level and the modulus drops several decades over 20-30 °C.

- in region III ($T > T_g$) or the *rubbery plateau region*, polymers exhibit significant rubber-like elasticity and the modulus after a sharp drop, as described above, again becomes nearly constant. In region III three cases can be distinguished: (1) if the polymer is linear, the solid line is followed. The modulus will drop off slowly and the width of the plateau depends on the molecular weight of the polymer, i.e., the higher the molecular weight, the longer the plateau. (2) If the polymer is semi-crystalline, the dotted line is followed and the height of the plateau (i.e., the modulus) depends on the degree of crystallinity. (3) If the polymer is crosslinked, the dashed line is followed and improved rubber elasticity is observed, with the creep portion suppressed.
- in region IV ($T \gg T_g$) or the *rubbery flow region*, the polymer exhibits both rubber elasticity and flow properties depending on the time scale of the experiment. When subjected to stress for a short time, the entanglements of polymer chains are not able to relax and the material still shows rubbery behavior, but over a longer duration under stress at the increased temperature, the chains can move, resulting in a visible flow.
- in region V ($T \ggg T_g$ *or* $T \approx T_m$) or the *liquid flow region*, which is reached at still higher temperatures where the increased kinetic energy of the chains permits them to wriggle out through entanglements rapidly and move as individual molecules, often producing highly viscous flow.

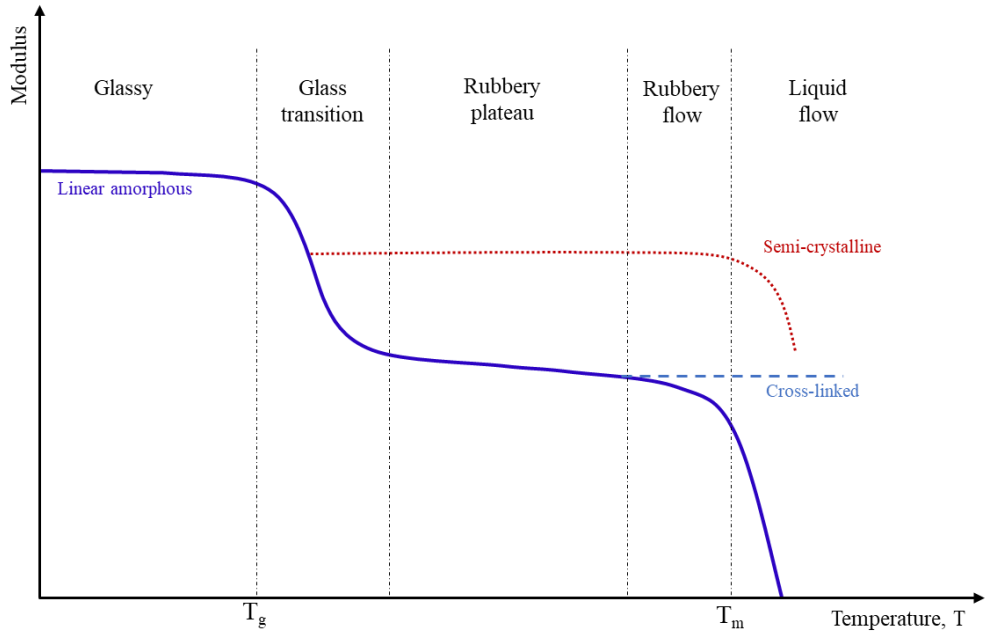

Figure 1.3: Five regions of viscoelastic behavior for a linear, amorphous polymer. Also illustrated are effects of crystallinity (dashed line) and cross-linking (dotted line).

Relaxation Processes in Polymers

The glass transition is directly related to the so-called structural (or α-) relaxation, which is a process that not only takes place in polymers, but in all kind of glass-forming materials. In addition to the α-relaxation, there are other dynamical processes detected as secondary processes such as β and γ relaxations that can be observed in the glassy state, i.e. below the T_g, which involve smaller scale molecular rearrangements and concern some specific functional groups or side groups attached to the main backbone.

The Segmental α-Relaxation

The segmental α-relaxation is strongly connected to the glass transition of polymers and the molecular motions involved in this process depend drastically on temperature. Approaching T_g from the melt, the molecular motions drastically slow down and the system appears frozen. The temperature dependence of the characteristic relaxation time associated can be described by the Vogel-Fulcher-Tamann function:[3–5]

$$\tau = \tau_\infty exp\left(\frac{DT_0}{T-T_0}\right) \quad (1.3)$$

where D (temperature independent) is the fragility parameter and T_0 is the Vogel temperature and represent the temperature at which the characteristic relaxation time diverges. The fragility determines how quickly the dynamics of a given material slow down as it is cooled toward the glass transition. Figure 1.4 shows a T_g-scaled Arrhenius representation of liquid viscosities,[6,7] Angell has proposed a useful classification of liquids along a 'strong' to 'fragile' scale: if the relaxation temperature dependence deviates from the Arrhenius behavior (see below, Eq. 1.4)[8], the glass-former presents a high fragility and it is called 'fragile', while if it obeys the Arrhenius law it exhibits a low fragility and it is called 'strong'.[7] Hence, the most fragile glass-forming systems are those presenting small D values.

Temperature dependence of the α-relaxation has usually been interpreted as due long-range cooperative movements.[9]

The Secondary Relaxation Processes

The dynamics of the small portions, side groups/or chain-end groups are defined as β-relaxation, γ-relaxation, and so on. Below T_g polymer chains are frozen, and therefore these secondary relaxations cannot be assigned to the long-range cooperative motions of the main chain as it occurs for the segmental relaxation. The secondary relaxation processes correspond to localized molecular motions that still remain below T_g. Depending on the molecules, the motions can be more or less cooperative. The amplitude of the secondary processes is generally weak compared to the main segmental relaxation. The temperature dependence of the characteristic time, in the glassy state, can be described by the Arrhenius law:[8]

$$\tau = \tau_0 exp\left(\frac{E_\alpha}{k_B T}\right) \quad (1.4)$$

where τ_0 is the parameter that represents the relaxation time at $T \to \infty$, E represents the activation energy of the process and k_B is the Boltzmann's constant.

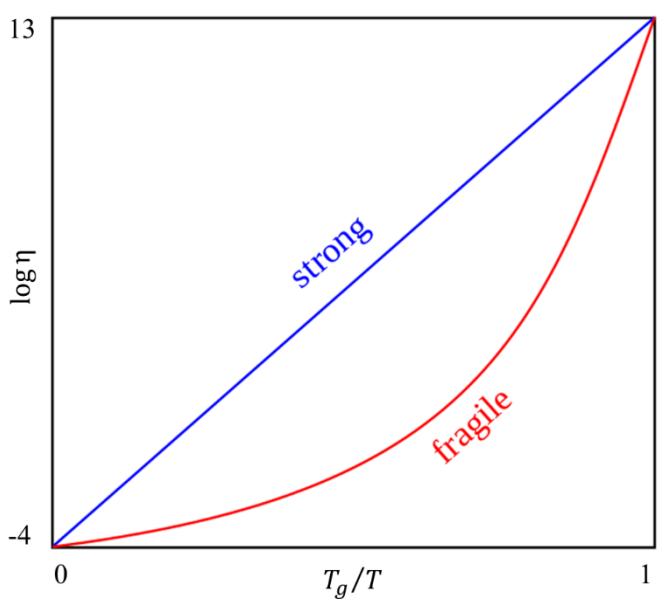

Figure 1.4: T_g-scaled Arrhenius representation of liquid viscosities (η) showing Angell's strong–fragile classification.

1.3 Polymer Blends

Polymer blends are systems consisting of at least two components mixed together to create a novel polymeric structure with different physical properties. One of the component can be a polymer of advantageous properties regarding the application or a *plasticizer*. Blending is an efficient way to obtain material with new properties optimized for the end-use by combing the properties of the starting polymer involved.

Usually, polymer blends are classified unto three different types:

- *Immiscible* polymer blends or *heterogenous* polymer blends: mixtures are composed by several different phases due to the repulsive interaction between the components. They exhibit two different $T_g s$ attributed to each of the pure polymers.

- *Partially miscible* polymer blends: mixtures are phase-separated and exhibit two different $T_g s$ intermediate between the pure polymers each associated to one of the segregated phases.
- *Miscible* polymer blends or *homogenous* polymer blends: mixtures are uniform and the components of the blend are intermixed on a molecular scale, they are presented as a single-phase structure. They exhibit a broad glass transition process intermediate between those of the pure polymers.

In this work oligomers are used as one of the component. Low molecular substances are usually called plasticizer. Commonly, a plasticizer, made of oil or small molecules, inserts itself in between the polymer chains and space them out from each other increasing the free volume. In this way, the polymer chains can slide past each other more easily, and move around at different temperatures than they would without the plasticizer. This component makes it possible to achieve improved compound processing characteristics, while also providing flexibility in the end-use product. In our case the oligomers have a much higher glass transition temperature than the long chain in the mixture and therefore the effect on the mixtures is the opposite to that found in common plasticizer.

1.3.1 Thermodynamics of Mixing

The entropy and the energy changes on mixing are the key parameter in order to determine if an equilibrium state of a given polymer blend is homogenous of heterogenous.

Polymer miscibility is governed by the thermodynamic function:[10]

$$\Delta G_m = \Delta H_m - T \cdot \Delta S_m \tag{1.5}$$

where ΔG_m is the Gibbs free energy variation, ΔH_m is enthalpy of mixing, and ΔS_m is the entropy of mixing. Miscibility depends on how the Gibbs free energy G_m varies

with temperature and with composition ϕ_i; so, a system is miscible when the variation of ΔG_m is negative:

$$\Delta G_m < 0 \tag{1.6}$$

and when the following condition is also fulfilled to avoid phase separation:

$$\left(\frac{\partial^2 \Delta G_m}{\partial \phi_i^2}\right)_{T,P} > 0 \tag{1.7}$$

where ϕ_i is the volume fraction for each component forming the blend. Negative values of Eq. 1.7 (even $\Delta G_m < 0$) can yield an area of the phase diagram where the mixture will separate into a phase rich in component 1 and a phase rich in component 2.

The entropy of mixing (ΔS_m) can be defined by the theory of Flory-Huggins:[11]

$$\Delta S_m = -N_{Av} k_B (n_A \, ln \, \phi_A + n_B \, ln \, \phi_B) \tag{1.8}$$

where N_{Av} is the Avogadro's constant, n refers to the number of moles.

While applying the concept of regular solution and assuming all pair interactions, the enthalpy can be defined as:

$$\Delta H_m = N_{Av} k_B T \chi \phi_A \phi_B \tag{1.9}$$

where χ refers to the Flory-Huggins binary interaction parameter.

Thus, the expression obtained before for the Gibbs free energy variation (Eq. 1.5) for a binary system can be written as:

$$\Delta G_m = N_{Av} k_B T [(\chi \phi_A \phi_B) + (n_A \, ln \, \phi_A + n_B \, ln \, \phi_B)] \tag{1.10}$$

where the first term refers to the enthalpic contribution and the second to entropic contribution. Accordingly, for polymers with very high molecular weights the entropic

contribution becomes very small (low n values) and the miscibility, or immiscibility, of the binary blends mainly depend on the enthalpic contribution. Therefore, for high molecular weights the miscibility is only achieved when the Flory-Huggins binary interaction parameter (χ) is negative. For a miscible blend, χ can be deduced also from Small-Angle Neutron Scattering (SANS) technique by measuring the concentration fluctuations (see chapter 4 for more details).

Figure 1.5 shows a schematic representation of the most representative phase diagrams:

- *Lower Critical Solution Temperature* (LCST) phase diagrams: as temperature increases, a monophasic system separates into two phases. Below the LCST, the system remains as monophasic independently on the composition.
- *Upper Critical Solution Temperature* (UCST) phase diagrams: by increasing the temperature, a two phases system (immiscible) goes toward a single-phase system.

The coexistence curve (also called binodal curve) denotes the condition at which two distinct phases may coexists, while the spinodal curve identifies the boundary between unstable and metastable region. The spinodal decomposition occurs because the mixture is locally unstable and any small composition fluctuation is enough to start the phase separation process.

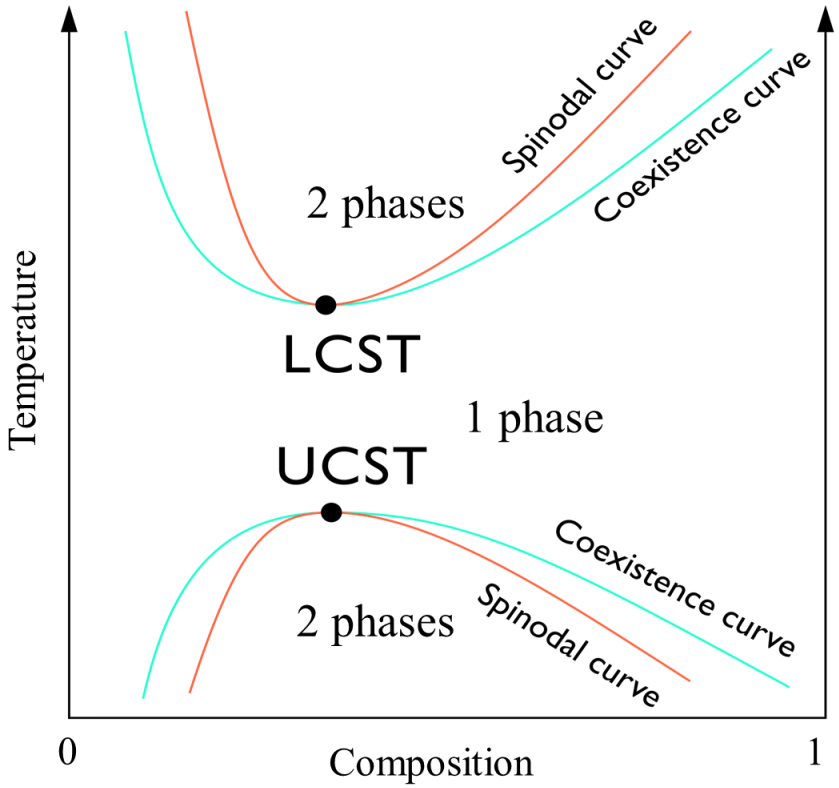

Figure 1.5: Phase diagram showing LCST and UCST behaviour for polymer blends.

1.3.2 Phenomenology of Thermodynamically Miscible Polymer Blends

The glass transition temperature and the α-relaxation of the two components in the blend is strongly modified depending on both the composition and the interactions between the components, resulting in properties not observed in the pure components. Differential scanning calorimetry (DSC) is probably the widest used technique to corroborate miscibility in polymer blends, since the most extended traditional criterion for miscibility is the observation of a single glass-transition temperature T_g in the calorimetric trace.[12–14] Contrarily to the rather abrupt step in the specific heat C_p of homopolymers, blends usually show a monotonic increase in C_p extending over a broad temperature range between the two T_gs of the neat polymers.[15,16] The position and broadening of these extended steps depend on composition. As for the homopolymers, from the inflection point of C_p, a glass-transition temperature can be deduced for the

blend. Traditionally, it was believed that miscibility implies a single glass transition for the blend components.[12,14] Regarding the α-relaxation, the major difference respect to the homopolymer components is that the relaxation as followed, e. g. dielectric spectroscopy, in the mixtures occurs at frequencies/temperatures intermediate to those of the pure components. Intuitively, for a perfect and homogeneous blend one would expect to observe only a single average relaxation time for the α-relaxation. This would translate into a single T_g measured by DSC.

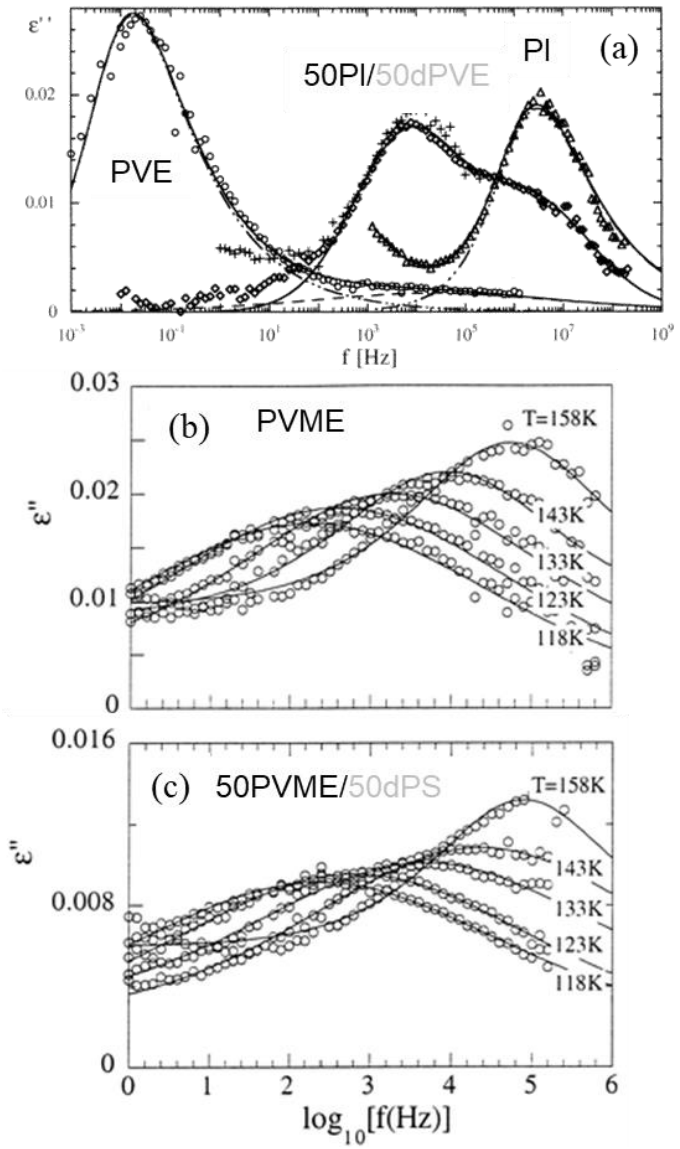

Figure 1.6: Dielectric loss curves at several temperatures for the system PI/PVE (a),[17] pure PVME (b) and PVME50 (c).[18] The loss peak in (a) correspond to the α-relaxation representation, while in (b) and (c) to the β-relaxation.

Figure 1.6 shows a comparison between the dielectric relaxation behavior of pure polyisoprene (PI), poly(vinyl ethylene) (PVE) and the blend PI/dPVE with 50 wt % dPVE (fully deuterated PVE) (panel a); and of pure poly(vinyl methyl ether) PVME and the blends of deuterated polystyrene (dPS) and PVME with 50 wt % dPS (PMVE50) (panel b and c respectively), above and below T_g, respectively. As can be seen, by comparing pure components with the blends, it is apparent that the segmental dynamics (α-relaxation) -shown as a main loss peak which depends strongly on temperature- is strongly affected by blending (Fig. 1.6a).[17] The secondary relaxation (β-relaxation) -a weaker, much less temperature-dependent high-frequency peak- has no significant changes (Fig. 1.6b-c).[18] In particular, the main loss maxima of the blends are shifted toward lower frequencies, indicating a slowing down of the PI dynamics by the presence of dPVE chains.

However, for athermal miscible blends with the two pure polymer components presenting a large difference in the respective glass-transition temperature, what is found is that the frequency/ temperature range of the dielectric relaxation becomes dramatically broad.[16] The effects are more pronounced at lower temperatures and when the T_g values of the components are very different. This is also manifested in the standard differential scanning calorimetric (DSC) experiments of these systems that reveal a broad feature ranging almost between the two pure polymers' T_gs.

Typical systems where this has been observed are: polyisoprene/poly(vinyl ethylene) (PI/PVE), polystyrene/poly(vinyl methyl ether) (PS/PVME) and poly(ethylene oxide)/poly(methyl methacrylate) (PEO/PMMA), among others.[14,16] In those systems it was found that an effective glass transition temperature, $T_{g,eff}$, can be identified for each blend component[19] as shown in Figure 1.7 for the blends polyisoprene/poly(*tert*-butylstyrene) (PI/PtBS),[13] which reflects the underlying dynamic heterogeneity[15,20–22] – i. e., the existence of two different mean relaxation, each of them corresponding to the dynamics of the α-relaxation of each component modified by blending as shown in Fig. 1.6a.[16,17] This finding is known as dynamic heterogeneity of miscible blends and is particularly prominent in this kind of systems referred to as dynamically asymmetric mixtures.

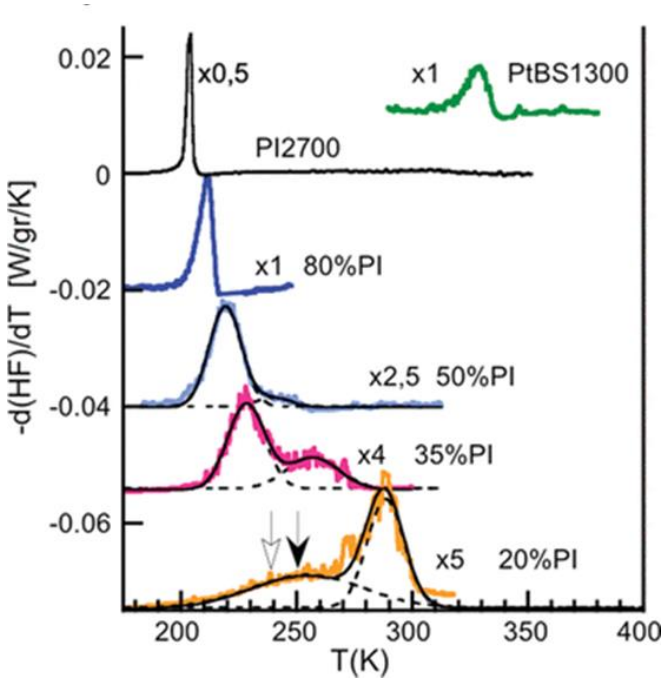

Figure 1.7: Temperature derivatives of heat flow for PI/PtBS blends showing broadening of glass transition and two distinct glass transition ranges as PI content decreases.[13]

1.3.3 Self-Concentration and Thermally Driven Concentration Fluctuations

The complex dynamical behavior of polymer blends arises from the combination of two main ingredients: (i) the chain connectivity (or self-concentration), (ii) and the thermally driven concentration fluctuations.

Self-Concentration

The origin of the dynamic heterogeneity in dynamically asymmetric mixtures is nowadays attributed to intra-molecular connectivity: since a given monomer is covalently bonded to other monomers of the same chain, a certain fraction of the 'averaging volume' around–the relevant volume for segmental relaxation– is occupied by this particular component, which defines the 'self- concentration' (SC).[23–25] As a consequence, the mean composition experienced by this segment is biased toward its corresponding pure

component. The self-concentration concept was raised as main ingredient of the phenomenology observed for polymer blends by Kornfield et al.[19,26] and incorporated in their model by Lodge and McLeish.[23]

Since the average T_g in the blend depends on composition, both components experience different 'effective glass-transitions' $T_{g,eff}$s. This implicitly translates into different relaxation times for both components, i.e., the observation of dynamic heterogeneity in the system. The presence of two effective glass transitions in polymer blends was first attributed to the chain connectivity of each component,[23] although it has been shown that it is a more general phenomenon that also occurs in mixtures of smaller molecules.[24,27] A main idea behind this concept is that the relevant cooperativity size at the glass transition could be comparable to the repeating unit (or molecular) size. Thus, as illustrated in figure 1.8, in a volume around a given component *c* the fraction occupied by units of this same component is larger than the average ("macroscopic") concentration (φ^c), giving rise to an effective concentration of this blend component φ^c_{eff} higher than the average one. This fact was captured with the concept of self-concentration (φ_{self}),[23] which allows connecting the effective and the macroscopic concentration as:

$$\varphi^c_{eff} = \varphi^c_{self} + \left(1 - \varphi^c_{self}\right)\varphi^c \tag{1.11}$$

In this way, the effective glass transition $T^c_{g,eff}$ of a given blend component in the blend can be defined as:

$$T^c_{g,eff} = T_g\left(\varphi^c = \varphi^c_{eff}\right) \tag{1.12}$$

where $T_g(\varphi^c)$ refers to the above-mentioned average concentration-dependent overall T_g determined e.g. from the broad DSC trace.

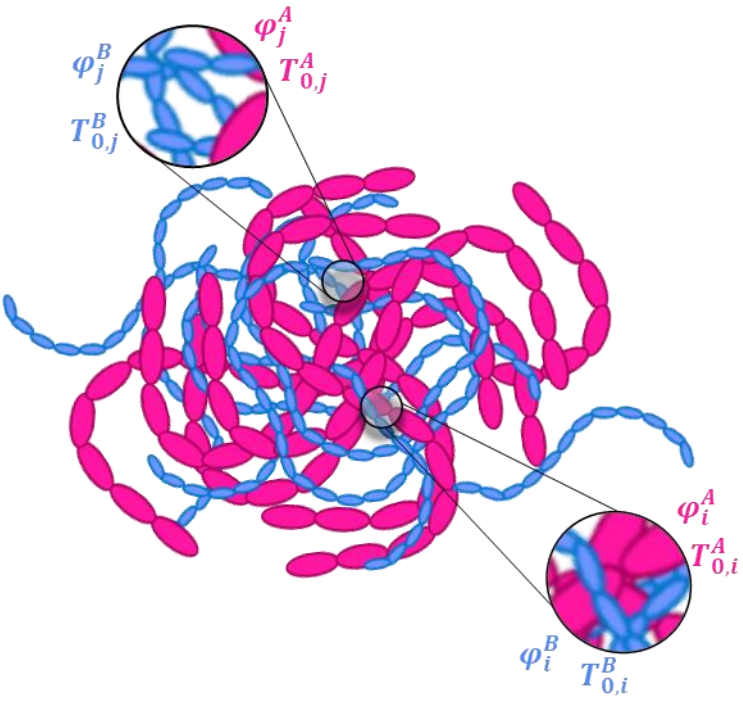

Figure 1.8: Schematic representation of different sub-volumes 'i' and 'j' composing the macroscopic blend of polymer chain A (pink) and chain B (blue). Each sub-volume contains both A and B components, and is characterized not only by its average concentration but also by the effective concentration of each blend component.

Thermally Driven Concentration Fluctuations (TCF)

In addition to this dynamic heterogeneity, blends' response is characterized by a strong broadening of the measured magnitudes (e. g. the frequency dependent region of the dielectric permittivity or the mechanical relaxation) with respect to the homopolymers results. The origin of this effect is believed to rest on the thermally driven concentration fluctuations (TCF) existing in miscible blends. Their importance was first put forward by Fischer et al.[28,29] and later developed by Kumar and co-workers.[30,31] The idea is that the local concentration fluctuations, inherent to any miscible blend, are quasi-stationary near the glass transition (typically $T_g < T < T_g + 60\text{K}$), since their average relaxation time is much longer that that of the α-relaxation in that temperature range. This leads to a distribution of local concentration throughout the blend and thereby to a distribution of characteristic relaxation times for the segmental dynamics of each component. This

allows to understand the temperature dependence broadening observed for the relaxation function of each component in the blend compared to that of the pure component. However, the concentration fluctuations cannot explain the presence of two relevant time scales and effect of chain connective has to be considered.[23]

The combination of two existing approaches (the self-concentration concept and the thermal concentration fluctuations approach) leads to a suitable way of describing the main features of the segmental dynamics in miscible polymer blends. This phenomenology was well established by many groups working on different miscible systems and with different experimental approaches. Some few examples of canonical miscible blends are: polyisoprene/poly(vinyl ethylene) (PI/PVE), polystyrene/poly(vinyl methyl ether) (PS/PVME) and poly(ethylene oxide)/poly(methyl methacrylate) (PEO/PMMA) and polyisoprene/poly(*tert*-butylstyrene) (PI/PtBS).[13,14,16]

A direct insight on concentration fluctuations is only directly provided by scattering techniques. Concentration fluctuations give rise to scattering at small angles for radiation with standard wavelength of the order of some Å. They can be particularly well investigated by means of neutron techniques (SANS) on samples where one of the components is deuterated and the other protonated. In this kind of samples, a high contrast is induced between the components, enhancing the neutron scattered-intensity from the concentration fluctuations.

1.3.4 Industrial Blends

Formulations of materials with industrial interest may involve macromolecules with intricate repeating units, polydisperse in size/microstructure and/or internal architecture, among other factors. One key question to design materials with the desired end-use properties is whether the concepts and theoretical frameworks developed for academic blends can be applied also to describe the segmental dynamics of such 'real' systems. With these ideas in mind, a recent research was carried out[32] based on the investigation of the dynamics of a mixture of high interest in the tire industry, since it involves Styrene-Butadiene Rubber (SBR) as one of the components. SBR –the main component of tires– is the synthetic polymer with highest production worldwide. In the binary system

explored, SBR was mixed (50/50) with polystyrene (PS). To improve miscibility, the PS was of low-molecular weight, containing 8 monomers in average. Its glass-transition temperature (≈280 K) was still about 70 K higher than that of the SBR component (≈213 K), qualifying thus the blend as a dynamically asymmetric mixture. In that work, dielectric spectroscopy (DS) was combined with quasielastic neutron scattering, in order to unravel the component dynamics of the mixture. It was found that, in fact, the 'academic' concepts deduced for 'canonical' blends –impact of SC and TCF– also apply in this system. In a further work on this line,[33] the possibility of exploring an extremely broad frequency/temperature range offered by DS was exploited in order to fully characterize the component dynamics of mixtures of different concentrations in terms a model involving both the concepts of SC and TFC, and elaborate a predictive approach for mechanical relaxation based on it. This simple modeling was based on a first description of the relaxation behavior of the component materials combined with a series of simplifying assumptions to limit the number of unknown parameters. Particularly, it was assumed that the SC values remained temperature and composition independent and the TCF effects are also temperature independent.

1.4 Objectives

The general objective of this thesis work is: establishing a quantitative connection between the glass transition process, and in particular the broadening of the transition region, with the thermally driven concentration fluctuations in miscible blends.

This is addressed by a two-step approach:

- First mapping the TCF as observed by SANS on the blend segmental dynamics at equilibrium (above T_g), as determined by broad-band dielectric spectroscopy and analyzed using previously developed simple modeling.

- Establish a univocal relationship between the blend segmental dynamics at equilibrium and the glass transition process of the blends as observed by DSC, which provides the manifestation of how the thermodynamic equilibrium is lost by decreasing temperature below T_g in these miscible binary systems.

Beyond this main objective, the comparison between the macroscopically resolved glass transition phenomena associated to each blend component and the microscopically signatures of the vitrification process as accessed by neutron scattering, at time-scales close to 100 ps, is also addressed.

1.5 Manuscript Outline

The presentation of this PhD thesis manuscript is organized as follows.

After this introduction, in chapter 2 the samples used along this work are presented. In addition, a detailed description about the set of the different techniques and the conditions used for the characterization of the samples is provided.

In chapter 3 the battery of experimental method described in the previous chapter has been applied to the investigation of the dynamics of the neat components of a simplified industrial system, particularly styrene-butadiene rubber (SBR) and oligomers of polystyrene (PS). As experimental techniques, in this chapter, DSC, BDS, SANS and quasielastic neutron scattering (elastic fixed window scan measurements) were used.

In chapter 4 the experimental results obtained by DSC, BDS and SANS on SBR/PS blends are presented for three different systems. The DSC and BDS results are described from a phenomenological point of view, while the scattering results are analyzed in detail to obtain information about TCF and determine the phase diagram of the mixtures.

In chapter 5 a quantitative connection between the thermally driven concentration fluctuations in the investigated blends, as characterized above by SANS, and the glass transition behaviour, particularly the width of the transition region has been established. For this end, first the effects of thermally driven concentration fluctuations are included in the modeling of the dielectric relaxation data. Next, a direct connection between this modeling and the behavior of the DSC curves is proposed, which allows connecting the component segmental dynamics in the blend above the glass-transition temperature (at equilibrium) and the way the equilibrium is lost when cooling down towards the glassy state. The model developed for this purpose, based on self-concentration and thermally driven concentration fluctuations concepts, is described in details and allows to extract the two 'macroscopic' contributions to the calorimetric trace, i.e., the 'effective T_g' of each of the blend component.

In chapter 6 the 'macroscopic' effective glass transitions of the components are compared with the 'microscopic' counterparts, determined by the atomic displacements

at some tens of ps observed by the EFWS and sensitive to the onset of liquid-like motions across the calorimetric glass transition. These 'microscopic' effective glass-transition temperatures are accessible for the individual components thanks to the neutron scattering selectivity when combined with isotopic labelling. Also, the different relevant length scales from structural, thermodynamical, and dynamical points of view, in these complex mixtures, have been determined and their possible interplays are discussed

In chapter 7 the major conclusions of this thesis are summarized.

1.6 References

(1) Fried, J. R. *Polymer Science and Technology*, Prentice Hall.; 2014.

(2) Chanda; Manas. *Introduction to Polymer Science and Chemistry*; 2012.

(3) Narros, A.; Arbe, A.; Alvarez, F. Atomic Motions in The-Merging Region of 1,4-Polybutadiene: A Molecular Dynamics Simulation Study. *J. Chem. Phys* **2008**, *128*, 224905.

(4) Alvarez, F.; Alegría, A.; Colmenero, J. Interconnection between Frequency-Domain Havriliak-Negami and Time-Domain Kohlrausch-Williams-Watts Relaxation Functions. *Phys Rev B* **1993**, *47* (1), 125.

(5) Havriliak, S.; Negami, S. A Complex Plane Analysis of α-Dispersions in Some Polymer Systems. *Journal of Polymer Science Part C: Polymer Symposia* **1966**, *14* (1), 99–117.

(6) Angell, C. A. The Old Problems of Glass and the Glass Transition, and the Many New Twists Abbreviation: MCT, Mode-Coupling Theory. *Proceedings of the National Academy of Sciences* **1995**, *92*, 6675–6682.

(7) Ediger, M. D.; Angell, C. A.; Nagel, S. R. Supercooled Liquids and Glasses. *J. Phys. Chem.* **1996**, *100* (31), 13200–13212.

(8) Debenedetti, P. G.; Stillinger, F. H. Supercooled Liquids and the Glass Transition. *Nature* **2001**.

(9) Starr, F. W.; Douglas, J. F.; Sastry, S. The Relationship of Dynamical Heterogeneity to the Adam-Gibbs and Random First-Order Transition Theories of Glass Formation. *Journal of Chemical Physics* **2013**, *138* (12).

(10) Robenson, L. M. Polymer Blends: A Comprehensive Review Hanser. *New York* **2007**.

(11) Flory, P. J. *Principles of Polymer Chemistry*; Cornell university press, 1953.

(12) Utracki, L. A.; Mukhopadhyay, P.; Gupta, R. K. Polymer Blends: Introduction. *Polymer blends handbook* **2014**, *1*, 3–170.

(13) Arrese-Igor, S.; Alegría, A.; Colmenero, J. Comparison of Calorimetric and Dielectric Single Component Glass Transitions in PtBS-PI Blends. *Macromolecules* **2010**, *43* (15), 6406–6413.

(14) Isayev, A. I. *Encyclopedia of Polymer Blends, Volume 1: Fundamentals*; John Wiley & Sons, 2010.

(15) Lodge, T. P.; Wood, E. R.; Haley, J. C. Two Calorimetric Glass Transitions Do Not Necessarily Indicate Immiscibility: The Case of PEO/PMMA. *J Polym Sci B Polym Phys* **2006**, *44* (4), 756–763.

(16) Colmenero, J.; Arbe, A. Segmental Dynamics in Miscible Polymer Blends: Recent Results and Open Questions. *Soft Matter* **2007**, *3* (12), 1474–1485.

(17) Arbe, A.; Alegria, A.; Colmenero, J.; Hoffmann, S.; Willner, L.; Richter, D. Segmental Dynamics in Poly (Vinylethylene)/Polyisoprene Miscible Blends Revisited. A Neutron Scattering and Broad-Band Dielectric Spectroscopy Investigation. *Macromolecules* **1999**, *32* (22), 7572–7581.

(18) Cendoya, I.; Alegría, A.; Alberdi, J. M.; Colmenero, J.; Grimm, H.; Richter, D.; Frick, B. Effect of Blending on the PVME Dynamics. A Dielectric, NMR, and QENS Investigation. *Macromolecules* **1999**, *32* (12), 4065–4078.

(19) Chung, G. C.; Kornfield, J. A.; Smith, S. D. Component Dynamics Miscible Polymer Blends: A Two-Dimensional Deuteron NMR Investigation. *Macromolecules* **1994**, *27* (4), 964–973.

(20) Arbe, A.; Alegria, A.; Colmenero, J.; Hoffmann, S.; Willner, L.; Richter, D. Segmental Dynamics in Poly (Vinylethylene)/Polyisoprene Miscible Blends Revisited. A Neutron Scattering and Broad-Band Dielectric Spectroscopy Investigation. *Macromolecules* **1999**, *32* (22), 7572–7581.

(21) Alegria, A.; Colmenero, J.; Ngai, K. L.; Roland, C. M. Observation of the Component Dynamics in a Miscible Polymer Blend by Dielectric and Mechanical Spectroscopies. *Macromolecules* **1994**, *27* (16), 4486–4492.

(22) Shenogin, S.; Kant, R.; Colby, R. H.; Kumar, S. K. Dynamics of Miscible Polymer Blends: Predicting the Dielectric Response. *Macromolecules* **2007**, *40* (16), 5767–5775.

(23) Lodge, T. P.; McLeish, T. C. B. Self-Concentrations and Effective Glass Transition Temperatures in Polymer Blends. *Macromolecules* **2000**, *33* (14), 5278–5284.

(24) Cangialosi, D.; Alegría, A.; Colmenero, J. "Self-Concentration" Effects on the Dynamics of a Polychlorinated Biphenyl Diluted in 1, 4-Polybutadiene. *J Chem Phys* **2007**, *126* (20), 204904.

(25) Painter, P.; Coleman, M. Self-Contacts, Self-Concentration, and the Composition Dependence of the Glass Transition Temperature in Polymer Mixtures. *Macromolecules* **2009**, *42* (3), 820–829.

(26) Chung, G.-C.; Kornfield, J. A.; Smith, S. D. Compositional Dependence of Segmental Dynamics in a Miscible Polymer Blend. *Macromolecules* **1994**, *27* (20), 5729–5741.

(27) Kahlau, R.; Bock, D.; Schmidtke, B.; Rössler, E. A. Dynamics of Asymmetric Binary Glass Formers. I. A Dielectric and Nuclear Magnetic Resonance Spectroscopy Study. *J Chem Phys* **2014**, *140* (4), 044509.

(28) Zetsche, A.; Fischer, E. W. Dielectric Studies of the α-Relaxation in Miscible Polymer Blends and Its Relation to Concentration Fluctuations. *Acta Polymerica* **1994**, *45* (3), 168–175.

(29) Katana, G.; Fischer, E. W.; Hack, T.; Abetz, V.; Kremer, F. Influence of Concentration Fluctuations on the Dielectric α-Relaxation in Homogeneous Polymer Mixtures. *Macromolecules* **1995**, *28* (8), 2714–2722.

(30) Kumar, S. K.; Colby, R. H.; Anastasiadis, S. H.; Fytas, G. Concentration Fluctuation Induced Dynamic Heterogeneities in Polymer Blends. *J Chem Phys* **1998**, *105* (9), 3777.

(31) Kamath, S.; Colby, R. H.; Kumar, S. K.; Karatasos, K.; Floudas, G.; Fytas, G.; Roovers, J. E. L. Segmental Dynamics of Miscible Polymer Blends: Comparison of the Predictions of a Concentration Fluctuation Model to Experiment. *J Chem Phys* **1999**, *111* (13), 6121–6128.

(32) Gambino, T.; Alegría, A.; Arbe, A.; Colmenero, J.; Malicki, N.; Dronet, S.; Schnell, B.; Lohstroh, W.; Nemkovski, K. Applying Polymer Blend Dynamics Concepts to a Simplified Industrial System. A Combined Effort by Dielectric Spectroscopy and Neutron Scattering. *Macromolecules* **2018**, *51* (17), 6692–6706.

(33) Gambino, T.; Alegría, A.; Arbe, A.; Colmenero, J.; Malicki, N.; Dronet, S. Modeling the High Frequency Mechanical Relaxation of Simplified Industrial Polymer Mixtures Using Dielectric Relaxation Results. *Polymer* **2020**, *187*, 122051.

Chapter 2

Materials and Experimental Techniques

2.1 Materials

In this part the neat components, styrene-butadiene rubber (SBR) as a polymer matrix and polystyrene (PS) as a plasticizer, and their blends are presented.

2.1.1 Pure Components

Styrene-Butadiene Rubber (SBR)

Protonated and deuterated styrene-butadiene rubbers (SBRs) were synthesized by anionic polymerization by the Michelin Company.[1] Before their use for copolymerization, the monomers, styrene and butadiene, were first dried over butyllithium (BuLi) for butadiene and over calcium hydride and dibutyl magnesium for styrene and then distilled to get purified monomers. The copolymerization was initiated by BuLi in methylcyclohexane at 50 °C. The deuterated monomers, d_8-styrene supplied by Cortectnet (purity of 99%) and d_6-butadiene supplied by Eurisotop (purity of 99%), were mixed in appropriate conditions to reach a microstructure as close as possible to the one of the hydrogenated chains (table 2.1). As illustrated in figure 2.1, the butadiene occurs as two isomers, the isomer 1,4 and the isomer 1,2 also called vinyl. The 1,4 isomer occurs in configuration *cis* and *trans*.

The randomness of the copolymer has been checked by ^{1}H-NMR following the procedure described in the literature.[2] Since a similar synthesis procedure has been followed for obtaining dSBR and hSBR, similar randomness is expected in both cases: for the hSBR samples, it was found that 99% of the styrene monomers are organized in short sequences of 1, 2 up to 3 following monomers, corresponding to a statistical repartition. For dSBR it was not possible to quantify the sequence distribution of styrene units being the very low amount of protons of the deuterated sample widely masked by the protons of the different antioxidants and impurities present in the sample.

In order to prevent oxidative degradation, these random copolymers also contain 0.25% of antioxidants.

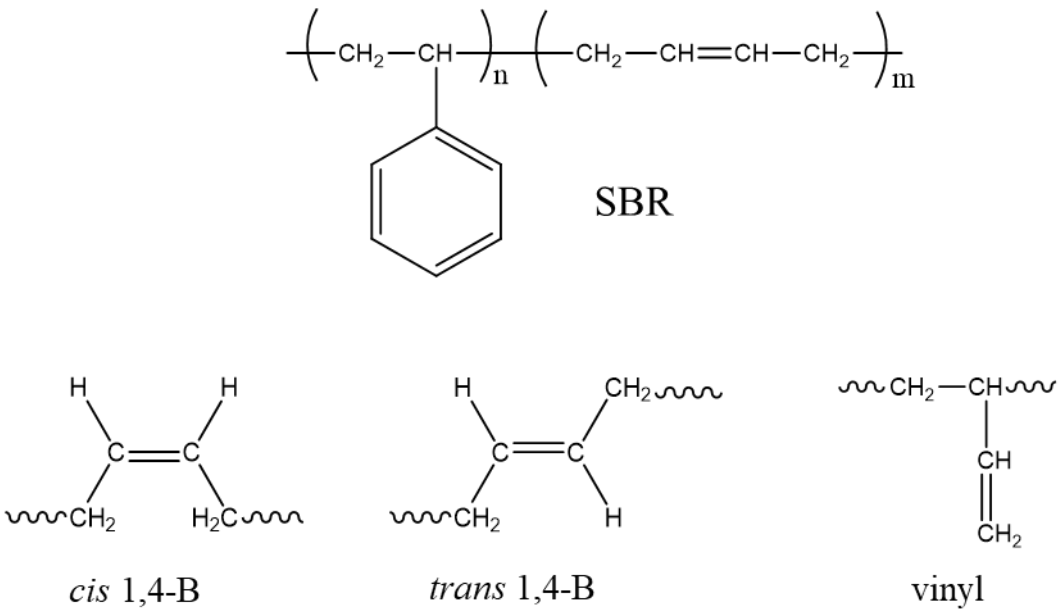

Figure 2.1: Chemical structure of protonated styrene-butadiene rubber (hSBR), 1,4-butadiene in the configuration *cis* and *trans*, and 1,2-butadiene or vinyl.

Polystyrene (PS)

The protonated and deuterated polystyrene (hPS and dPS) samples were purchased from Polymer Source, synthesized by living anionic polymerization of styrene for hPS and d_8-styrene for dPS, using sec-BuLi as initiator. In figure 2.2 the chemical structure of the hPS is illustrated. The molecular weight and polydispersity index (PDI, defined as M_w/M_n), as shown in table 2.1, are obtained by size exclusion chromatography (SEC) in Tetrahydrofuran (THF).

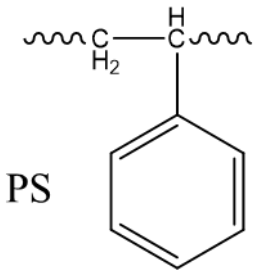

Figure 2.2: Chemical structure of protonated polystyrene (hPS).

Table 2.1: Weight fractions of styrene (S), 1,2-butadiene (1,2-B) and 1,4-butadiene (1,4-B), molecular weights, polydispersities and densities of the pure components investigated.

Sample	w_s	$w_{1,2-B}$	$w_{1,2-B}$	M_n (Kg/mol)	M_w (Kg/mol)	PDI	d (g/cm^3)
$hSBR_1$	0.138	0.218	0.644	69.90	76.20	1.09	0.94
$dSBR_1$	0.180	0.189	0.63	38.10	43.10	4.13	1.06
$hSBR_2$	0.278	0.178	0.544	101.60	105.90	1.04	1.01
hPS_1	-	-	-	0.50	0.60	1.20	0.99
dPS_1	-	-	-	0.50	0.55	1.12	1.07
dPS_2	-	-	-	0.90	0.98	1.09	1.12

Parameters of interest for the neutron scattering investigation are compiled in table 2.2. Taking into account the microstructure of SBR and PS, an 'effective monomer' has been defined, to which correspond a monomeric volume. The scattering length density ρ is calculated as the scattering length of the monomer divided by the monomeric volume. The end groups of dPS were hydrogenated; magnitudes of relevance for the scattering experiments have been calculated accordingly. Note that the values of some parameters as the effective monomer volume or the scattering length density are specific for the particular materials investigated, since they depend on the microstructure, molecular weight and isotopic labeling considered. Therefore, the values obtained in these cases cannot be considered as characteristic for 'generic' SBR and 'generic' PS.

Table 2.2: Composition, mass, volume, their average number in the chains and scattering length of the effective monomers, and scattering length densities for the homopolymers.

Sample	Effective monomer	M_0 $(\mathrm{g/mol})$	v $(10^{-22}\mathrm{cm}^3)$	$\overline{N}$	b $(10^{-12}\mathrm{cm})$	ρ $(10^{9}\mathrm{cm}^{-2})$
$hSBR_1$	$[C_8H_8]_{0.077}[C_4H_6]_{0.923}$	57.85	1.022	1317	0.5632	5.512
$dSBR_1$	$[C_8D_8]_{0.105}[C_4D_6]_{0.895}$	65.46	1.025	658	7.081	69.07
$hSBR_2$	$[C_8H_8]_{0.167}[C_4H_6]_{0.833}$	62.35	1.025	1698	0.87125	8.50
hPS_1	$[C_8H_8]_{0.81}[C_4H_{10}]_{0.19}$	95.26	1.580	6.3	1.680	10.61
dPS_1	$[C_8D_8]_{0.80}[C_4H_{10}]_{0.20}$	101.20	1.570	5.4	8.309	52.91
dPS_2	$[C_8D_8]_{0.88}[C_4H_{10}]_{0.12}$	105.52	1.661	9.3	9.841	59.25

2.1.2 Blending Preparations

Blends of different compositions -for the three systems investigated $hSBR_1/dPS_1$, $dSBR_1/hPS_1$ and $hSBR_2/dPS_2$- were prepared by solution casting using THF as a solvent. The compositions were chosen such that the molar composition was the same independently of the isotopic label, and correspond to SBR weight fraction (w_{SBR}) of 0.8, 0.6, 0.5, 0.3 and 0.2 for the case of a mixture of fully protonated components. The obtained films were carefully dried under vacuum at 343 K for 24 h to remove the solvent completely. Reference samples of the neat polymers were prepared in a similar way.

2.2 Experimental Techniques

Characterization techniques have played an essential role in the development of this thesis. A large set of techniques has been combined to extract information concerning different properties of all the samples investigated. The study has been done using a combination of macroscopic methods such as Broadband Dielectric Spectroscopy (BDS), Differential Scanning Calorimetry (DSC), and scattering techniques that provide a great help to unveil the properties of the system at microscopic level. In this chapter, a brief description about these techniques and the conditions used for the characterization of the samples is provided.

2.2.1 Broad-band Dielectric Spectroscopy (BDS)

Dielectric spectroscopy was invented by the Dutch-American physicist Peter Debye in 1912[3] and is one of the most powerful relaxation spectroscopy techniques used to study the molecular dynamics of materials. The interaction of electromagnetic waves with matter in the frequency regime between 10^{-6} and 10^{12} Hz is the domain of broad-band dielectric spectroscopy (BDS).[4] Such extended range of frequency allows to study molecular and collective dipolar fluctuations, charge transport, polarization effects and to determine the dielectric properties of the material under study with high accuracy in a relative short time, and also makes it possible to isolate the dynamics of one of the components in the blend if the dielectric relaxation of one of the components is negligible.

BDS measures the response of the dielectric sample in the presence of an electric field. If the sample contains any mobile charges (ions or electrons), the external electrical field induces their displacements in space, and the material is polarized. In the case of dielectric materials, there are four main types of polarization mechanisms, represented in figure 2.3. They are, in decreasing characteristic frequency ranges: electronic polarization, ionic polarization, dipolar or orientation polarization, and interfacial polarization. In polymeric systems the polarization due to charge migration and to the reorientation of permanent dipoles are the mainly studied phenomena for characterizing

molecular mobility. The dipolar orientation depends on the frequency of the applied field, and it is related to the dielectric permittivity (ε).

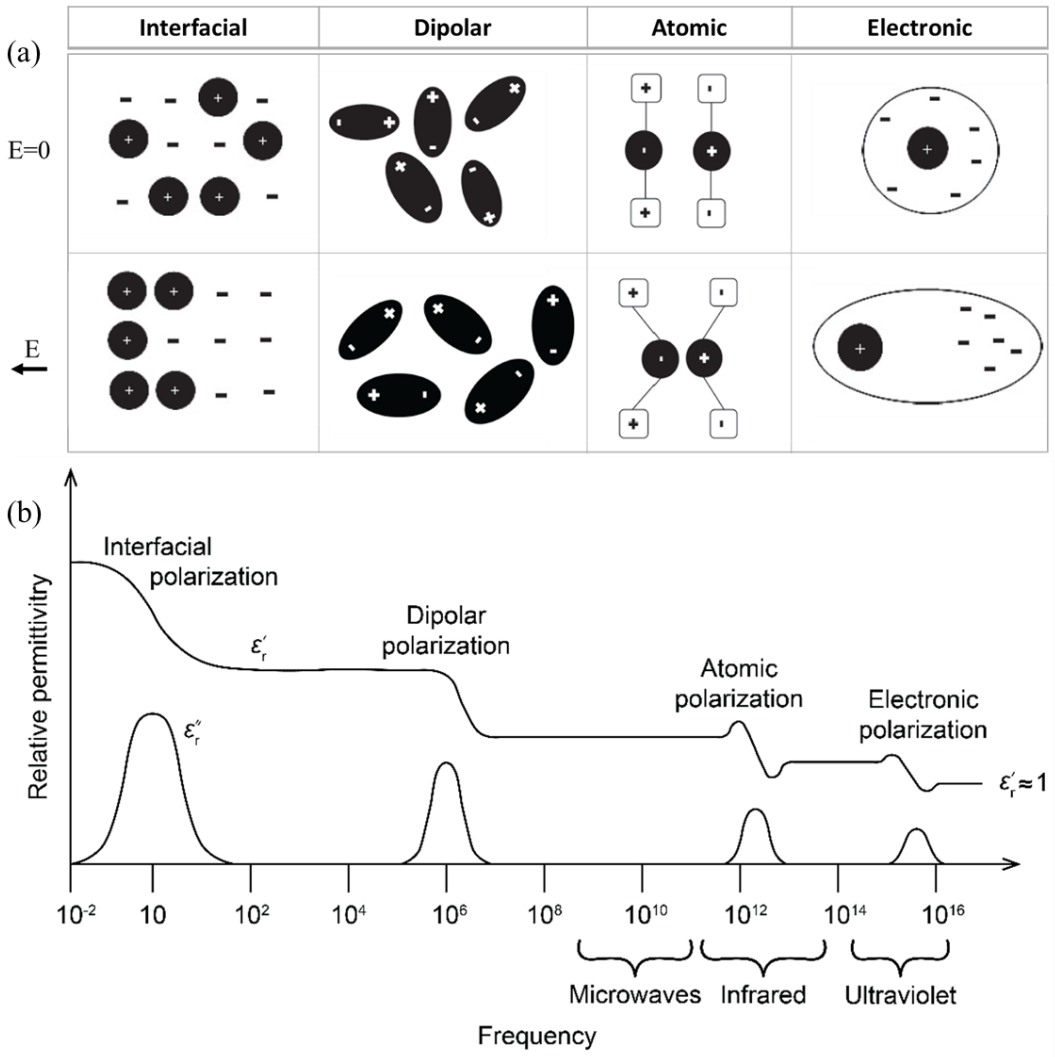

Figure 2.3: Different types of polarization mechanisms (a) and frequency dependence of the complex relative permittivity (b): interfacial and dipolar polarizations exhibiting relaxation processes whereas ionic and electronic polarizations exhibiting resonant processes.

Dielectric Properties

The dielectric permittivity is usually written as function of the frequency in the complex form:[4]

$$\varepsilon^*(\omega) = \varepsilon'(\omega) - i\varepsilon^{"}(\omega) \tag{2.1}$$

where $\varepsilon'(\omega)$ and $\varepsilon^{"}(\omega)$ are the real and the imaginary (loss) part of the complex dielectric permittivity $\varepsilon^*(\omega)$, being ω the angular frequency ($\omega = 2\pi\nu$, with ν the ordinary frequency). The real part of the permittivity is related to the stored energy in the sample, and the imaginary part to the dissipation of energy within the medium. The ratio between the dissipated and the stored energies is known as loss factor and given by $\tan\delta \equiv \frac{\varepsilon''}{\varepsilon'}$. The dielectric permittivity $\varepsilon^*(\omega)$ can be derived -using a sinusoidal electric field $E(t) = E_0 exp(-i\omega t)$- by measuring the complex impedance $Z^*(\omega)$ of a parallel plate capacitor, with vacuum capacitance C_0, filled with the material under study:

$$\varepsilon^*(\omega) = \frac{1}{i\omega Z^*(\omega) C_0} \tag{2.2}$$

The dynamic properties of the sample can be investigated by studying the dielectric permittivity $\varepsilon^*(\omega)$; as can be observed in figure 2.4, in a typical relaxation process the real part of the permittivity $\varepsilon'(\omega)$ shows a step-like decrease with increasing frequency and the imaginary part $\varepsilon^{"}(\omega)$ shows a peak. In contrast, conduction phenomena show an increase of $\varepsilon^{"}(\omega)$ with decreasing frequency. In general, the frequency ω_{max} of the maximum of the peak of $\varepsilon^{"}(\omega)$ is related to the characteristic relaxation time $\tau_{max} = 1/\omega_{max}$ of the fluctuating dipoles.

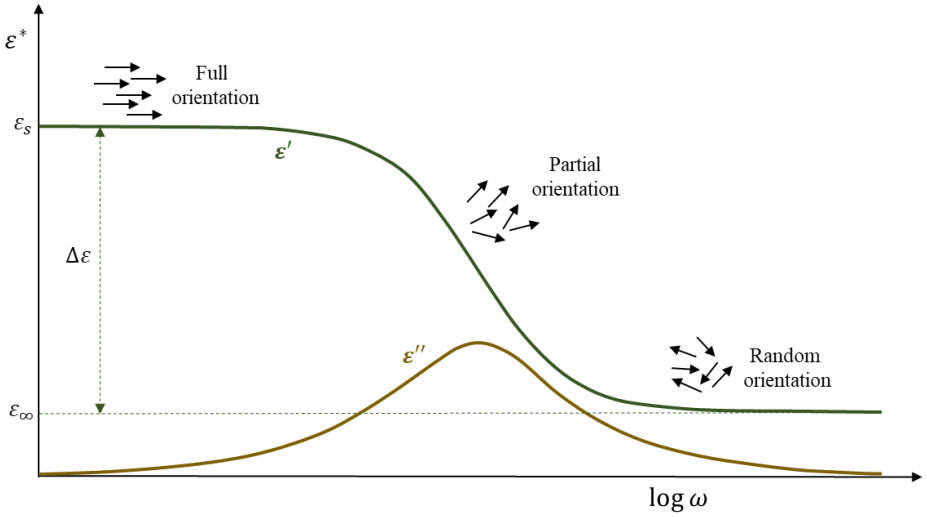

Figure 2.4: Evolution of the dielectric permittivity in function of the frequency.

Theoretical Models to Analyze Dielectric Spectra

Different model functions are available in order to describe the relaxational processes observed by BDS. The simplest model is the Debye theory, a model of non-interacting dipoles subjected to friction in which the complex permittivity is described as:[4]

$$\varepsilon^*(\omega) = \varepsilon_\infty + \frac{\Delta\varepsilon}{1+(i\omega\tau_D)} \tag{2.3}$$

where $\Delta\varepsilon = \varepsilon_s - \varepsilon_\infty$ is the dielectric relaxation strength with $\varepsilon_\infty = \lim_{\omega\to\infty}\varepsilon^*(\omega)$ and $\varepsilon_s = \lim_{\omega\to 0}\varepsilon^*(\omega) = \varepsilon_\infty + \Delta\varepsilon$ the high and low frequency limiting values of the dielectric permittivity, τ_D is the relaxation time often referred as the Debye time.

For most of the systems this model fails in the description of the relaxation behavior since the actual relaxations show significantly asymmetric and broader loss peaks. This causes the necessity for empirical relationships, which formally take into account a distribution of the relaxation times, to describe the non-Debye process. In most cases the experimental relaxation behavior is described by the Havriliak and Negami (HN) function in the frequency domain:[5,6]

$$\varepsilon^*_{HN} = \varepsilon_\infty + \frac{\Delta\varepsilon}{(1+(i\omega\tau_{HN})^\alpha)^\gamma} \tag{2.4}$$

where τ_{HN} is the characteristic relaxation time, α and γ are the fractional shape parameters describing the symmetric and asymmetric broadening of the complex dielectric function, respectively, maintaining the condition $0 < \gamma$ and $\alpha \cdot \gamma \leq 1$. The frequency ω_{max} of the maximal loss depends on τ_{HN} and of the parameters α and γ according to:[4]

$$\tau_{max} = \omega_{max}^{-1} = \tau_{HN}\left[sin\left(\frac{\alpha\,\gamma\,\pi}{2+2\,\gamma}\right)\right]^{1/\alpha} \cdot \left[sin\left(\frac{\alpha\,\pi}{2+2\,\gamma}\right)\right]^{-1/\alpha} \tag{2.5}$$

The specific case $\alpha = 1,\ \gamma = 1$ gives the Debye relaxation law; $\alpha \neq 1,\ \gamma = 1$ corresponds to the symmetrically broadened function (so-called Cole– Cole (CC)

equation[7]) and $\alpha = 1$, $\gamma \neq 1$, corresponds to the asymmetric Cole–Davidson (CD) function[8].

In the time domain the non-Debye relaxation function can frequently be described by the empirical Kohlraush-Williams-Watts (KWW) function, which is also currently called 'stretched exponential', in the following way:

$$\varepsilon(t) - \varepsilon_\infty = \Delta\varepsilon \left[1 - exp\left(\left(-\frac{1}{\tau_{KWW}}\right)^{\beta_{KWW}}\right)\right] \tag{2.6}$$

A relationship between the Cole-Davidson and the KWW functions was derived by Patternson and Lindsay[9] and then extended by Colmenero *et al*[10,11] leading to the following relations between KWW and HN parameters, namely:

$$\log\left[\frac{\tau_{HN}}{\tau_{KWW}}\right] = 2.6(1-\beta)^{0.5} exp(-3\beta) \tag{2.7}$$

for the relaxation times, and:

$$\alpha\gamma = \beta^{1.23} \tag{2.8}$$

for the shape parameters, and allow a direct way of transformation from the HN parameters into the KWW ones.

Experimental Set-Up

In this work, all the dielectric measurements were carried out in a *Novocontrol Alpha* broad-band dielectric spectrometer at the Material Physic Center (MPC) in San Sebastian. The experiments were conducted in the frequency range 10^{-1} to 10^{7} Hz by using an Alpha dielectric analyzer to determine the complex dielectric permittivity $\varepsilon^*(\omega)$. Independently of the frequency range, the temperature was controlled by a nitrogen jet-stream by Quatro cryosystem from Novocontrol with a temperature error during every single frequency sweep of $\pm$ 0.1 ºC.

The sample capacitor preparation for this setup consisted of an upper gold-coated electrode of 20 mm placed on a prepared film of the sample over a 30 mm gold-coated electrode (see figure 2.5). The films were prepared by solvent casting on the lower electrode and dried at 343 K under dynamic vacuum for 24 h, in order to remove any trace of moisture and / or solvent residues. Then, when the sample was still hot, a 0.1 mm thick cross-shaped spacer of Teflon of negligible area was placed between the electrodes before compressing the sample to avoid short circuit. Finally, the sample was inserted into the dielectric analyzer, and measured in a broad temperature range typically between 130-360 K and data were recorded every 5-10 K.

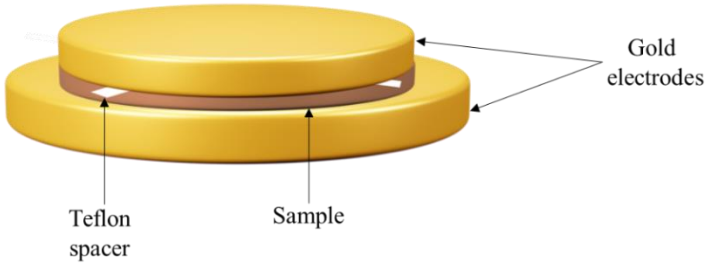

Figure 2.5: Sandwich sample capacitor for dielectric measurements.

2.2.2 Differential Scanning Calorimetry (DSC)

Calorimetry is a primary technique for measuring the thermal properties of materials to establish a connection between temperature and specific physical properties of materials[12] and is the only method to determine directly the enthalpy associated with the process of interest.[13,14] Caloric measurements have been carried out since the middle of the 18th century. Differential scanning calorimeter (DSC) was developed in 1964 and has become a popular one amongst various types of calorimeters.[15]

According to the International Confederation for Thermal Analysis and Calorimetry (ICTAC) the definition of Differential Scanning Calorimetry is as follows:

'A technique in which the heat-flow rate (power) to the sample is monitored against time or temperature while the temperature of the sample, in a specified atmosphere, is programmed.'

The heat flow difference is related to the temperature changes of the sample. These might indicate both physical phase transitions and/or chemical reactions.[13]

Differential Scanning Calorimetry can be classified in two types: 'heat-flux' DSCs and 'power-compensate' DSCs.[16] In a 'power-compensated' DSC, the sample, enclosed in a pan, and an empty reference pan are placed in separate furnaces heated by separate heaters.[16,17] The concept of operation of this instrument is based on keeping the temperature of the reference and the sample the same, and the difference in thermal power required to maintain them at the same temperature is measured and recorded as a function of temperature or time.

In a 'heat-flux' mode – used in this work – the sample and the reference pans are placed each on a thermoelectric disk, which is in good contact with the sample and the reference holder, surrounded by a furnace.[16,18] The furnace is heated at a linear heating rate, and the heat is transferred to the sample and reference pan through the thermoelectric disk and the temperature difference between them is recorded. Whenever the studied sample experiences a transition process, a temperature difference is observed. The process is called endothermic if it leads to energy absorption and exothermic when some heat is released.

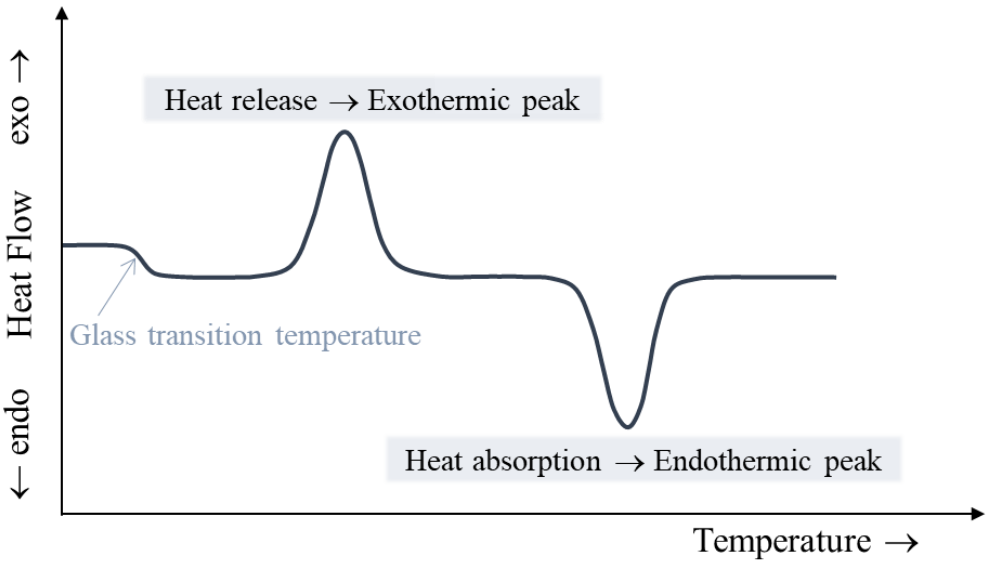

Figure 2.6: Schematic DSC curve showing different transitions.

Figure 2.6 shows a schematic DSC curve for a pure crystallizable polymer as it is progressively heated from a low temperature to high temperature. Starting from the lowest temperature, the first discontinuity observed is the glass transition, which appears as a shit of the base line corresponding to the heat capacity difference of the sample before and after the transition. As the temperature increases, there may be a cold crystallization peak (T_c, exotherm), followed by a melting peak (T_m, endotherm).

In the last decades, various DSC-based techniques have been developed; one of the best known being modulated-temperature DSC (MTDSC). In the following, MTDSC will be described, being the one used in this work.

Modulated-Temperature Differential Scanning Calorimetry (MTDSC)

Modulated-Temperature Differential Scanning Calorimetry (MTDSC) is an advanced technique introduced in 1992 by Reading and co-workers, that provides both the amplitude and phase signals [alternative current (AC) signals] and the total heat flow signal equivalent to that given by DSC simultaneously in a single experiment.[19,20,21,22,23] The method uses a conventional DSC, and the signals are produced by a deconvolution

procedure carried out by computer.[24] The accepted name MTDSC for this method was copyrighted by TA Instruments.[24] The family of MTDSC techniques includes different instruments: modulated DSC (MDSC®) offered by TA Instruments, alternating DSC (ADSC) by Mettler Toledo, and oscillating DSC (ODSC) by Seiko Instruments.[25] In this work, the operation and use of the TA Instruments model, modulated DSC (MDSC) is considered.

In MDSC a different heating profile (temperature regime) is applied to the sample and reference. Specifically, a sinusoidal modulation (oscillation) is overlaid on the conventional linear heating or cooling ramp to yield a profile in which the average sample temperature continuously changes with time (Fig. 2.7). The average heating rate, corresponding to the rate for a conventional DSC experiment, is called the underlying heating rate.

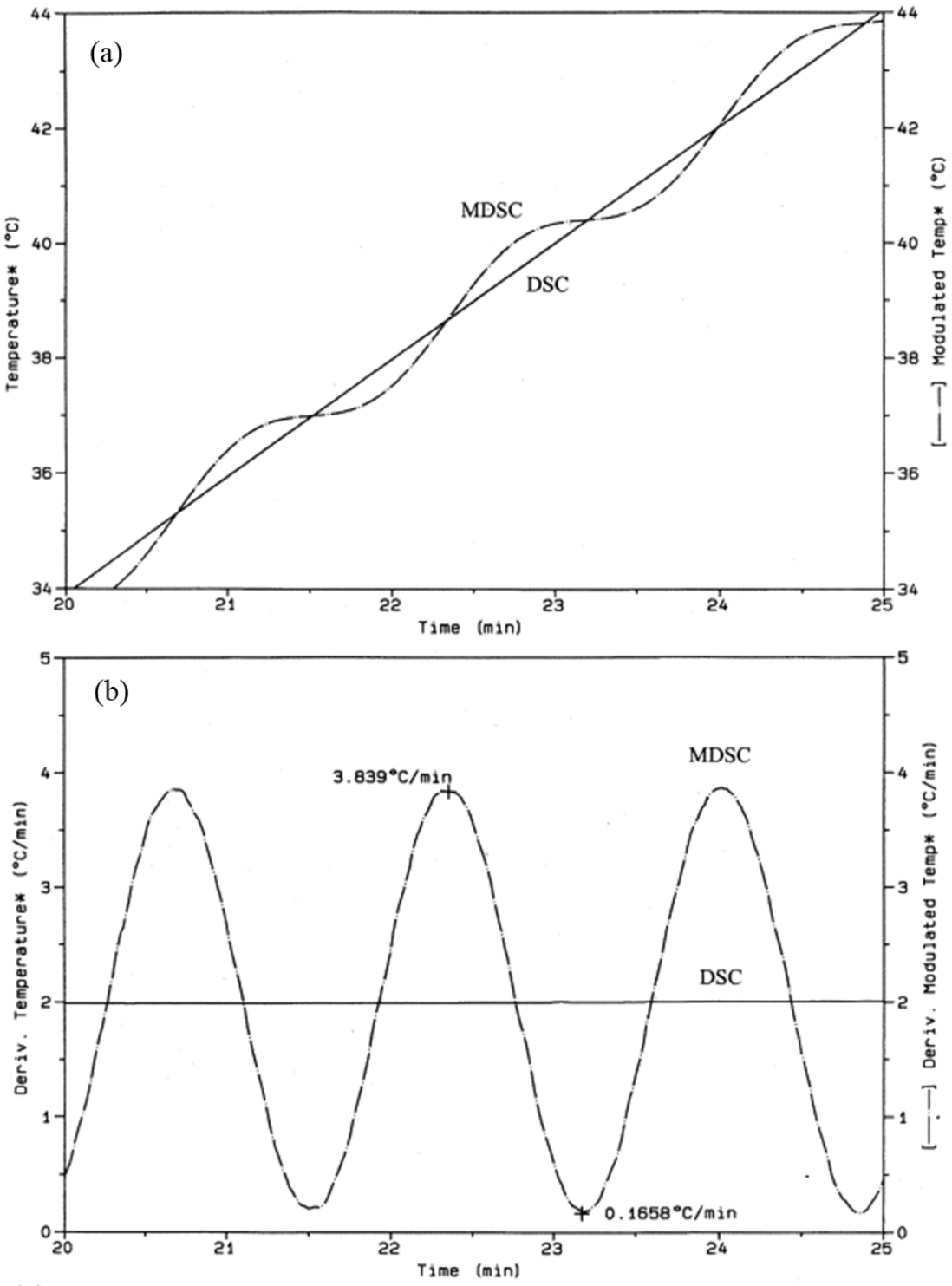

Figure 2.7: Temperature (a) and heating rate (b) as a function of time for a typical DSC and MDSC experiment.

The best-known advantage of MDSC is the ability to separate the total heat flow rate into two other signals -'kinetic' and 'heat capacity' responses- by deconvolution of the raw data. One of this is a reversible signal (heat capacity component, e.g. glass transition event), and the other a nonreversible signal (kinetic component, e.g. molecular relaxation, cold crystallization, evaporation, polymer cure, elastomer vulcanization, or decomposition). Both magnitudes are calculated from three measured signals: time, modulated temperature, and modulated heat flow.

In an MDSC experiment the modulated temperature can be expressed in the following way:

$$T(t) = T_o + \beta t + B\sin(\omega t) \tag{2.9}$$

where T_o is the initial temperature, ω is the angular frequency of the modulation (i.e. $2\pi f$), β is the linear heating rate and B is the amplitude of the temperature modulation. The time dependent heating rate will be:

$$dT/dt = \beta + \omega B\cos(\omega t) \tag{2.10}$$

Thus, the resultant heat flow signal:

$$dQ/dt = C_p\, dT/dt + f(t,T) \tag{2.11}$$

where dQ/dt is the average DSC heat flow signal, C_p is the 'thermodynamic' heat capacity (i.e. that due to the energy stored in vibrations, rotations and translations of molecular constituents of the sample). C_p is obtained from the ratio between amplitudes of the heat flow and heating rate oscillations. dT/dt is the measured heating rate, which has both a linear and a modulated component, T is the absolute temperature and the function $f(t,T)$ corresponds to the kinetic component of the total heat flow and is calculated from the difference between the Total Signal and the Heat capacity components. In this sense $C_p\, dT/dt$ gives the reversing heat flow component of the total heat flow. MDSC allows to measure the total heat flow, the heat capacity component and

then obtain the kinetic component from their difference. The MDSC ability to resolve complex transitions into specific components facilitates data interpretation.

Figure 2.8 shows an example of an MDSC experiment on quenched polyethylene terephthalate (PET), the most widely cited MSDC 'pilot' substance: the modulated heating rate (stimulus) as well as the modulated heat flow (response) in Fig. 2.8a and the total, reversing and non-reversing heat flow signals in Fig. 2.8b. The glass transition is seen in the reversing heat flow signal, whereas the recrystallisation appears in the non-reversing heat flow signal. The melting endotherm appears in both.[26]

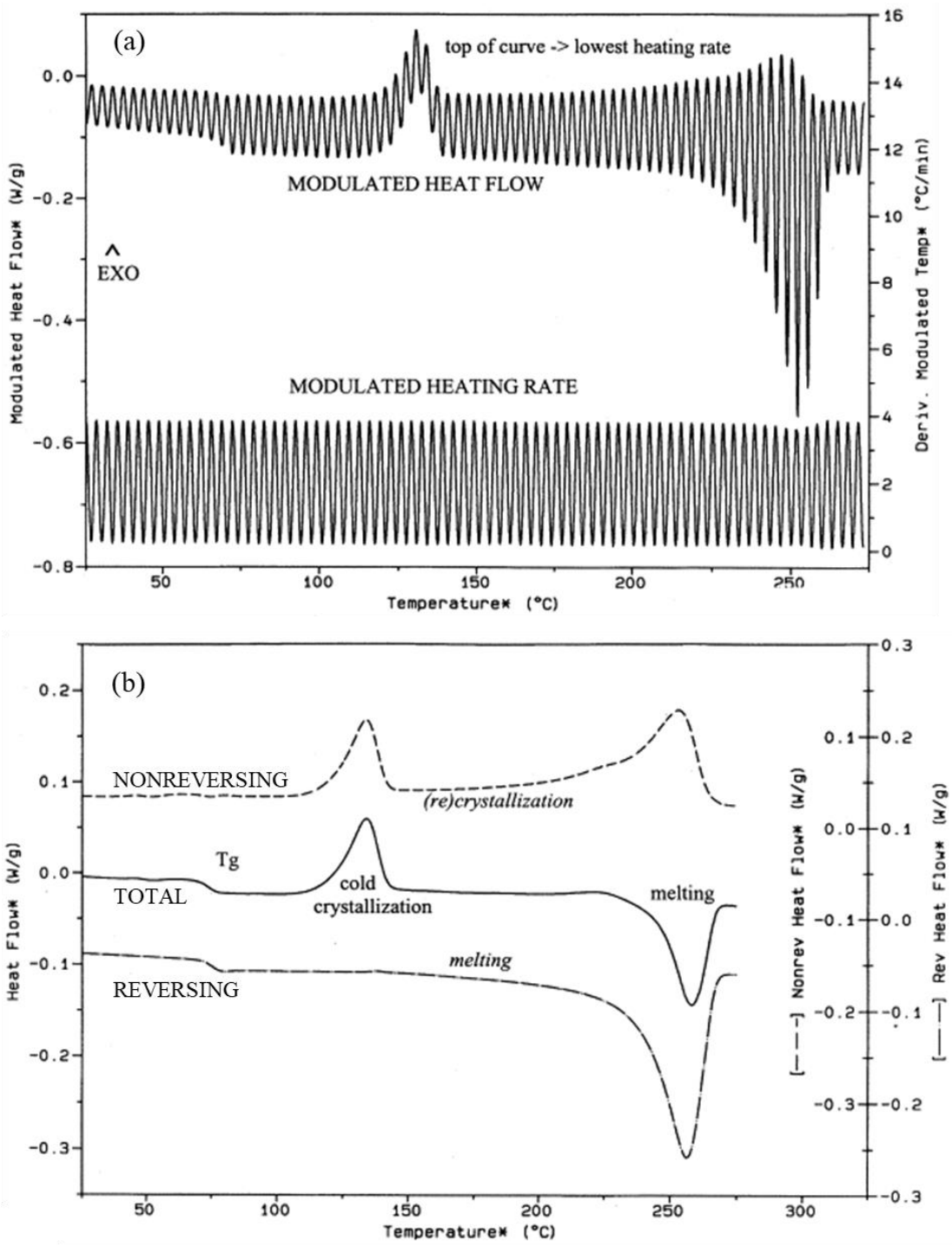

Figure 2.8: (a) Modulated heating rate (input) and modulated heat flow (output) for the MDSC heating experiment. (b) Deconvoluted signals (total heat flow, reversing heat flow, non-reversing heat flow) for the MDSC heating experiment of a quenched PET sample.

It is clear that the MDSC technique is a powerful addition to DSC that allows a more sophisticated understanding of the thermal properties of materials. As discussed above, the use of MDSC allows the deconvolution of the total heat flow signal into reversing and non-reversing components, while conventional DSC heat flow signal represents the sum of the two types of process. In addition, the combination of a high modulation amplitude and low underlying heating rate satisfies the conditions for both high resolution and sensitivity which permits the detection of weak transitions which are not detectable by conventional DSC. MDSC typically involves heating rates of 1-5 $Kmin^{-1}$, the amplitude of the temperature modulation is typically selected from a range $\pm$ 0.1 to $\pm$ 1.0 K and the period time -that time taken for one complete oscillation, i.e. reciprocal frequency- of the temperature modulation is usually selected from the range 30-80 s.

Experimental Set-Up

DSC measurements were carried out on approximately 10 mg of samples using a Q2000 TA instruments at the Material Physic Center (MPC) in San Sebastian. A key contributor to the quality of the DSC results is the sample preparation: samples are encapsulated in Tzero aluminum hermetic pans using the Tzero press (see figure 2.9). The use of small, thin, completely encapsulated samples minimizes temperature gradients and maximizes conductivity during the heating and cooling cycles. A Liquid Nitrogen Cooling System (LNCS) was used with 25 ml/min Helium flow rate.

The following protocol was applied in all of the samples studied. First, the samples were heated up until 400 K to erase any previous thermal history. The data were acquired during cooling at 3 K/min from 353 to 173 K. Temperature-modulated experiments (MDSC) were performed using a sinusoidal variation of 0.5 K amplitude and 60 s period.

Figure 2.9: Equipment used for the calorimetric analysis: (a) TA instrument Q2000 calorimeter. (b) Tzero sample encapsulation press; (c) Tzero aluminum hermetic pan (lid and bottom).

2.2.3 Neutron Scattering

Why do we need neutrons?

The importance of neutron scattering techniques was confirmed with the Nobel Prize award in 1994 to Shull for "the development of the neutron diffraction technique"[27] and Brockhouse for "for the development of neutron spectroscopy".[28] Neutrons tell us "*where atoms are and how they move*". When the neutrons are scattered by atoms in the sample being investigated, their directions change, depending on the atoms' relative positions. These scattering events show how the atoms are arranged in relation to each other revealing the structure of the sample. The changes in the neutron's velocity give information on the atoms individual and collective motions revealing their dynamic behavior.

Neutrons were discovered by Chadwick in 1932 when he presented conclusive experimental evidence on the existence of a neutral particle (nearly) isobaric with the

proton.[29] The first use of these "neutral protons" as probe dates back to neutron-diffraction experiments at Oak Ridge National Laboratory (USA) in the mid-1940s. Figure 2.10 shows the first prototype of present-day neutron spectrometers, installed in mid-1949 at Oak Ridge.

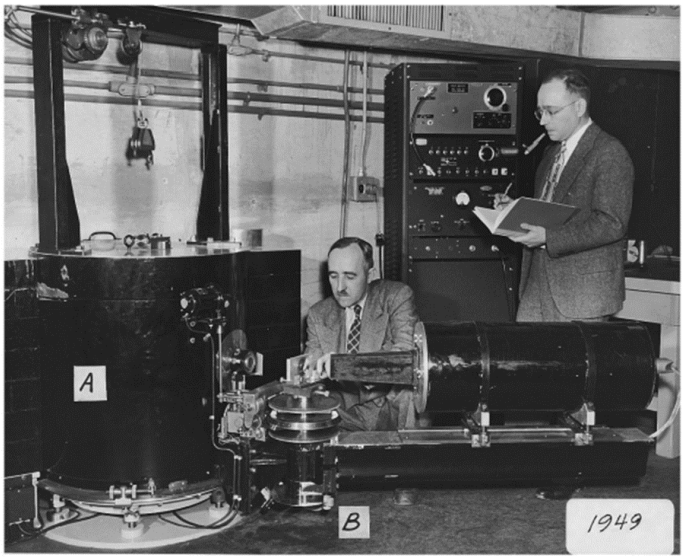

Figure 2.10: Neutron diffraction spectrometer with Ernest Wollan (kneeling) and Clifford Shull. This has many of the features of present-day spectrometers.

Basic Properties of Neutrons

The neutron is an elementary particle, a nucleon, consisting of three valance quarks, which are hold together by gluons, characterized by the following physical properties (figure 2.11):

- Mass $m = 1.675 \times 10^{-27}$Kg
- Magnetic moment $\eta = -1.913\mu_N$ in which $\mu_N = e\hbar/2m_p$
- Spin ½ and zero charge.

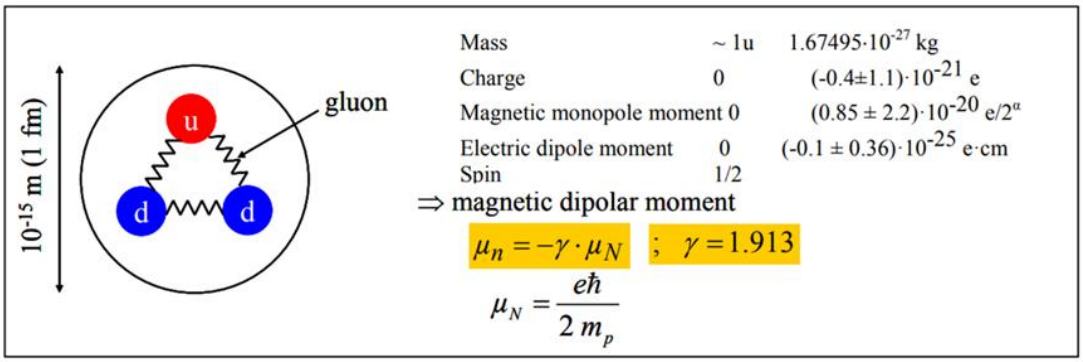

Figure 2.11: Schematics of the neutron being composed of three quarks and gluons and the main quantities characterizing the neutron as a particle.

These very specific properties make neutrons extremely useful for condensed matter investigation:

- due to the weak interaction, outside the nucleus, the neutron is not a stable particle. A free neutron undergoes a β-decay after an average lifetime of about 15 minutes. This leaves ample time for scattering investigations;

$$n \xrightarrow{15\ min} p + e^- + \bar{\nu} \tag{2.12}$$

- in contrast to the massless photon, the neutron has a mass m of about one atomic mass unit $\sim 1.675 \cdot 10^{-27}$Kg. The finite neutron mass is comparable to the mass of a nucleus and thus an appreciable amount of energy can be transferred during the scattering process;
- the neutron is a charge-less particle and thus does not show the strong Coulomb interaction with matter. This results in large penetration depths, beneficial for the study of bulk properties of matter and for the investigation of materials under extreme conditions such as very low and very high temperatures, high pressures, high magnetic and electric fields, or several of these together;
- due to their low energy (usually in meV range), neutrons are also nondestructive and samples can easily be irradiated for a long time (days) and reused after a neutron experiment;

- the neutron has a nuclear spin $1/2$ giving rise to a magnetic dipolar moment of $\mu_n = \gamma\mu_N; \gamma = 1.91; \mu_n = 5.05 \cdot 10^{-27}$ J/T; due to this magnetic moment, the neutron can interact with the magnetic field of unpaired electrons in a sample leading to *magnetic scattering*. Thus, magnetic structures and excitations can also be studied by neutron scattering.

As argued above, neutrons allow insight on both the static average chemical structure and the dynamic properties of atomic arrangements, which directly determine the physical properties of materials. The accessible scattering wavevector range allows analysis of structural properties and geometry of molecular motions on length scales from below an Angstrom to dozens of nanometers. The motions probed by neutrons cover a very broad range, from the measurement of momentum distributions on the fs time scale (eV), to slow dynamics such as the relaxation of whole polymer chains in the melt in the $\sim$100 ns (neV) timescale. Applications of neutron scattering spectroscopy to soft materials can be divided in inelastic (energy transfer peaks centered at finite energies) –to study vibrational modes and complementing Raman or Infra-red spectroscopy– and quasi-elastic scattering (energies close to the elastic line, i. e, small energy transfers centered at zero energy) – to study rotational and diffusional and other relaxational processes. These experiments nicely complement e. g. dielectric relaxation spectroscopy and NMR. In particular for Soft Matter studies, the large contrast achieved by the isotopic substitution of hydrogen (one of the main components of soft materials) with deuterium, without changing the intrinsic properties of the material, allows the selective study of specific units of a molecule or components in a multicomponent system.

Fundamental Concepts Involved in Neutron Scattering Experiments

In figure 2.12 a scheme of a generic scattering spectroscopy experiment is illustrated. The neutron beam, characterized by an initial energy E_0 and initial wave vector $\boldsymbol{k_0}$ is incident on the sample. A detector covering the solid angle $\boldsymbol{\Omega}$ counts the neutrons scattered by the sample, arriving with a final energy E and wavelength $\boldsymbol{k}$, different from the initial ones.

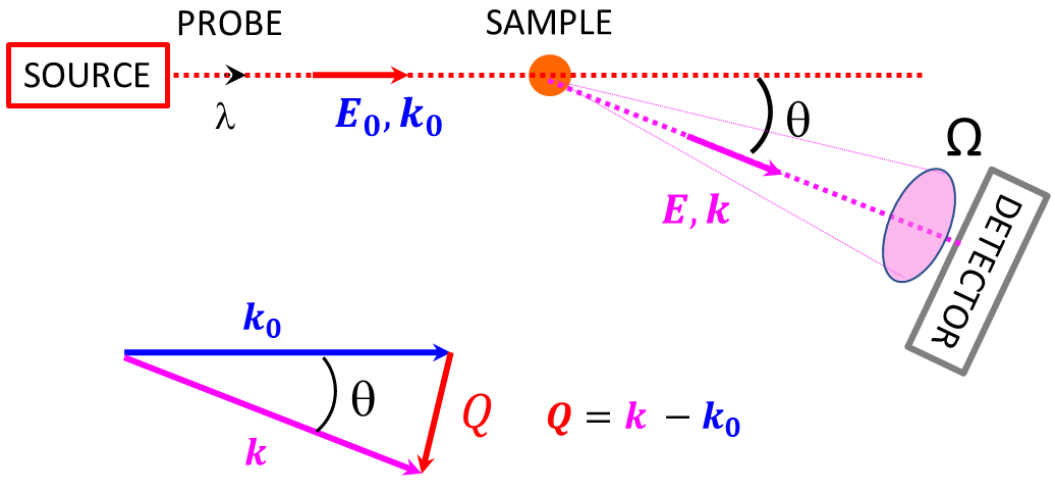

Figure 2.12: Schematic representation of neutron scattering experiment.

The difference between the incident and the final wavevectors is called scattering vector $\boldsymbol{Q}$:

$$\boldsymbol{Q} = \boldsymbol{k} - \boldsymbol{k_0} \tag{2.13}$$

The modulus of $\boldsymbol{Q}$, Q, is determined (under elastic, or close to elastic conditions) as:

$$Q = \frac{4\pi \sin(\theta/2)}{\lambda} \tag{2.14}$$

being θ the scattered angle and λ the wavelength of the neutron. Hence, we can change the explored Q-value by varying the scattering angle and/or the wavelength of the incident neutrons. The difference between the scattered energy E and the incident E_0 is the energy transferred from the sample to the neutron:

$$\hbar\omega = E - E_0 = \frac{\hbar^2}{2m}(k^2 - k_0^2) \tag{2.15}$$

There are three different types of scattering events:

1. The scattering is defined elastic when no energy is transferred to the sample ($E_0 = E$).

2. The inelastic scattering is found when a neutron loses or gains energy and it is scattered with a final energy and wavelength different from the initial ones ($E_0 \neq E$).
3. The quasi-elastic scattering is a type of inelastic scattering involving very small energy transfers. It is in fact a Doppler effect found when a neutron interacts elastically with a moving particle and its velocity undergoes a Doppler shift. It manifests itself as a broadening of the elastic peak.

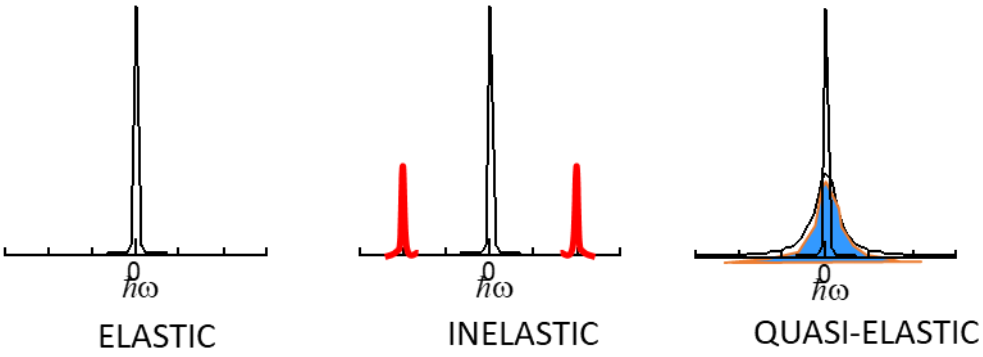

Figure 2.13: Schematic representation of types of scattering events. The broadening of the elastic line with respect to a delta function is due to the finite instrumental resolution.

In neutron scattering experiments cross-sections are measured. The double differential scattering cross-section $\partial^2\sigma/\partial\Omega\partial\hbar\omega$ is the number of neutrons scattered into a solid angle comprised between Ω and $\Omega + d\Omega$, which have experienced a change in energy between $\hbar\omega$ and $\hbar\omega + d\hbar\omega$, with respect to the total number of incident neutrons. The interpretation of $\partial^2\sigma/\partial\Omega\partial\hbar\omega$ is straightforward in terms of the *correlation functions* defined in the van Hove (1954) formalism:[30]

$$\frac{\partial^2\sigma}{\Omega\partial\hbar\omega} \propto \sum_{\alpha,\beta}\langle b_\alpha\rangle\langle b_\beta\rangle S_{\alpha\beta}^{coh}(\boldsymbol{Q},\omega) + \sum_\alpha\langle\Delta b_\alpha^2\rangle S_\alpha^{inc}(\boldsymbol{Q},\omega) \qquad (2.16)$$

The indexes α and β run over all the possible kinds of isotopes in the sample (α, β: H, D, C, O,…). Equation (2.16) involves the so-called *scattering length b* that is the parameter which describes the interaction between the neutron and the scattering nucleus.

It is a property of each single nucleus and depends on the isotope considered and the relative orientation of the neutron-nuclear spin pairs. Thus, isotopes of single atom species are characterized by different values of the scattering length. In $\partial^2\sigma/\partial\Omega\partial\hbar\omega$ a coherent (coh) and an incoherent (inc) contribution can be identified, that are weighted by the scattering lengths and their deviations from their mean value. The incoherent one arises from the random distribution of the deviations of the scattering lengths from their mean value $\langle\Delta b_\alpha^2\rangle = \langle {b_\alpha}^2\rangle - \langle b_\alpha\rangle^2$. The incoherent and coherent scattering cross section are defined as:

$$\sigma_{inc} = 4\pi\langle\Delta b_\alpha^2\rangle; \sigma_{coh} = 4\pi\langle b\rangle^2 \tag{2.17}$$

The features ($\boldsymbol{Q}$ and ω-dependencies) of both contributions to Eq. 2.16 are determined by the corresponding scattering functions [$S_{\alpha\beta}^{coh}(\boldsymbol{Q},\omega)$ involving nuclei of kinds α and β, and $S_\alpha^{inc}(\boldsymbol{Q},\omega)$ involving nuclei of kind α]. These are related, *via* Fourier transformation, with the intermediate scattering functions [$S_{\alpha\beta}^{coh}(\boldsymbol{Q},t)$ and $S_\alpha^{inc}(\boldsymbol{Q},t)$] and the van Hove correlation functions [$G_{\alpha\beta}(\boldsymbol{r},t)$ and its self-part $G_\alpha^{self}(\boldsymbol{r},t)$]. In the classical limit, $G_{\alpha\beta}(\boldsymbol{r},t)$ can be written as:

$$G_{\alpha\beta}(\boldsymbol{r},t) = \langle\frac{1}{N}\sum_{i\alpha,j\beta}^{N_\alpha N_\beta}\delta\{\boldsymbol{r} - [\boldsymbol{r}_{i\alpha}(t) - \boldsymbol{r}_{j\beta}(0)]\}\rangle \tag{2.18}$$

Here $\boldsymbol{r}_{i\alpha}(t)$ [$\boldsymbol{r}_{j\beta}(0)$]is the position vector of the i^{th} th atom of kind α [j^{th} th atom of kind β] at time $= t$ [time $= 0$] and the sum runs over all the different atoms of kinds α and β [$N_\alpha(N_\beta)$: total number of atoms of kind α (β);$N = \sum_\alpha N_\alpha$]. Thus, $G_{\alpha\beta}(\boldsymbol{r},t)d\boldsymbol{r}$ is the probability that, given a particle of kind α at the origin at time $t = 0$, any particle of kind β is in the volume element $d\boldsymbol{r}$ around position $\boldsymbol{r}$ at time t. It can easily be seen that in the static case $G_{\alpha\beta}(\boldsymbol{r},t=0) = \delta_{\alpha\beta}(\boldsymbol{r}) + g_{\alpha\beta}(\boldsymbol{r})$, where $g_{\alpha\beta}(\boldsymbol{r})$ is the static pair distribution function. Thus, *neutrons tell us where atoms are* and, through the time-dependent correlation functions, they also tell us *what the pairs of atoms do*. On the other hand, the self-part of the van Hove correlation function $G_\alpha^{self}(\boldsymbol{r},t)$ is obtained by restricting the correlations considered in Eq. 2.18 to those relating the positions of a single particle of kind α at different times:

$$G_{\alpha}^{self}(\boldsymbol{r},t) = \langle \frac{1}{N} \sum_{i\alpha}^{N_{\alpha}} \delta\{\boldsymbol{r} - [\boldsymbol{r}_{i\alpha}(t) - \boldsymbol{r}_{i\alpha}(0)]\} \rangle \quad (2.19)$$

$G_{\alpha}^{self}(\boldsymbol{r},t)$ is the Fourier transform of $I_{\alpha}^{inc}(\boldsymbol{Q},t)$ in space: incoherent scattering relates to single particle motions. So, *neutrons also tell us what a single atom does*.

Usually the systems considered in soft matter behave isotropically and therefore the above magnitudes can be expressed in terms of the moduli of the vectors. This approach will be considered in the rest of the Thesis.

The main equation 2.16 shows that the weights of the coherent and incoherent contributions to the scattered intensity are determined by the scattering lengths of the isotopes involved. The most important example, due for its implications in the soft matter field, is found for hydrogen and deuterium (table 2.3).

Table 2.3: Scattering lengths and cross sections for the isotopes commonly present in soft materials.

Isotope	$\langle b \rangle$(fm)	$\sqrt{(\langle b^2 \rangle - \langle b \rangle^2)}$(fm)	$\sigma_{coh}(10^{-24}\text{cm}^2)$	$\sigma_{inc}(10^{-24}\text{cm}^2)$
^{1}H	-3.7409	25.274	1.76	80.26
^{2}H(D)	6.674	4.04	5.59	2.05
^{12}C	6.6484	0	5.551	0.001

From table 2.3 it is clear that:

- Due to the large value of $\sigma_{inc,H}$, in H-containing systems the signal is dominated by the incoherent scattering from hydrogens, revealing their self-motions.
- Substituting H by D this incoherent contribution is drastically reduced and we obtain differently weighted coherent contributions.

- The intensity scattered by fully deuterated samples is mainly coherent and, since $b_D \cong b_C$, all pair correlations are almost equally weighted.
- The large difference between b_H and b_D provides also an elegant – and unique – way to experimentally access another kind of correlation functions: the dynamic structure factor of isotopically labeled molecular groups or macromolecules and its static counterpart, the corresponding form factor. These functions are revealed by the cross-section measured on a mixture of protonated and deuterated objects at low scattering angles.

Sources and Instrumentations

Neutron scattering experiments are realized in large facilities including a neutron source and dedicated instrumentation.

Neutron Source

The free neutron has a mean lifetime of about 900 s, therefore it is necessary to produce the free neutrons continuously as the experiment is running. Nowadays, free neutrons for scientific research are produced by nuclear reactions mainly in fission reactors or spallation sources (see figure 2.14). The typical features of a neutron beam such as the energy or the time structure of the flux are determinant parameters in order to choose the optimal set up for a given experiment. These characteristics are determined by the kind of neutron source and by the thermic moderator used. The different energy ranges of neutrons are classified according to the moderator temperature as ultra-cold, cold, thermal and epithermal.

1. Neutrons produced by nuclear fission: in order to produce neutrons by nuclear fission, a low energy thermal neutron is captured by a fissile heavy isotope such as ^{235}Uranium. The splitting uranium isotope gives rise to 2-3 neutrons with energies in the MeV range, lighter elements and release of energy. One neutron per fission is necessary to assure the continuity of the chain reaction. Finally, 1-2 neutrons are available for carrying out the scientific experiment.

2. Neutrons produced by spallation: another way to release neutrons from nuclei is via spallation reaction. High energy protons are accelerated and then hit a target made of material rich in neutrons. The excitation of the target leads to an evaporation of 20 to 30 neutrons in the MeV range per event. Therefore, more neutrons can be produced per proton pulse in a spallation source.

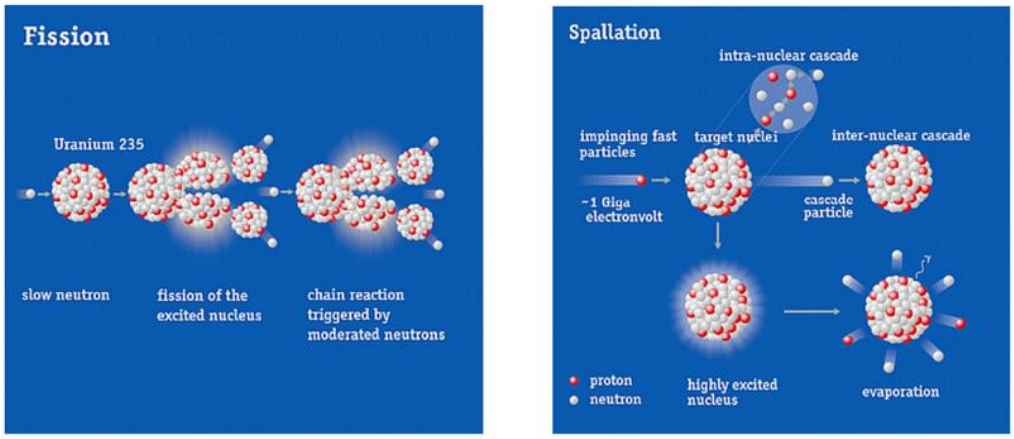

Figure 2.14: Schematic representation of the fission (a) and spallation (b) process.

Neutron Scattering Instruments Employed in this Thesis

In this thesis, three kinds of neutron scattering instruments have been employed: a diffractometer with polarization analysis, a small angle neutron scattering (SANS) instrument, and a thermal backscattering spectrometer.

Diffuse Scattering Spectrometer

Diffraction with polarization analysis was carried out by using the Diffuse Neutron Scattering Spectrometer (D7) at the Institut Laue-Langevin (ILL) in Grenoble (France). This kind of technique is usually employed on magnetic systems, since diffuse scattering yields detailed information on magnetic configurational disorder, and of the interplay between such disorder and local atomic defect structures. However, magnetic disorder scattering is generally small in amplitude and often coexists with nuclear disorder

scattering and spin-incoherent scattering. In order to separate each of these components it is necessary to use polarized neutron techniques. The diffuse scattering spectrometer D7 is a cold neutron multidetector diffractometer with full XYZ polarization analysis, with the option of time-of-flight energy analysis, in order to examine this diffuse scattering. This allows to study nuclear and magnetic short range ordered material and magnetic defect structures.

There are two modes of operation of D7, diffraction and spectroscopy:

i. The most common use of the instrument is as a diffractometer, the data are analyzed in the static approximation.[31] Depending on the experiment, the polarization direction at the sample position is usually manipulated in one of the following manners:

- *Uniaxial Polarization Analysis:* the polarization direction is fixed normal to the scattering plane and the spin-flip and non-spin-flip scattering is measured. This configuration is used for separation of coherent and spin-incoherent scattering in non-magnetic samples. Coherent scattering does not lead to spin flip, while incoherent scattering leads to 2/3 of the neutrons to spin flip. This allows discriminating the two contributions.
- *XYZ Polarization Analysis:* the polarization direction alternates between three orthogonal directions and the spin-flip and non-spin-flip scattering is measured at each direction. This configuration is used for the separation of the magnetic, incoherent, and coherent nuclear contributions to the total scattering from disordered/antiferromagnetic/paramagnetic samples.[31–33]

ii. D7 has a Fermi chopper and can be operated as a time-of-flight spectrometer with permanent polarization analysis. The Fermi chopper cuts the incident beam flux by a factor ~ 150. Thus, spectroscopy measurements need substantially more measurement time.

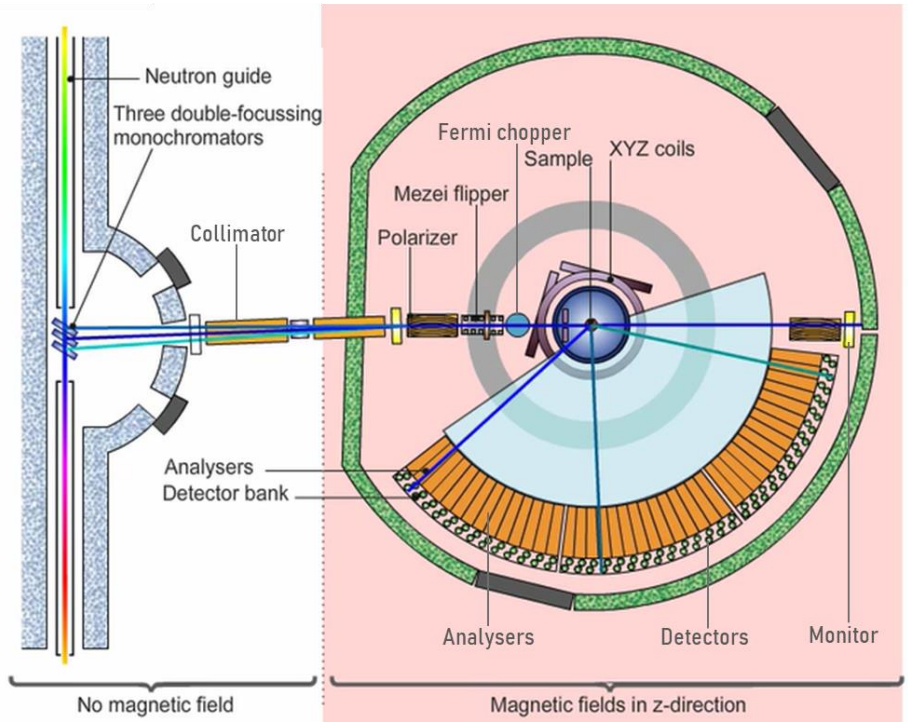

Figure 2.15: Schematic showing of the diffuse scattering spectrometer D7 at the ILL.

Figure 2.15 shows the current version of D7, which is situated on the cold neutron guide H15. Wavelengths of 3.1, 4.8 or 5.8 Å can be selected. The beam is polarized using a focusing supermirror polarizer.[34] The polarized neutron flux is 1.5×10^6 neutrons$cm^{-2}s^{-1}$ at an incident wavelength of 4.8 Å. The neutron polarization is manipulated using a Mezei-type flipper, which is "off" when measuring non-spin-flip cross-sections, and "on" when measuring spin-flip cross-sections, followed by a set of orthogonal xyz field coils situated around the sample position – which adiabatically rotate the incoming beam polarization in each of the x, y and z directions alternately. The scattered neutrons are analyzed for final spin state by supermirrors over a 132° angular range. For example, in the spin-flip (SF) configuration -illustrated in figure 2.16- the spin-up neutrons are transmitted and spin-down neutrons are absorbed by the supermirror bender analyzer before being detected.

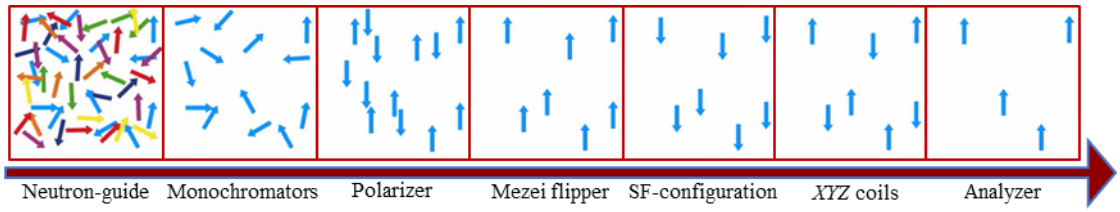

Figure 2.16: Neutron spin behaviour in spin-flip (SF) configuration.

Experimental Set-Up

Diffraction measurements with uniaxial polarization analysis were carried out in this work. Samples were filling flat aluminum sample holders (Fig. 2.17), and the thicknesses were calculated to yield a transmission of about 90%. The experiments were carried out at 300 K, where the incident neutron wavelength was set to $\lambda = 4.8$ Å to cover a Q-range from 0.13 to 2.46 $Å^{-1}$. A Vanadium sheet was used to calibrate the detector efficiency. The raw data were corrected for detector efficiency, flipping ratio, sample container and absorption using ILL standard programs.

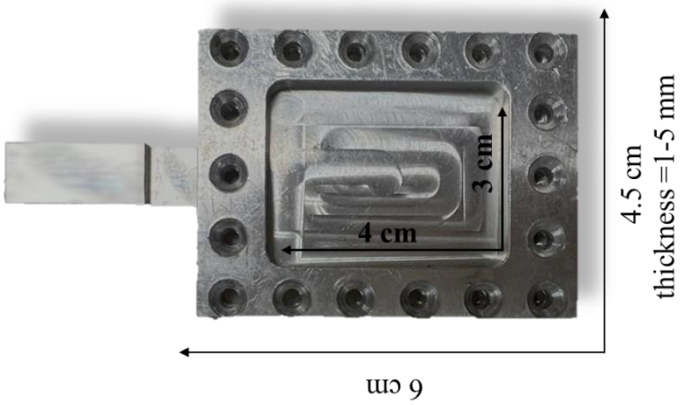

Figure 2.17: Aluminum sample holder for D7 and IN13 experiments.

Small Angle Neutron Scattering (SANS)

Small-angle neutron scattering (SANS) is a technique that measures the deviation at small angles (much less than one degree to several degrees) of a neutron beam due to

structures of characteristic dimensions of a few tenths to about 100 nanometers, such as clusters in alloys, polymers, or biological macromolecules.

Small-angle scattering due to the presence of such structural heterogeneities can also be observed with other probes as X-rays. In fact, it was discovered in the late 1930s by Guinier during X-ray diffraction experiments on metal alloys.[35] The main principles and equations still in use were exposed by Guinier and Fournet[36] in the very first monograph on SAXS (Small-Angle X-ray Scattering). The development of SANS experiments started 30 years later, in the 1960s, when neutron sources developed. The increase of interest was related to the pioneering work of Sturhmann et al.[37,38] where contrast variation experiments demonstrated that neutrons were a powerful tool to investigate materials.

The schematic representation of a small-angle scattering experiment is presented in Figure 2.18 which involves the fundamental four steps followed for any scattering experiment: monochromatization, collimation, scattering and detection. The position of the detector can usually be shifted back and forth such that different sample-detector distances can be chosen, changing thereby the Q-range explored with a given value of the incident wavelength.

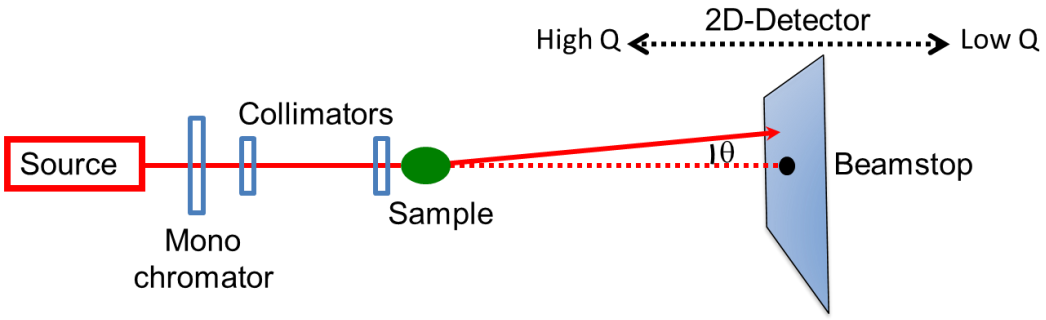

Figure 2.18: Schematic of small angle scattering experiment.

In this thesis, SANS experiments were performed on the instrument D22 at the Institute Laue Langevin in Grenoble. The schematic layout of the instrument is given in Figure 2.19. D22 was commissioned in 1995 and represents a typical pinhole SANS

instrument where, combining the pinhole mode using different neutron wavelengths in the range $\lambda = 0.45 - 4$ nm and sample detector distances from 1.1 to 17.6 Å^{-1}, a wide Q-range between $4 \cdot 10^{-4}$ and 0.44 Å^{-1}(no detector off-set) or 0.85 Å^{-1} (with detector off-set) can be explored. D22 possesses the largest area multidetector (^{3}He) of all SANS instruments currently available. The high neutron flux $(\text{up to } 10^8\ \text{neutron/s/cm}^2)$ and the flexibility of its setup make D22 an instrument that is particularly suited for real-time experiments and weakly scattering samples.[39]

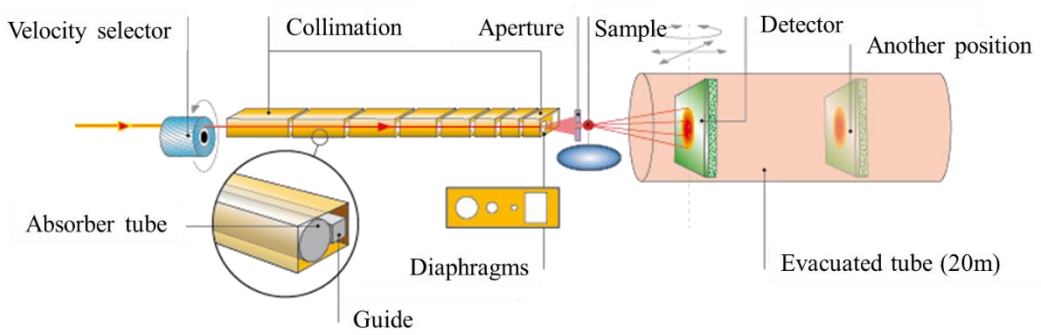

Figure 2.19: Representation of the small angle neutron scattering instrument D22, ILL.

Experimental Set-Up

The SANS experiments were performed using an incident wavelength $\lambda = 6$ Å and sample-detector distances (SSD): 17, 5.6 and 1.5 m, a Q-range between 0.003 and 0.58 Å^{-1}. The samples with thickness of 1 mm were sandwiched between aluminum foils (Fig. 2.20). Experiments were carried out first at 298 K. Then the samples were heated well above the glass transition temperature and data were collected in isothermal conditions at different temperatures. The data were reduced using ILL in-house software, correcting measured intensities for the transmission, deadtime, sample background and detector background (with B_4C as a neutron absorber at the sample position).

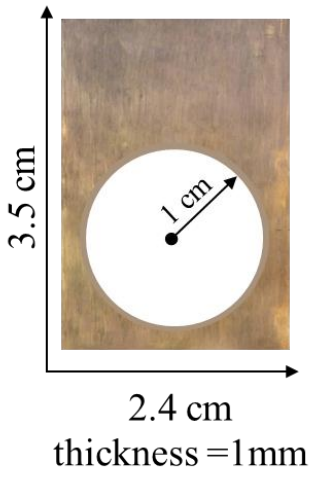

Figure 2.20: Sample holder for D22 experiments, that was covered with aluminum foils after placing the sample film in the circular hole.

Thermal Neutron Backscattering Spectrometer

The backscattering technique was proposed in 1966 by Maier-Leibnitz.[40] Until the invention of the spin echo technique, backscattering spectrometers provided the finest energy resolution available.

The thermal neutron backscattering (BS) spectrometer IN13 was designed in the 1980s at the ILL for the study of tunneling effects.[41] IN13 was built in order to achieve a good energy resolution with a large Q-range, as these are the important conditions for tunneling experiments. The shorter wavelength allows specially to access a much larger Q-range compared to a cold instrument (see equation 2.16). In the case of IN13 a scattering vector Q of up to $4.9\,\text{Å}^{-1}$ is available. IN13 is operated since 1998 as a Collaborating research group (CRG) instrument.[42]

A schematic layout of the spectrometer is displayed in figure 2.21. The instrument is situated on the H24 guide of the ILL which is fed with thermal neutrons coming from the reactor core. The neutrons have a Maxwellian distribution centered around 2 Å due to the moderator temperature of $300\,\text{K}$. A monochromator made out of CaF_2 crystals is employed to extract neutrons with a wavelength of $2.23\,\text{Å}$ from the guide. For this purpose, the (422) reflection of the crystals is used. Several types of scans can be

performed on the spectrometer. For elastic scans, the energy of the incoming neutrons is kept fix and equal to that of the neutrons detected after interacting with the sample. To perform inelastic scans, the energy of the neutrons hitting the sample is changed. This is achieved by heating or cooling the monochromator, which results in a change of the lattice constant of the monochromator crystals. To obtain a good energy resolution an almost backscattering condition is employed already at this stage.

The sample is normally contained in a closed cycle cryostat (displex) or a cryofurnace for temperature control. The displex allows experiments in a temperature range from 3 K to 550 K. A set of seven analyzer crystals (again CaF_2, (422) reflection) installed in perfect backscattering condition selects the neutrons of the right energy, which pass a second time through the sample before reaching the detectors. A sample transmission of the order of 90% or higher provides a reasonably low probability that the neutrons are scattered again while they pass a second time through the sample. Finally, the neutrons are detected by 35 ^{3}He counters and in the small angle region by a Position Sensitive Detector (PSD). In order to suppress the neutrons which are scattered directly from the sample onto the detectors and thus do not fulfil the backscattering condition, a chopper is used. Only neutrons which were selected by the analyzers are counted. Neutrons that pass the sample without being scattered are stopped by a cadmium coated beam stop, which can be replaced by a monitor to measure transmission. In total IN13 makes use of two monitors. The first one is permanently installed in the beam, positioned between chopper and sample. It is used to normalize the scattered intensity to the incoming flux. The second one is used to measure transmission and is mounted on a linear stage after the sample position. During data acquisition it is moved out of the beam, for transmission measurements it is put in. Elastic scattering (energy transfer $= 0$) or inelastic scattering (energy transfer up to 200 μeV) is analyzed as a function of the scattering angle. This gives access to the dynamical characteristics of the scattering sample, and mostly to the hydrogen atoms it contains, as explained above.

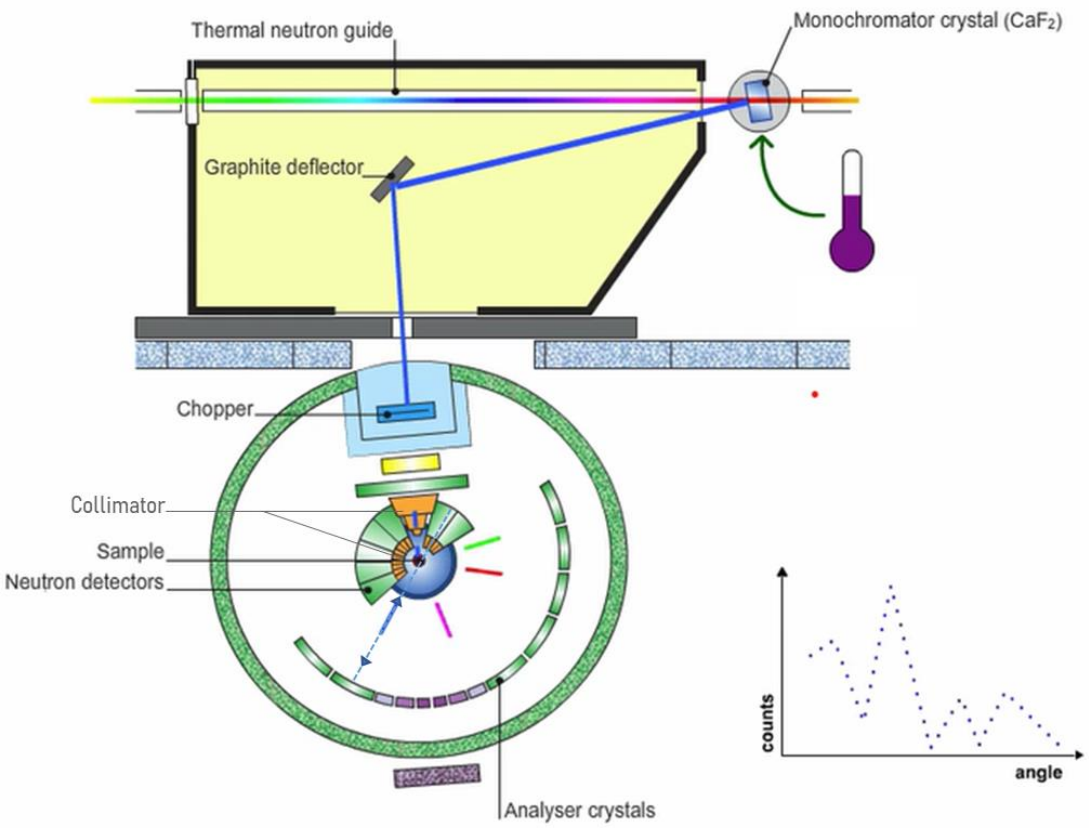

Figure 2.21: Schematic layout of the IN13 backscattering spectrometer.

The high energy resolution of the order of few μeV and the availability of high momentum transfer ($Q<4.9Å^{-1}$) makes IN13 particularly useful for the microscopic study of single particle motions (jump reorientations, rotational and translational diffusion tunneling) observed by incoherent neutron scattering.

In Elastic Fixed Window Scans (EFWS) the energies of the incident and the detected neutrons after interacting with the sample are identical. The recorded intensity includes contributions with energy transfers smaller than the resolution of the spectrometer $\delta\hbar\omega$.

Experimental Set-Up

The EFWS were carried out with $\lambda=2.23$ Å. IN13 offers an energy resolution of $\delta\hbar\omega \approx 8$ μeV. The neat protonated samples and blends of both isotopic label with SBR concentration of 80, 50 and 20% were investigated. The thicknesses of the samples were

chosen such that a transmission of about 90% was expected. They were filling flat aluminum sample holders (Figure 2.17) and placed at 135° with respect to the incident beam. The experiments consisted of recording the elastically scattered intensity in isothermal conditions for the different scattering angles, covering an effective Q-range $0.52 \leq Q \leq 4.5$ Å^{-1}. At every temperature considered the measuring time was of about 3 h. The samples were first cooled down to 20 K, where the reference measurement was performed. Thereafter, measurements were carried out in the temperature interval $50 \leq T \leq 300$ K, with step of 50 or 20 K (glassy state) and 10 K (around and above the calorimetric T_g's). The perpendicular transmission of the samples was determined to properly subtract the background signal measured on an empty cell at 285 K. The results at each temperature were normalized to the reference measurement at 20 K.

Magnitudes Accessed by the Neutron Scattering Experiments in this Thesis

As a representative example, Fig. 2.22 shows the differential scattering cross section measured by SANS on the sample with $50/50$ composition (50hSBR$_1$-50dPS$_1$). These data are combined with the information obtained from D7. Using both instruments, the Q-range from about 0.003 to 2.5 Å^{-1} has been covered. This is equivalent to spatial scales ($\sim 1/Q$) ranging from about the bond length to several nanometers. In addition to the diffraction experiments, also EFWS on IN13 was carried out which cover the high-Q regime $0.52 \leq Q \leq 4.5$ Å^{-1} . Let consider the origin of the contributions to the scattered intensity, taking Fig. 2.22 as illustration.

The interaction of a given nucleus with neutrons is characterized by the scattering length b. This magnitude depends on the relative orientation of the neutron-nuclear spin pairs and varies from one isotope to another. The huge difference of the scattering length values for hydrogen and deuterium ($b_H = -3.74$ fm, $b_D = 6.67$ fm, $b_D \sim b_C = 6.65$ fm) produces a high contrast between h/d isotopically labeled macromolecules. Therefore, SANS diffraction experiments accessing low values of Q –exploring thus large-scale properties– on mixtures where one of the components is protonated and the other is deuterated are highly sensitive to thermally driven concentration fluctuations (TCF). In such a Q-range also long-range density fluctuations contribute to the scattered intensity,

though this contribution is usually expected to be much less important than that of TCF. Both, concentration and density fluctuations, give rise to coherent scattering. Toward high-Q values –local length scales– the contribution of TCF tends to vanish, and coherently scattered neutrons reflect instead the (partial) structure factors revealing the short-range order in the sample. Its main manifestation in glass-forming systems like polymers is the broad peak usually appearing in the Q-range of about 1 $Å^{-1}$ reflecting inter-molecular correlations.

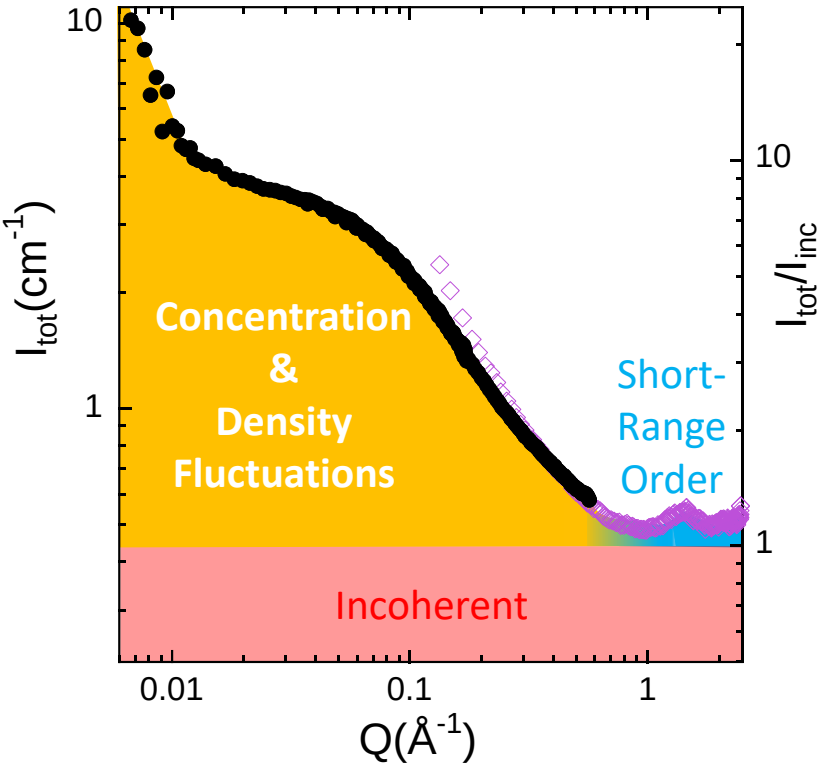

Figure 2.22: SANS (circles, scale on the left) and D7 (diamonds, scale on the right) results on the sample 50hSBR$_1$-50dPS$_1$ around RT. Areas with different colors show the different contributions to the differential scattering cross-section: the Q-independent incoherent scattering (red) and the coherent contributions mainly dominated by concentration and long-range density fluctuations at low Q (yellow) and reflecting the short-range order at high Q (blue).

Superimposed to these coherent contributions, incoherent scattering of very different nature is also present in the measured signal. The incoherent differential scattering cross

section is Q-independent and appears as a flat background in diffraction experiments. Incoherent scattering is particularly important by hydrogen nuclei. The incoherent scattering cross-section of H amounts to $\sigma_{inc}^{H} \approx 80$ barn, while its coherent cross-section is $\sigma_{coh}^{H} \approx 2$ barn.

In general, in hydrogenated samples, or samples containing hydrogens, the incoherent cross section (summed up over all nuclei of the system) is much higher than the coherent one. However, this does not imply that in a given Q-region the incoherent scattering always dominates the spectrum, since –as in the example of Fig. 2.22– coherent scattering strongly depends on Q. As can be seen in Fig. 2.22, D7 results tell us that for the sample 50hSBR$_1$-50dPS$_1$ the incoherent contribution dominates the scattered intensity in the high-Q range above ≈ 0.5 Å^{-1}. This is the range explored by IN13. On IN13, no polarization analysis is performed. Therefore, the intensity recorded in the EFWS has both, incoherent and coherent contributions.

Even if deuterons also scatter incoherently, their incoherent cross-section (2 barn) is negligible compared to that of hydrogen. Carbon scatters only coherently. Thus, incoherent scattering from the samples investigated basically stems from hydrogens. Contrarily to coherent scattering, incoherent scattering does not tell anything about structural features of the sample. However, it carries very valuable information on the self-atomic displacements that can be unveiled by energy-transfer ($\hbar\omega$) resolved experiments. The incoherent double differential cross-section is in fact proportional to the incoherent scattering function $S^{inc}(Q,\omega)$. $S^{inc}(Q,\omega)$ is the Fourier transform of the intermediate incoherent scattering function $I^{inc}(Q,t)$ and the double Fourier transform yields the self-part of the van Hove correlation function $G^{self}(r,t)$. In the classical limit, $G^{self}(r,t)$ is the probability of a given nucleus to be at a distance r from the position where it was located at a time t before. Incoherent scattering looks at correlations between the positions of the same nucleus at different times. Since IN13 EFWS record the intensity of neutrons scattered with energy transfers smaller or equal to the instrument energy resolution ($\delta\hbar\omega \approx 8$ μeV), the accessed function corresponds to the intermediate incoherent scattering function at the time corresponding to the IN13 resolution $I^{inc}(Q,t_R)$, with $t_R = \delta\hbar\omega \approx 8$ μeV.

3.3 References

(1) Bouty, A.; Petitjean, L.; Chatard, J.; Matmour, R.; Degrandcourt, C.; Schweins, R.; Meneau, F.; Kwasńiewski, P.; Boué, F.; Couty, M.; Jestin, J. Interplay between Polymer Chain Conformation and Nanoparticle Assembly in Model Industrial Silica/Rubber Nanocomposites. *Faraday Discuss* **2016**, *186*, 325–343.

(2) Tanaka, Y.; Sato, H.; Saito, K.; Miyashita, K. Determination of Sequence Distribution in Styrene-Butadiene Copolymer I. 1H-NMR Study of Styrene Oligomers. *Rubber Chemistry and Technology* **1981**, *54* (4), 685–691.

(3) Debye, P. Einige Resultate Einer Kinetischen Theorie Der Isolatoren. *Physik Z.* **1912**, *13*, 97.

(4) Kremer, F.; Schönhals, A. *Broadband Dielectric Spectroscopy*; Springer-Verlag Berlin Heidelberg, 2003.

(5) Havriliak, S.; Negami, S. A Complex Plane Analysis of α-Dispersions in Some Polymer Systems. *Journal of Polymer Science Part C: Polymer Symposia* **1966**, *14* (1), 99–117.

(6) Havriliak, S.; Negami, S. A Complex Plane Representation of Dielectric and Mechanical Relaxation Processes in Some Polymers. *Polymer* **1967**, *8* (C), 161–210.

(7) Cole, K. S.; Cole, R. H. Dispersion and Absorption in Dielectrics I. Alternating Current Characteristics. *J. Chem. Phys* **1941**, *9*, 341.

(8) Davidson, D. W.; Cole, R. H. Dielectric Relaxation in Glycerol, Propylene Glycol, and n-Propanol. *The Journal of Chemical Physics* **1951**, *19*, 1417.

(9) Lindsey, C. P.; Patterson, G. D. *The Journal of Chemical Physics* **1980**, *73*, 341.

(10) Alvarez, F.; Alegria, A.; Colmenero, J. Relationship between the Time-Domain Kohlrausch-Williams-Watts and Frequency-Domain Havriliak-Negami Relaxation Functions. *Phys Rev B* **1991**, *44*.

(11) Alvarez, F.; Alegría, A.; Colmenero, J. Interconnection between Frequency-Domain Havriliak-Negami and Time-Domain Kohlrausch-Williams-Watts Relaxation Functions. *Phys Rev B* **1993**, *47* (1), 125.

(12) Gill, P.; Moghadam, T. T.; Ranjbar, B. *Differential Scanning Calorimetry Techniques: Applications in Biology and Nanoscience*; 2010.

(13) Höhne, G. W. H.; Hemminger, W. F.; Flammersheim, H. J. *Differential Scanning Calorimetry: An Introduction for Practitioners*; 1996.

(14) Privalov, P. L.; Potekhin, S. A. Scanning Microcalorimetry in Studying Temperature-Induced Changes in Proteins. *Methods Enzymol* **1986**, *131* (C), 4–51.

(15) Watson, E. S.; O'Neill, M. J.; Justin, Joshua.; Brenner, Nathaniel. A Differential Scanning Calorimeter for Quantitative Differential Thermal Analysis. *Anal Chem* **1964**, *36* (7), 1233–1238.

(16) Haines, P. J.; Reading, M.; Wilburn, F. W. Differential Thermal Analysis and Differential Scanning Calorimetry. *Handbook of Thermal Analysis and Calorimetry* **1998**, *1*, 279–361.

(17) Zucca, N.; Erriu, G.; Onnis, S.; Longoni, A. An Analytical Expression of the Output of a Power-Compensated DSC in a Wide Temperature Range. *Thermochim Acta* **2004**, *413* (1–2), 117–125.

(18) Danley, R. L. New Heat Flux DSC Measurement Technique. *Thermochim Acta* **2002**, *395* (1–2), 201–208.

(19) Reading, M.; Elliott, D.; Hill, V. L. A New Approach to the Calorimetric Investigation of Physical and Chemical Transitions. *Journal of Thermal Analysis* **1993**, *40*, 949–955.

(20) Reading, M. Modulated Differential Scanning Calorimetry-a New Way Forward in Materials Characterization. *Trends Polym. Sci.* **1993**, *1.8*, 248–253.

(21) Reading M.; Luget A.; Wilson R. *Thermochim. Acta, 238 (1994).*

(22) Jones, K. J.; Kinshott, I.; Reading, M.; Lacey, A. A.; Nikolopoulos, C.; Pollock, H. M. The Origin and Interpretation of the Signals of MTDSC. *Thermochim Acta* **1997**, *304–305* (SPEC. ISS.), 187–199.

(23) Haines, P. J.; Reading, M.; Wilburn, F. W. Differential Thermal Analysis and Differential Scanning Calorimetry. *Handbook of Thermal Analysis and Calorimetry* **1998**, *1*, 321.

(24) Reading, M.; Hourston, D. Modulated Temperature Differential Scanning Calorimetry: Theoretical and Practical Applications in Polymer Characterisation. *Springer Science & Business Media* **2006**, *6*.

(25) Menczel Joseph D.; R. Bruce Prime. *Thermal Analysis of Polymers: Fundamentals and Applications*; John Wiley & Sons, Ed.; 2009; Vol. Chapter 2.

(26) Verdonck, E.; Schaap, K.; Thomas, L. C. A Discussion of the Principles and Applications of Modulated Temperature DSC (MTDSC). *Int J Pharm* **1999**, *192*, 3–20.

(27) Shull, C. G. Early Development of Neutron Scattering. *Nobel lecture* **1994**.

(28) Brockhouse, B. N. Slow Neutron Spectroscopy and the Grand Atlas of the Physical World. *Nobel lecture* **1994**.

(29) Chadwick, J. Possible Existence of a Neutron. *Nature* **1932**, *129* (3252), 312.

(30) Lovesey, S. W. Theory of Neutron Scattering from Condensed Matter. **1984**.

(31) Braden, M. Introduction to the Theory of Thermal Neutron Scattering. *Acta Crystallogr A* **2012**, *68* (5), 665–665.

(32) Schaerpf, O.; Capellmann, H. The XYZ-Difference Method with Polarized Neutrons and the Separation of Coherent, Spin Incoherent, and Magnetic Scattering Cross Sections in a Multidetector. *Physica Status Solidi A Appl Res* **1993**, *135* (2), 359–379.

(33) Stewart, J. R.; Deen, P. P.; Andersen, K. H.; Schober, H.; Barthélémy, J. F.; Hillier, J. M.; Murani, A. P.; Hayes, T.; Lindenau, B. Disordered Materials Studied Using Neutron Polarization Analysis on the Multi-Detector Spectrometer, D7. *J Appl Crystallogr* **2009**, *42* (1), 69–84.

(34) Schärpf, O. Thin-Film Devices and Their Role in Future Neutron Spectroscopic Investigations. *Physica B Condens Matter* **1991**, *174* (1–4), 514–527.

(35) Guinier, A. La Diffraction Des Rayons X Aux Très Petits Angles: Application à l'étude de Phénomènes Ultramicroscopiques. *Ann Phys (Paris)* **1939**, *11* (12), 161–237.

(36) Guinier, A.; Fournet, G. Small Angle Scattering of X-Rays Wiley Interscience. *New York* **1955**.

(37) Stuhrmann, H. B.; Duee, E. D. The Determination of the Scattering Density Distribution of Polydisperse Solutions by Contrast Variation: A Neutron Scattering Study of Ferritin. *J. Appl. Cryst* **1975**, *8*, 538.

(38) Stuhrmann, H. B. Neutron Small-Angle Scattering of Biological Macromolecules in Solution. *J Appl Crystallogr* **1974**, *7* (2), 173–178.

(39) Grillo, I. *Small-Angle Neutron Scattering and Applications in Soft Condensed Matter*.

(40) Maierlei, H. Grundlagen fur die Beurteilung von Intensitats-und Genauigkeitsfragen bei Neutronenstreumessungen. *Nukleonik* **1966**, *8* (2), 61.

(41) Prager, M.; Heidemann, A. *Rotational Tunneling and Neutron Spectroscopy: A Compilation*; 1997.

(42) Deriu, A.; Paciaroni, A.; Zaccai, J. First Experimental Results from the IN13-Collaborative Research Group (CRG) at the ILL. *Physica B Condens Matter* **2000**.

Chapter 3

Characterization of the Neat Components

The aim of this chapter is to apply the methodology described in the previous chapter to the investigation of the dynamics of the neat components of a simplified industrial system, particularly styrene-butadiene rubbers ($hSBR_1$, $hSBR_2$, $dSBR_1$) and oligomers of polystyrene (hPS_1, dPS_1, dPS_2). The dynamical properties of the pure components are noticeable affected by relatively small differences in copolymer composition and/or microstructure. As experimental techniques, in this chapter, DSC, BDS and neutron scattering (elastic fixed window scan measurements) were used. To exploit neutron scattering selectivity, the use of samples where one of the components is deuterated is mandatory.

3.1 Dielectric Relaxation Response

Figure 3.1 shows an example of the dielectric loss as a function of the frequency for the pure polymers both protonated and deuterated, $hSBR_1$, $hSBR_2$, $dSBR_1$ at 230 K and hPS_1, dPS_1, dPS_2 at 300 K. In this representation $\tan\delta = \frac{\varepsilon''}{\varepsilon'}$ has been used to minimize the impact of sample geometry changes that could occur for measurements over a large temperature interval. The main loss peak is due to the segmental dynamics or α-relaxation, for both SBR and PS, detected by BDS through the motions of the dipolar groups of the chains. The origin of the dipole moment is the positive and negative charge concentrations in the material under investigation, that depend on the chemical structure (figure 3.2).

The dielectric loss peaks of the different protonated and deuterated homopolymers are centered at different frequencies for the same temperature considered. Since dielectric spectroscopy is not sensitive to deuteration, these differences must be due to the different microstructures of the polymers, leading to distinct segmental dynamics. For SBR, the relaxation spectrum depends on vinyl content[1]. As shown in table 2.1 $hSBR_2$ has the lowest amount of vinyl content around $\sim$18%, while $hSBR_1$ and $dSBR_1$ has $w_s \sim 22\%$ and $w_{1.2-B} \sim 19\%$. For the PS oligomers the differences in the peak position depend on the M_w due to the pronounced influence of end groups in the dynamics.

Regarding the amplitude, it is also apparent that $hSBR_2$, having lowest vinyl content, has a stronger dielectric relaxation than $hSBR_1$; while $dSBR_1$ has a stronger dielectric relaxation than $hSBR_1$. Concerning PS, dPS_2 has a stronger dielectric relaxation than dPS_1, while hPS_1 and dPS_1 have similar loss peak area.

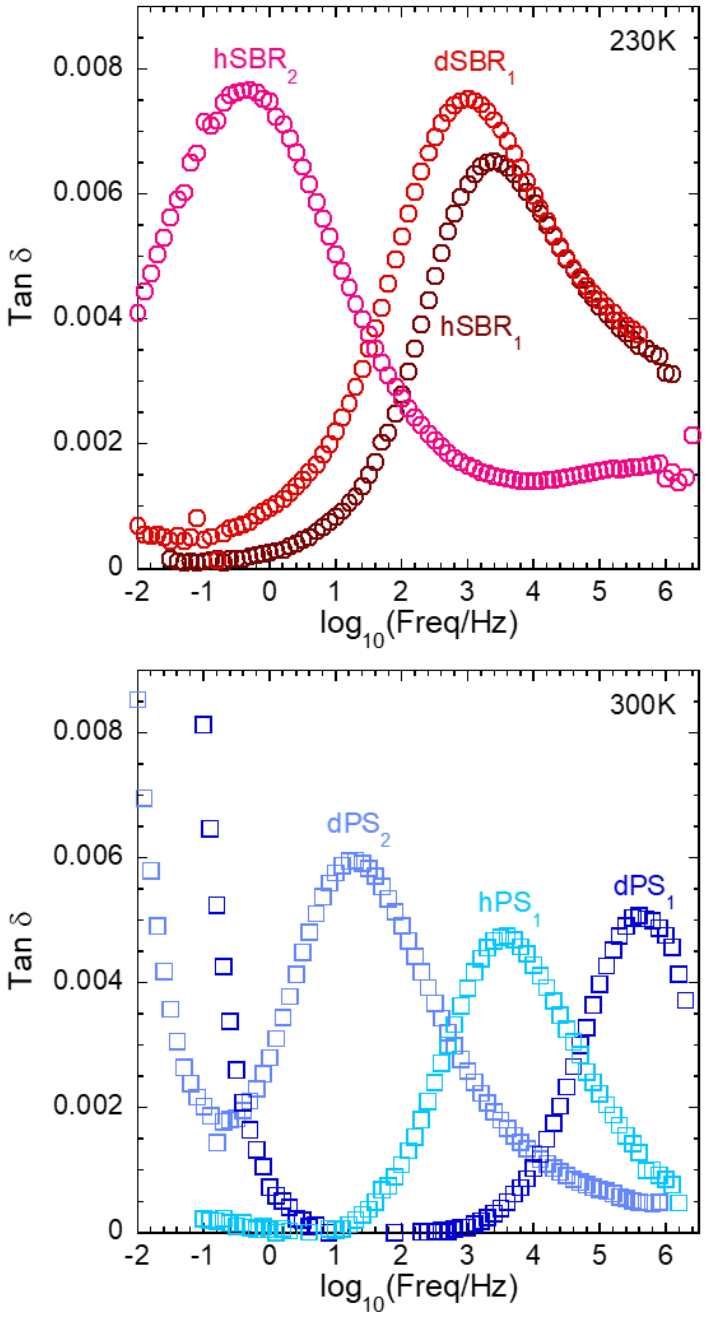

Figure 3.1: Frequency dependence of the dielectric tan δ at 230 K for SBR and at 300 K for PS, showing both the protonated and deuterated polymers.

In all cases, SBR has a stronger dielectric relaxation than PS, it shows a larger loss peak area but both contributions will be relevant for the dielectric relaxation of the mixtures.

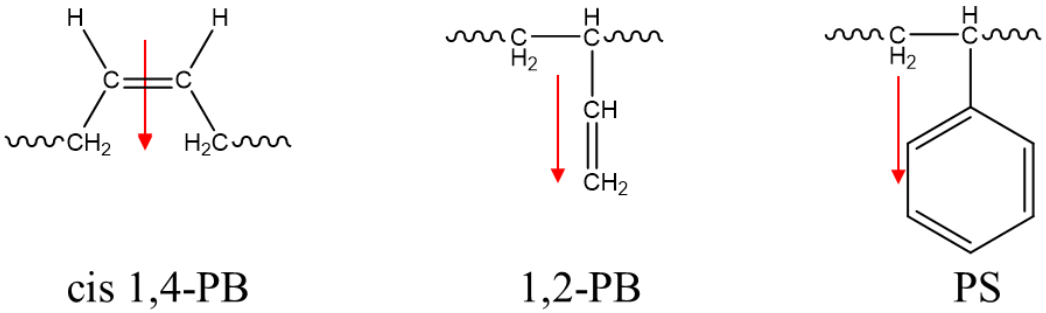

Figure 3.2: Chemical structures of different components and schematics of their dipole components (red arrows).

A full but simple characterization of the dielectric response of the pure polymers has been done first. In figure 3.3 are shown the tridimensional representations of the dielectric loss for the neat samples $hSBR_2$ and dPS_2, where the β and α relaxations can clearly be identified. The low-frequency increase of the data is due to conductivity effects. In the isothermal representation (figure 3.4a) --frequency dependence of the dielectric $\tan\delta$ at constant temperature-- it is observed that the segmental peak position strongly depends on temperature and the dielectric peaks of the two homopolymers are centered at similar frequencies at much lower temperatures for SBR than for PS. Figure 3.4b shows an isochronal dielectric representation for $hSBR_2$. In an isochronal representation the evolution of the dielectric relaxation as a function of temperature is followed at fixed frequency, in this case 10^4 Hz. A β and an α relaxation for SBR can clearly be detected, the peak centered at lower temperature being the one corresponding to the β relaxation, due to the local motion of *cis* 1,4-polybutadiene.[2,3]

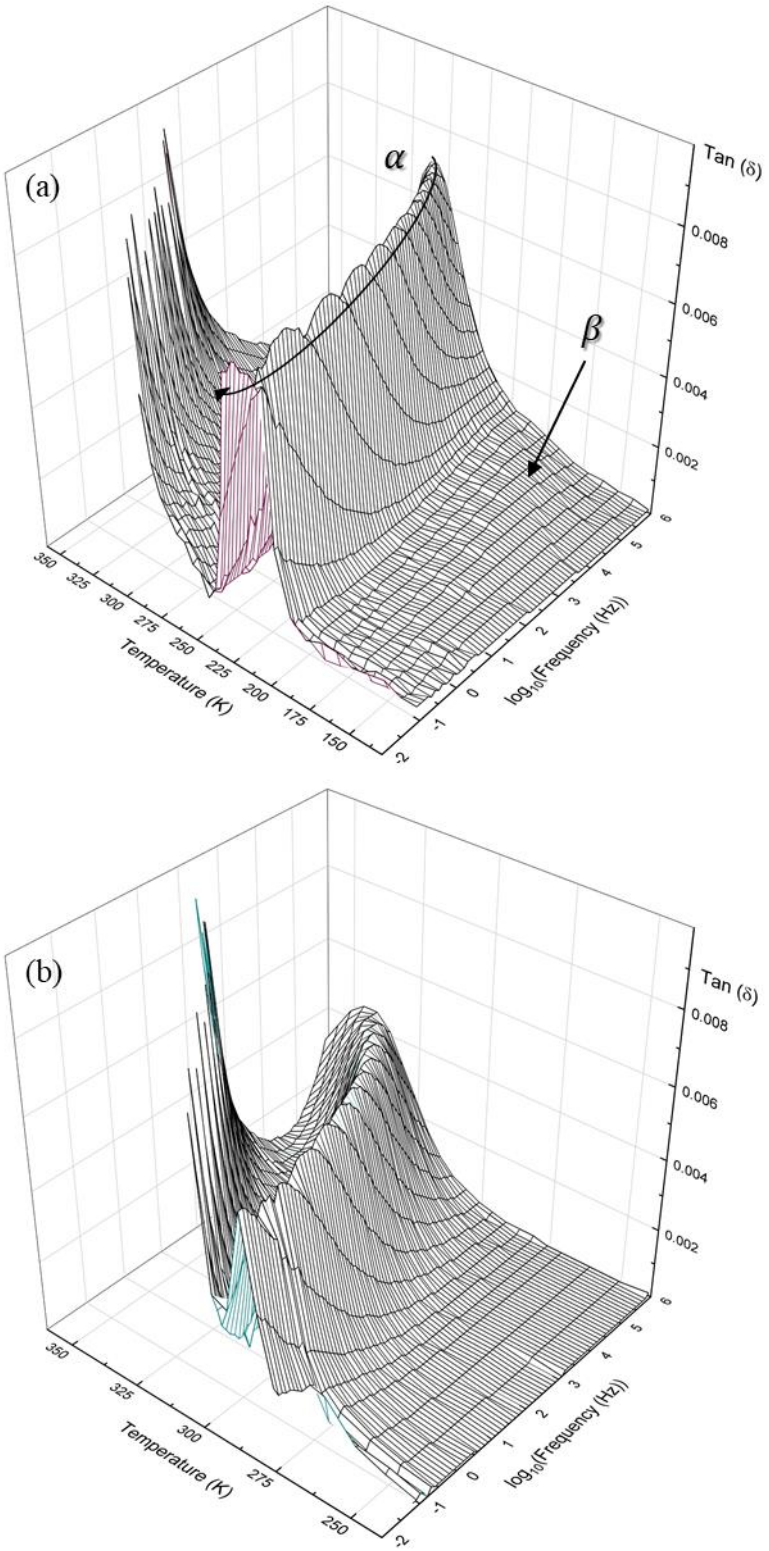

Figure 3.3: Tridimensional representation of the dielectric loss as a function of the temperature and the frequency (a) for $hSBR_2$ and (b) for dPS_2.

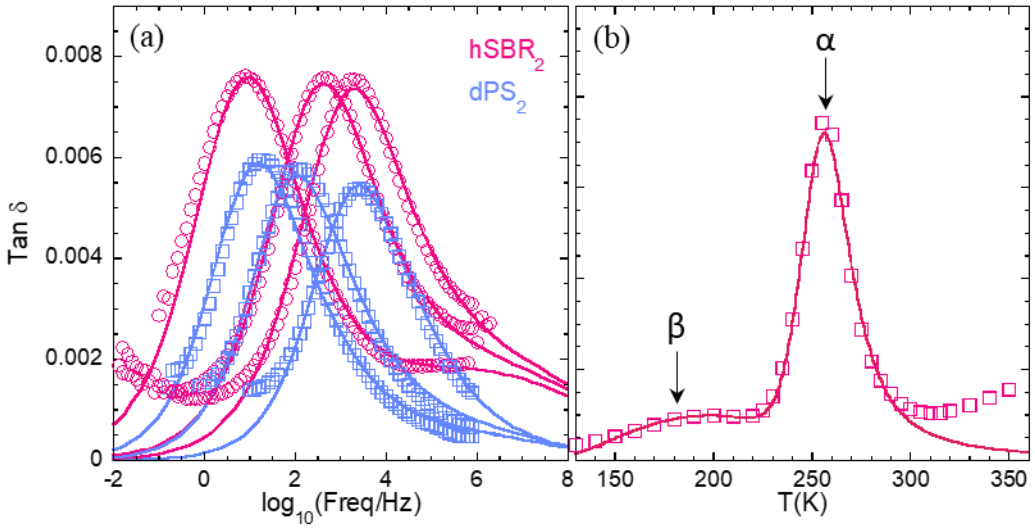

Figure 3.4: (a) Frequency dependence of the dielectric tan δ at 235 K, 245 K, and 250 K for SBR (empty circles) and at 300 K, 305 K, and 315 K for PS (empty squares). (b) Dielectric tan δ as a function of temperature at 10^4 Hz for $hSBR_2$. The solid lines represent the fits by means of the Havriliak-Negami equation for the α-relaxation and the addition of the β-relaxation calculated by extrapolating the lower temperature description using Eq. 2.4 and 3.1.

The dielectric segmental α-relaxations can be described by means of the Havriliak-Negami (HN) equation (see Eq. 2.4).[4–7] In order to improve the description of the experimental data of the neat components, for both SBR and PS the contribution of the β-relaxation has been taken in account, which occurs at low-temperatures/high-frequencies due to local dynamics. At low temperatures, the dielectric losses corresponding to the β-relaxation can be fitted to a good approximation with a Gaussian function:

$$\varepsilon_{\beta}^{''} = A_{\beta} exp\left[-\frac{1}{2}\left(\frac{log_{10}(\omega\tau_{\beta})}{\sigma_{\beta}}\right)^2\right] \tag{3.1}$$

Where A_β is the amplitude, τ_β is the relaxation time, and σ_β is a parameter accounting for the broadness of the peak. They are temperature dependent parameters, which were determined by fitting experimental data below T_g. The temperature dependent values of

the parameters have been characterized by the expressions given in table 3.1 for the different samples considered.

Table 3.1: Parameters involved in the description of the dielectric β-relaxation of the pure components $hSBR_1$, $hSBR_2$, $dSBR_1$, hPS_1, hPS_2 and dPS_1, obtained by fitting experimental data by means of the Gaussian function.

Sample	$\tau_\beta(T)$	$\sigma_\beta(T)$	$A_\beta(T)$
$hSBR_1$	$3.12 \cdot 10^{-15}\, exp\left[\frac{3910\ K}{T}\right]$	$-1.0358 + \left(\frac{592\ K}{T}\right)$	$0.0029576 - \left(\frac{0.33526\ K}{T}\right)$
$dSBR_1$	$3.12 \cdot 10^{-15}\, exp\left[\frac{3910\ K}{T}\right]$	$-1.0358 + \left(\frac{592\ K}{T}\right)$	$0.0029576 - \left(\frac{0.33526\ K}{T}\right)$
$hSBR_2$	$5.41 \cdot 10^{-15}\, exp\left[\frac{3898\ K}{T}\right]$	$1.5984 + \left(\frac{174\ K}{T}\right)$	$0.0024533 - \left(\frac{0.27784\ K}{T}\right)$
hPS_1	$5.7 \cdot 10^{-12}\, exp\left[\frac{5733\ K}{T}\right]$	1.8	0.000005
dPS_1	$5.7 \cdot 10^{-12}\, exp\left[\frac{5733\ K}{T}\right]$	1.8	0.000005
dPS_2	$1.50 \cdot 10^{-9}\, exp\left[\frac{1376\ K}{T}\right]$	1.8	$0.000399 - \left(\frac{0.01436\ K}{T}\right)$

These equations provided a good description of the experimental data below T_g and have been assumed to remain valid at higher temperatures. Conductivity was not included in the description.

The total dielectric loss relaxation of each pure component can be written as:

$$\varepsilon^{"}(\omega) = \varepsilon^{"}_{\beta}(\omega) + \varepsilon^{"}_{\alpha}(\omega) \tag{3.2}$$

The HN parameters $\Delta\varepsilon, \alpha, \gamma$ of the $hSBR_2$ α-relaxation were determined by fitting the data in the temperature interval from 230 K to 280 K assuming α and γ as temperature independent and $\Delta\varepsilon$ proportional to reciprocal temperature, $\Delta\varepsilon(T) = \Delta\varepsilon\left(T_g\right)\frac{T_g}{T}$. The parameters for dPS_2 were also determined with equivalent assumptions by fitting the data

in the temperature interval from 290 K to 340 K. In these calculations $\varepsilon_\infty = 2.35$ for SBR and $\varepsilon_\infty = 2.70$ for PS have been used.[8] Figure 3.4 shows that in this way a quite good description of the experimental data is obtained using a few parameters (see table 3.2). The same procedure has been applied on the other neat components investigated, $hSBR_1$, $dSBR_1$, hPS_1 and dPS_1; the description is illustrated in figure 3.5 where the solid lines fitting the experimental data were obtained by using Eq. 2.4 and 3.1 with parameters given in table 3.1 and 3.2.

Table 3.2: Parameters involved in the description of the dielectric α-relaxation of the pure components $hSBR_1$, $hSBR_2$, $dSBR_1$, hPS_1, hPS_2 and dPS_1. The dielectric strength and the Havriliak-Negami parameters were obtained fitting the curves well centered in the experimental frequency window. In the VFT equation describing $\tau_{max}(T)$, $\tau_\infty = 10^{-13}$s was fixed.

Sample	α	γ	$\Delta\varepsilon\, T_g/T$	D	T_0(K)
$hSBR_1$	0.65	0.42	0.09	8.6	161.80
$dSBR_1$	0.56	0.51	0.11	8.6	163.58
$hSBR_2$	0.54	0.70	0.096	8.6	176.70
hPS_1	0.73	0.52	0.06	6.3	228.00
dPS_1	0.67	0.55	0.07	6.3	210.75
dPS_2	0.63	0.54	0.074	6.3	239.80

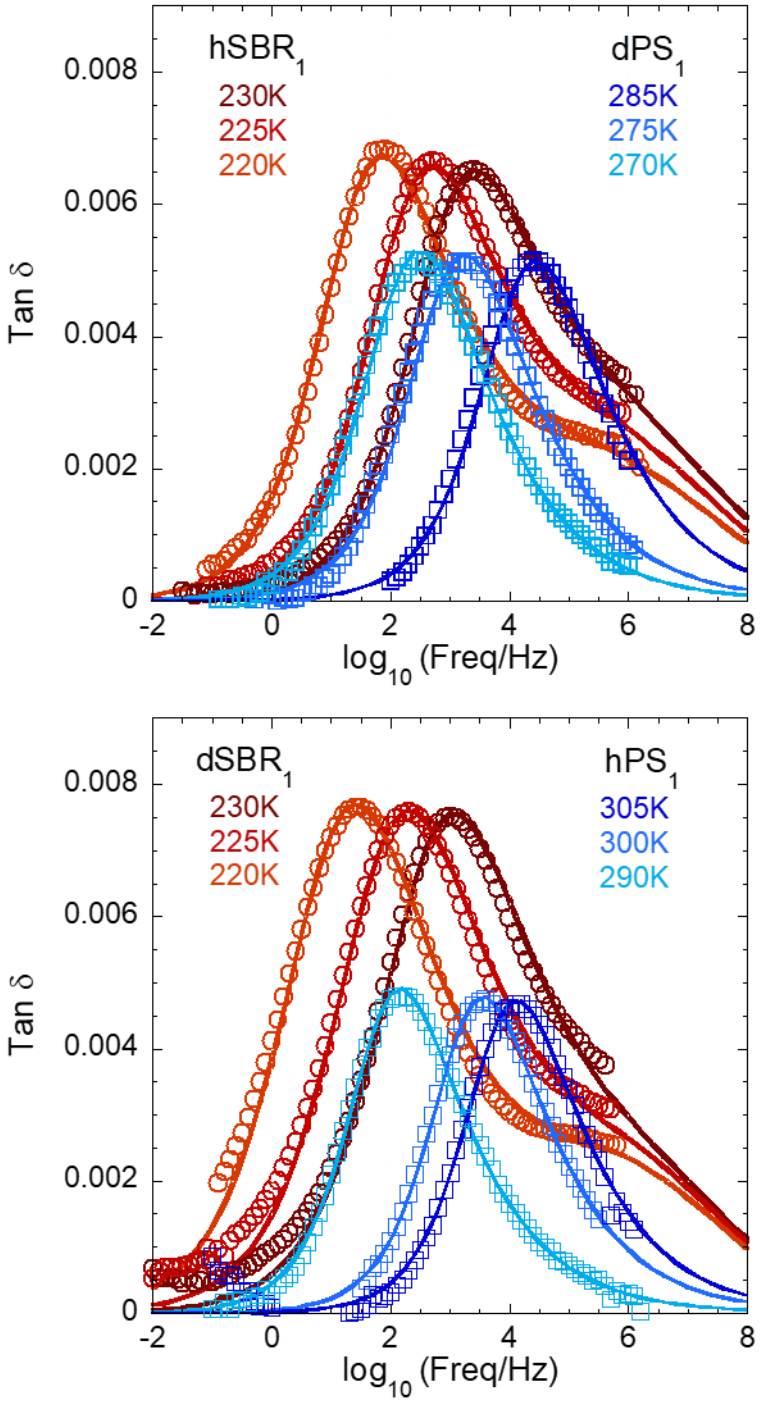

Figure 3.5: Frequency dependence of the dielectric tan δ for SBR (empty circles) and for PS (empty squares) at different temperatures. The solid lines represent the fits by means of the Havriliak-Negami equation for the α-relaxation and the addition of the β-relaxation calculated by extrapolating the lower temperature description using Eq 3.1.

The characteristic time τ_{max} at each temperature can be defined as the inverse of the angular frequency at the dielectric loss maximum of the α-relaxation process, which was calculated from the fitting parameters (see Eq. 2.5).[7] Figure 3.6 shows the temperature dependence of the τ_{max} for SBR and PS. The lines in the figure correspond to the data description by means of the Vogel-Fulcher-Tammann (VFT) equation: [3-5]

$$\tau_{max}(T) = \tau_{\infty} exp\left(\frac{DT_0}{T-T_0}\right) \tag{3.3}$$

Table 3.2 includes the values obtained for the fragility parameter, D, and the Vogel temperature T_0. In the fits the prefactor value $\tau_{\infty} = 10^{-13}$s in the VFT equation was kept constant.

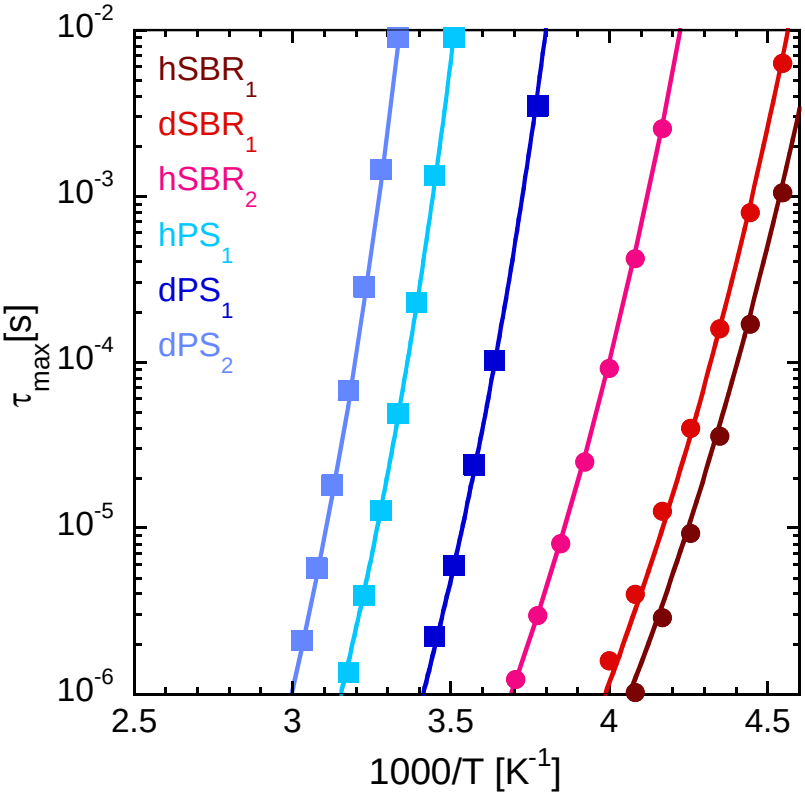

Figure 3.6: Temperature dependence of the characteristic times defined from the inverse of the frequencies of the dielectric loss maxima for the α-relaxation process of the neat samples investigated $hSBR_1$, $hSBR_2$, $dSBR_1$, hPS_1, hPS_2 and dPS_1. The lines stand for the fits by means of the VFT equation.

3.2 Calorimetric Traces of the Glass Transition

The glass transition manifests as a step in the specific heat. Even in homopolymers, this process usually extends over a given temperature range, and therefore to properly characterize it not only the average value of the glass transition temperature has to be determined, but also its width.[9] The average T_g-value is usually determined from the inflection point of the specific heat C_p (correspondingly, from the position of the maximum in the T-derivative of C_p). The initial ($T_{g,init}$) and final ($T_{g,fin}$) transition temperatures are representative for the temperatures where C_p departs from the glassy and 'equilibrium' supercooled-liquid behavior, respectively. They are determined using constructions as that illustrated in figure 3.7. The width of the glass transition is defined as $\Delta T_g = T_{g,fin} - T_{g,init}$.

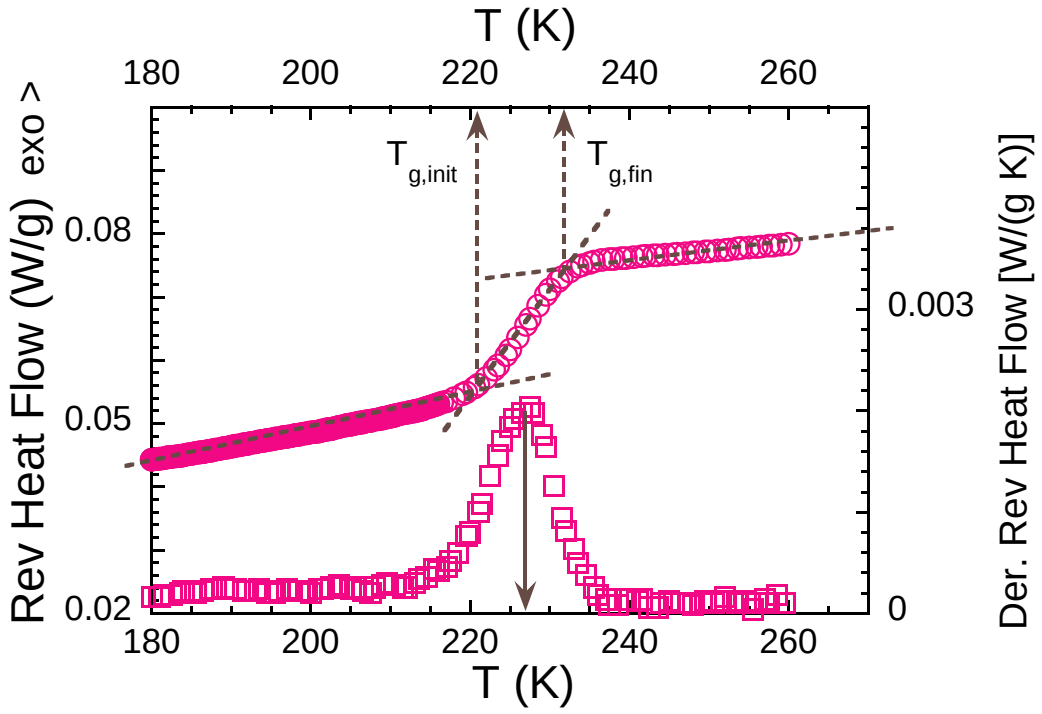

Figure 3.7: Reversible heat flow and its temperature derivative during cooling at 3 K/min hSBR$_2$. The filled symbols correspond to the linear description of the glassy part. Dashed lines show the usual construction to determine the initial and final glass-transition temperature values. Solid arrow marks the glass-transition temperature as directly determined from the maximum of the derivative.

Figure 3.7 shows an example of the results on the reversible part of the heat flow during cooling at 3 K/min corresponding to $hSBR_2$. To give account for the broadening of the glass transition, the construction illustrated in this figure is usually made. For this sample, we deduce a value of $T_g = 227$ K, with initial and final glass-transition temperature values of $T_{g,init} = 221$ and $T_{g,fin} = 231$ K respectively (see the dashed arrows). The temperature-derivative of rev heat flow is also included in this figure; the glass transition is reflected as a peak in this function, where the position of the maximum corresponds to the inflection point of rev heat flow and thus directly gives the value of T_g as usually defined. This function also reflects very clearly the width of the glass transition process and may allow resolving multiple transitions, if present in the sample.[10,11]

The calorimetric T_gs of all the neat components were determined using MDSC following the above-mentioned procedure; the respective glass transition traces are illustrated in figure 3.8. The values of the temperatures characterizing the glass-transition processes are listed in table 3.3.

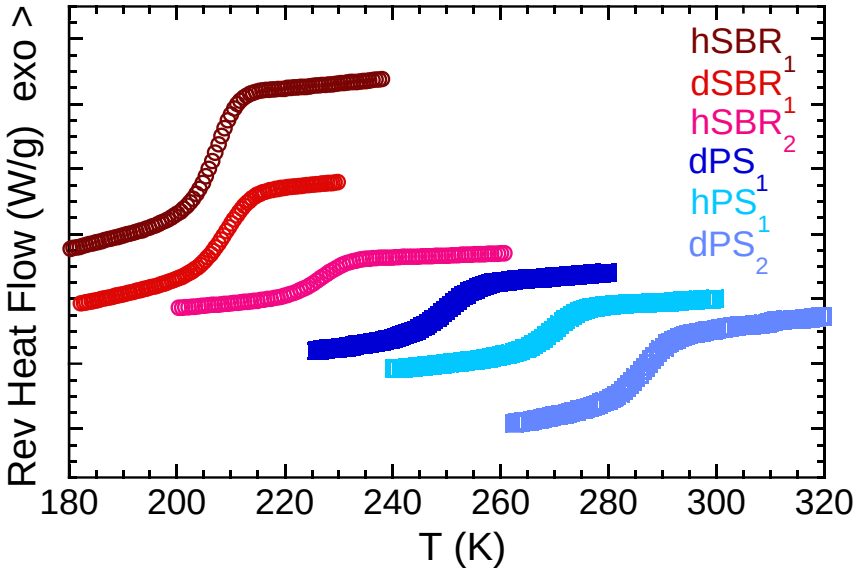

Figure 3.8: Reversible heat flow during cooling at 3 K/min for the pure components. Data were vertically shifted for the sake of clarity.

Table 3.3: Average, initial and final temperatures and widths of the calorimetric glass-transitions obtained from DSC for the pure components.

Sample	T_g(K)	$T_{g,init}$(K)	$T_{g,fin}$(K)	ΔT_g(K)
$hSBR_1$	207.0	202.4	211.3	9
$dSBR_1$	208.8	203.5	213.9	10
$hSBR_2$	227.1	220.9	231.4	11
hPS_1	269.6	264.1	274.1	10
dPS_1	249.8	243.8	255.8	12
dPS_2	286.1	279.0	291.2	12

We note some differences in T_g between the protonated polymer and its respective deuterated counterpart for both SBR and PS ($hSBR_1$ vs $dSBR_1$ and hPS_1 vs dPS_1) that could be attributed to the small differences in their microstructures, molecular masses and/or to isotopic effects. The SBR homopolymers, $hSBR_1$ and $dSBR_1$, present similar T_g and ΔT_gvalues: $T_g = 207$ K ($hSBR_1$) and 209 K ($dSBR_1$), $\Delta T_g = 9$ K ($hSBR_1$) and 10 K ($dSBR_1$). In the PS, hPS_1 and dPS_1, samples the T_g values differ more: $T_g = 250$ K (dPS_1) and 270 K (hPS_1), with $\Delta T_g = 12$ and 10 K, respectively. Isotopic effect may be one the reasons for the difference in T_g-values; however, the main origin in the PS case can be attributed to the difference in the molecular size of these oligomers. From the M_w values it can be inferred that in average the hydrogenated molecule has 6 phenyl rings while the deuterated one has 5. The T_g value of dPS_2 is around 286 K, having higher M_w. Also, $hSBR_2$ manifests even higher T_g due to the higher styrene content.

3.2.1 Segmental Heat Capacity $s - C_p$

In order to analyze the contributions to the experimental DSC trace of the segmental dynamics responsible for the glass transition, first the glassy behavior has been accounted for with a linear function (for the sake of simplicity) and subtracted from the DSC cooling scan of the reversible heat flow (figure 3.8). The resulting calorimetric traces will be referred to as segmental heat capacity, $s - C_p$. They are illustrated in the figure 3.9 for $hSBR_2$ and dPS_2, as an example, and in Figure 4.2 for the other pure polymers. It should be noted that the subtraction of a linear function does not alter the inflection point temperature determining T_g.

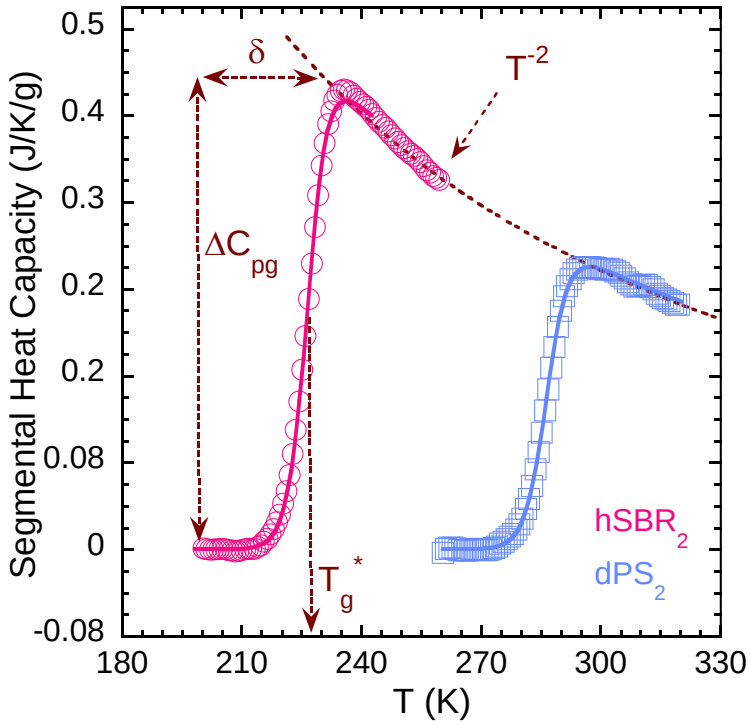

Figure 3.9: Calorimetric traces after the subtraction of the glassy part. The solid lines fitting the neat polymers data were obtained by using Eq. 3.4 with parameters given in table 3.4.

The aim was to achieve a relatively simple full characterization of the homopolymers' DSC behavior, which would encode the unsolved intricate connection between the segmental dynamics and the glass formation process. The description of the DSC traces in the glass transition range for the neat polymers required quantifying the three main quantities for each component: a characteristic temperature, a measure of the width of the glass transition range and the associated heat capacity jump. A simple but satisfactory way to describe the experimental segmental heat capacity of the neat polymers is by combining a sigmoidal function with a T^{-2} law as:

$$\text{s-C}_p = \Delta C_{pg} \left(\frac{T_g^*}{T}\right)^2 \frac{1}{1+e^{(T_g^*-T)/\delta}} \tag{3.4}$$

where ΔC_{pg} is the heat capacity jump, δ measures the width of the glass transition range and T_g^* is a characteristic temperature defined as the inflection point of the sigmoidal function. As can be appreciated in figure 3.9, the description of the experimental data for the neat components, both $hSBR_2$ and dPS_2, is very good. The parameters determined by fitting the curves are given in table 3.4. Note that minor differences exist between T_g defined as the inflection point of the full function and T_g^* values. This is a technically important point. The glass transition temperatures reported in this work were always obtained from the inflection point of either the heat-flow or the reversible C_p signal.

Table 3.4: Parameters obtained by fitting equation Eq. 3.4 to the segmental component of the reversible heat flow of the neat components.

Sample	δ/K	ΔC_{pg}/Jg^{-1}K^{-1}	T_g^*/K
$hSBR_1$	0.23	0.45	207.01
$dSBR_1$	0.21	0.39	208.96
$hSBR_2$	0.20	0.46	226.6
hPS_1	0.19	0.23	269.59
dPS_1	0.14	0.32	250.22
dPS_2	0.19	0.28	286.5

3.2.2 Connection Between the Segmental Dynamics and Glass Transition

The DSC traces on cooling contain the information of how the α-relaxation equilibrium behavior is lost. It is quite generally accepted that in bulk polymer systems the segmental dynamics fully controls the way thermal equilibrium is lost when decreasing temperature (the liquid to glass transition phenomenon). Despite the fact that several theoretical approaches exist,[12,13] a fundamental quantitative link between segmental dynamics and the way thermodynamic equilibrium is lost has not been established by now. For instance, the Adam and Gibbs equation establishes a direct link between the characteristic times and the configurational entropy on the basis of the so-called cooperatively rearranging regions (CRR).[13] In this framework as the temperature is reduced the configurational entropy decreases and the time needed for maintaining thermodynamic equilibrium rapidly increases. In this way once the equilibration time exceeds typical laboratory values (ca. 1 - 1000 s, depending of the experimental conditions), equilibrium is lost and the supercooled liquid state transforms into a glassy state, the glass-transition phenomena. When comparing the relaxation times for the segmental dynamics and the calorimetric glass transition temperatures, a semiquantitative

connection can be established, namely that the relaxation time measured at the calorimetric T_g (taken as the inflection point) is of the order of ten seconds.[14] Using the neat polymers DSC and BDS results we can connect the DSC T_g^* value and the segmental relaxation time evaluated at this temperature $\tau(T_g^*)$. The relationship between the dielectric α-relaxation time and the calorimetric T_g^* obtained from the analysis of the data of the pure polymers SBR and PS is displayed in table 3.5. The values for PS are systematically larger than those for SBR. An explanation of this finding is beyond the aim of this work.

Table 3.5: Relationship between the dielectric α-relaxation time and the calorimetric T_g^*.

	$hSBR_1$	$dSBR_1$	$hSBR_2$	hPS_1	dPS_1	dPS_2
$\tau_{max}(T_g^*)$/s	2.3	2.9	1.7	99.8	40.7	11.2

3.3 Elastic Fixed Window Scans: Microscopic Insight into Proton Displacements

We now move to the microscopic information offered by the EFWS experiments. Figure 3.10 shows the elastically scattered intensity recorded in the EFWS for the different pure polymers investigated - $hSBR_1$, hPS_1- at selected temperatures, normalized by its value at a very low temperature (20 K). This magnitude decreases with increasing temperature and scattering vector Q. The intensity scattered by our samples in the Q-region explored by these experiments is predominantly of incoherent nature and has its origin in the hydrogens. This means that for the homopolymers it reflects the atomic (H) displacements in the bulk system.

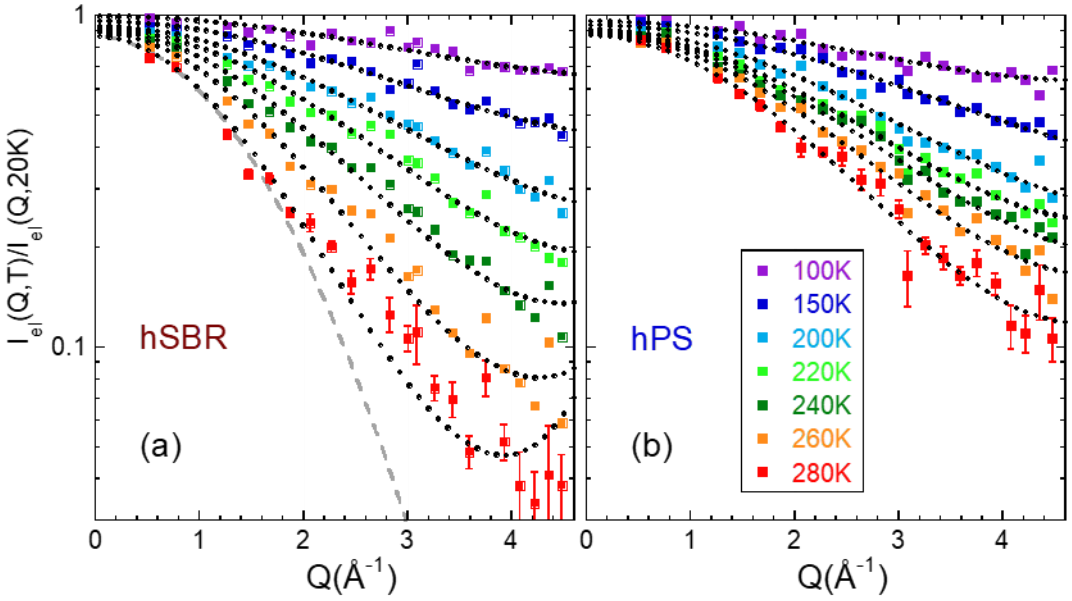

Figure 3.10: EFWS results obtained on the protonated neat components ($hSBR_1$ (a) and hPS_1 (b)). Different colors correspond to the different temperatures indicated in panel (b). Representative error bars are shown for the 280 K data. Dotted lines are fits of Eq. 3.6; dashed line in (a) shows the description if only the leading term in Eq. 3.6 is considered.

The EFWS results correspond, to a good approximation, to the incoherent intermediate scattering function $I_{inc}(Q,t)$ of the hydrogens in the sample at a time $t_R = \hbar/\delta\hbar\omega \approx 80\ ps$. In general, $I_{inc}(Q,t)$ can be expressed as an expansion in Q^2:

$$I_{inc}(Q,t,T) = exp\left(-\frac{\langle r^2(t,T)\rangle}{6}Q^2 + \frac{\alpha_2(t,T)\langle r^2(t,T)\rangle^2}{72}Q^4 + \cdots\right) \qquad (3.5)$$

Here the leading Q^2-term is determined by the atomic mean squared displacement $\langle r^2(t)\rangle$ –the second moment of the van Hove self-correlation function $G_s(r,t)$. The second term in the expansion accounts for deviations from the Gaussian form of $I_{inc}(Q,t)$, (equivalently, of $G_s(r,t)$) through the second-order non-Gaussian parameter $\alpha_2(t)$. $\alpha_2(t)$ is defined in terms of the even moments of $G_s(r,t)$ as $\alpha_2(t) = 3\langle r^4(t)\rangle/(5\langle r^2(t)\rangle) - 1$. Usually a temperature dependent prefactor I_o accounting for multiple scattering effects and normalization uncertainties[15–17] has to be considered when dealing with experimental EFWS results; thus, the EFWS can be described by:

$$\frac{I_{el}(Q,T)}{I_{el}(Q,T\approx 0)} = I_o exp\left(-\frac{\langle r^2(t_R,T)\rangle}{6}Q^2 + \frac{\alpha_2(t_R,T)\langle r^2(t_R,T)\rangle^2}{72}Q^4 + \cdots\right) \qquad (3.6)$$

The first term of the expansion is usually enough to describe the EFWS results for small Q-values. In a glassy solid the extracted values of $\langle r^2(t_R)\rangle$ can be identified with the average atomic (H) displacements within the cage imposed by the neighbors. However, at high temperatures the meaning of the such obtained MSD has to be cautiously considered. When quasielastic contributions become of the same order as the instrumental resolution the $\langle r^2(t_R)\rangle$ values are affected by them. In fact, they depend on the considered instrumental resolution (time-dependent MSD). In general, the MSD results reflect the decay of $I_{inc}(Q,t)$ through fast processes (vibrations and rapid motions) and also relaxational processes.

Equation 3.6 was fitted to the EFWS results (see Fig. 3.10). As shown in panel (a) for the example of pure $hSBR_1$, the huge Q-range covered by IN13 clearly demands for the use of the second term in Eq. 3.6 accounting for deviations from Gaussian behavior. Very good descriptions of the experimental data were obtained in this way, delivering also information on $\alpha_2(t_R)$. The resulting values of the fitting parameters $\langle r^2(t_R)\rangle$ and

$\alpha_2(t_R)$ are displayed in Fig. 3.11. Panel (a) shows the results for neat $hSBR_1$, and panel (b), those on hPS_1. In all cases the MSD $\langle r^2(t_R)\rangle$ increases with temperature, while the deviations from Gaussian behavior decrease.

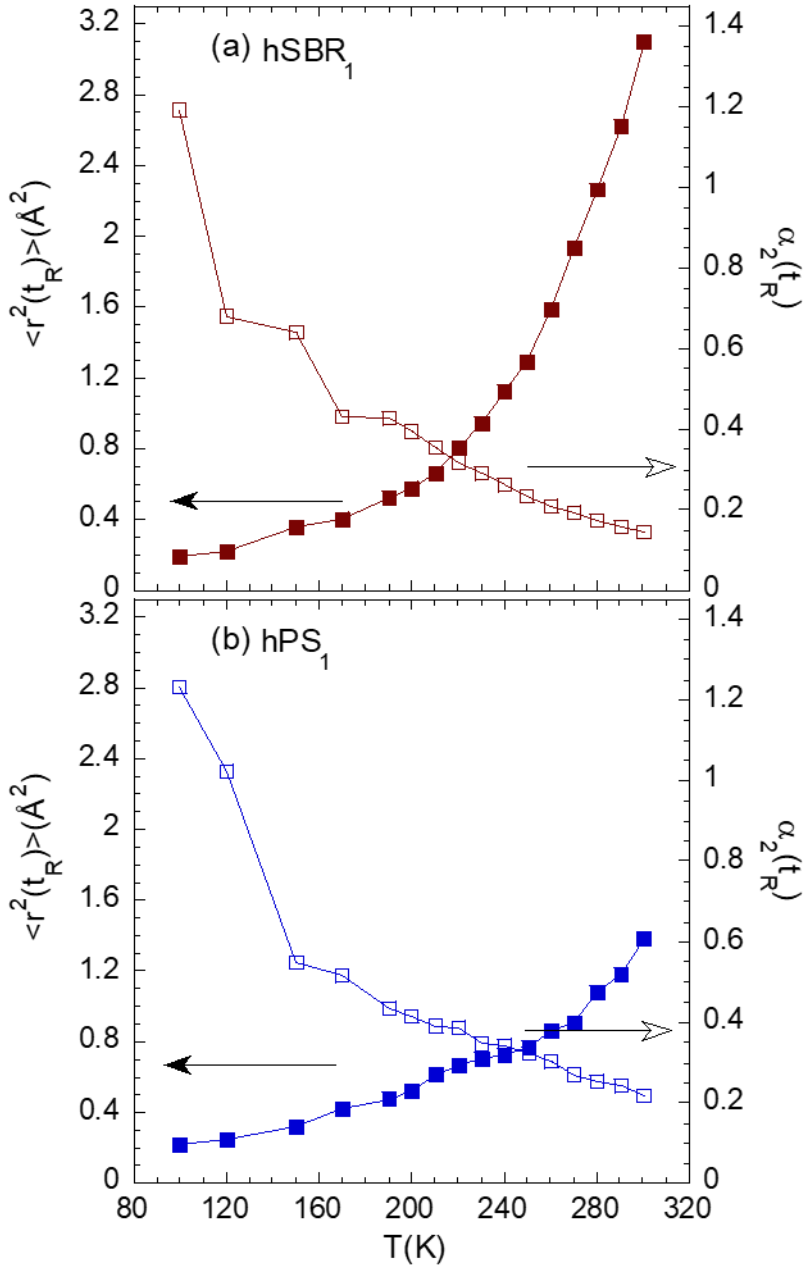

Figure 3.11: Mean squared proton displacement (filled symbols, scale on the left) and non-Gaussian parameter (empty symbols, scale on the right) at the IN13 instrumental resolution time deduced from the fits of Eq. 3.6 to the IN13 results on the $hSBR_1$ samples (a) and on the hPS_1 samples (b). Lines connecting points are guides for the eye.

3.3.1 'Microscopic' T_g vs 'Macroscopic' T_g

The microscopic insight on the hydrogen displacements provided by the EFWS can be compared with the results of the 'macroscopic' DSC technique. This is done in Fig. 3.12 for the two homopolymers. In both cases, the hydrogen MSD follows well a linear temperature dependence in the glassy state above $150\,K$: $\langle r^2(t_R)\rangle(\text{Å}^2) = 0.551 + 0.00563T$ [K] for hSBR$_1$ and $\langle r^2(t_R)\rangle(\text{Å}^2) = 0.450 + 0.00498T$ [K] for hPS$_1$. At a given temperature, additional contributions to the extrapolated low-T linear behavior can clearly be detected in $\langle r^2(t_R)\rangle$. As can be appreciated in Fig. 3.12, the onset temperature of these contributions (solid arrow) is located in the neighborhood of the calorimetric glass transition (dashed-dotted arrow). These results corroborate in these homopolymers such a commonly found coincidence (see, e. g.,[18–21]). The MSD at times of the order of tens of ps thus constitutes a sensitive probe to detect motions involved in the supercooled liquid regime, when the dynamic arrest induced in the glassy state is released. This microscopic magnitude clearly reveals at which temperature the environment of H nuclei softens enough for accommodating atomic displacements characteristic for the supercooled liquid that are not allowed in a frozen medium. This temperature can thus be identified with the 'microscopic' T_g in the system and shall denote it as T_g^m. For hSBR$_1$, $T_g^m = 207.5 \pm 2.5$ K and for hPS$_1$, $T_g^m = 271.0 \pm 4$ K.

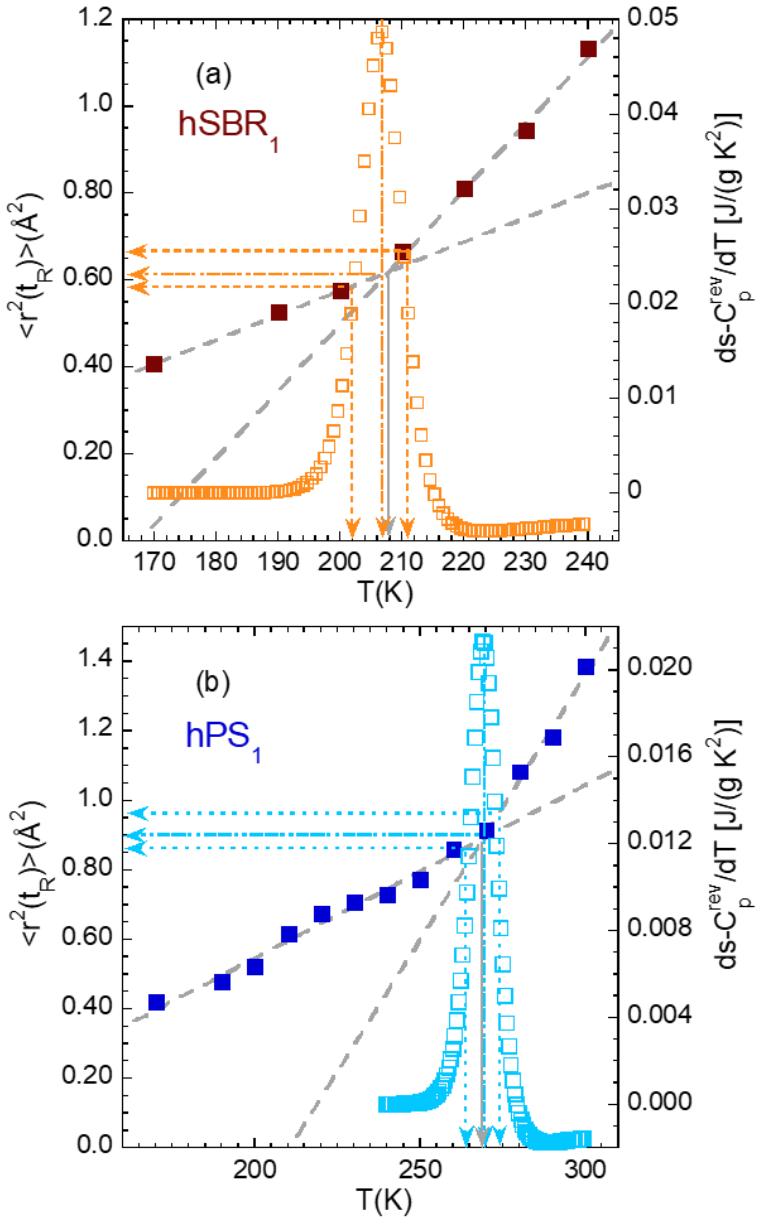

Figure 3.12: Mean squared proton displacement at the IN13 resolution time (filled symbols, scale on the left) and temperature derivative of the segmental part of the reversible heat flow from DSC (empty symbols, scale on the right) corresponding to the neat protonated systems: $hSBR_1$ (a) and hPS_1 (b). The dashed lines represent the linear dependence of $\langle r^2(t_R)\rangle$ in the glassy state above 150 K ($\langle r^2(t_R)\rangle$) and in the supercooled state (between T_g and $T_g + 30$ K approx.). From their crossing, the T_g^m-value is obtained (marked by the solid arrow). The vertical arrows show the average (dashed-dotted), initial and final (dotted) calorimetric glass-transition temperatures, and the corresponding horizontal arrows mark the values of the MSD at these temperatures.

A connection between the α-relaxation process –with associated characteristic times of the order of seconds in the vicinity of the glass transition– and mean-squared displacements in the picosecond-nanosecond timescale is apparently surprising, but it has been repeatedly reported in the literature; a seminal work in this direction is the study on Selenium by Buchenau and Zorn in Ref.[22] However, while the α-process is slow, the barrier transitions underlying this relaxation are fast. This is at the basis of the so-called elastic models.[23,24]

It has been suggested that the well-known Lindemann criterion that applies for crystalline systems can be extended to inhomogeneous systems[25] and even proteins.[26,27] A Lindemann-like criterion for the glass transition can be deduced in a straightforward way in the framework of elastic models,[28] and also invoking different arguments (see, e. g.[29,30]). We recall that the Lindemann criterion predicts the melting of crystals on the basis of the relative magnitude of thermal atomic fluctuations and the crystal lattice constant. When this magnitude exceeds about 0.1–0.2, melting occurs. The analogous parameter in glass-forming systems related with the glass-transition phenomenon (Δ_{Lg}) would be the ratio between the root of the mean-squared fluctuation MSF at T_g and the average inter-molecular distance. The MSF in the harmonic approximation MSD=2MSF, and $\Delta_{Lg}= \sqrt{MSD(T_g)/2}/d_{chain}$ would be an estimation of the Lindemann parameter. Taking into account the values of the MSD at the glass-transition temperature (see Fig. 3.12) and the values of d_{chain} determined from the X-Ray diffraction experiments (see chapter 6.4.1), we can determine $\Delta_{Lg}= \sqrt{MSD(T_g)/2}/d_{chain} = 0.12$ for $hSBR_1$ and 0.14 for hPS_1. Thus, the value for $hSBR_1$ is slightly smaller than for hPS_1, and both are in the range reported for crystals, as mentioned above, as well as for the melting of proteins.[31] Our findings would also support the results obtained by Leporini et al.[32] However, the existence of a universal Lindemann criterion as predicted in Ref.[33] was not confirmed in some molecular liquids. Interestingly, by investigating in Ref. the MSD at various temperatures and pressures for a number of molecular glass-forming liquids, an intrinsic Lindemann criterion was found for any given liquid. The existence of an intrinsic Lindeman criterion is in fact predicted by the above-mentioned elastic models.[34,35]

3.4 References

(1) Hofmann, A.; Alegría, A.; Colmenero, J.; Willner, L.; Buscaglia, E.; Hadjichristidis, N. Secondary and Segmental Relaxation in Polybutadienes of Varying Microstructure: Dielectric Relaxation Results. *Macromolecules* **1996**, *29*, 129–134.

(2) Arbe, A.; Richter, D.; Colmenero, J.; Farago, B. *Merging of the and Relaxations in Polybutadiene: A Neutron Spin Echo and Dielectric Study*; 1996.

(3) Narros, A.; Arbe, A.; Alvarez, F.; Colmenero, J.; Richter, D. Atomic Motions in the AB -Merging Region of 1,4-Polybutadiene: A Molecular Dynamics Simulation Study. *Journal of Chemical Physics* **2008**, *128* (22).

(4) Alvarez, F.; Alegría, A.; Colmenero, J. Interconnection between Frequency-Domain Havriliak-Negami and Time-Domain Kohlrausch-Williams-Watts Relaxation Functions. *Phys Rev B* **1993**, *47* (1), 125.

(5) Havriliak, S.; Negami, S. A Complex Plane Representation of Dielectric and Mechanical Relaxation Processes in Some Polymers. *Polymer* **1967**, *8* (C), 161–210.

(6) Havriliak, S.; Negami, S. A Complex Plane Analysis of α-Dispersions in Some Polymer Systems. *Journal of Polymer Science Part C: Polymer Symposia* **1966**, *14* (1), 99–117.

(7) Kremer, F.; Schönhals, A. *Broadband Dielectric Spectroscopy*; Springer-Verlag Berlin Heidelberg, 2003.

(8) *Scientific Polymer Products*. https://scipoly.com/technical-library/refractive-index-of-polymers-by-index/ (accessed 2022-12-08).

(9) Arbe, A.; Genix, A. C.; Arrese-Igor, S.; Colmenero, J.; Richter, D. Dynamics in Poly(w-Alkyl Methacrylates): A Neutron Scattering, Calorimetric, and Dielectric Study. *Macromolecules* **2010**, *43* (6), 3107–3119.

(10) Bhowmik, D.; Pomposo, J. A.; Juranyi, F.; García-Sakai, V.; Zamponi, M.; Su, Y.; Arbe, A.; Colmenero, J. Microscopic Dynamics in Nanocomposites of Poly(Ethylene Oxide) and Poly(Methyl Methacrylate) Soft Nanoparticles: A Quasi-Elastic Neutron Scattering Study. *Macromolecules* **2014**, *47* (1), 304–315.

(11) Bhowmik, D.; Pomposo, J. A.; Juranyi, F.; García Sakai, V.; Zamponi, M.; Arbe, A.; Colmenero, J. Investigation of a Nanocomposite of 75 Wt % Poly(Methyl Methacrylate) Nanoparticles with 25 Wt % Poly(Ethylene Oxide) Linear Chains: A Quasielatic Neutron Scattering, Calorimetric, and WAXS Study. *Macromolecules* **2014**, *47* (9), 3005–3016.

(12) Kob, W.; Andersen~, H. C. *Testing Made-Coupling Theory for a Supercooled Binary Lennard-Jones Mixture: The van Hove Correlation Function*; 1995; Vol. 51.

(13) Narros, A.; Alvarez, F.; Arbe, A.; Colmenero, J.; Richter, D.; Farago, B. Hydrogen Motions in the α-Relaxation Regime of Poly(Vinyl Ethylene): A Molecular Dynamics Simulation and Neutron Scattering Study. *Journal of Chemical Physics* **2004**, *121* (7), 3282–3294.

(14) Kob, W.; Donati, C.; Plimpton, S. J.; Poole, P. H.; Glotzer, S. C. *Dynamical Heterogeneities in a Supercooled Lennard-Jones Liquid*; 1997.

(15) Doster, W.; Busch, S.; Gaspar, A. M.; Appavou, M. S.; Wuttke, J.; Scheer, H. Dynamical Transition of Protein-Hydration Water. *Phys Rev Lett* **2010**, *104* (9).

(16) Doster, W.; Settles, M. Protein-Water Displacement Distributions. *Biochimica et Biophysica Acta - Proteins and Proteomics*. June 1, 2005, pp 173–186.

(17) Zorn, R. *Deviation from Gaussian Behavior in the Self-Correlation Function of the Proton Motion in Polybutadiene*; 1997.

(18) Frick, B.; Richter, D.; Petry, W.; Buchenau, U. *Study of the Glass Transition Order Parameter in Amorphous Polybutadiene by Incoherent Neutron Scattering*; 1988; Vol. 70.

(19) Niss, K.; Dalle-Ferrier, C.; Frick, B.; Russo, D.; Dyre, J.; Alba-Simionesco, C. Connection between Slow and Fast Dynamics of Molecular Liquids around the Glass Transition. *Phys Rev E Stat Nonlin Soft Matter Phys* **2010**, *82* (2).

(20) Fujara, F.; Petry, W. *Fast Local Motion around Tg in a Molecular Glass as Observed by Incoherent Neutron Scattering*; 1987; Vol. 4.

(21) Stillinger, F. H.; Weber, T. A.; Bbhmer, R.; Ngai, K. L.; Angell, C. A.; Plazek, D. J.; Frick, B.; Richter, D. *15. C. A. Angell, in Relaxations in Complex Systems*; 1959; Vol. 183.

(22) Matsukawa, M.; Nagai, I.; Tanaka, T. *A Relation Between Fast and Slow Motions in Glassy and Liquid Selenium The Effect of Crosslinks on Ultrasonic Properties in Glassy Epoxy Resin*.

(23) Kämmerer, S.; Kob, W.; Schilling, R. Test of Mode Coupling Theory for a Supercooled Liquid of Diatomic Molecules. II. *Phys Rev E* **1998**, *58* (2), 2141.

(24) Hurley, M. M.; Harrowell, P. Non-Gaussian Behavior and the Dynamical Complexity of Particle Motion in a Dense Two-dimensional Liquid. *J Chem Phys* **1998**, *105* (23), 10521.

(25) Caprion, D.; Matsui, J.; Schober, H. R. Dynamic Heterogeneity of Relaxations in Glasses and Liquids. *Phys Rev Lett* **2000**, *85* (20), 4293.

(26) Kob, W.; Donati, C.; Plimpton, S. J.; Poole, P. H.; Glotzer, S. C. Dynamical Heterogeneities in a Supercooled Lennard-Jones Liquid. *Phys Rev Lett* **1997**, *79* (15), 2827.

(27) Ayyagari, C.; Bedrov, D.; Smith, G. D. Structure of Atactic Polystyrene: A Molecular Dynamics Simulation Study. *Macromolecules* **2000**, *33* (16), 6194–6199.

(28) Frick, B.; Richter, D.; Ritter, C. Structural Changes near the Glass Transition–Neutron Diffraction on a Simple Polymer. *Europhys Lett* **1989**, *9* (6), 557.

(29) Fetters, L. J.; Lohse, D. J.; Milner, S. T.; Graessley, W. W. Packing Length Influence in Linear Polymer Melts on the Entanglement, Critical, and Reptation Molecular Weights. *Macromolecules* **1999**, *32* (20), 6847–6851.

(30) Lodge, T. P.; McLeish, T. C. B. Self-Concentrations and Effective Glass Transition Temperatures in Polymer Blends. *Macromolecules* **2000**, *33* (14), 5278–5284.

(31) Berthier, L.; Biroli, G.; Bouchaud, J. P.; Cipelletti, L.; el Masri, D.; L'Hôte, D.; Ladieu, F.; Pierno, M. Physics: Direct Experimental Evidence of a Growing Length Scale Accompanying the Glass Transition. *Science (1979)* **2005**, *310* (5755), 1797–1800.

(32) Wignall, G. D.; Melnichenko, Y. B. Recent Applications of Small-Angle Neutron Scattering in Strongly Interacting Soft Condensed Matter. *Reports on Progress in Physics* **2005**, *68* (8), 1761–1810.

(33) Yun, S. I.; Melnichenko, Y. B.; Wignall, G. D. Small-Angle Neutron Scattering from Symmetric Blends of Poly(Dimethylsiloxane) and Poly(Ethylmethylsiloxane). *Polymer* **2004**, *45* (23), 7969–7977.

(34) Dyre, J. C. Colloquium: The Glass Transition and Elastic Models of Glass-Forming Liquids. *Rev Mod Phys* **2006**, *78* (3), 953–972.

(35) Dyre, J. C.; Olsen, N. B.; Christensen, T. Local Elastic Expansion Model for Viscous-Flow Activation Energies of Glass-Forming Molecular Liquids. *Phys. Rev. B* **1996**, *53*, 2171–2174.

Chapter 4

Results on the Blends

The aim of this chapter is to present the experimental results obtained by DSC, BDS and SANS on blends composed by styrene-butadiene rubbers SBR and oligomers of polystyrene PS. The DSC and BDS results are described from a phenomenological point of view (their modeling and interpretation will be subject of the next chapter), while the scattering results are analyzed in detail to obtain information about TCF and determine the phase diagram of the mixtures. To enhance scattering contrast, the use of samples where one of the components is deuterated is mandatory. The systems investigated are three: $hSBR_1/dPS_1$, $hSBR_2/dPS_2$ or $dSBR_1/dPS_1$; for each system the following blend compositions have been studied:

i. $hSBR_1/dPS_1 \rightarrow w_{SBR} = 0.8, 0.65, 0.5$ and 0.2 (the blends are named as 80h, 65h, 50h and 20h).
ii. $dSBR_1/hPS_1 \rightarrow w_{SBR} = 0.8, 0.65, 0.5$ and 0.2 (the blends are named as 80d, 65d, 50d and 20d).
iii. $hSBR_2/dPS_2 \rightarrow w_{SBR} = 0.8, 0.60, 0.5, 0.3$ and 0.15 (the blends are named as 80, 60, 50, 30 and 20).

The details of sample preparation have already been described in detail in Chapter 2.

4.1 Calorimetric Trace of the Glass Transition

Figure 4.1 shows the glass transition traces of the $hSBR_2/dPS_2$ blends determined from the reversible heat flow during cooling at 3 K/min. The calorimetric T_g values of the blends were determined in the same way as in the homopolymers (figure 3.7), namely by picking up the inflexion point of the reversible part of the heat flow, using MDSC. The values of the temperatures characterizing the glass-transition processes of the systems here reported are listed in table 4.1.

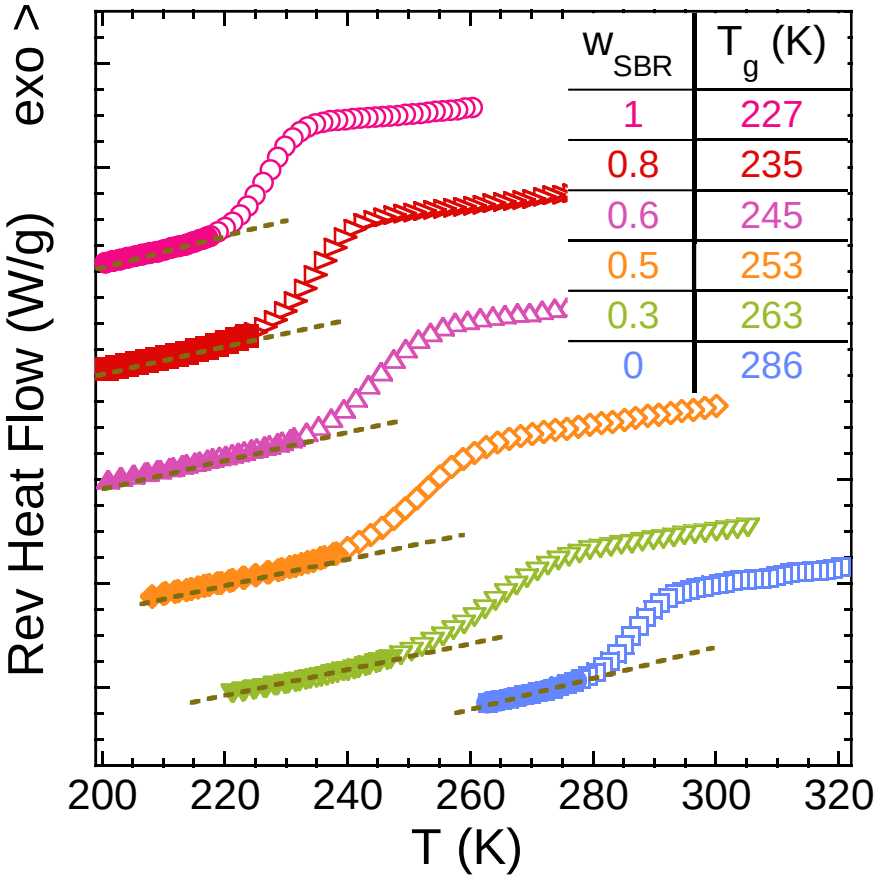

Figure 4.1: Reversible heat flow during cooling at 3 K/min for the pure components and $hSBR_2/dPS_2$ blends. Data were vertically shifted for the sake of clarity. The composition and the glass transition temperatures are specified for each sample. The dashed lines correspond to the linear description of the glassy part.

Table 4.1: Average, initial and final temperatures and widths of the calorimetric glass-transitions obtained from DSC, and spinodal decomposition temperature obtained from SANS.

Sample	T_g(K)	$T_{g,init}$(K)	$T_{g,fin}$(K)	ΔT_g(K)	T_s(K)
$hSBR_1$	207.0	202.4	211.3	8.9	-
80h	216.1	210.2	221.3	11.1	118.6
65h	221.8	215.1	228.3	13.2	155.9
50h	229.8	221.4	238.0	16.6	188.5
20h	239.4	229.8	249.3	19.5	235.5
dPS_1	249.8	243.8	255.8	12.0	-
$dSBR_1$	208.8	203.5	213.9	10.4	-
80d	216.5	210.2	222.9	12.7	82.5
65d	223.4	215.4	231.4	16.0	143.3
50d	228.6	219.2	237.7	18.5	178.3
20d	252.2	241.8	264.2	22.4	232.2
hPS_1	269.6	264.1	274.1	10.0	-
$hSBR_2$	227.1	220.9	231.4	10.5	-
80	234.8	227.6	241.2	13.6	123.7
60	244.1	235.5	251.9	16.4	199.2
50	253.6	242.0	261.0	19.0	219.1
30	263.2	252.8	274.2	21.4	243.5
15	276.2	264.4	285.4	21.0	257.4
dPS_2	286.1	278.6	291.1	12.5	-

The difference between the T_gs of the two neat systems is around $50 - 60$ K – it depends on the system considered, $hSBR_1/dPS_1$, $hSBR_2/dPS_2$ or $dSBR_1/dPS_1$ – allowing to categorize the mixtures as dynamically asymmetric binary blends.[1] In these systems, PS is the high-T_g or slow component and SBR is the low-T_g or fast component. The glass-transition processes of the blends manifest broad features in the range between the T_gs of the pure components; as the content of PS is increased the heat flow jump range becomes broader. The T_g and also $\Delta T_g = T_{g,fin} - T_{g,init}$ values in the blends increase with PS content –see table 4.1. The width of the glass transition is not symmetric with composition: while the PS-rich blends show a very broad glass-transition process, the DSC traces in SBR-rich mixtures are only slightly broadened with respect to SBR homopolymers.

4.1.1 Segmental Heat Capacity $s - C_p$

Following the procedure described in the previous chapter 3.2.1, also for the blends the glassy behavior has been accounted for with a linear function (for the sake of simplicity) and subtracted from the DSC cooling scan of the reversible heat flow (figure 4.1). The resulting calorimetric traces that will be used for the following analysis are shown Figure 4.2 for the SBR/PS blends and will be referred to as segmental heat capacity, $s - C_p$. Interestingly enough, the behavior at temperatures well above T_g for all samples nearly superimposes, and can be approximately described by a power law (T^{-n}) with $n = 2$.

The results presented in figures 4.1 and 4.2 suggest a good miscibility (in the 'traditional' meaning) of the SBR/PS blends in the full range of concentrations investigated, which will be confirmed in the following section from a thermodynamic point of view.

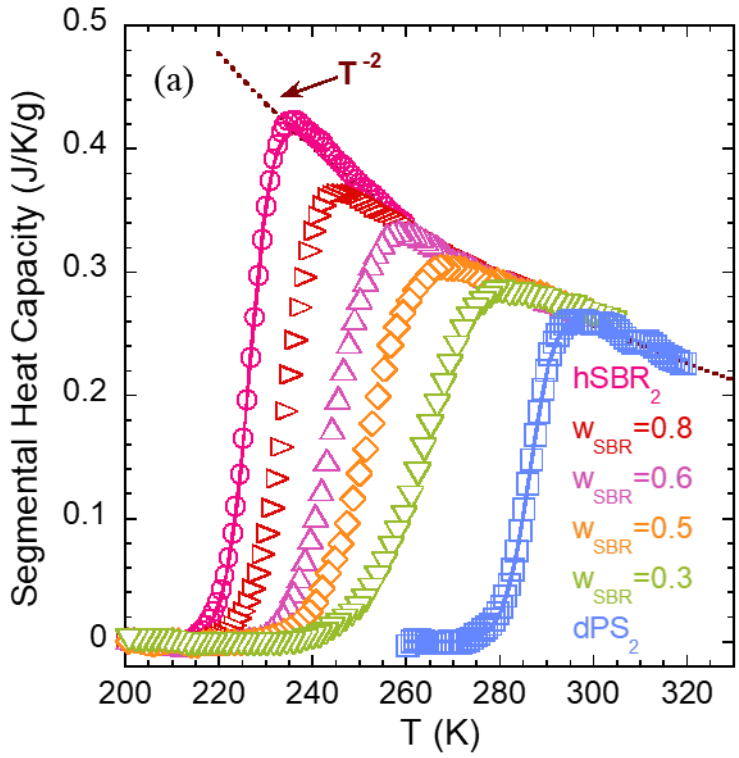
(a)
T^-2
hSBR2
wSBR=0.8
wSBR=0.6
wSBR=0.5
wSBR=0.3
dPS2
Segmental Heat Capacity (J/K/g)
T (K)
0.5
0.4
0.3
0.2
0.1
0
200
220
240
260
280
300
320

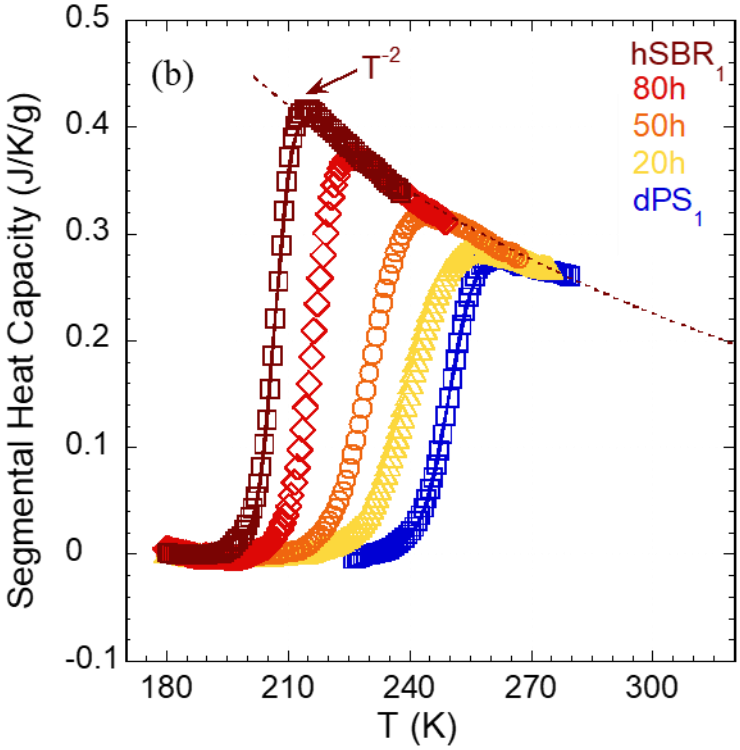
(b)
T^-2
hSBR1
80h
50h
20h
dPS1
Segmental Heat Capacity (J/K/g)
T (K)
0.5
0.4
0.3
0.2
0.1
0
-0.1
180
210
240
270
300

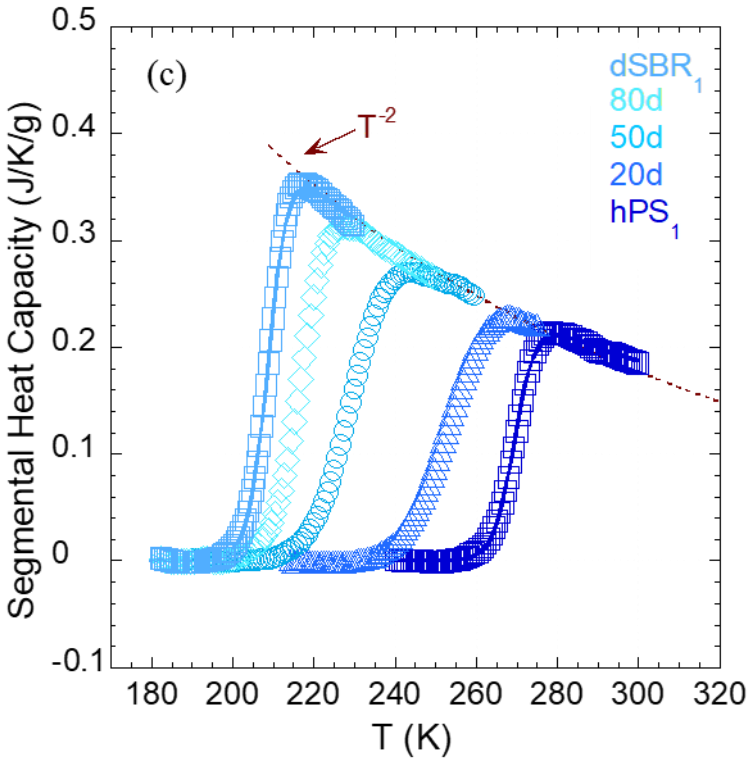

Figure 4.2: Calorimetric traces of the system $hSBR_2/dPS_2$ (a), $hSBR_1/dPS_1$ (b) and $dSBR_1/hPS_1$ (c) after the subtraction of the glassy part; the same procedure has been applied on the neat components and the mixtures. The solid lines fitting the neat polymers data were obtained by using eq. 3.4 with parameters given in table 3.4.

4.1.2 Composition Dependence of the Glass Transition of the Blends

Figure 4.3 shows the composition dependence of the glass transition temperatures defined from the inflection point for the blends as well as the pure components. T_g decreases monotonously as the content of SBR in the blends is increased.

The whole set of data is well described using the Gordon-Taylor (G-T) equation: [2,3]

$$T_g^{blend} = \left[(1-\varphi)T_g^{PS} + k_{G-T}\varphi T_g^{SBR}\right]/\left[(1-\varphi) + k_{G-T}\varphi\right] \qquad (4.1)$$

where φ is the weight fraction of SBR and k_{G-T} a fitting parameter. [12] When $k_{G-T} = T_g^{SBR}/T_g^{PS}$ Eq. 4.1 transforms in the well-known Fox equation:[4]

$$1/T_g^{Blend} = \varphi/T_g^{SBR} + (1-\varphi)/T_g^{PS} \quad (4.2)$$

The G-T equation provides a satisfactory fit of the data for the three systems (figure 4.4(b)) and yields $k_{G-T} = 1.3$ for the $hSBR_1/dPS_1$, $k_{G-T} = 1.6$ for the inverse labeling $dSBR_1/hPS_1$ and $k_{G-T} = 1.3$ for $hSBR_2/dPS_2$.

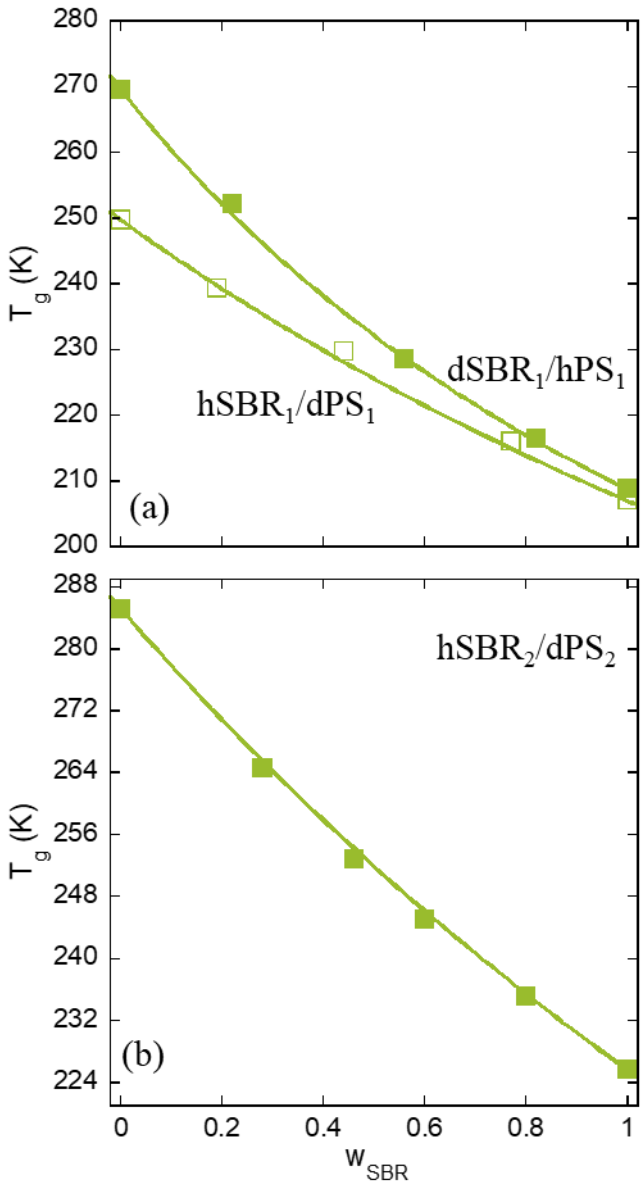

Figure 4.3: Evolution of the glass-transition temperature as a function of composition for $hSBR_1/dPS_1$ blends (empty squares) and for $dSBR_1/hPS_1$ (filled squares) in panel (a) and for $hSBR_2/dPS_2$ in panel (b). The prediction of the Gordon-Taylor equation (eq. 4.1) for the blends is shown as solid lines.

4.2 Small Angle Neutron Scattering

Representative SANS results are shown in figure 4.4 at 298 K for the different samples investigated corresponding to $hSBR_2/dPS_2$ mixtures, and in figure 4.4(b) for the sample with $hSBR_2$ content $w_{SBR} = 0.5$ as function of temperature. Figure 4.5 shows the results corresponding to the other blends. In all cases, with decreasing Q, the data show a first clear increase of the scattered intensity followed by a plateau. This regime is dominated by thermally driven concentration fluctuations (TCF) in the mixture. The amplitude of this contribution strongly depends on composition. For a given sample, as shown figure 4.4(b), the amplitude of TCF increases with decreasing temperature. To characterize the TCF the Ornstein-Zernike (OZ) expression is usually invoked:

$$I_{OZ}(Q) = \frac{I_{OZ}(0)}{1+(Q\xi)^2} \tag{4.3}$$

where $I_{OZ}(0)$ --the Q→0 value of the function-- is the amplitude and ξ is the correlation length for TCF. The OZ function is in general a good approximation of the structure factor of polymer blends in the random phase approximation (RPA).[5–8] Below $Q \approx 0.015 \text{Å}^{-1}$, an additional contribution to the scattered intensity is found which varies as $\sim Q^{-x}$ with $x \approx 4$. The origin of this contribution to the scattering is controversial. It has been tentatively attributed to well-defined or 'sharp' boundaries due the presence of large domains,[9] to excess inhomogeneity resulting from stress-diffusion coupling during temperature change[10] or to pronounced long-range density fluctuations.[11] Its interpretation is beyond the scope of our work. We just parameterize it with a Porod-like power law $\sim Q^{-4}$ to properly obtain the information on the OZ contribution. In order to describe the SANS results, we also need to consider a background (BG), accounting for incoherent contributions. These are higher for samples richer in protonated component, i.e., with increasing SBR concentration. With all, the data were fitted by the following expression:

$$I_{exp}(Q) = \frac{C}{Q^4} + \frac{I_{OZ}(0)}{1+(Q\xi)^2} + BG \tag{4.4}$$

Figure 4.4 and 4.5 show that this kind of description works rather well.

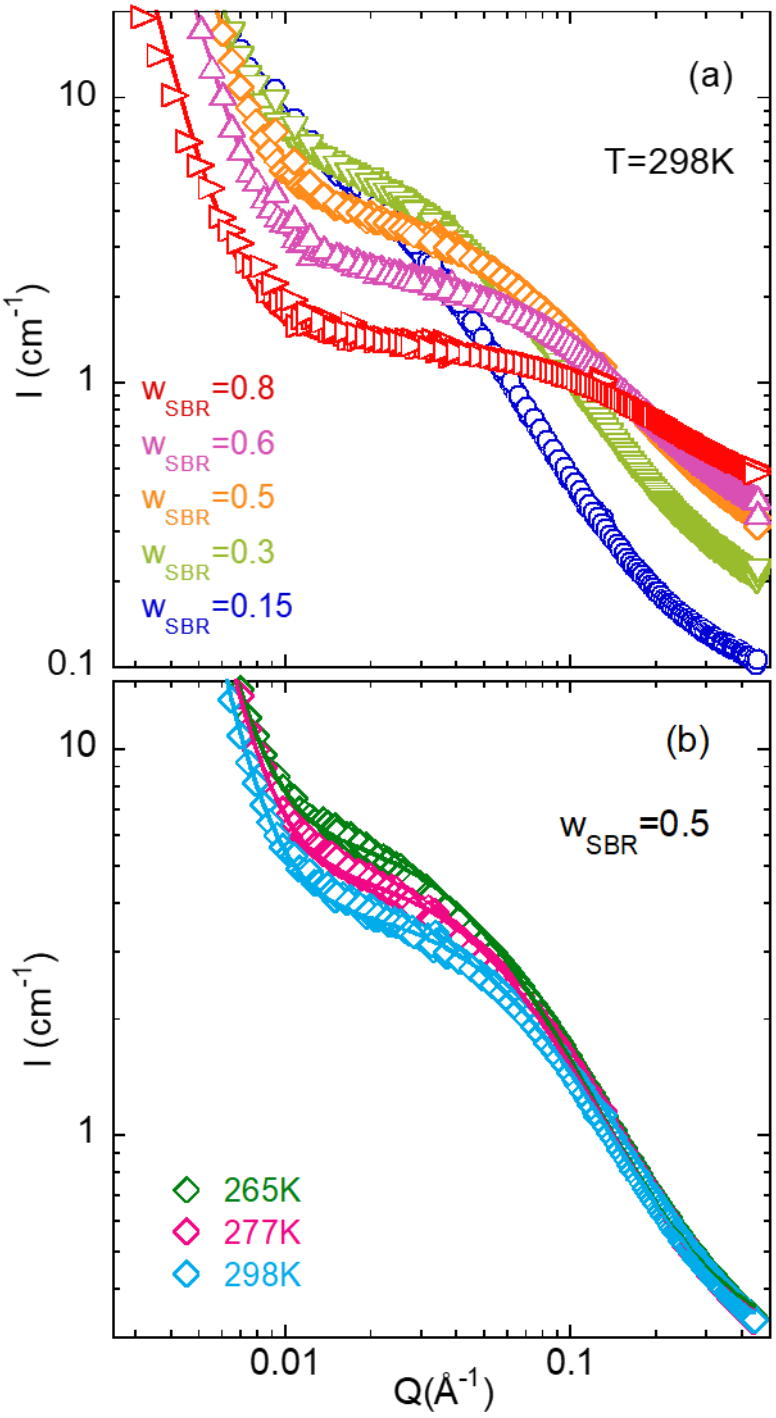

Figure 4.4: SANS results on the different $hSBR_2/dPS_2$ blends at 298 K (a) and for $w_{SBR} = 0.5$ at the three temperatures investigated (b). Solid lines are fits using Eq. 4.4.

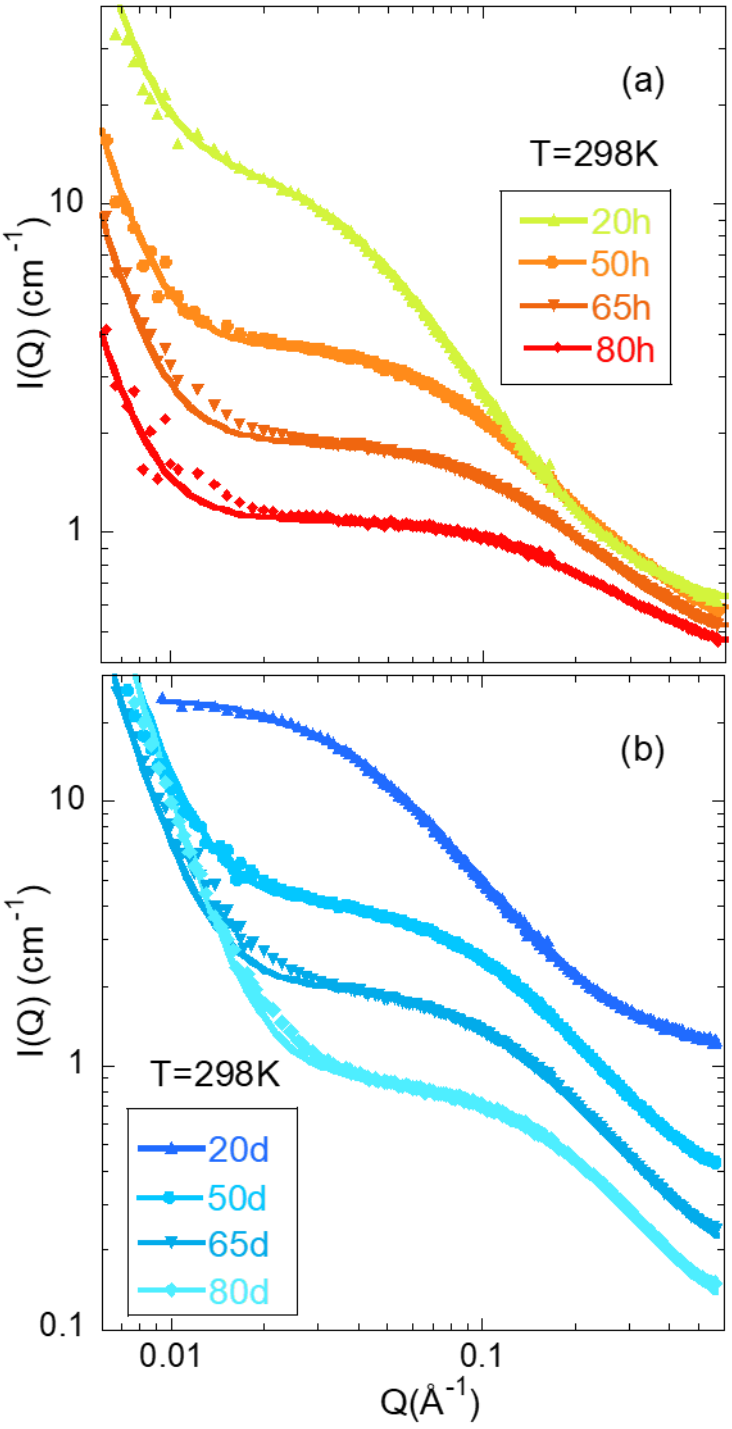

Figure 4.5: SANS results on (a) $hSBR_1/dPS_1$ and (b)$dSBR_1/hPS_1$ blends at 298 K. Solid lines are fits using Eq. 4.4.

4.2.1 The Spinodal Decomposition Temperature T_s

To determine the spinodal decomposition temperature T_s (where the amplitude of TCF diverges) for the different compositions, the inverse values of the OZ amplitudes $I_{OZ}(0)$ is represented as function of the inverse temperature, as shown in figure 4.6(a) for the system $hSBR_2/dPS_2$. Actually, the results have been plotted against the variable T_g/T– where the T_g value has been previously determined as the inflection point of the DSC trace— to clearly discern whether the spinodal temperature is below or above the calorimetric average glass transition. In this plot we discarded the lowest temperature (265 K) results for the $w_{SBR} = 0.3$ and $w_{SBR} = 0.15$ sample, because this temperature is very close to the T_g of the blend and total equilibrium was not assured, even with the long equilibration time employed in the measurements. From figure 4.6(a) it can be seen that the signatures of TCF are amplified with decreasing temperature. At the same time, the correlation length ξ increases (see figure 4.6(b)). These observations point to phase separation of the mixtures at low temperatures (UCST-type phase behavior). The values of T_s were obtained as the intercept of the linear fit of the data in figure 4.6(a) with the *x*-axis. These values are represented in figure 4.7 together with the calorimetric results on the vitrification phenomenon and compiled in table 4.1.

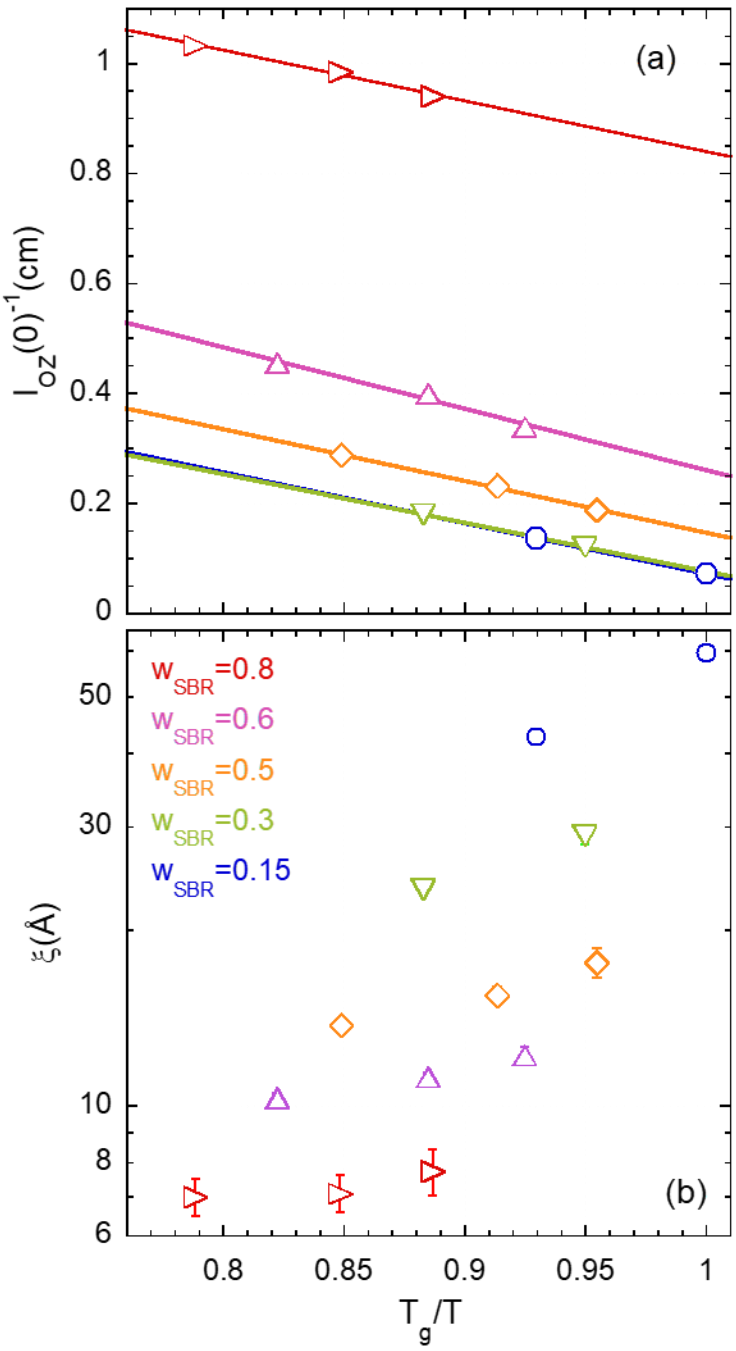

Figure 4.6: Inverse amplitudes (a) and correlation length (b) of the Ornstein-Zernike contribution to the SANS patterns as functions of T_g/T, where T_g is the calorimetric average glass-transition temperature of the corresponding sample of the $hSBR_2/dPS_2$ blends. Lines in (a) are linear fits. The code for the $hSBR_2$ weight fraction of the different blends is shown in (b).

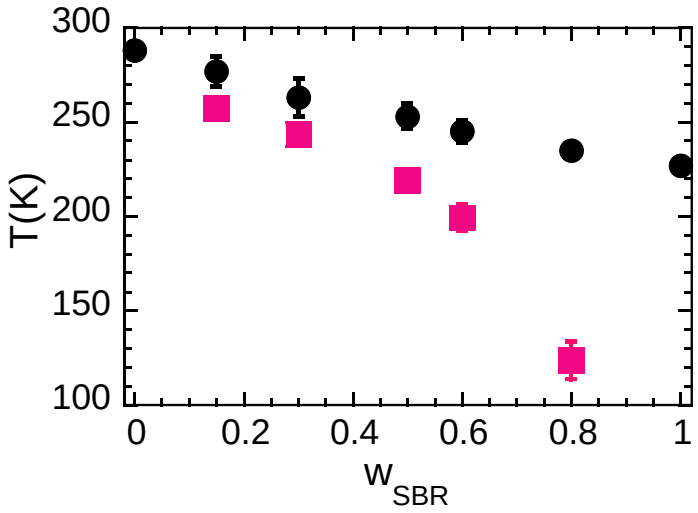

Figure 4.7: Average glass-transition temperature for the $hSBR_2/dPS_2$ blends obtained from DSC (T_g, circles) and spinodal decomposition temperature deduced from SANS (T_s, squares). Bars on T_g-values display the limits of the calorimetric glass transition range (initial and final temperatures of the heat flow step as seen in figure 4.1) and bars on T_s data represent the estimated uncertainties in their determination.

The correlation length ξ for the systems $hSBR_1/dPS_1$ and $dSBR_1/hPS_1$ are presented in figure 4.8. In a similar way as explained above the spinodal decomposition temperature T_s was determined as the value at which $I_{OZ}(0)$ tends to diverge. The resulting values are compiled in figure 4.9 together with calorimetric results.

In all cases the correlation length ξ increases with increasing content of PS and with decreasing temperature, being this tendency particularly strong in the samples with highest concentration of PS. The correlation length ξ is rather small: at RT $\xi \approx 5–10$ Å in SBR-rich blends, 10-15 Å in $50/50$ blends and around 20-30 Å in PS-rich mixtures (see Fig. 4.6 and 4.8).

For all the compositions investigated, the value of T_g is always higher than T_s: upon cooling, the sample becomes a glass before demixing. In other words, in the supercooled liquid regime the blends are stable mixtures from a thermodynamic point of view.

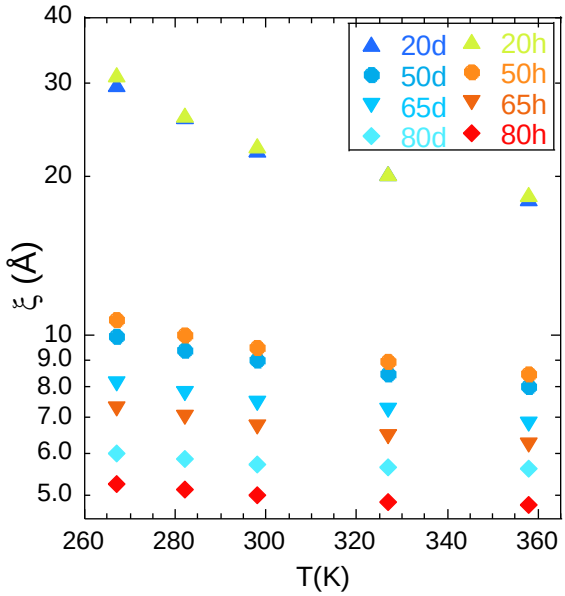

Figure 4.8: Temperature dependence of the correlation length for thermally driven concentration fluctuations of $hSBR_1/dPS_1$ and $dSBR_1/hPS_1$ blends.

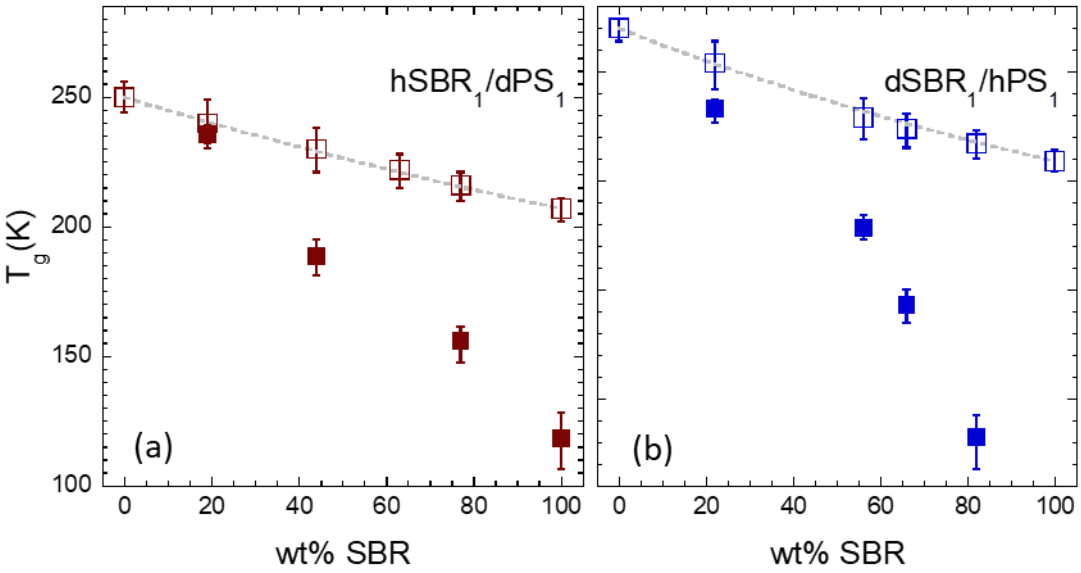

Figure 4.9: Average glass-transition temperature for the $hSBR_1/dPS_1$ (a) and $dSBR_1/hPS_1$ (b) blends obtained from DSC (T_g, empty squares) and spinodal decomposition temperature deduced from SANS (T_s, filled squares). Bars on T_g-values display the limits of the calorimetric glass transition range (initial and final temperatures of the heat flow step) and bars on T_s data represent the estimated uncertainties in their determination.

4.2.2 Determination of the Effective Interaction Parameter

SANS results also allow determining the effective interaction parameter between components χ. The Flory interaction parameter between PS and SBR can be obtained from the composition-dependence of the zero wavevector limit of the scattering function $S(0)$. For a binary blend of interacting polymer chains of species A and B with corresponding degrees of polymerization N_A and N_B, monomeric volumes v_A and v_B and average volume fractions φ_A and φ_B =1 − φ_A, the Random Phase Approximation (RPA) predicts that[7]

$$\frac{1}{S(0)} = \frac{(\Delta\rho)^2}{I(0)} = \frac{1}{N_A\langle\varphi_A\rangle v_A} + \frac{1}{N_B\langle 1-\varphi_A\rangle v_B} - \frac{2\chi}{v_0} \tag{4.5}$$

Here v_0 is the molar volume of a reference unit cell $v_0 = (v_A v_B)^{1/2}$. The fits of the SANS results yield $I(0) = I_{OZ}(0)$. Using the values calculated for polymerization degrees, monomeric volumes and scattering length densities of the blend components (see table 2.2), Eq. 4.5 was fitted to the experimentally obtained values of $S(0)$ at different temperatures, as can be seen in figure 4.10 for $hSBR_2/dPS_2$ blends. Note that for this and the $w_{SBR} = 0.3$ sample, the results at the lowest temperature (265 K) were discarded, since it is very close to the glass-transition temperature of these blends and equilibration was probably not achieved. The χ-values obtained from the fits are represented in Figure 4.11. In the whole temperature range investigated the effective χ parameter presents positive values, indicative for repulsive interactions between the components. Its temperature dependence can be described by the law $\chi = -0.124 + 46.05\,\mathrm{K}/T$.

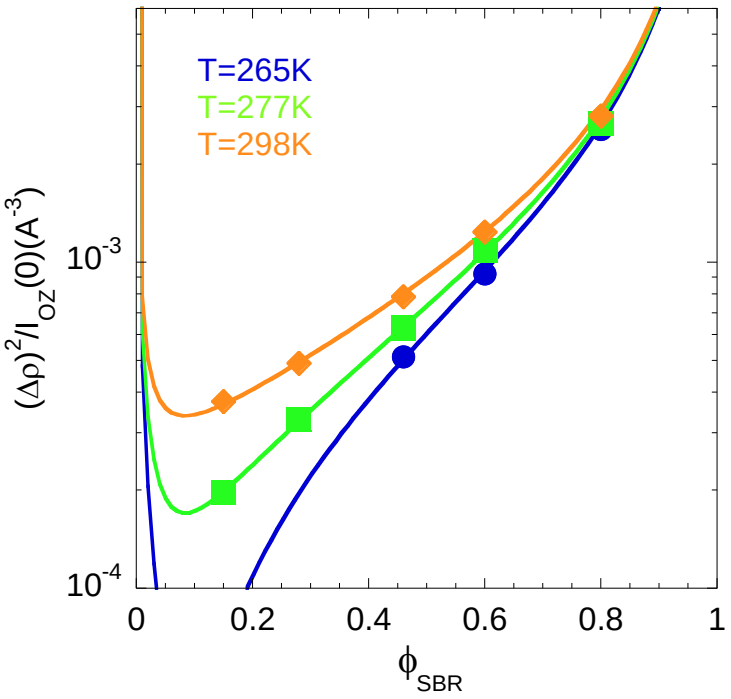

Figure 4.10: Concentration dependence of the inverse of the OZ amplitude for the three temperatures investigated for $hSBR_2/dPS_2$ blends. Lines are fits of Eq. 4.5.

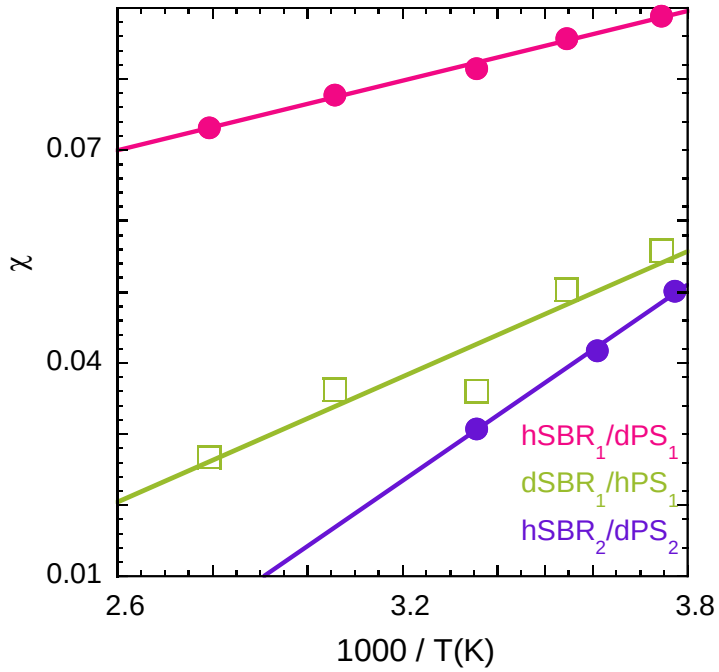

Figure 4.11: Inverse temperature dependence of the χ parameter obtained in this work. Lines are fits by the laws $\chi = -0.124 + 46.05\,\mathrm{K}/T$ for hsBR2/dPS2, $\chi = -0.0274 +$

$16.36\,\mathrm{K}/T$ and $\chi = -0.0535 + 7.36\,\mathrm{K}/T$, for $hSBR_1/dPS_1$ and $dSBR_1/hPS_1$ respectively.

Also, for the systems $hSBR_1/dPS_1$ and $dSBR_1/hPS_1$ the Flory interaction parameter χ has been determined; figure 4.12 shows the concentration dependence of the inverse of the OZ amplitude for the different temperatures investigated and its description by equation 4.5.

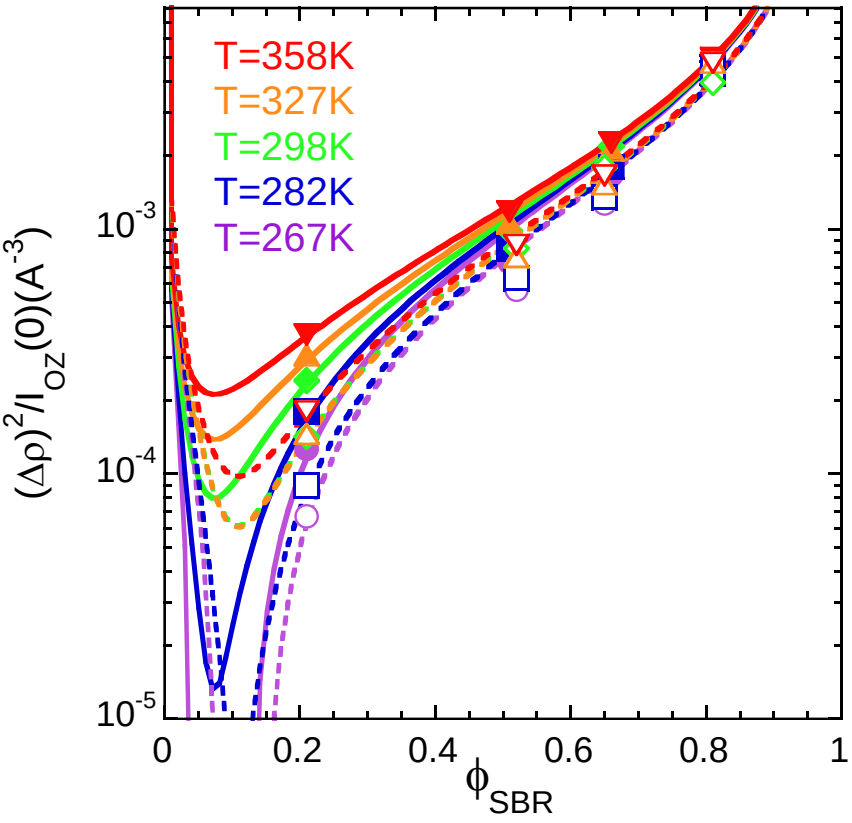

Figure 4.12: Concentration dependence of the inverse of the OZ amplitude for the different temperatures investigated for $hSBR_1/dPS_1$ and $dSBR_1/hPS_1$ blends. Lines are fits of Eq. 4.5.

In Figure 4.11 the χ values for the three different systems investigated are reported. For the system $hSBR_1/dPS_1$ they follow the law $\chi = -0.0274 + 16.36\,\mathrm{K}/T$, while for $dSBR_1/hPS_1$ $\chi = -0.0535 + 7.36\,\mathrm{K}/T$.

The χ-values obtained for $hSBR_2/dPS_2$ are lower than those reported for blends $hSBR_1/dPS_1$ and $dSBR_1/hPS_1$ of PS oligomers low molecular weight ($900 g/mol$ vs $500 g/mol$) and SBR of different microstructure (lower styrene content, leading to a lower glass-transition temperature and thereby enhanced dynamic asymmetry). This result reflects an improved compatibility of the components when the co-polymer has more chemical and dynamic similarity with the oligomer. Finally, it is worthy of remark that the analysis of the Q-dependence of the SANS results in terms of the habitual RPA[6] is not trivial due to the oligomeric character of the PS component. This would require the description of the form factor for a finite number of monomers with some chain stiffness. This kind of analysis is beyond the scope of this Thesis.

4.2.3 Mean-Squared Concentration Fluctuation $\langle \delta\varphi^2 \rangle$

From the insight on TCF by SANS also the mean-squared concentration fluctuation $\langle \delta\varphi^2 \rangle$ in a given sample volume can be deduced. Based on previous works of Fischer et al.,[12,13] Colby, Kumar et al.[14] proposed that in an incompressible binary blend the mean-squared concentration fluctuation $\langle \delta\varphi^2 \rangle$ is given by

$$\langle \delta\varphi^2 \rangle = \frac{\sqrt{v_A v_B}}{4\pi^2} \int_0^\infty S(Q)\, Q^2\, F(Q)\, dQ \tag{4.6}$$

where v_A and v_B are the monomeric volumes of the components A and B and $F(Q)$ is the form factor of the considered volume. For a sphere of radius R_c, and if, as in the present case, an OZ function (see Eq. 4.3) is used to describe the structure factor $S(Q)$, Eq. 4.6 can be expressed as

$$\langle \delta\varphi^2 \rangle (R_c) = \frac{3\sqrt{v_A v_B}}{8\pi} \frac{S(0)}{R_c^3} \left\{ 1 - \frac{3(1+R_c/\xi)^2}{2(R_c/\xi)^3} \left[\frac{R_c/\xi - 1}{R_c/\xi + 1} + e^{-2R_c/\xi} \right] \right\} \tag{4.7}$$

Here $S(0) = I_{OZ}(0)/(\Delta\rho)^2$, with $(\Delta\rho)$ the difference in scattering length density of the two components. Introducing the values of v_A, v_B and $(\Delta\rho)$ corresponding to the blend components here considered (see table 2.2) and the values experimentally determined for $I_{OZ}(0)$ and ξ (Figures 4.6 and 4.8), the concentration-dependent $\langle \delta\varphi^2 \rangle$-values for a given

value of the length scale $2R_c$ can be calculated. Figure 4.13(a) shows the results obtained for $\sigma^{SANS}(R_c) = \sqrt{\langle\delta\varphi^2\rangle(R_c)}$ for some explored values of $2R_c$ using the SANS data at 298 K (the highest explored temperature) for the system $hSBR_2/dPS_2$. Despite of the fact that $I_{OZ}(0)$ and ξ change very clearly with temperature in the temperature range investigated, for each value of $2R_c$, $\langle\delta\varphi^2\rangle$ values varied very little with temperature, within typical uncertainties (see figure 4.13b). Thus, in good approach $\langle\delta\varphi^2\rangle$-values can be considered as temperature independent.

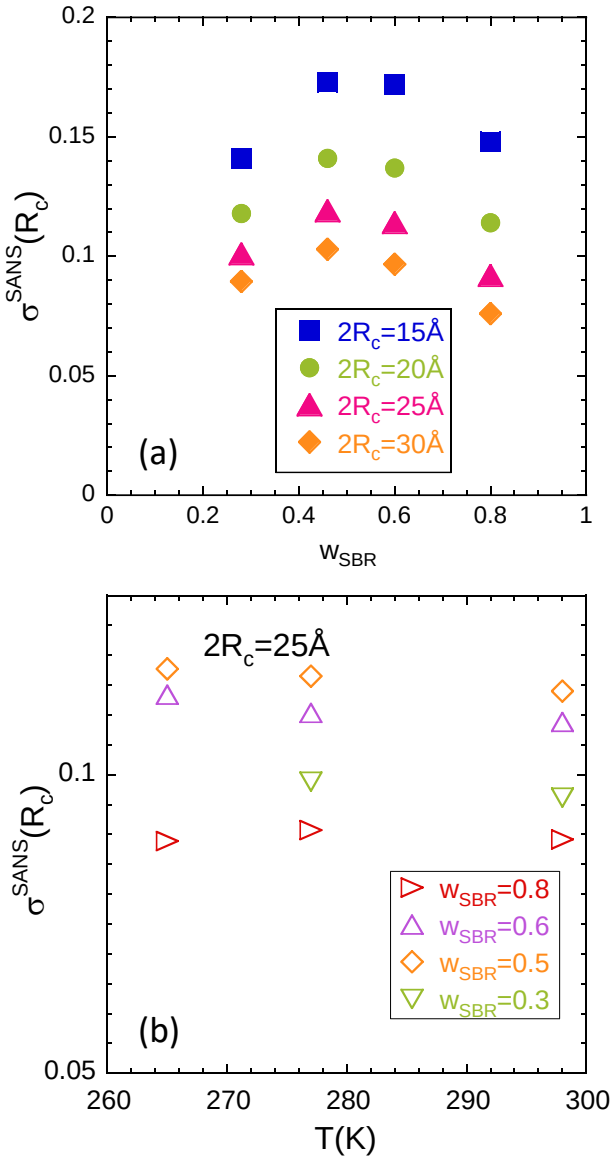

Figure 4.13: (a) Concentration dependence of the width of the Gaussian distributions of concentration fluctuations deduced from the SANS results assuming different explored

spherical volumes with diameter $2R_c$. (b) Temperature dependence of the width of the Gaussian distributions of concentration fluctuations deduced from the SANS results for a spherical volume of 25 Å diameter.

This information will be used in chapter 5 to be compared with BDS and DSC results in order to estimate a fundamental magnitude, namely the relevant length scale involved in the α-relaxation.

4.3 Dielectric Relaxation Response

For the different blends of the system $hSBR_2/dPS_2$, Figure 4.14 shows the dielectric loss tangent as a function of frequency at 260 K (a) and at temperatures where the α-relaxation peak is well centered in the explored frequency window (b). Results are compared with those of the neat polymers in the same figure. From the shape and the position of the peaks, it is clear that the α-relaxation is strongly affected by blending. As PS is added to SBR in the blend, a broader and slower α-relaxation is observed compared to that of pure SBR. So, blending affects the α-relaxation by producing a broadening of the relaxation, evidencing the dynamic heterogeneity. However, the β-relaxation does not seem to be significantly affected by blend composition, beyond the relaxation intensity that is in good approximation proportional to the corresponding weight fraction.

Figure 4.15 shows the results corresponding to the other blends at about 20 K above the glass transition temperature of each sample for the system $dSBR_1/dPS_1$ (Fig. 4.15a), and 25 K above for the system $hSBR_1/dPS_1$ (Fig. 4.15b).

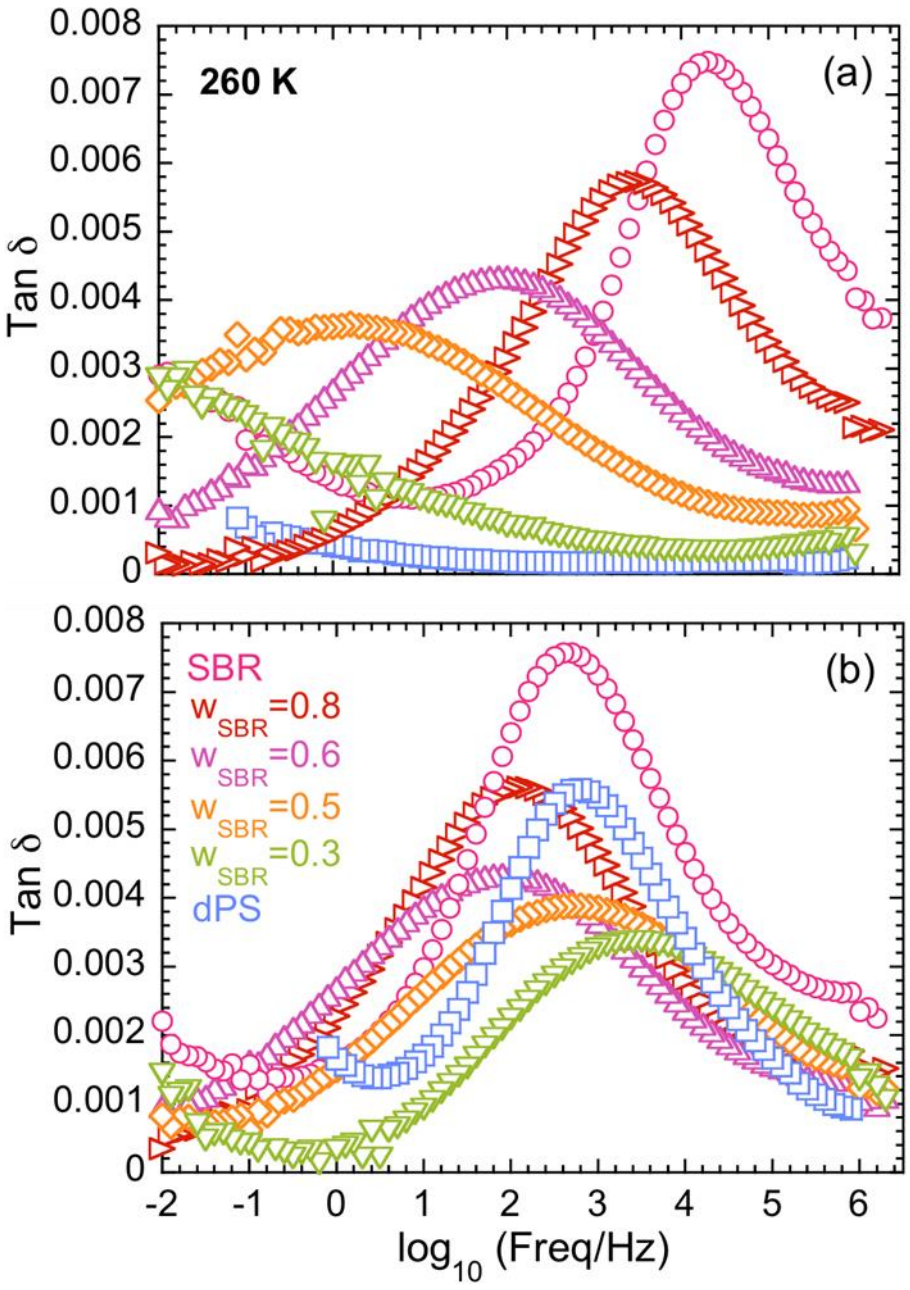

Figure 4.14: (a) Dielectric spectra at 260 K from the pure components $hSBR_2$ and dPS_2, and from blends (b) Comparison of dielectric spectra at representative temperatures from the pure components and from blends. The corresponding temperatures are 245 K for $hSBR_2$, 310 K for dPS_2, 250 K for $w_{SBR} = 0.8$, 260 K for $w_{SBR} = 0.6$, 275 K for $w_{SBR} = 0.5$, and 295 K for $w_{SBR} = 0.3$.

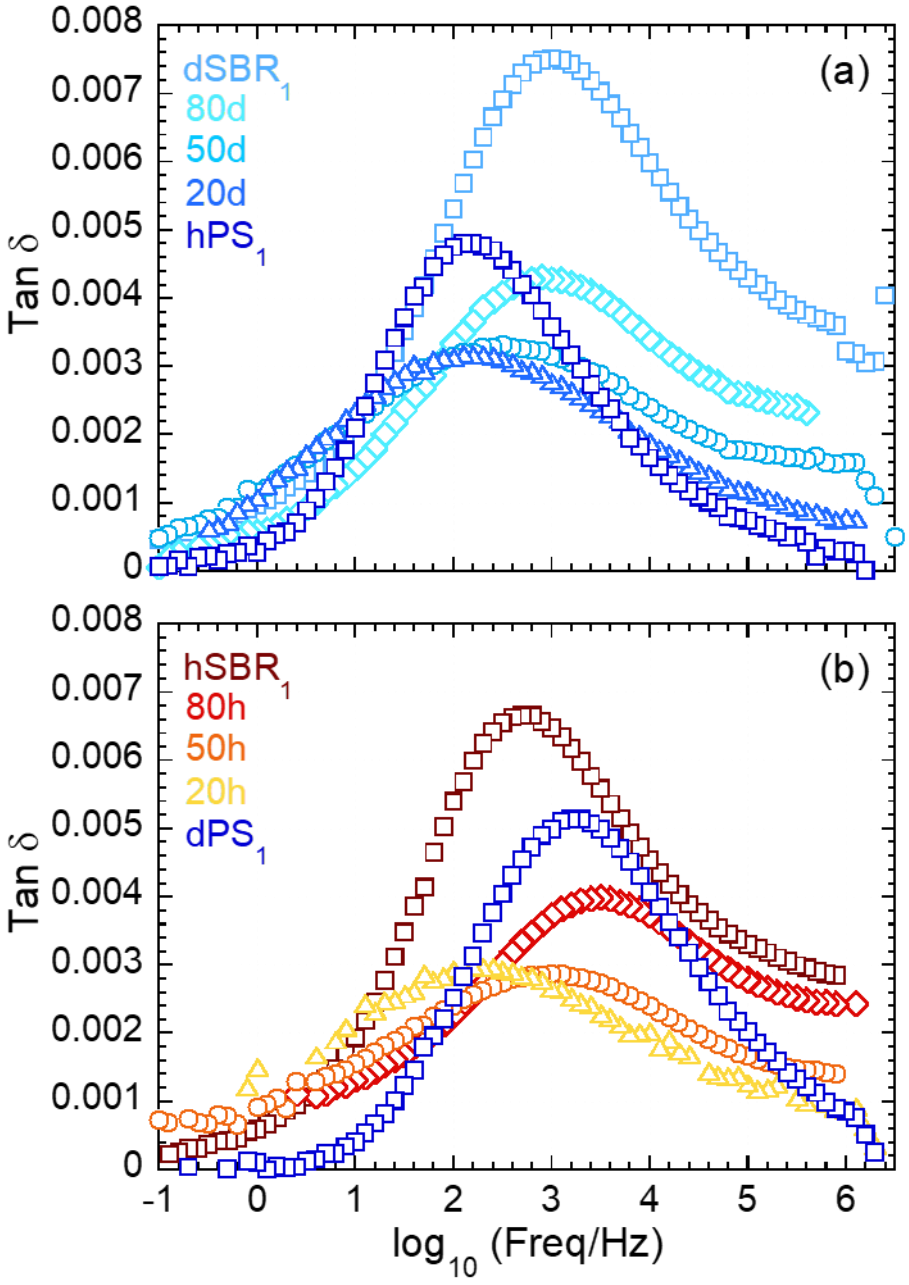

Figure 4.15: Frequency dependence of the dielectric tan δ for $dSBR_1/hPS_1$ at $T = T_g +$ 20K (a), and for $hSBR_1/dPS_1$ at $T = T_g + 25$K (b).

In all the systems a broadening of the relaxation time distribution is observed by adding PS into the blends. By comparing the results on the mixtures with those of the neat components, it is apparent that the dielectric response of the blends is broader and intermediate between those of the neat systems. Note that the BDS results of the three

systems are centered at different frequencies; the peak observed for the sample where the SBR component is protonated (Fig. 4.14 and 4.15b) is centered at clearly higher frequencies, and less broad, than that displayed by the blend with the inverse isotopic labeling (Fig. 4.15a). Since the dielectric spectroscopy is not sensitive to deuteration, this difference has to be attributed to the different microstructure and M_w of the blend components, as reflected in the DSC results commented above.

4.4 References

(1) Colmenero, J.; Arbe, A. Segmental Dynamics in Miscible Polymer Blends: Recent Results and Open Questions. *Soft Matter* **2007**, *3* (12), 1474–1485.

(2) Weng, L.; Vijayaraghavan, R.; MacFarlane, D. R.; Elliott, G. D. Application of the Kwei Equation to Model the Tg Behavior of Binary Blends of Sugars and Salts. *Cryobiology* **2014**, *68* (1), 155–158.

(3) Gordon, M.; Taylor, J. S. Ideal Copolymers and the Second-order Transitions of Synthetic Rubbers. I. Non-crystalline Copolymers. *Journal of Applied Chemistry* **1952**, *2* (9), 493–500.

(4) Fox, T. G. Influence of Diluent and of Copolymer Composition on the Glass Temperature of a Poly-Mer System. *Bull. Am. Phys. Soc.* **1956**, *1*, 123.

(5) Wignall, G. D.; Melnichenko, Y. B. Recent Applications of Small-Angle Neutron Scattering in Strongly Interacting Soft Condensed Matter. *Reports on Progress in Physics* **2005**, *68* (8), 1761–1810.

(6) Higgins, J. S.; Benoit, H. C. Polymers and Neturon Scattering. **1994**.

(7) Rubinstein, M.; Colby, R. H. *Polymer Physics*; Oxford university press New York, 2003; Vol. 23.

(8) de Gennes, P.-G.; Gennes, P.-G. *Scaling Concepts in Polymer Physics*; Cornell university press, 1979.

(9) Schwahn, D.; Yee-Madeira, H. Spinodal Decomposition of the Polymer Blend Deutereous Polystyrene (d-PS) and Polyvinylmethylether (PVME) Studied with High Resolution Neutron Small Angle Scattering. *Colloid Polym Sci* **1987**, *265* (10), 867–875.

(10) Koizumi, S. UCST Behavior Observed for a Binary Polymer Mixture of Polystyrene/Poly (Vinyl Methyl Ether)(PS/PVME) with a PS Rich Asymmetric Composition as a Result of Dynamic Asymmetry & Imbalanced Local Stress, Viscoelastic Phase Separation, and Pinning by Vitrification. *Soft Matter* **2011**, *7* (8), 3984–3992.

(11) Schwahn, D.; Pipich, V.; Richter, D. Composition and Long-Range Density Fluctuations in PEO/PMMA Polymer Blends: A Result of Asymmetric Component Mobility. *Macromolecules* **2012**, *45* (4), 2035–2049.

(12) Lubchenko, V.; Wolynes, P. G. Theory of Structural Glasses and Supercooled Liquids. *Annu. Rev. Phys. Chem.* **2007**, *58*, 235–266.

(13) Zetsche, A.; Fischer, E. W. Dielectric Studies of the α-Relaxation in Miscible Polymer Blends and Its Relation to Concentration Fluctuations. *Acta Polymerica* **1994**, *45* (3), 168–175.

(14) Shenogin, S.; Kant, R.; Colby, R. H.; Kumar, S. K. Dynamics of Miscible Polymer Blends: Predicting the Dielectric Response. *Macromolecules* **2007**, *40* (16), 5767–5775.

(15) Hu, Y. C.; Tanaka, H. Origin of the Boson Peak in Amorphous Solids. *Nat Phys* **2022**, *18* (6), 669–677.

(16) Starr, F. W.; Douglas, J. F.; Sastry, S. The Relationship of Dynamical Heterogeneity to the Adam-Gibbs and Random First-Order Transition Theories of Glass Formation. *Journal of Chemical Physics* **2013**, *138* (12).

(17) Katana, G.; Fischer, E. W.; Hack, T.; Abetz, V.; Kremer, F. Influence of Concentration Fluctuations on the Dielectric α-Relaxation in Homogeneous Polymer Mixtures. *Macromolecules* **1995**, *28* (8), 2714–2722.

(18) Gambino, T.; Alegría, A.; Arbe, A.; Colmenero, J.; Malicki, N.; Dronet, S. Modeling the High Frequency Mechanical Relaxation of Simplified Industrial Polymer Mixtures Using Dielectric Relaxation Results. *Polymer* **2020**, *187*, 122051.

Chapter 5

BDS & DSC Modeling

The aim of this chapter is to establish the quantitative connection between the thermally driven concentration fluctuations in the investigated blends, as characterized above by SANS, and the glass transition behaviour, particularly the breath of the transition region. For this end, first the effects of thermally driven concentration fluctuations are included in the modeling of the dielectric relaxation data. Next, a direct connection between this modelling and the behavior of the DSC curves is stablished, which allows connecting the component segmental dynamics in the blend above the glass-transition temperature (at equilibrium) and the way the equilibrium is lost when cooling down towards the glassy state. The model developed for this purpose, that is based on self-concentration and thermally driven concentration fluctuations concepts, is first described in detail in this chapter.

5.1 Modeling the Dynamics of SBR/PS Blends

The model used for describing the α-relaxation of SBR/PS blends[1,2] is based on thermally driven concentration fluctuations (TCF)[3–8] and self-concentration (SC)[9] concepts. Following the works in Refs.[1,2], it is assumed that the TCF evolve on a much longer time scale than that of the segmental relaxation. This entails that the polymer blend can be viewed as a set of sub-volumes 'i' each with a different SBR concentration, $0 \leq \varphi_i \leq 1$.

This quasi-static distribution of concentration $g(\varphi_i)$ in the blends, can be described by a Gaussian function centered around the bulk concentration of the blend φ :

$$g(\varphi_i) \propto exp\frac{-(\varphi_i-\varphi)^2}{2\sigma^2} \tag{5.1}$$

where σ is the standard deviation of the distribution of concentration. When applying the model to describe a given measurable extensive magnitude Φ (e.g., $\Phi = \varepsilon^*(\omega)$ in a BDS experiment, $\Phi = C_p$ in a DSC experiment, etc.) the contribution of the components to the total magnitude Φ of the blend can be written as:

$$\Phi_{SBR} = \sum_i g(\varphi_i) \times \varphi_i \Phi_{SBR,i} \tag{5.2a}$$

$$\Phi_{PS} = \sum_i g(\varphi_i) \times (1 - \varphi_i) \Phi_{PS,i} \tag{5.2b}$$

where $\Phi_{SBR,i}$and $\Phi_{PS,i}$—the function associated to SBR and PS, respectively, in region '*i*'— are assumed to have the same characteristics as the same function of the corresponding homopolymers (e.g. shape parameters, strength etc.) except the time scale/characteristic temperature.

The time scale of the dynamics of a given polymer segment located in region '*i*' of a miscible blend is controlled by the local composition in a small region around the segment c of this component. This local composition is described by an effective concentration $\varphi_{eff,i}$, which for the SBR and PS components is given by:

$$\varphi_{eff,i}^{SBR} = \varphi_{self}^{SBR} + \left(1 - \varphi_{self}^{SBR}\right)\varphi_i \tag{5.3a}$$

$$\varphi_{eff,i}^{PS} = \varphi_{self}^{PS} + \left(1 - \varphi_{self}^{PS}\right)(1 - \varphi_i) \tag{5.3b}$$

where the self-concentration parameters, φ_{self}^{SBR} and φ_{self}^{PS}, will be assumed to be concentration and temperature independent. This is a crude approach when using the self-concentration parameters for data fitting; however, it can be justified by considering their fundamental significance.[10] Note that self-concentration was introduced in connection with both the relatively small size of the region around a given segment determining its dynamical behavior and the molecular characteristics (persistence length) of the particular component of the mixture.[9]

The relaxation time values of each component in a given sub-volume are then calculated using the Vogel-Fulcher-Tammann (VFT) equation:[11–13]

$$\tau_i(T) = \tau_\infty exp\left[D_i T_{0,i} / \left(T - T_{0,i}\right)\right]. \tag{5.4}$$

The same value of the prefactor $\tau_\infty = 10^{-13}$s (corresponding to a typical vibrational frequency) is assumed for the pure components and for each component in any of the

regions. The other VFT parameters, D (related with the so-called dynamic fragility) and T_0 (Vogel temperature), are evaluated from the neat components D^{SBR}, T_0^{SBR}, D^{PS} and T_0^{PS} (see chapter 3) and obtained for each component in a given region "*i*" by using mixing rules with the corresponding effective concentrations. Particularly, a linear mixing rule is assumed for D_i:

$$D_i^{SBR} = D^{SBR}\varphi_{eff,i}^{SBR} + D^{PS}(1 - \varphi_{eff,i}^{SBR}) \tag{5.5a}$$

$$D_i^{PS} = D^{PS}\varphi_{eff,i}^{PS} + D^{SBR}(1 - \varphi_{eff,i}^{PS}) \tag{5.5b}$$

For $T_{0,i}$ a Gordon-Taylor-like equation is used, i.e. $T_{0,i}$ values are calculated as

$$T_{0,i}^{SBR} = \frac{T_0^{PS}\left[\left(1-\varphi_{eff,i}^{SBR}\right)\right]+K_{G-T}\varphi_{eff,i}^{SBR}T_0^{SBR}}{\left(1-\varphi_{eff,i}^{SBR}\right)+K_{G-T}\varphi_{eff,i}^{SBR}} \tag{5.6a}$$

$$T_{0,i}^{PS} = \frac{T_0^{PS}\varphi_{eff,i}^{PS}+K_{G-T}\left(1-\varphi_{eff,i}^{PS}\right)T_0^{SBR}}{\varphi_{eff,i}^{PS}+K_{G-T}\left(1-\varphi_{eff,i}^{PS}\right)} \tag{5.6b}$$

using the values of K_{G-T} determined in previous chapter. In the framework of this model the total function Φ of the blends is obtained summing up the contribution of each component in the blend.

$$\Phi_{BLEND} = \Phi_{SBR} + \Phi_{PS} \tag{5.7}$$

The only parameters involved in the modeling are the self-concentrations of both components φ_{self}^{SBR} and φ_{self}^{PS} determining the local composition in each region, and the widths σ of the distributions of concentration associated to the spontaneous thermal concentration fluctuations, described by means of Gaussian functions, $g(\varphi_i)$, Eq. 5.1.

5.2 Describing the Dielectric Response with the Input of SANS

BDS results in the blends were described using the simple model presented above (Eqs. 5.1-5.7 with $\Phi = \varepsilon^*(\omega)$), based on the simple description of the dielectric relaxation of the neat components, explained in detail in chapter 3.1. In the dielectric relaxation modeling it was assumed that the relaxation shape and intensity of the neat components and those of these components inside each of the regions "*i*" forming the mixtures are the same. As presented in chapter 3.1 the dielectric α-relaxation of each neat component can be described by a Havriliak-Negami equation[42] with temperature independent shape parameters. These characteristics are maintained for the contribution of the considered component to the relaxation of the blend, being the relaxation time the parameter assumed to be affected by blending as above detailed, and φ_{self}^{SBR} and φ_{self}^{PS} and the widths σ the only parameters to be determined.

In a previous preliminary work[1], the self-concentration values for SBR and PS in the blends with $w_{SBR} = 0.8, 0.7, 0.6$ and 0.5 ($\varphi_{self}^{SBR} = \varphi_{self}^{PS} = 0.2$) were assumed to be valid over the whole range of concentration and temperature and the only parameter to be determined was the concentration and temperature dependent σ, obtained from fitting the model to the BDS experimental results. The values of σ could be considered, to a good approximation, independent of temperature. The σ-values determined from BDS can be directly compared with those deduced from SANS for TCF depending on the size of the relevant volume, namely of the radius of the assumed spherical volume R_c (see Chapter 4.2.3). This allows to deduce the relevant length scale for the α-relaxation as monitored by BDS.[14] This relevant length scale will be called $2R_c^{\alpha}$. In that work the value of $2R_c^{\alpha}$ was found to be close to 15-20 Å, independent of concentration and temperature within the uncertainties. Based on these results, the information from SANS experiments can be used to directly obtain concentration-dependent values of σ , imposing a constant value for $2R_c^{\alpha}$. To do this, the value of the relevant length scale $2R_c^{\alpha}$ has to be first determined. The procedure followed is now explained in detail and applied to the $hSBR_2/dPS_2$ system.

In a first step, representative BDS curves of the four mixtures at intermediate temperatures have been analyzed --$hSBR_2/dPS_2$ with $w_{SBR} = 0.8, 0.6, 0.5$ and 0.3--

allowing the three parameters (assumed to be independent of temperature), φ_{self}^{SBR} , φ_{self}^{PS} and σ, to vary freely. In this way, composition-dependent σ values have been obtained (called σ^{BDS}). They are represented in Fig. 5.2 as empty down-triangles. In a second step, these values of σ^{BDS} were compared with those calculated before from the SANS investigation (chapter 4.2.3) for different values of R_c determining the explored volume. These widths are called $\sigma^{SANS}(R_c)$. In figure 4.10, σ^{SANS} results for some explored values of $2R_c$ using the SANS data at 298 K for the different blends were presented as an illustrative example. They are shown again in Fig. 5.2, together with σ^{BDS}. From this comparison, it is clear that the obtained values from BDS are close to SANS values for $2R_c = 25$ Å. Thus, for the hSBR$_2$/dPS$_2$ system, the value deduced for the relevant length scale for the α-relaxation as observed by BDS $2R_c^{\alpha}$ is 25 Å.

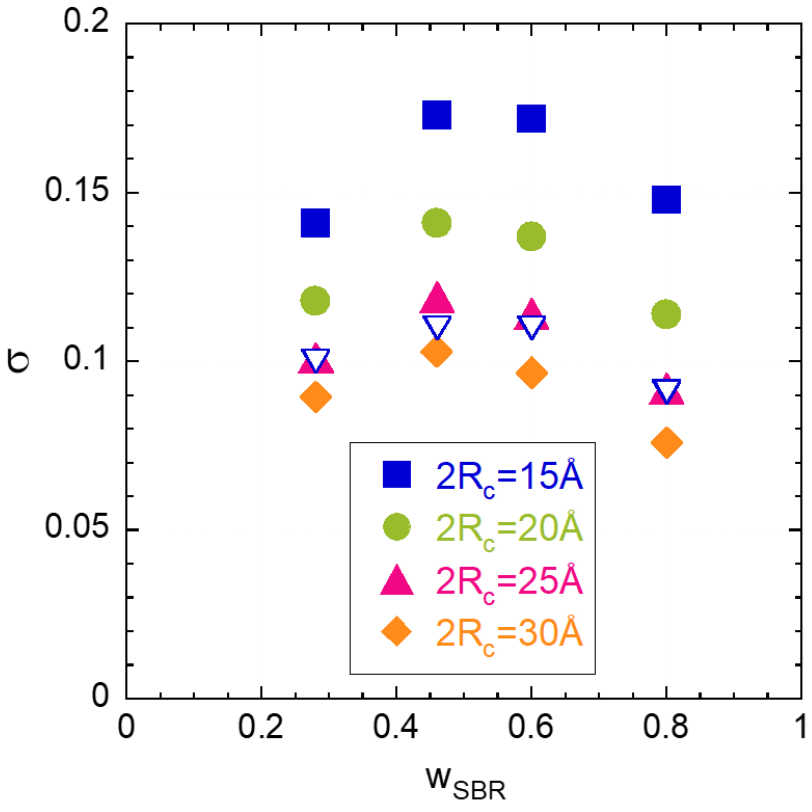

Figure 5.2: Concentration dependence of the width of the Gaussian distributions of concentration fluctuations for hSBR$_2$/dPS$_2$ blends. Empty symbols correspond to values obtained by fitting BDS data, σ^{BDS} deduced without constraints, at temperatures where the dielectric loss peak is well centered in the experimental frequency window

(experimental results in figure 5.3). Filled symbols correspond to the SANS results assuming different values for the length scale $2R_c$, σ^{SANS} (R_c) (same as in figure 4.13).

Consequently, in a third step the σ values were fixed to those obtained from SANS for $2R_c = 2R_c^{\alpha} = 25$ Å, namely: $\sigma_{0.8} = 0.09$, $\sigma_{0.6} = 0.11$, $\sigma_{0.5} = 0.115$, and $\sigma_{0.3} = 0.10$ (where the sub-index refers to the nominal SBR weight fraction). Selecting for each case the temperatures where the relaxation peak is well centered in the experimental frequency window (see figure 5.3) and with these fixed σ^{SANS}-values, the minimization on the 4 mixtures has been run again, allowing φ_{self}^{SBR} and φ_{self}^{PS} to vary. From the resulting values, the corresponding average self-concentration values $\varphi_{self}^{hSBR_2} = 0.14\ (\pm 0.04)$ and $\varphi_{self}^{dPS_2} = 0.19\ (\pm 0.05)$ have been obtained, which in the following will be taken as temperature and composition independent.

As it can be seen in figure 5.3, in this way the model presented here allows to describe the dielectric relaxation of the SBR/PS blends, over a broad range of temperatures and compositions, in a very satisfactory way with only three free parameters, φ_{self}^{SBR} and φ_{self}^{PS}, accounting for self-concentration effects, and $2R_c^{\alpha}$, which establishes the relevant length scale for the α-relaxation in these blends. Note that in the followed method the uncertainty in $2R_c^{\alpha}$ is ± 5 Å (see figure 5.2), the corresponding uncertainty of σ is about 15%.

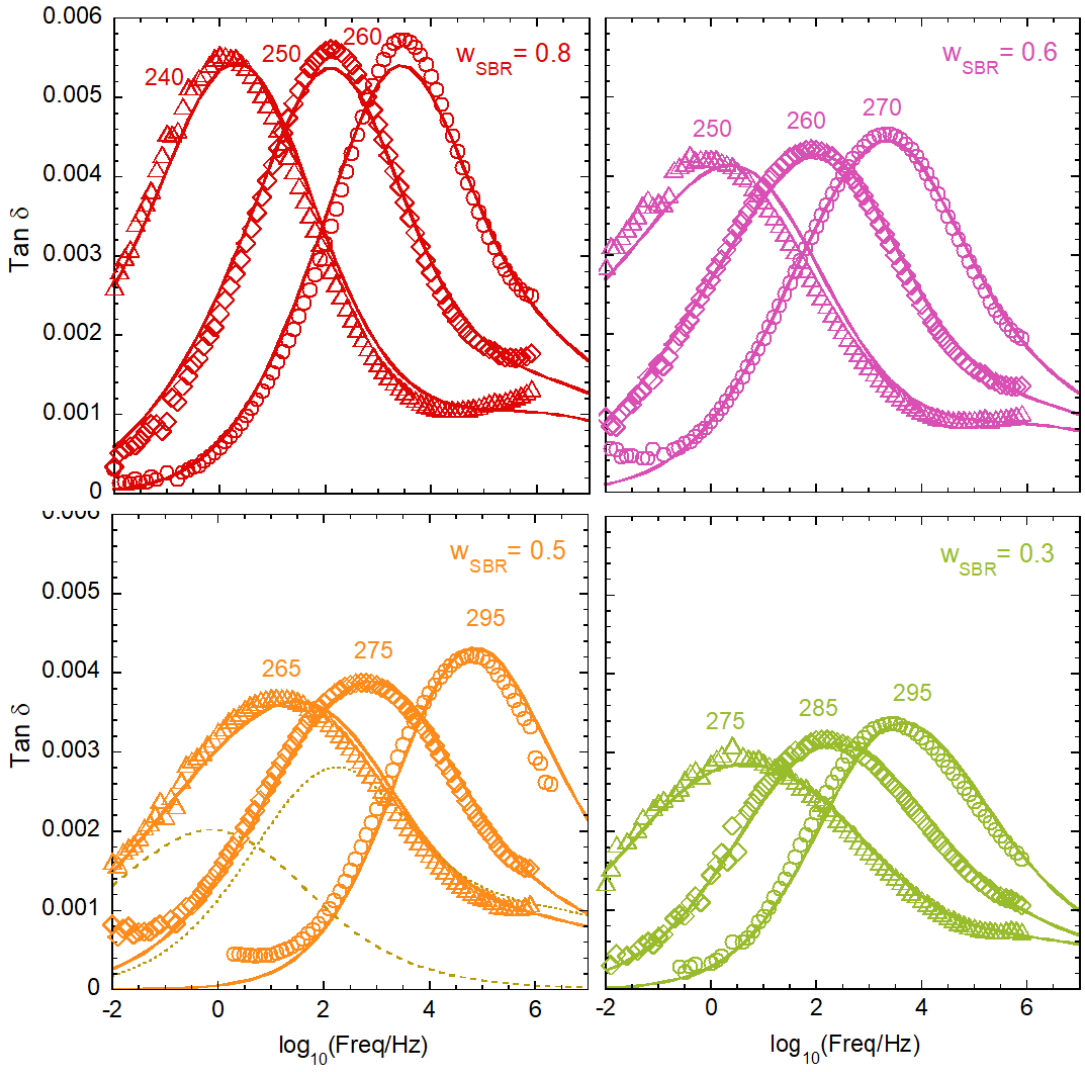

Figure 5.3: Dielectric loss tangent as a function of frequency for $hSBR_2/dPS_2$ blends at three different temperatures where the main loss peak is centered. The corresponding composition and temperatures (K) are also indicated. Solid lines correspond to the model description of the experimental data; dotted and dashed lines show respectively the model contributions of SBR and PS components for the $w_{SBR} = 0.5$ blend at 265 K.

When comparing the self-concentration values obtained by this analysis with literature results they are found to be within the usual range.[9] Nevertheless, the involved uncertainties prevent a detailed comparison. Moreover, it is noteworthy that the present approach involves many a priori assumptions and the best values for the fitting parameters could be influenced by the limited validity of some of these assumptions. Concerning the

relevant length scale for the α-relaxation, the value $2R_c^{\alpha} = 25(\pm 5)$ Å is also in the nanometer range, which is, for instance, where evident confinement effects on the segmental dynamics have been reported.[15] It is worth mentioning the good agreement with the value found in Ref.[14], where experiments were performed on similar not yet the same SBR/PS blends (SBR of different microstructure and molecular weight, and protonated PS[1,14]). Concerning the possible increase of this length scale by reducing temperature,[16] which is usually invoked for explaining the temperature dependence of the relaxation times, the uncertainties involved in our approach also prevent resolving it.

5.3 Predicting and Disentangling the DSC Response of the Blends

5.3.1 Constructing the DSC Response of the Blends on the Basis of BDS Information

In an equivalent way to that followed for the BDS modeling, for the calorimetric description it is assumed the observed behavior is the result of the superposition of contributions to the segmental heat capacity from different regions, and within each region the result of the individual contributions from the blend components. Thus, the whole calorimetric signal can be obtained by summing up the respective contributions of SBR and PS:

$$s\text{-}C_{p,blend}(T) = s\text{-}C_p^{SBR}(T) + s\text{-}C_p^{PS}(T) \tag{5.8}$$

(equation 5.7 for the calorimetric case).

Also, in parallel with the BDS modeling, the contribution of each component in a region *i* of the blend is taken having the shape and amplitude corresponding to the pure component and weighted by its concentration. According to equation 5.6 for the calorimetric case, and taking into account eq. 3.4 for the description of $s-C_p$, the segmental heat capacity as a function of temperature for each component can be calculated as:

$$s\text{-}C_p^{SBR}(T) = \sum g(\varphi_i)\,\varphi_i\,\Delta C_{pg}^{SBR}\left(\frac{T_{g,i}^{*,SBR}}{T}\right)^2 \frac{1}{1+e^{(T_{g,i}^{*,SBR}-T)/\delta^{SBR}}} \tag{5.9a}$$

$$s\text{-}C_p^{PS}(T) = \sum g(\varphi_i)\,(1-\varphi_i)\,\Delta C_{pg}^{PS}\left(\frac{T_{g,i}^{*,PS}}{T}\right)^2 \frac{1}{1+e^{(T_{g,i}^{*,PS}-T)/\delta^{PS}}} \tag{5.9b}$$

assuming that in the description of the segmental heat capacity the only parameter affected by blending is $T_{g,i}^{*}$. This approach is in line with the BDS modeling where it has

been considered that in each region in the blend only the relaxation time of the components is affected. The usual identification of the glass transition temperature with that where the characteristic time for polymer segmental motions takes a given value (commonly in the range 1 - 100 s), provides the way of connecting DSC and BDS modeling. Using the neat polymers DSC and BDS results we can connect the DSC T_g^* value and the dielectric relaxation time evaluated at this temperature $\tau(T_g^*)$ for the two components. From the analysis of the pure polymers, $hSBR_2$ and dPS_2, data (see chapter 3.2.2) respectively, the relationship between the dielectric α-relaxation time and the calorimetric T_g^* is $\tau_g^{SBR} \equiv \tau^{SBR}(T_g^*) = 1.68$ s and $\tau_g^{PS} \equiv \tau^{PS}(T_g^*) = 11.2$ s. Assuming that these connections remain valid in each region of the blend, the $T_{g,i}^*$ values appearing in equations 5.8a and 5.8b can be calculated from the BDS modeling (table 5.1). Figure 5.4 illustrates this assumption for the high-T_g component. From the calorimetric T_g^* of the pure polymer, the dielectric relaxation time $\tau_g = \tau(T_g^*)$ is first evaluated as above explained (blue arrows). Afterwards, the temperature $T_{g,i}^*$ where the same component located in a given region *i* of the blend contributes to the heat capacity jump is calculated from the corresponding relaxation time curve as obtained by the dielectric modeling (red arrows). This means that, in the present approach, for each component there is a one-to-one correspondence between the local dielectric relaxation time characterizing the segmental dynamics and the glass transition temperature determining the temperature range where the thermodynamic local equilibrium is lost.

Table 5.1: Parameters involved in the description of the dielectric α-relaxation of the blends that are also relevant for the corresponding description of the calorimetric data.

Sample	D	T_0/K	$\tau_{max}(T_g^*)$/s	φ_{self}
$hSBR_2$	8.6	176.7	1.68	0.14
dPS_2	6.3	239.8	11.2	0.19

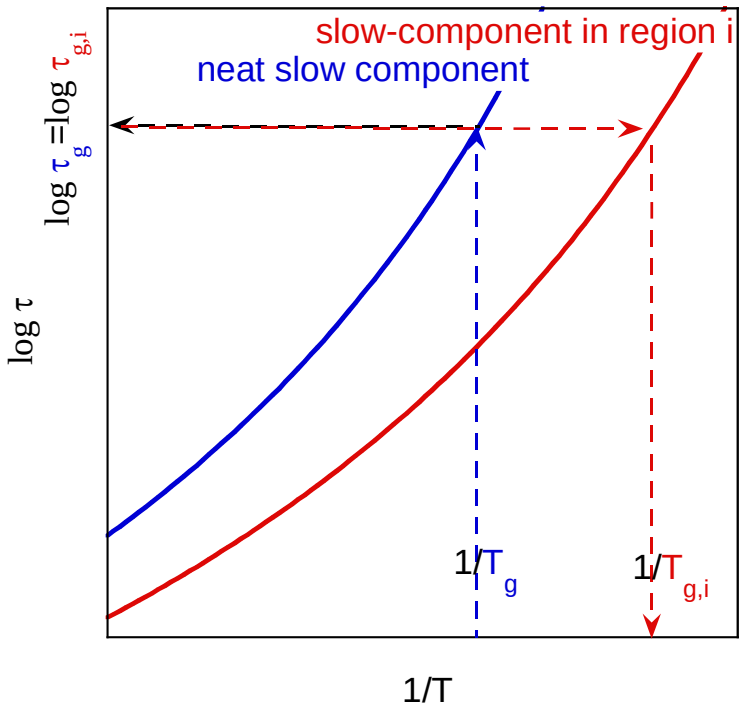

Figure 5.4: Schematics of the temperature dependence of the characteristic times of a neat component and the corresponding component in a given region of the blend. The lines with arrows show how the connection between BDS relaxation time data and T_g^* value is done.

After establishing this connection between the local segmental dynamics of each component and the glass transition temperature, the DSC curves were evaluated using the model describing the BDS results presented above. For the DSC calculations the local composition was described in terms of the same values of the self-concentrations $\varphi_{self}^{hSBR_2}$ and $\varphi_{self}^{dPS_2}$ (table 5.1), and the distributions of concentration by means of same Gaussian functions $g(\varphi_i)$ with the σ^{SANS}-values, i.e. $2R_c^{\alpha} = 25$ Å: $\sigma_{0.8} = 0.09$, $\sigma_{0.6} = 0.11$, $\sigma_{0.5} = 0.115$, and $\sigma_{0.3} = 0.10$. Thus, the DSC curves for the blends can be constructed with no additional free parameters. The resulting curves are shown in figure 5.5 in comparison with the experimental data for the different blends investigated, where an overall excellent agreement between the two sets of data can be observed.

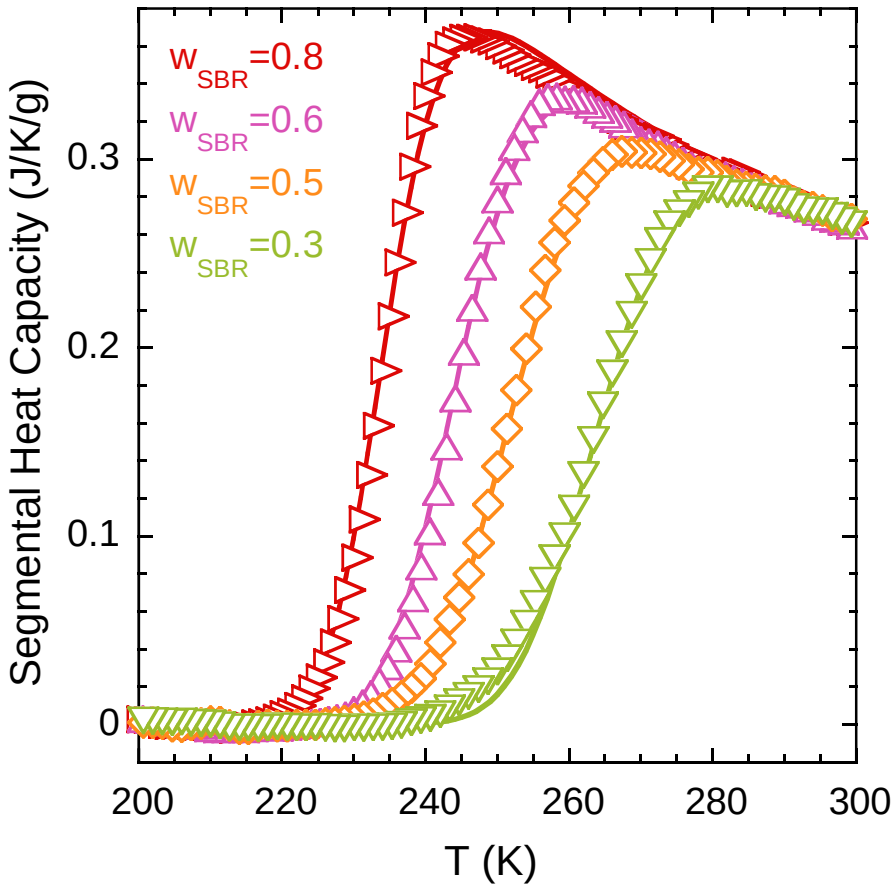

Figure 5.5: Segmental heat capacity for $hSBR_2/dPS_2$ blends with the indicated compositions. Solid lines stand for the output of the model described in the text.

The presented modeling provides thus not only a good description of the BDS data characterizing the segmental dynamics of the blends at equilibrium, but also, without extra variables, allows obtaining the DSC behavior that reflects how the thermodynamic equilibrium is lost when cooling the mixtures below the glass transition range.

The good agreement between the DSC traces and the calculated curves is also corroborated when the temperature derivative of the DSC data and model curves are compared (see figure 5.6). In this representation, the glass transition processes appear as peaks and the extension of the transition range is more clearly quantified; thereby, the good quality of the DSC data description is emphasized, both in the peak position and in the breadth of the glass transition range.

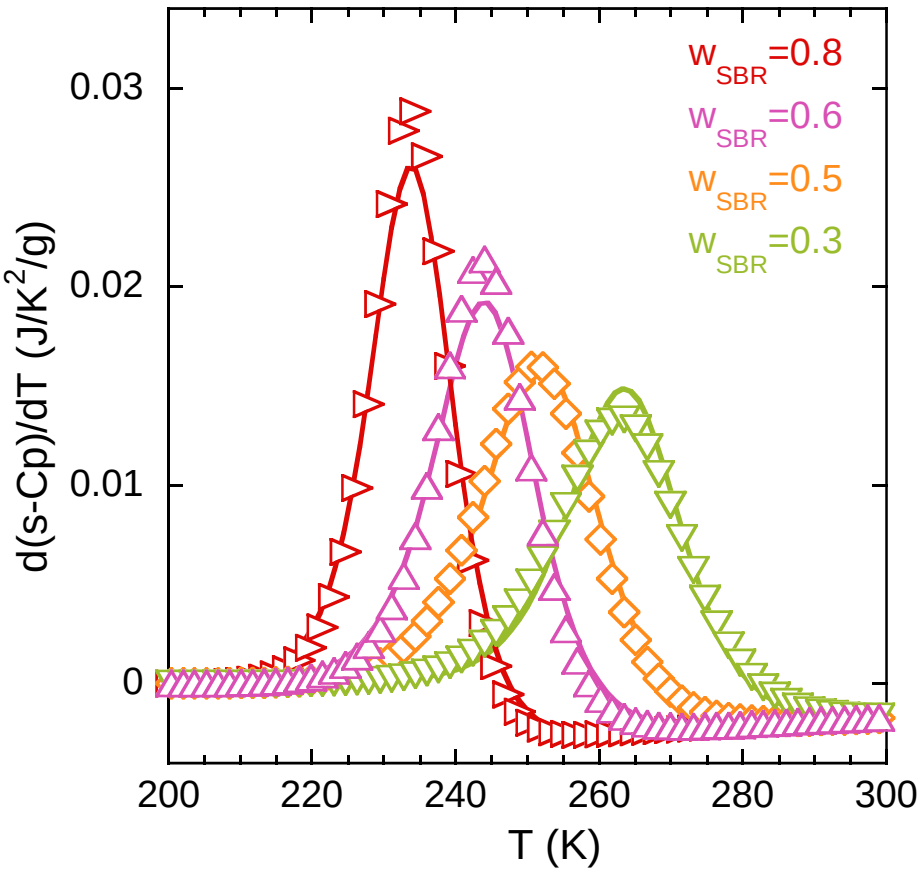

Figure 5.6: Comparison of the temperature derivative of the DSC data of $hSBR_2/dPS_2$ blends from figure 5.5 with the corresponding model curves.

5.3.2 Evaluation of the Components' Effective T_g Values

As a further test of the ability of the model in accounting for the calorimetric behavior, figure 5.7 shows the direct comparison between experimental and calculated values of T_g as a function of blend composition, both series calculated from the inflection point of the segmental heat capacity $s - C_p(T)$ curves (peak temperatures in figure 5.6). A very good agreement is obtained in this comparison. The whole set of data is very well described by the Gordon-Taylor equation (see Eq. 4.1) with $k_{G-T} = 1.3$.

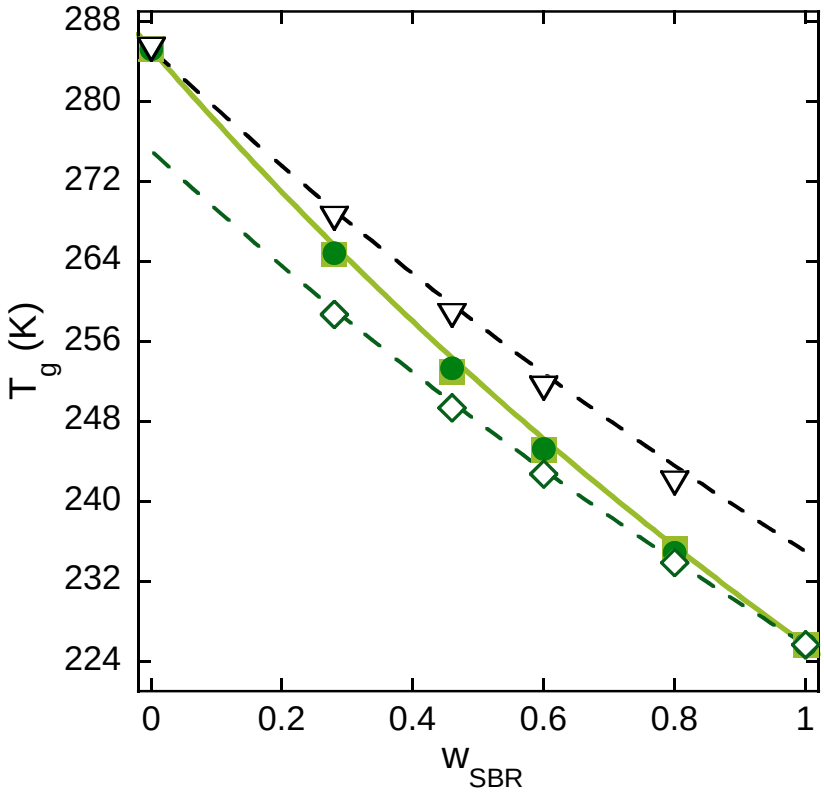

Figure 5.7: Comparison of the concentration dependence of the glass transition temperature as determined from: the experimental curves (filled squares), the whole model curve (filled circles) and the effective values from the model curves of the components (inverted empty triangles for dPS_2 and empty diamonds for $hSBR_2$). The lines are the prediction of the Gordon-Taylor equation (Eq. 4.1) for the blends (solid line) and for the components using the model φ_{self} values (dashed lines) and calculated with Eq. 5.10.

The modeling provides not only the overall DSC curves but also the individual contributions from SBR and PS components (see dashed and dotted lines in figure 5.8). From the inflection point of the such calculated $s - C_p(T)$ curves for the components, the so-called effective glass transition temperature[17] can be defined for each component of the blend. These effective $T_{g,eff}$ values have been included in figure 5.7. They can also be very well described with the Gordon and Taylor-like equation (see dashed lines in

figure 5.7) by using the effective concentration as calculated with the same self-concentration values deduced from the modeling of the BDS results, i.e.

$$T_{g,eff}^{SBR} = \frac{T_g^{SBR} K_{G-T}\left[\varphi_{self}^{SBR} + \left(1-\varphi_{self}^{SBR}\right)\varphi\right] + T_g^{PS}\left[\left(1-\varphi_{self}^{SBR}\right)(1-\varphi)\right]}{K_{G-T}\left[\varphi_{self}^{SBR} + \left(1-\varphi_{self}^{SBR}\right)\varphi\right] + \left[\left(1-\varphi_{self}^{SBR}\right)(1-\varphi)\right]} \quad (5.10a)$$

$$T_{g,eff}^{PS} = \frac{T_g^{SBR} K_{G-T}\left[\left(1-\varphi_{self}^{PS}\right)\varphi\right] + T_g^{PS}\left[\varphi_{self}^{PS} + \left(1-\varphi_{self}^{PS}\right)(1-\varphi)\right]}{K_{G-T}\left[\left(1-\varphi_{self}^{PS}\right)\varphi\right] + \left[\varphi_{self}^{PS} + \left(1-\varphi_{self}^{PS}\right)(1-\varphi)\right]} \quad (5.10b)$$

Note that these two equations are formally similar to Eqs. 5.6a and 5.6b used in the model when evaluating the values of $T_{0,i}$ as a function of the local concentration, but here the $T_{g,eff}$ values of each component are calculated.

The presented results suggest that the loss of equilibrium in a polymer blend as detected by the DSC glass transition phenomenon can be accounted for by the simple superposition of contributions, each following a neat-polymer like behavior but occurring at different temperatures depending on the local concentration around the considered component. Thus, in every region of the blend the equilibrium is lost in a way that can be considered as independent of the neighboring regions. In addition, the glassy state would be reached in two steps within each region, each associated to one of the components.

The very satisfactory description of the evolution with composition of the T_g values (global and effective) evidences that, despite of the simplicity of the present approach, it correctly captures the connection of the component segmental dynamics in the blend above T_g (at equilibrium) and the way the thermodynamic equilibrium is lost when crossing over to the glassy state. This is to some extent surprising, since the model of the dielectric curves was built to describe the equilibrium dynamics, and the connection between the equilibrium dynamics and how the equilibrium is lost below T_g is made in a very phenomenological way, using only the individual polymer component for parameterization. The results suggest that the $\tau_g \equiv \tau\left(T_g^*\right)$ is an intrinsic magnitude of a given material, which is not affected by blending.

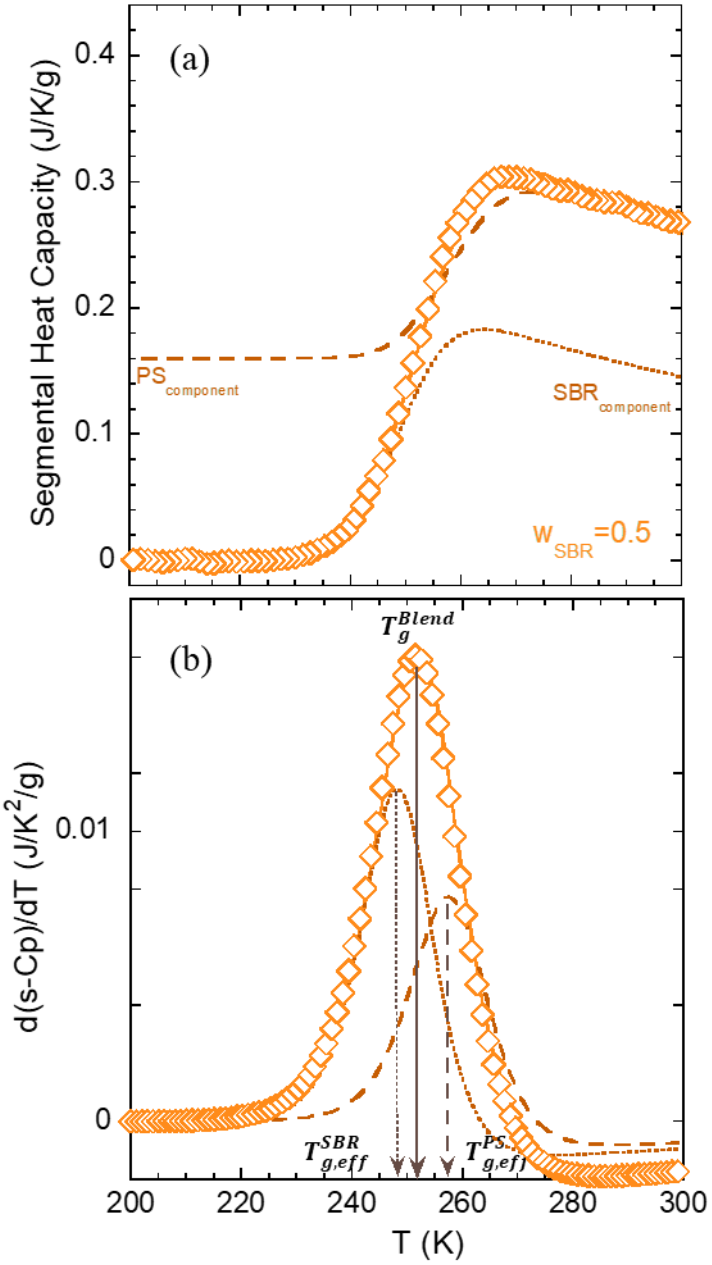

Figure 5.8: Segmental heat capacity (a) and temperature derivative of the segmental heat capacity (b) and corresponding output model (solid line) for the $w_{hSBR_2} = 0.5$; dashed and dotted lines show respectively the model contribution of SBR and PS components. Vertical arrows mark the corresponding values of T_g.

5.4 From DSC to BDS

5.4.1 Description of the DSC Results in a Direct Way

The power of the model to reproduce the DSC has been demonstrated (see Fig.5.5). The next step is to extract the model parameters just by using the DSC data, anticipating the dynamical properties of the mixture from those of the pure components. This route has been first explored with the same system $hSBR_2/dPS_2$, to check the reproducibility of the description. Furthermore, the two other systems $hSBR_1/dPS_1$ and $dSBR_1/hPS_1$ have been considered, to see if the model also works for blends composed by SBR and PS of different microstructure and molecular weight.

The approach proposed to model the DSC behavior in the SBR/PS blends is based on the direct connection between DSC and broad band dielectric spectroscopy (BDS) experiments previously explained. The first step is to analyze the glass transition and the dielectric relaxation of the neat components, as presented in chapter 3. Using the neat polymers DSC and BDS results it is possible to connect the DSC T_g^* value and the segmental relaxation time evaluated at this temperature $\tau(T_g^*)$ for the two components (see table 3.5). After determining the $T_{g,i}^*$ values as:

$$T_{g,i}^* = T_{0,i}\left(1 + D_i/ln\left(\frac{\tau_g}{\tau_\infty}\right)\right) \tag{5.11}$$

the DSC curves can be described with the parameters above determined (table 5.1 and 3.4) for the pure components and three fitting parameters: the self-concentrations of both components $\varphi_{self}^{hSBR_2}$ and $\varphi_{self}^{dPS_2}$ and the widths σ of the distributions of concentration.

In the previous procedure presented above, the composition dependent values of σ and the values of $\varphi_{self}^{hSBR_2}$ and $\varphi_{self}^{dPS_2}$ were obtained from fitting the BDS experimental results (with the input of SANS information), but here, the DSC curves of the four mixtures of each system have been analyzed to obtain these fitting parameters. To do that, in a first step the three parameters, $\varphi_{self}^{hSBR_2}$, $\varphi_{self}^{dPS_2}$ and σ, were allowed to vary freely.

Using these values of $\varphi_{self}^{hSBR_2}$ and $\varphi_{self}^{dPS_2}$ (see figure 5.9) the corresponding average self-concentration values $\varphi_{self}^{hSBR_2} = 0.15$ and $\varphi_{self}^{dPS_2} = 0.18$ have been obtained, which in the following will be taken composition independent. With these fixed values of φ_{self} the minimization routine for the different compositions has been run again allowing only σ to change. The final σ values obtained (called σ^{DSC}),were composition dependent, $\sigma_{0.8} = 0.09$, $\sigma_{0.6} = 0.10$, $\sigma_{0.5} = 0.10$, and $\sigma_{0.3} = 0.11$. The resulting curves are shown in figure 5.10 in comparison with the experimental data for the different blends investigated, where an overall excellent agreement between the two sets of data can be observed. When comparing the values of called σ^{DSC} with the values obtained before from fitting BDS data we observe that differences are small, within uncertainties. The same applies for the obtained values of $\varphi_{self}^{hSBR_2}$ and $\varphi_{self}^{dPS_2}$(see figure 5.9).

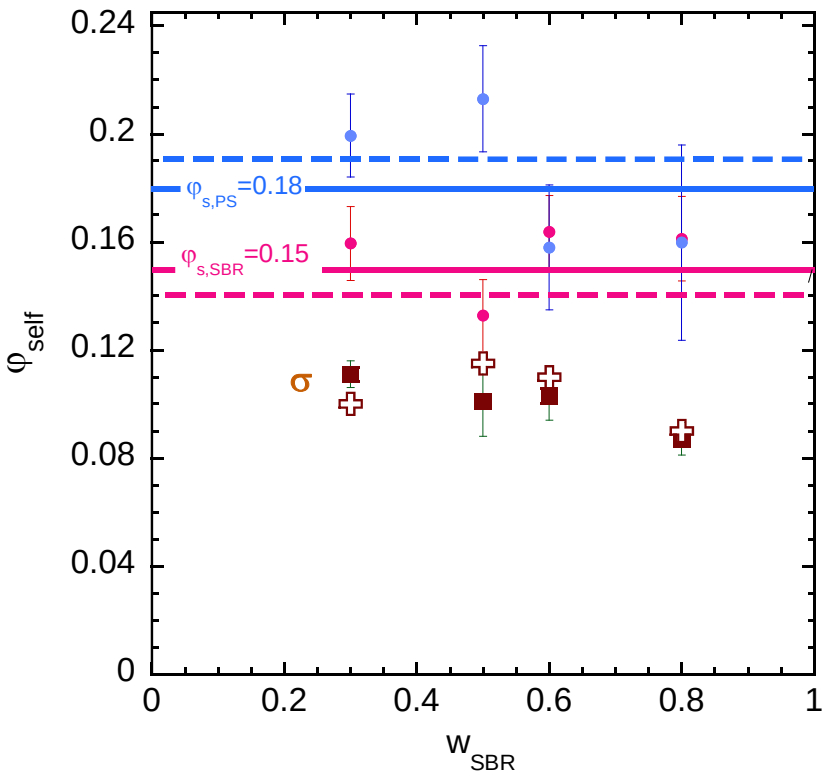

Figure 5.9: Evolution of the model parameters as function of the concentration of $hSBR_2$ in the blend. The red circles represent $\varphi_{self}^{hSBR_2}$ and the blue circles represent the $\varphi_{self}^{dPS_2}$ for each composition; solid lines in respective colors are the average value, $\varphi_{self}^{hSBR_2} = 0.15$

and $\varphi_{self}^{dPS_2} = 0.18$. Squares stand for σ^{DSC} values, composition dependent, for the different blends, keeping $\varphi_{self}^{hSBR_2}$ and $\varphi_{self}^{dPS_2}$ fixed. These values are compared with those obtained in chapter 5.2.1 for BDS: $\varphi_{self}^{hSBR_2} = 0.14$ and $\varphi_{self}^{dPS_2} = 0.19$ represented by dotted lines and σ^{SANS} by crosses.

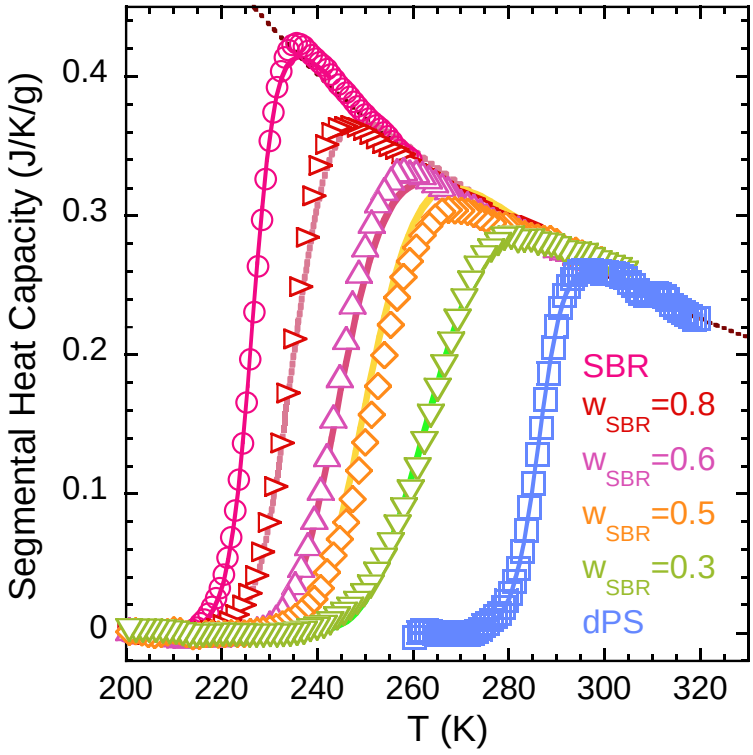

Figure 5.10: Segmental heat capacity for $hSBR_2/dPS_2$. Solid lines stand for the output of the model.

5.4.2 Anticipating the Dynamical Properties of the Mixtures

Can one anticipate the dielectric response of the mixtures? The emerging question has its reply in figure 5.11, where an overall excellent agreement between the output of the model and the experimental data can be observed using the parameters $\varphi_{self}^{hSBR_2} = 0.15$, $\varphi_{self}^{dPS_2} = 0.18$ and $\sigma_{0.8} = 0.09$, $\sigma_{0.6} = 0.10$, $\sigma_{0.5} = 0.10$, and $\sigma_{0.3} = 0.11$, obtained above for the fitting of the DSC data.

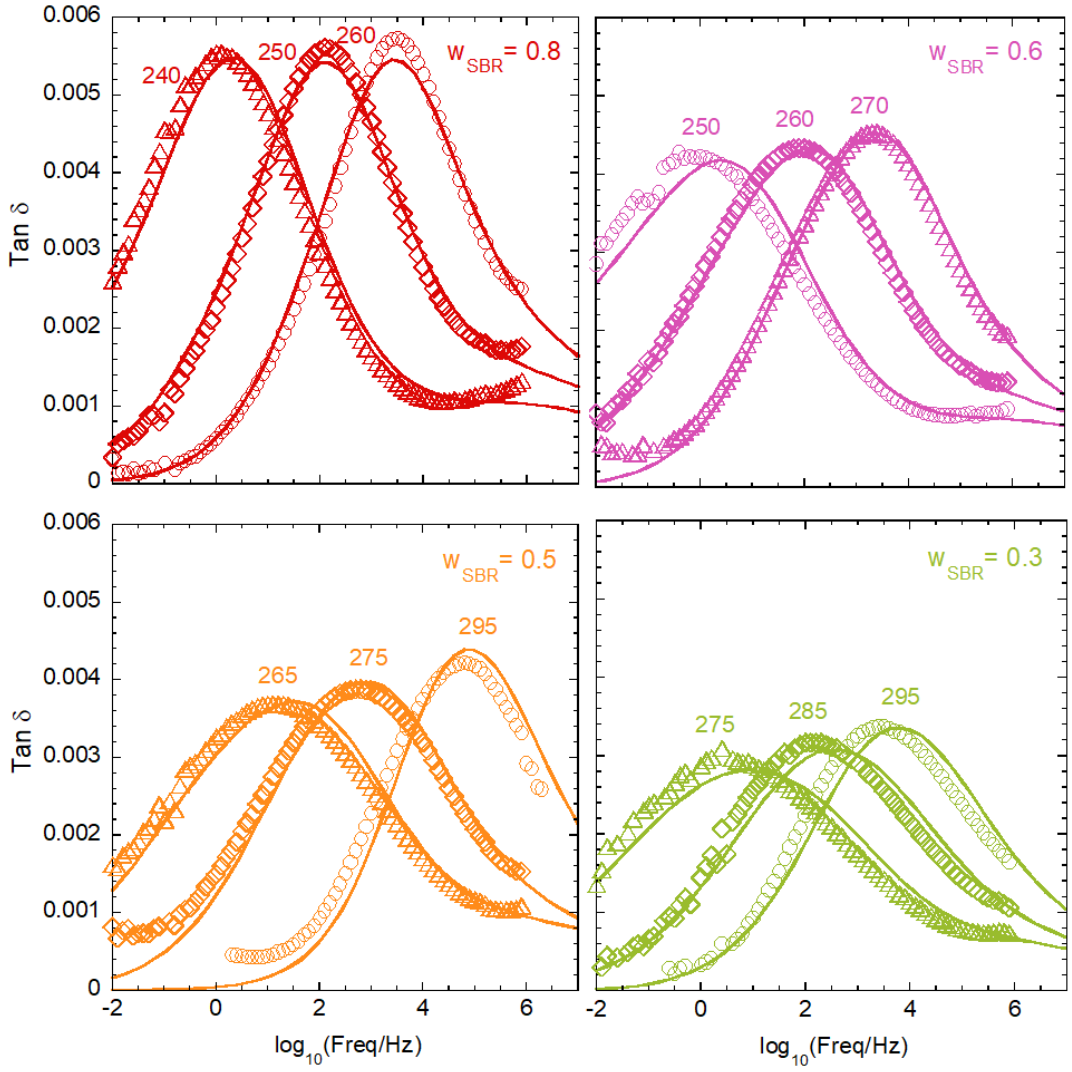

Figure 5.11: Dielectric loss tangent as a function of frequency for $hSBR_2/dPS_2$ blends at three different temperatures where the main loss peak is centered. Solid lines correspond to the model description of the experimental data, using $\varphi_{self}^{hSBR_2} = 0.15$, $\varphi_{self}^{dPS_2} = 0.18$ and $\sigma_{0.8} = 0.09$, $\sigma_{0.6} = 0.10$, $\sigma_{0.5} = 0.10$, and $\sigma_{0.3} = 0.11$.

5.5 Applicability of the Model to Other Systems

The model has been applied to two other systems: $hSBR_1/dPS_1$ and $dSBR_1/hPS_1$; for each system three different compositions have been considered with $w_{SBR} = 0.8, 0.5$ and 0.2. In figure 5.12(a)-(d) it can be appreciated that the function above constructed for the DSC response describes with high accuracy the experimental results.

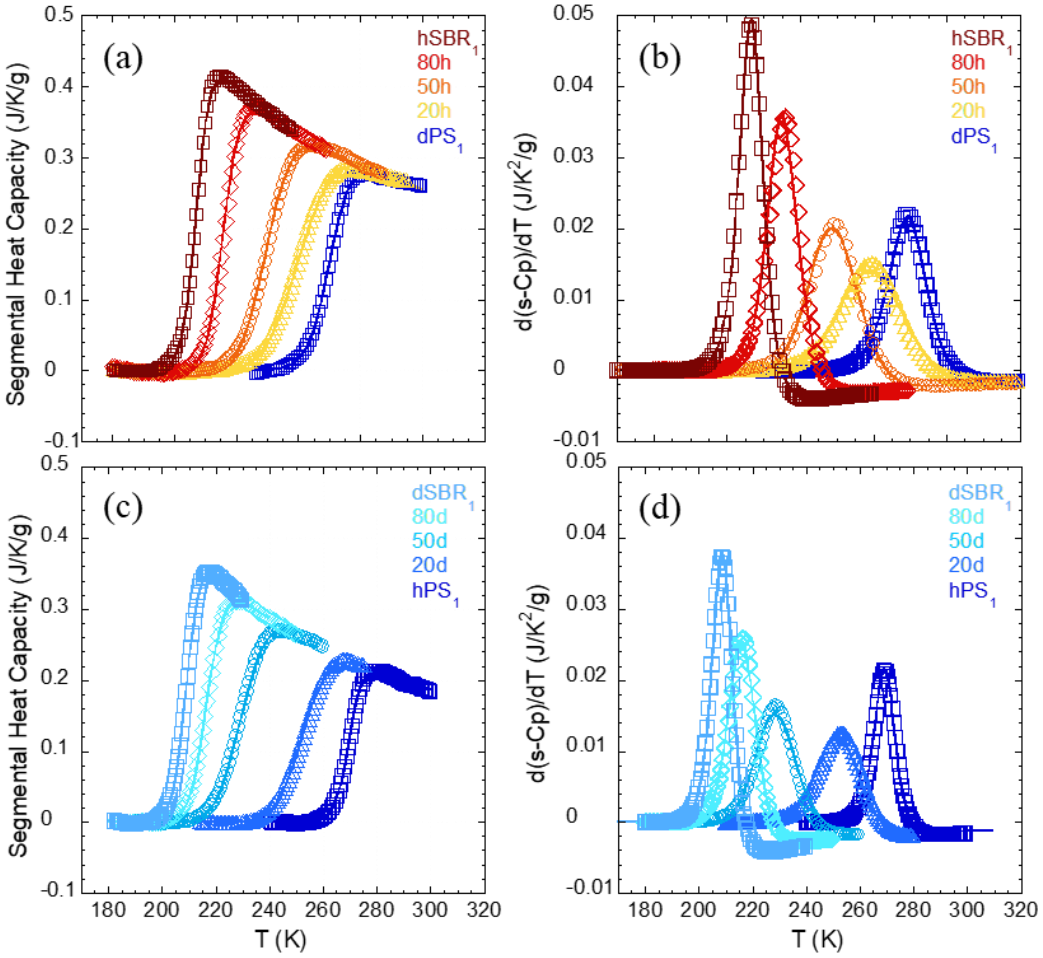

Figure 5.12: Calorimetric traces after the subtraction of the glassy part for the systems composed by $hSBR_1$ and dPS_1 (a) and of $dSBR_1$ and hPS_1 (c). The solid lines are fitting curves for the homopolymers and the output of the model. Panels (c) and (d) show the temperature-derivative of the corresponding functions in panel (a) and (b) respectively.

The parameters relevant for the description of the calorimetric data for these systems are given in tables 3.2 and 3.4. The composition-dependent values of σ and the values of φ_{self}^{SBR} and φ_{self}^{PS} are obtained following the procedure described previously in chapter 5.3 for $hSBR_2/dPS_2$ blends. To this end, three mixtures of each system at three different temperatures have been analyzed. Figure 5.13 shows the steps needed to define the final parameter values: with the first step for each composition the best values of φ_{self} for SBR and for PS are obtained, $\varphi_{self}^{SBR} = 0.03$ and $\varphi_{self}^{PS} = 0.21$ respectively. With these fixed values of φ_{self}, for each composition the final σ values, composition-dependent, are obtained: $\sigma = 0.044$ for the blend 80h, $\sigma = 0.108$ for the blend 50h, $\sigma = 0.156$ for the blend 20h, $\sigma = 0.065$ for the blend 80d, $\sigma = 0.112$ for the blend 50d, and $\sigma = 0.092$ for the blend 20d.

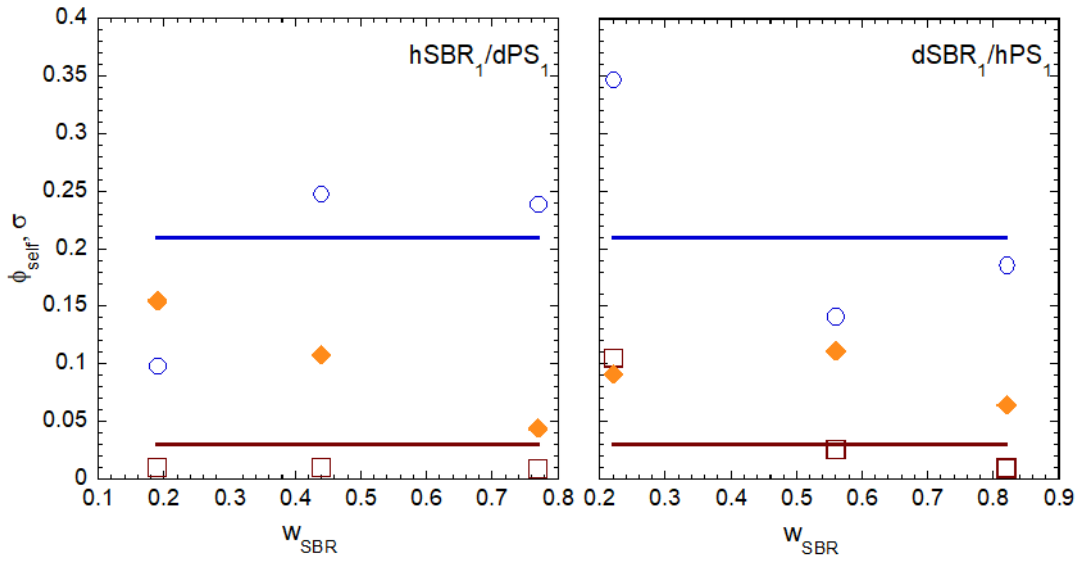

Figure 5.13: Evolution of the model parameter as function of the concentration of SBR in the blend. The red squares represent φ_{self}^{SBR} and the blue circles represent the φ_{self}^{PS} for each composition; solid lines in respective colors are the average value, $\varphi_{self}^{SBR} = 0.03$ and $\varphi_{self}^{PS} = 0.21$. Diamonds stand for σ^{DSC} values, composition dependent, for the different blends, keeping φ_{self}^{SBR} and φ_{self}^{PS} fixed.

Evaluation of the Components' Effective T_g Values

Figure 5.14 shows the direct comparison between calculated and experimental values of T_g as function of blend composition, both series calculated from the inflection point of the segmental heat capacity curves. A very good agreement is obtained in this comparison. The whole set of data is very well described by the Gordon-Taylor equation (eq. 4.1). Also, the effective $T_{g,eff}$ values have been included in figure 5.14, defined by the inflection point of the calculated $s - C_p(T)$ curves for the components through the modeling, that disentangle the two contributions to the DSC glass-transition process. The deduced values of the effective glass-transition temperatures of the two blend components are listed in table 6.1. They are also well described with the Gordon and Taylor-like equation (see dashed lines in figure 5.14) by using the effective concentration (see Eq. 5.10).

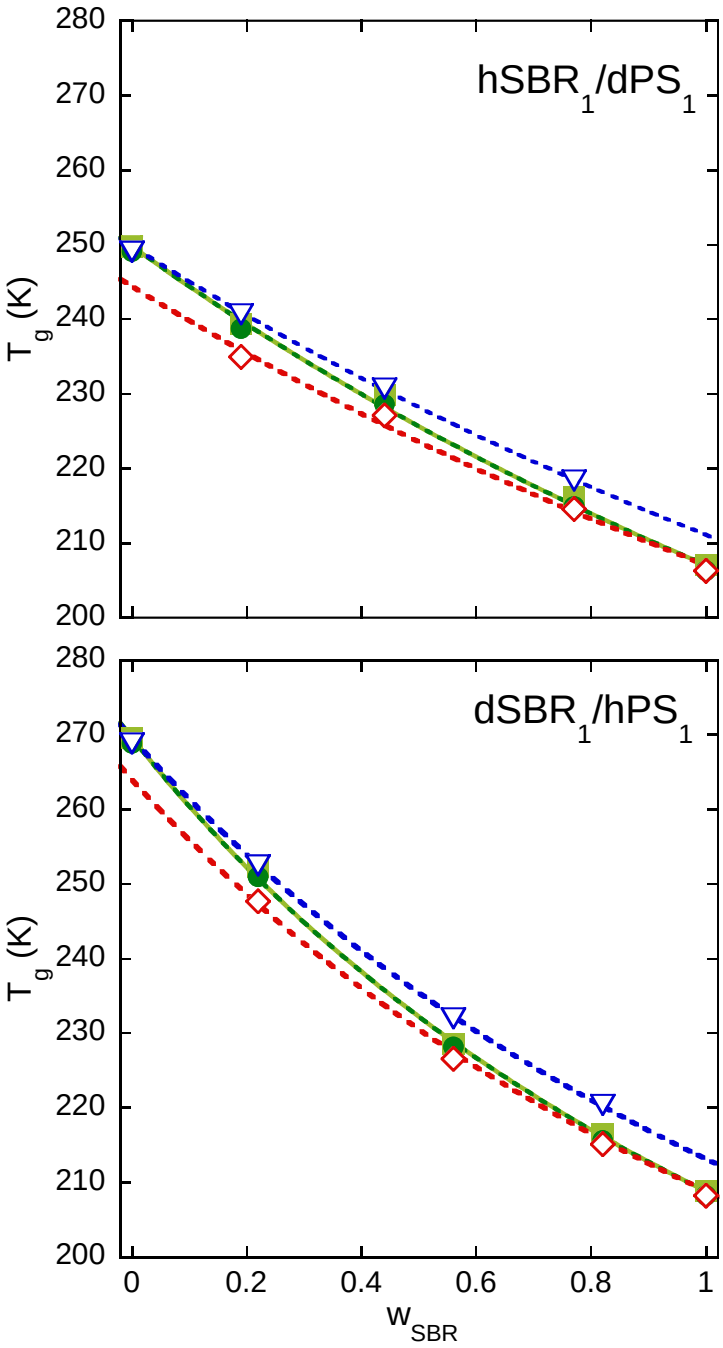

Figure 5.14: Comparison of the concentration dependence of the glass transition temperature as determined from: the experimental curves (filled squares), the whole model curve (filled circles) and the effective values from the model curves of the components (inverted empty triangles for PS and empty diamonds for SBR). The lines are the prediction of the Gordon and Taylor equation (Eq. 4.1) for the blends (solid line) and for the components using the model φ_{self} values (dashed lines) and calculated with Eq. 5.10.

Standard Deviation of the TFC: σ^{SANS} vs σ^{DSC}

Figure 5.15 shows the composition dependence of the width of the Gaussian distribution of concentration fluctuations deduced from the SANS results, $\sigma^{SANS}(R_c)$ (described in chapter 4.2) for four different values of the diameter of the explored sphere, $2R_c^{\alpha}$, compared with the σ values obtained by the DSC modeling, σ^{DSC}. From the comparison we can deduce that the relevant length scale for the α-relaxation would be of 30 ± 10 Å in these mixtures.

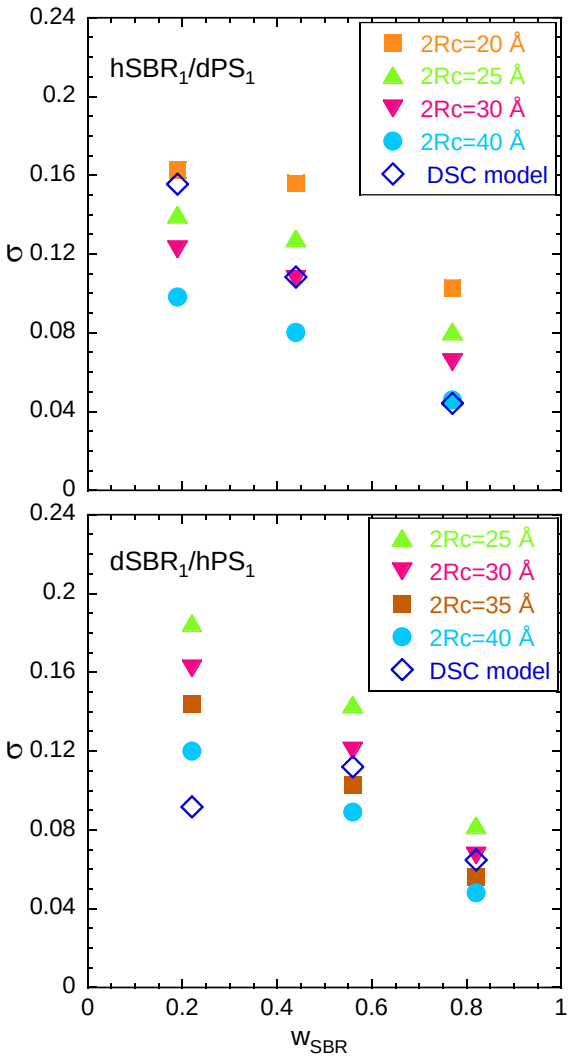

Figure 5.15: Concentration dependence of the width of the Gaussian distributions of concentration fluctuations deduced from the SANS results for different values for the explored length scale $2R_c, \sigma^{SANS}(R_c)$ (filled symbols). Empty symbols correspond to values obtained by fitting DSC data, σ^{DSC} (Fig. 5.12).

5.5 Conclusions

A model based on the combination of two main ingredients, namely the self-concentration[9] and the thermally driven concentration fluctuations,[3–8] has been invoked to account for the effects of blending. This model was been applied before to describe the equilibrium dynamics as monitored by BDS and mechanical spectroscopies.[1,2] The main contributions of this Thesis to the modeling are: (i) to use the microscopic SANS insight into TCF to fully characterize their impact on the broadening of the segmental dynamics observed by BDS; (ii) to connect the modeling of the segmental dynamics of the blends with the individual contributions of the blend components to the DSC behavior; (iii) to anticipate the dynamical properties of the mixture starting from those of the pure components based on rather routine experiments on the blends.

Thanks to the SANS input, blending effects not only on the equilibrium dynamics of the α-relaxation in the miscible state as monitored by BDS, but also on the DSC manifestation of the glass transition phenomenon reflecting how thermodynamic equilibrium is lost, have been successfully described by using only three free parameters: the self-concentration of the components and the width σ of the distributions of the TCF. The approach here proposed reproduces very well the experimental results in a wide range of temperatures and compositions, supporting the validity of the rather rough assumptions involved. The characteristic time of each component evaluated at the glass-transition temperature --the key parameter invoked to connect equilibrium and non-equilibrium observables-- is apparently not affected by blending. In addition, the present approach allows decomposing the DSC result into the component contributions, providing the composition-dependent values of the effective glass transition temperatures. They can be consistently described by the Gordon-Taylor equation using the self-concentration values.

Further support to the model is provided by the excellent agreement obtained invoking the same effect of TCF on both, BDS and DSC, pointing to the same relevant length scale for the dynamics of the α-relaxation and the loss of equilibrium at the glass transition. This length scale is of about 2.5-3 nm, in accordance with previous works on glass-forming systems.[18] Moreover, the values of self-concentration found are in the range one

could expect for this type of polymers for such length scale, which gives basic support for the various approximations involved in the modeling.

5.5 References

(1) Gambino, T.; Alegría, A.; Arbe, A.; Colmenero, J.; Malicki, N.; Dronet, S. Modeling the High Frequency Mechanical Relaxation of Simplified Industrial Polymer Mixtures Using Dielectric Relaxation Results. *Polymer* **2020**, *187*, 122051.

(2) Gambino, T.; Alegría, A.; Arbe, A.; Colmenero, J.; Malicki, N.; Dronet, S.; Schnell, B.; Lohstroh, W.; Nemkovski, K. Applying Polymer Blend Dynamics Concepts to a Simplified Industrial System. A Combined Effort by Dielectric Spectroscopy and Neutron Scattering. *Macromolecules* **2018**, *51* (17), 6692–6706.

(3) Colmenero, J.; Arbe, A. Segmental Dynamics in Miscible Polymer Blends: Recent Results and Open Questions. *Soft Matter* **2007**, *3* (12), 1474–1485.

(4) Zetsche, A.; Fischer, E. W. Dielectric Studies of the α-Relaxation in Miscible Polymer Blends and Its Relation to Concentration Fluctuations. *Acta Polymerica* **1994**, *45* (3), 168–175.

(5) Lutz, T. R.; He, Y.; Ediger, M. D.; Cao, H.; Lin, G.; Jones, A. A. Rapid Poly(Ethylene Oxide) Segmental Dynamics in Blends with Poly(Methyl Methacrylate). *Macromolecules* **2003**, *36* (5), 1724–1730.

(6) Chung, G. C.; Kornfield, J. A.; Smith, S. D. Component Dynamics Miscible Polymer Blends: A Two-Dimensional Deuteron NMR Investigation. *Macromolecules* **1994**, *27* (4), 964–973.

(7) Kumar, S. K.; Colby, R. H.; Anastasiadis, S. H.; Fytas, G. Concentration Fluctuation Induced Dynamic Heterogeneities in Polymer Blends. *J Chem Phys* **1998**, *105* (9), 3777.

(8) Leroy, E.; Alegría, A.; Colmenero, J. Segmental Dynamics in Miscible Polymer Blends: Modeling the Combined Effects of Chain Connectivity and Concentration Fluctuations. *Macromolecules* **2003**, *36* (19), 7280–7288.

(9) Lodge, T. P.; McLeish, T. C. B. Self-Concentrations and Effective Glass Transition Temperatures in Polymer Blends. *Macromolecules* **2000**, *33* (14), 5278–5284.

(10) Lipson, J. E. G. Global and Local Views of the Glass Transition in Mixtures. *Macromolecules* **2020**, *53* (17), 7219–7223.

(11) Tammann, G.; Hesse, W. Die Abhängigkeit Der Viscosität von Der Temperatur Bie Unterkühlten Flüssigkeiten. *Z Anorg Allg Chem* **1926**, *156* (1), 245–257.

(12) Fulcher, G. S. Analysis of Recent Measurements of the Viscosity of Glasses. *Journal of the American Ceramic Society* **1925**, *8* (6), 339–355.

(13) Vogel, H. The Law of the Relation between the Viscosity of Liquids and the Temperature. *Phys. Z* **1921**, *22* (1), 645–646.

(14) Gambino, T.; Shafqat, N.; Alegría, A.; Malicki, N.; Dronet, S.; Radulescu, A.; Nemkovski, K.; Arbe, A.; Colmenero, J. Concentration Fluctuations and Nanosegregation in a Simplified Industrial Blend with Large Dynamic Asymmetry. *Macromolecules* **2020**, *53* (16).

(15) Alegria, A.; Colmenero, J. Dielectric Relaxation of Polymers: Segmental Dynamics under Structural Constraints. *Soft Matter* **2016**, *12* (37), 7709–7725.

(16) Donth, E. The Size of Cooperatively Rearranging Regions at the Glass Transition. *J Non Cryst Solids* **1982**, *53* (3), 325–330.

(17) Saiter, J. M.; Grenet, J.; Dargent, E.; Saiter, A.; Delbreilh, L. Glass Transition Temperature and Value of the Relaxation Time at Tg in Vitreous Polymers. *Macromol Symp* **2007**, *258* (1), 152–161.

(18) Berthier, L.; Biroli, G.; Bouchaud, J. P.; Cipelletti, L.; el Masri, D.; L'Hôte, D.; Ladieu, F.; Pierno, M. Physics: Direct Experimental Evidence of a Growing Length Scale Accompanying the Glass Transition. *Science (1979)* **2005**, *310* (5755), 1797–1800.

Chapter 6

Microscopic vs Macroscopic Glass Transitions

The model based on the thermally driven concentration fluctuations (TCF) and self-concentration, described in the previous chapter, allows to extract the two 'macroscopic' contributions to the calorimetric trace, i.e., the 'effective T_g' of each of the blend component ($T_{g,eff}^{SBR}$ and $T_{g,eff}^{PS}$). The aim of this chapter is to compare these 'macroscopic' effective glass transitions of the components with the 'microscopic' counterparts, determined by the atomic displacements at some tens of ps observed by the EFWS and sensitive to the onset of liquid-like motions across the calorimetric glass transition. These 'microscopic' effective glass-transition temperatures are accessible for the individual components thanks to the neutron scattering selectivity when combined with isotopic labelling. To provide a whole picture, different techniques like Differential Scanning Calorimetry (DSC), X-Ray and neutron diffraction, Small Angle Neutron Scattering (SANS) and neutron Elastic Fixed Window Scans (EFWS) -addressing atomic motions in the ≈ 80 ps timescale and thereby heterogeneities and non-Gaussian effects at atomic level- have been combined to investigate dynamically asymmetric blends composed by isotopically labeled styrene-butadiene rubber (SBR) and polystyrene (PS), $hSBR_1$-dPS_1 and $dSBR_1$-hPS_1. With this approach, also the different relevant length scales from structural, thermodynamical, and dynamical points of view, in these complex mixtures, have been determined and their possible interplays are discussed.

6.1 Elastic Fixed Window Scans: Selective Microscopic Insight into Proton Displacements

Figure 6.1 shows the elastically scattered intensity recorded in the EFWS for the different blend samples investigated at selected temperatures, normalized by its value at a very low temperature (20 K). This magnitude decreases with increasing temperature and Q. The intensity recorded in the EFWS has both, incoherent and coherent contributions. Polarization analysis of the scattered intensities allows distinguishing between these two kinds of phenomena. This is the principle applied in the diffraction experiments carried out by means of D7. From the D7 results for the blends shown in Fig. 6.2 we can infer that in the IN13 Q-window, Q-range above ≈ 0.5 Å^{-1}, the coherent contribution from TCF is much smaller than the incoherent one, and that the scattered signal is dominated by the incoherent contribution. The exception is the sample rich in the deuterated component, but only in the neighborhood of the structure factor peak (around 1.3 Å^{-1}). D7 experiments were restricted to the 80 and 50% SBR compositions. For the 20% SBR samples, we could expect qualitatively similar results as those obtained for the 80% SBR systems with opposite labeling.

The intensity scattered by our samples in the Q-region explored by these experiments is predominantly of incoherent nature and has its origin in the hydrogens. This means that for the homopolymers (see figure 3.10) it reflects the atomic (H) displacements in the bulk system, while in the blends it selectively reveals those of the sample labeled with hydrogens.

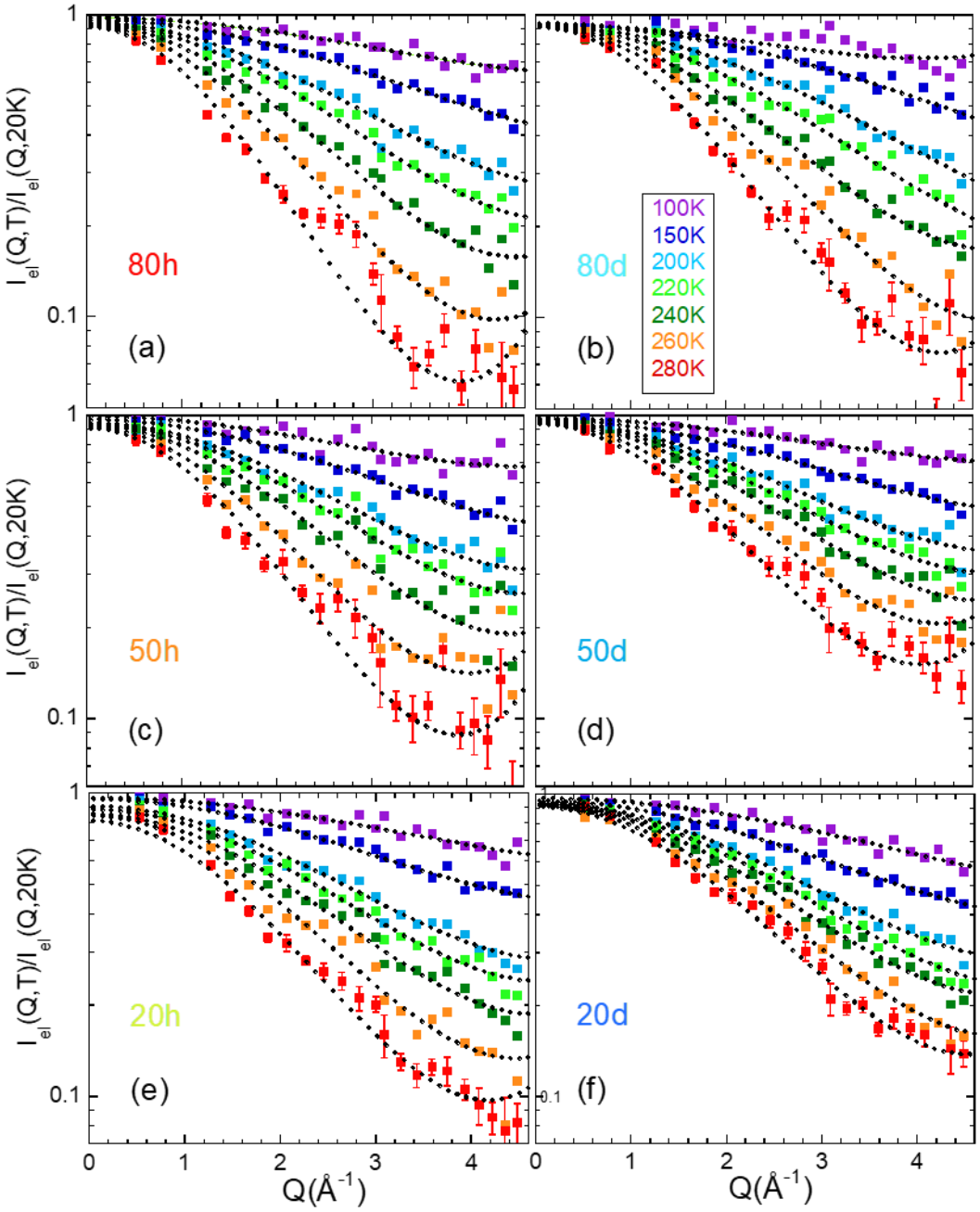

Figure 6.1: EFWS results obtained on blends with decreasing SBR content (80% (a,b), 50% (c,d) and 20% (e,f)); panels on the left (a,c,e) correspond to $hSBR_1/dPS_1$ samples – where the scattered intensity is dominated by the SBR component– and on the right to $dSBR_1/hPS_1$ samples (b,d,f) – where the results mainly reflect PS dynamics. Different colors correspond to the different temperatures indicated in panel (b). Representative error bars are shown for the 280 K data. Dotted lines are fits of Eq. 3.6.

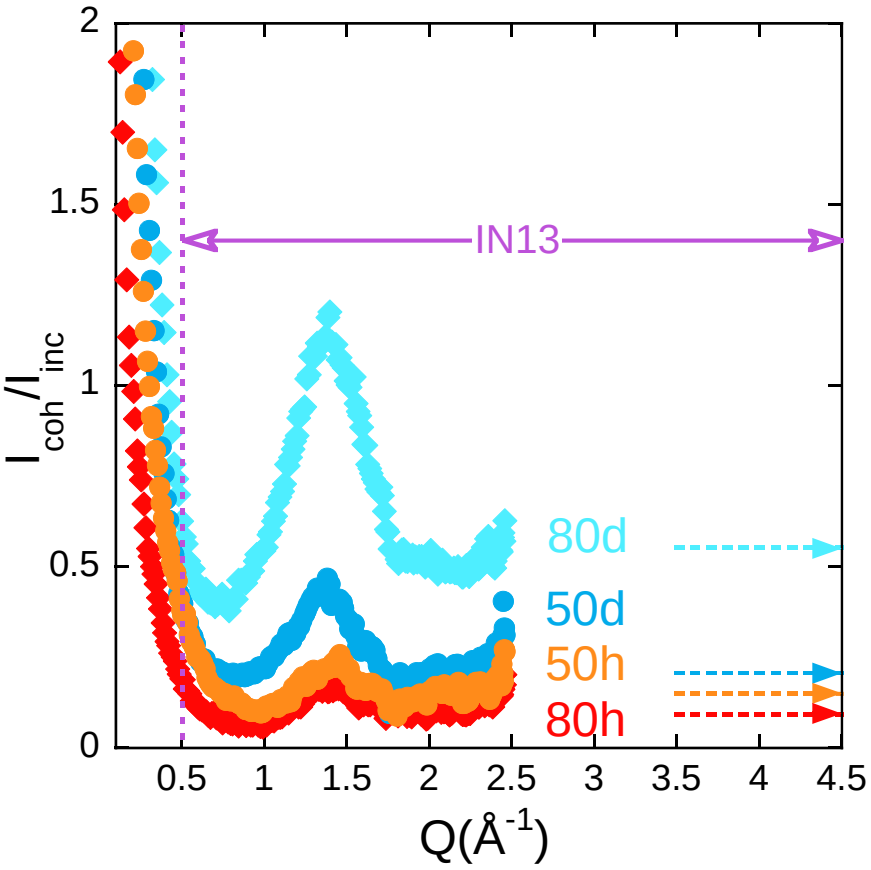

Figure 6.2: Ratio between the coherent and incoherent differential scattering cross-sections determined by diffraction with polarization analysis (D7) on the blend samples investigated by IN13 with 80 and 50% SBR composition. The Q-range covered by the IN13 experiments is marked by the horizontal solid arrow. Dotted horizontal arrows mark the theoretical value of the ratio $\sigma_{coh}/\sigma_{inc}$ for the different samples, which should be the high-Q asymptotic limit of the measured magnitude.

In particular, the results on the left panels of Fig. 6.1 are sensitive to the $hSBR_1$ component in the blends, while those on the right panels to the hPS_1 component. The EFWS results correspond, to a good approximation, to the incoherent intermediate scattering function $I_{inc}(Q,t)$ of the hydrogens in the sample at a time $t_R = \hbar/\delta\hbar\omega \approx$ 80 ps. (see chapter 3.3 for more details)

EFWS results have been fitted with Eq. 3.6 (Fig. 6.1). Very good descriptions of the experimental data were obtained in this way, delivering also information on $\alpha_2(t_R)$. The resulting values of the fitting parameters $\langle r^2(t_R)\rangle$ and $\alpha_2(t_R)$ are displayed in Fig. 6.3. Panel (a) shows the results for neat $hSBR_1$ and the $hSBR_1$ component in the blends, and panel (b), those on hPS_1 and the hPS_1 component in the mixtures. In all cases the MSD $\langle r^2(t_R)\rangle$ increases with temperature, while the deviations from Gaussian behavior decrease. At low temperatures, in the glassy state, all results for the MSD are practically identical, within the uncertainties, to those of the neat polymer. This could be expected, since blending does not appreciably affect dynamical processes involved in the glassy state, like vibrations or secondary relaxations.[1] At a given temperature that depends on composition, the displacements within the mixtures start to differ from those in the homopolymer. In the high temperature region, the SBR-MSD decreases with increasing PS content in the blend, while the PS displacements increase with increasing amount of surrounding SBR.

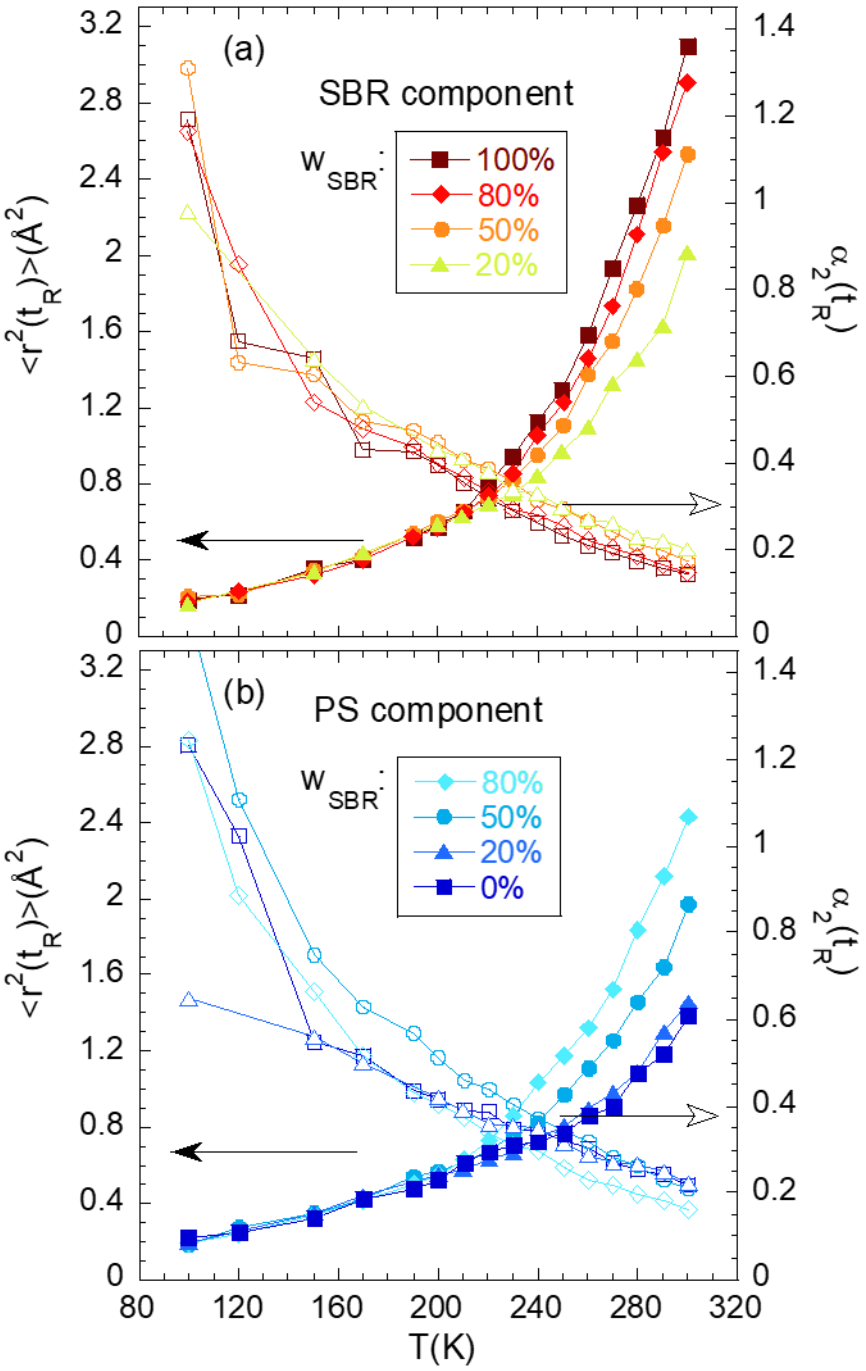

Figure 6.3: Mean squared proton displacement (filled symbols, scale on the left) and non-Gaussian parameter (empty symbols, scale on the right) at the IN13 instrumental resolution time deduced from the fits of Eq. 3.6 to the IN13 results on the $hSBR_1/dPS_1$ samples (a) and on the $dSBR_1/hPS_1$ samples (b). Different symbols correspond to the different SBR compositions indicated; lines connecting points are guides for the eye.

6.2 Effective Glass Transitions of the Blend Components

In chapter 3.3 it has been shown that the atomic displacement at the timescale explored by IN13 EFWS can be considered as an important magnitude related to the glass-transition phenomenon in the homopolymers. The case of the blends is more complicated, but the same hypothesis might be applied. As can be appreciated in Fig. 6.3, in the blends a qualitatively similar behavior of the MSD as for the homopolymers is found, though the onset of additional displacements with respect to the glassy behavior occurs at a different temperature. In analogy with the homopolymers, and taking into account the selectivity of the EFWS experiments to the protonated component in the mixture, this temperature can be identified as the 'microscopic T_g' of the labeled component in the blend. With the terminology used for macroscopic results as from BDS and DSC, it would thus be the 'effective microscopic' glass-transition temperature $T_{g,eff}^{m}$.

For a quantitative analysis of the EFWS results of the blends, the 'excess in mean squared displacement' has been calculated with respect to the expected value in the glassy state $\left(\langle r_e^2(t_R)\rangle \equiv \langle r^2(t_R)\rangle - \langle r_g^2(t_R)\rangle\right)$. The latter has been assumed to be independent of composition and equal to that previously determined for the corresponding neat polymer – remind that indistinguishable MSD has been observed, within the uncertainties, in the glassy state for all samples of a given family (see Fig. 6.3). The results for $\langle r_e^2(t_R)\rangle$ are shown in Fig. 6.4.

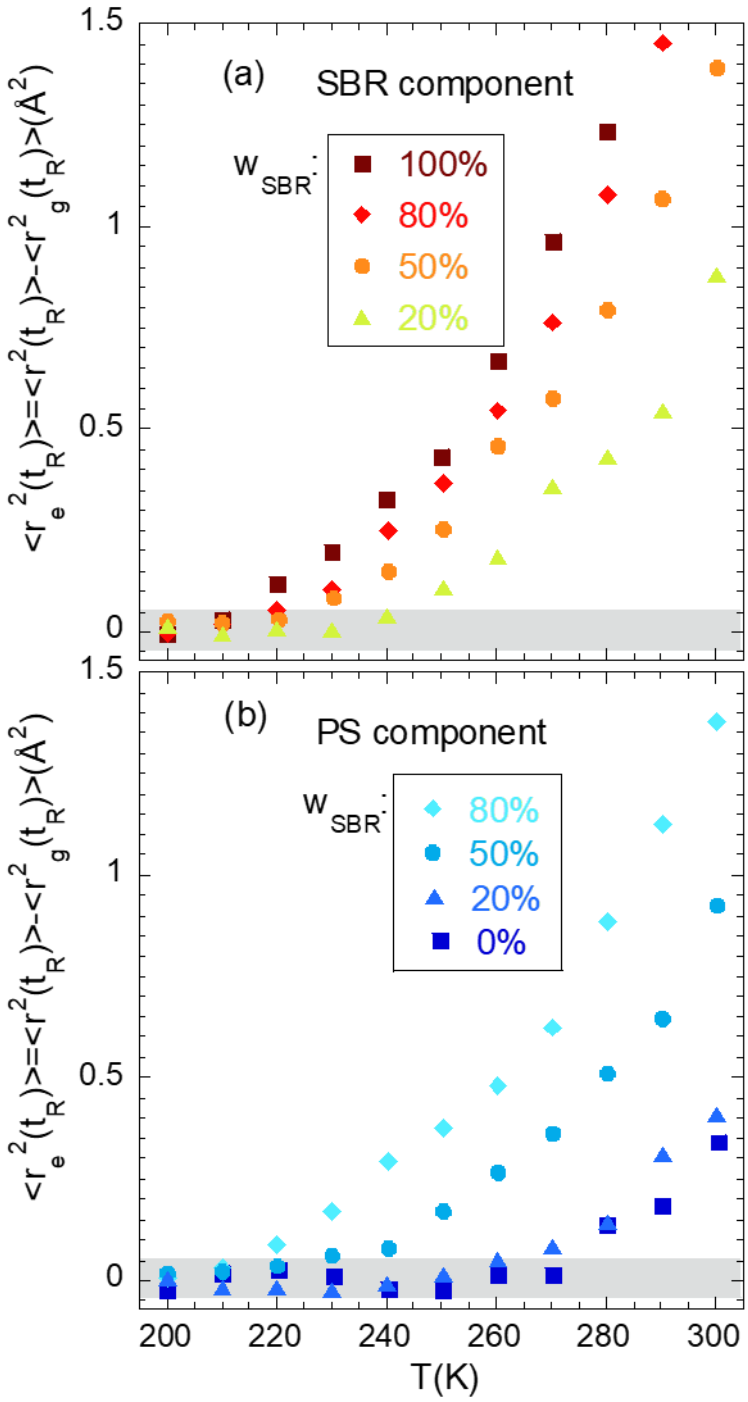

Figure 6.4: Temperature dependence of the 'Excess MSD', defined as the difference between $\langle r^2(t_R)\rangle$ and the expected 'glassy' value of this magnitude for the corresponding neat component (linear law fitting of $\langle r^2(t_R)\rangle$ in the range $150K \leq T \leq T_g$, dashed lines in Fig. 3.12). Panel (a) shows the results on the $hSBR_1/dPS_1$ blends and panel (b) on the $dSBR_1/hPS_1$ mixtures. The dashed area shows representative uncertainty in the reference level.

From this representation the range of the effective microscopic glass transition has been determined for both blend components at the different concentrations investigated. They are listed in table 6.1 and represented in figure 6.5 together with the calorimetric results obtained from the application of the model (chapter 5).

Table 6.1: Glass transition temperature and effective glass-transition temperatures of the two components obtained from the application of the model, and microscopic glass-transition temperature determined from the EFWS.

Sample	T_g(K)	$T_{g,eff}^{SBR}$(K)	$T_{g,eff}^{PS}$(K)	$T_{g,eff}^{m,SBR}$(K)	$T_{g,eff}^{m,PS}$(K)
$hSBR_1$	206.3	-	-	207.5±2.5	
80h	214.9	214.6	218.4	214.5±4.5	-
50h	228.6	227.1	230.7	224.5±3.5	-
20h	238.7	235.0	240.7	237.5±3.5	-
dPS_1	249.0	-	-	-	-
$dSBR_1$	208.2	-	-	-	-
80d	215.6	215.1	220.4	-	210.0±3.0
50d	228.2	226.6	232.0	-	231.5±3.5
20d	251.0	247.7	252.5	-	259.5±5.5
hPS_1	268.8	-	-	-	271.0±4.0

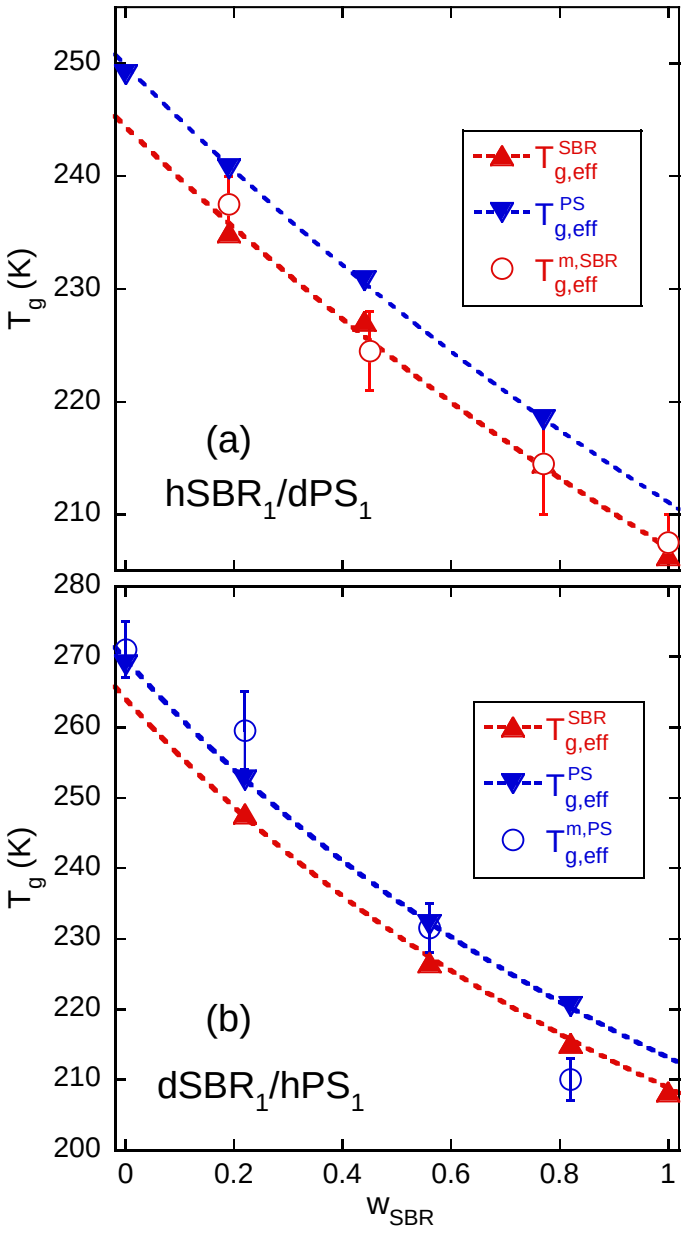

Figure 6.5: Composition dependence of the effective glass-transition temperatures identified on the systems based on $hSBR_1$ and dPS_1 (a) and on $dSBR_1$ and hPS_1 (b). Triangles represent the effective glass-transition temperatures obtained from the application of the model to the DSC results (up-triangle: SBR component; down-triangle: PS component). Dotted lines are the Gordon and Taylor equations accounting for self-concentration effects (see chapter 5). The values of the microscopic effective glass-transition temperature $T_{g,eff}^{m}$ determined from EFWS for the protonated component are represented by the circles. Error bars in these results arise from the uncertainties in their determination.

$T_{g,eff}^{m,SBR}$ determined for the $hSBR_1$ component from the EFWS coincides, within the uncertainties, with the 'macroscopic' effective $T_{g,eff}^{SBR}$ deduced by the application of the model to the DSC results [see figure 6.5(a)]. In the case of the $dSBR_1/hPS_1$ mixtures, where $T_{g,eff}^{m}$ corresponds to the onset of PS liquid-like displacements, its location seems to be close to the 'macroscopic effective $T_{g,eff}$' of the PS component for medium-high PS-content, and close to the 'macroscopic effective $T_{g,eff}$ ' of the $dSBR_1$ component for the highest $dSBR_1$-content [see figure 6.5(b)]. Thus, for the samples with medium or rich content in PS was found that the microscopic and macroscopic effective glass-transition temperatures coincide for PS as well as for SBR. In a given blend, these temperatures are different ($T_{g,eff}^{SBR} < T_{g,eff}^{PS}$), and this infers that the dynamics at microscopic level is heterogeneous. In the other extreme, when SBR is the majority component, $T_{g,eff}^{m}$ of PS is close to $T_{g,eff}$ of $dSBR_1$ (see Fig. 6.5(b)). This temperature is expected to coincide with $T_{g,eff}^{m}$ of $dSBR_1$ (as it does for the opposite labeling, Fig. 6.5(a)). In the case of SBR-rich samples, thus, a homogeneous dynamic behavior was found at microscopic level. We note that in these conditions, $T_{g,eff}^{hPS}$ is higher than its microscopic counterpart, implying that the loss of equilibrium observed by DSC occurs at higher temperatures. Between these two temperatures, i.e., $T_{g,eff}^{m,PS} \approx T_{g,eff}^{SBR} < T < T_{g,eff}^{PS}$ the system is 'liquid-like' at microscopic level but the PS component is 'glassy-like' at macroscopic level.

In a previous work[2] Gambino *et al*. applied EFWS to isotopically labeled samples of SBR and PS oligomers with $900\ \mathrm{g/mol}$ with $50/50$ composition. They found out that the signature of microscopic glass transition occurred when the (broadened) distribution of macroscopic effective glass transition temperatures of the targeted component started to present significant values. Those results support the present finding on the intermediate concentration samples. In a recent work[3] on a mixture of a high-T_g resin with SBR (being SBR the majority component), a coincidence of the microscopic glass-transition determined from EFWS for the resin with the overall calorimetric T_g of the blend has been noted. Though the model was not applied to the DSC data to determine the effective glass transitions, it can be expected that this result implies that also in that mixture both components experience their microscopic transition at the same temperature, as has been found in the present case for the SBR-rich blend. Also, in a previous related work by

Alba-Simionesco *et al.*,[4] a comparison of DSC and neutron scattering results was performed on a blend of high and low molecular weight PS chains. However, in that work the components' responses were not determined individually.

6.2.1 'Microscopic' vs 'Macroscopic' Self-Concentration

The value of the self-concentration for PS determined from the DSC analysis is $\varphi_{self} = 0.21$ independently of the isotopic label, hPS_1 and dPS_1. For dPS_2 oligomers of $900\ \mathrm{g/mol}$, the value found is 0.19. Thus, there is no strong dependence of this magnitude on molecular weight. For the case of SBR, $hSBR_1$ and $dSBR_1$, the value found for $\varphi_{self} = 0.03$ is lower than those reported for other SBR components in this kind of blends: $\varphi_{self}^{hSBR_2} = 0.14$ and $\varphi_{self} = 0.20$.[5,6] There is no clear correlation of φ_{self} with the molecular weight ($M_w = 106\ \mathrm{Kg/mol}$ for $hSBR_2$, $M_w = 23.5\ \mathrm{Kg/mol}$ in Ref.[5,6]). For SBR, a possible correlation could be found with the microstructure: the present samples, displaying a smaller value of φ_{self}, have a larger content in 1,4-butadiene units and a smaller content in styrene units. From the EFWS it is deduced that the microscopic effective glass-transition temperature $T_{g,eff}^{m}$ of SBR coincides with the 'macroscopic' one. Thus, for the fast component a small 'microscopic' self-concentration has been observed, similar to that 'macroscopically' found.

The PS slow component shows a different behavior: for medium-high PS concentrations, it displays an apparently large 'microscopic' self-concentration, similar to the macroscopic one. When it is the minority component, it 'looses its identity' and becomes 'animated' by the fast SBR majority component. For this composition, there is a significant difference between the atomic displacements of this component at t_R at the temperature where it 'feels' its microscopic glass-transition ($\langle r^2(t_R)\rangle\left(T_{g,eff}^{m,PS} = 210\ \mathrm{K}\right) = 0.63\ \mathrm{Å}^2$) and the temperature where it 'feels' its macroscopic glass-transition ($\langle r^2(t_R)\rangle\left(T_{g,eff}^{PS} = 220\ \mathrm{K}\right) = 0.74\ \mathrm{Å}^2$).

6.2.2. Lindemann Criterion in Blends

In Chapter 3.3.1 the extensibility of the Lindemann criterion to the glass-transition in homopolymers has been discussed. Now with the information provided by the EFWS on the blend components one can ask: How does the Lindemann criterion apply in the blends? Figure 6.6 shows the MSD of each component in the blend, at its 'microscopic' effective glass transition. Within the uncertainties, the displacements of both components when they feel the microscopic softening are very similar. This would allow to propose a kind of mixing rule for the Lindemann criterion in the blends.

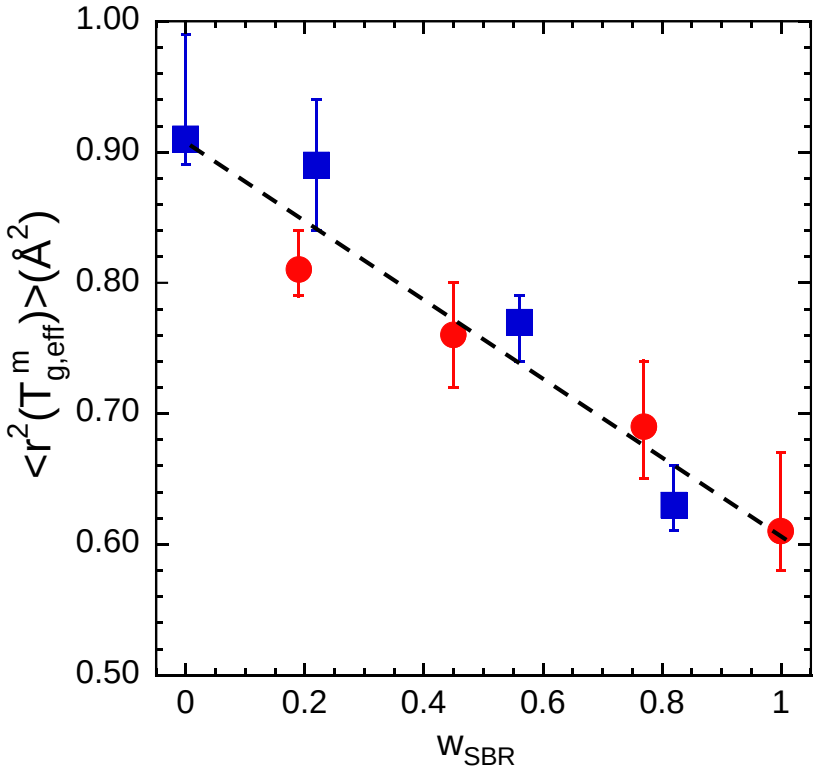

Figure 6.6: Composition dependence of the proton mean squared displacement of $hSBR_1$ (a) and hPS_1 (b) at the 'microscopic' effective glass-transition of the SBR component (circles) and PS component (squares) deduced from the IN13 results.

6.3 Non-Gaussian Effects and their Origin

The non-Gaussian parameter α_2 accounts for deviation of atomic displacements from Gaussian behavior. $\alpha_2(t_R)$ is shown as function of temperature in Fig. 6.3, and in Fig. 6.7 as function of composition (i) at 200 K, where all samples are in the glassy state, (ii) at 230 K, and (iii) at 280 K, all samples above their average macroscopic glass-transition.

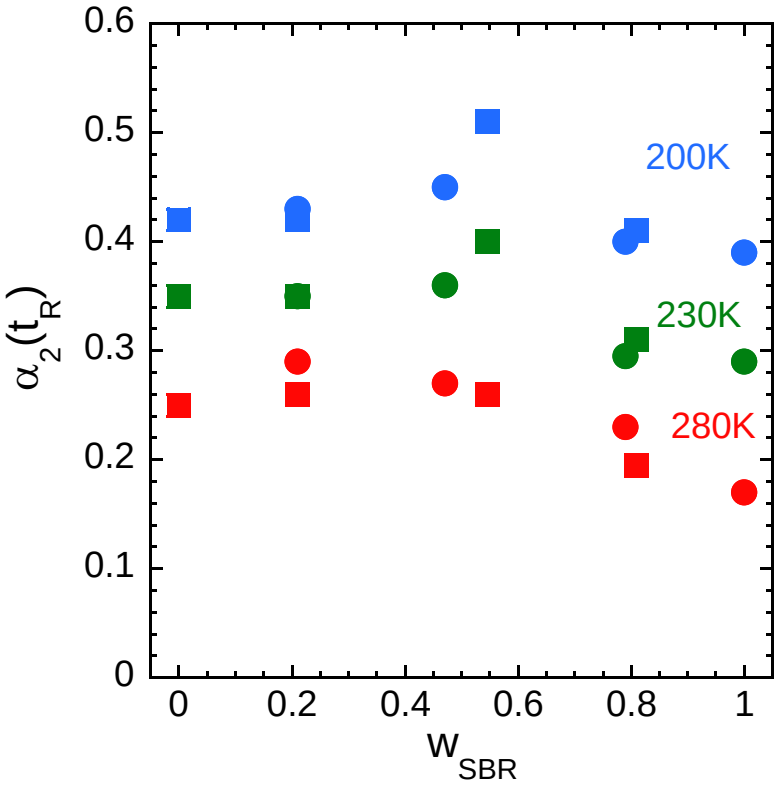

Figure 6.7: Composition dependence of the non-Gaussian parameter for three different temperatures. Circles correspond to SBR in $hSBR_1/dPS_1$ samples and squares to PS in $dSBR_1/hPS_1$ samples.

The deviations reflected by this parameter can have diverse origin. First of all, they can be due to intrinsic heterogeneities associated to different motions in different locations of the polymer chain: main-chain versus side-group motions, end-chain additional fluctuations, particular dynamics at the different kinds of monomers (styrene, 1,4-butadiene and 1,2-butadiene in the case of SBR, etc.);[7,8] these effects are present both,

in the neat polymers, as well as in the blends. They are expected to be less pronounced with increasing temperature –when usually characteristic times tend to converge– but would persist even at high temperatures. Secondly, as in any glass-forming system, non-Gaussian events associated to the cage dynamics, before the Gaussian subdiffusive regime is reached,[9] contribute to these deviations. For homopolymers and other glass-forming liquids, MD-simulations in a variety of systems[10–16] show that the α_2-parameter decreases with enhanced mobility (in particular, in relation with the dynamics of the α-relaxation). Thus, when the temperature increases, α_2 decreases indicating more Gaussian atomic displacements. This is the behavior found in our systems (see Figs. 6.3 and 6.7). Third, an additional source of contributions to deviations from Gaussian behavior, now specific for the polymeric mixtures, is the distribution of mobilities due to diverse environments associated to concentration fluctuations. The non-Gaussian parameter and the standard deviation of the distribution of concentration determined from the SANS analysis (compare Figs. 6.7 and 5.15) have similar concentration dependence. Also, as above argued from the comparison of the different effective glass-transition temperatures, from σ a more heterogeneous microscopic behavior in the blend with high PS content than for the high-SBR concentrations can be deduced, in accordance with the tendency observed for α_2.

6.4 The Relevant Length Scales in the Game

Several relevant length scales are involved in the characterization of the rich phenomenology exhibited by simple linear homopolymers (e. g., the average inter-chain distance, the relevant length scale of the segmental motions, the Kuhn length, the end-to-end average distance, etc). Even more relevant length scales can arise when considering more complex homopolymers as polymers with bulky side groups, or copolymers, for example (sizes of nano- aggregates or nano-phases). And, obviously, blending introduces an additional one associated with the TCF (the correlation length). In the following the information extracted from different scattering techniques and also from the combination of them with DSC on the different relevant length scales in the blends under investigation is put together. Three kinds of aspects are considered: structural, dynamic and thermodynamic aspects.

Structural Aspects

Since for X-Rays the contrast between the blend components is very small, these measurements are free from low-Q contributions from TCF and they were used to study the short-range order and possible nano-domain structuration of phenyl rings in the samples. X-Ray diffraction experiments were performed at the Materials Physics Center in San Sebastian, Spain at RT. Experimental details can be found in Ref.[6]

Figure 6.8 shows the results obtained for the different blends and homopolymers. Panel (a) corresponds to samples based on $hSBR_1$ and dPS_1 and panel (b), on $dSBR_1$ and hPS_1. Data have been normalized to their maximum value. This maximum is located at around $Q_{max} \approx 1.3\ \text{Å}^{-1}$, and corresponds to correlations between pairs of atoms belonging to nearest neighboring chains. From its position, using the Bragg approximation, the average inter-chain distance is inferred $d_{chain} = 2\pi/Q_{max}$. This is very close and nearly indistinguishable for all the samples: about 47 Å for SBR ($Q_{max} = 1.33\ \text{Å}^{-1}$) and 4.8 Å for PS ($Q_{max} = 1.30\ \text{Å}^{-1}$), and in between for the blends. These values are in the range reported for other glass-forming polymers like 1,4-PB.[17]

In addition, a peak centered at about $0.68\,\text{Å}^{-1}$ can be clearly seen for the PS homopolymers. This peak has been assigned to phenyl ring - phenyl ring correlations and thereby attributed to the nano-segregation of phenyl rings and main-chain atoms in PS.[18] These experiments thus prove that this kind of nano-segregation persists in oligomers as small as those here investigated. The location of this peak would be determined by the inter-domain distance D.

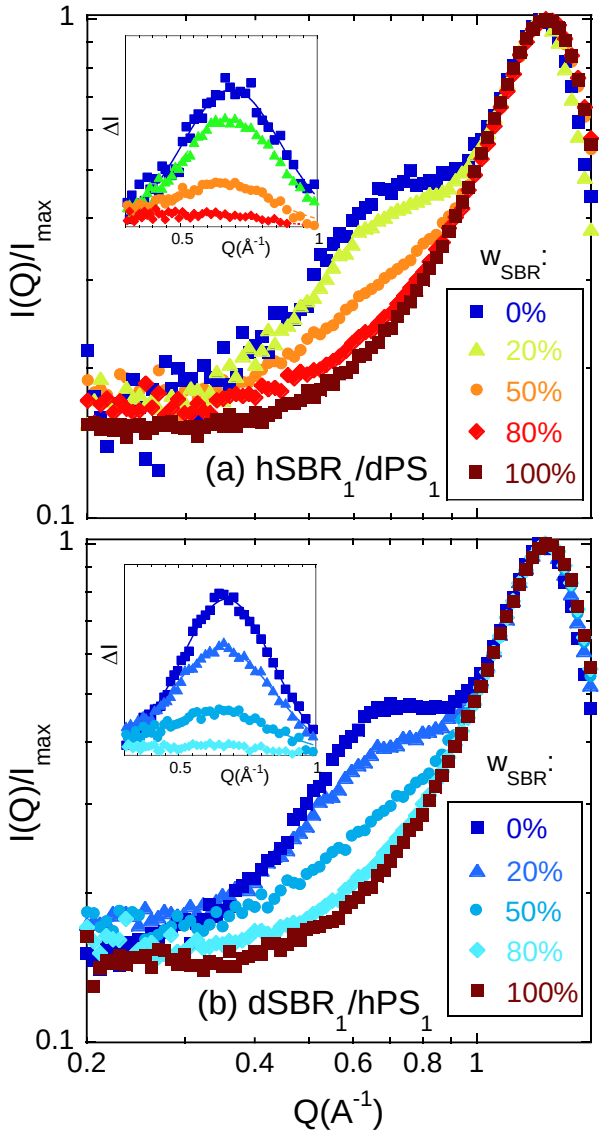

Figure 6.8: X-Ray diffraction results on the samples composed by (a) $hSBR_1$ and dPS_1 and (b) $dSBR_1$ and hPS_1, at the SBR-concentrations indicated, normalized to their value at the main peak. The insets show the peak resulting of subtracting the pure SBR results from each of the patterns. Lines are fits of a Gaussian function.

On the other hand, the pure SBR samples do not show any clear hint for the presence of such a low-Q peak. In the blends there is an extra-intensity with respect to that corresponding to the pure SBR results in the low-Q region, which increases with increasing PS content. This feature could be attributed to the persistence of nano-segregation of the phenyl rings with respect to the main-chains also in the blends. To analyze this contribution, in a first approximation is assumed that the scattered intensity is the simple addition of a low-Q peak arising from the nanodomain structure and a high-Q peak reflecting the pure inter-chain correlation contributions. To represent the latter, the pure SBR results are used. Thus, the difference between the total pattern and the SBR pattern would in a first order correspond to the nano-domain peak. This difference is shown in the insets of Fig. 6.8. Using a Gaussian function to describe it, the position of this peak is obtained. From the Bragg approximation, the inter-domain distance D has been deduced as function of composition. The values found are represented in figure 6.9 together with those obtained for the average inter-molecular distances d_{chain}.

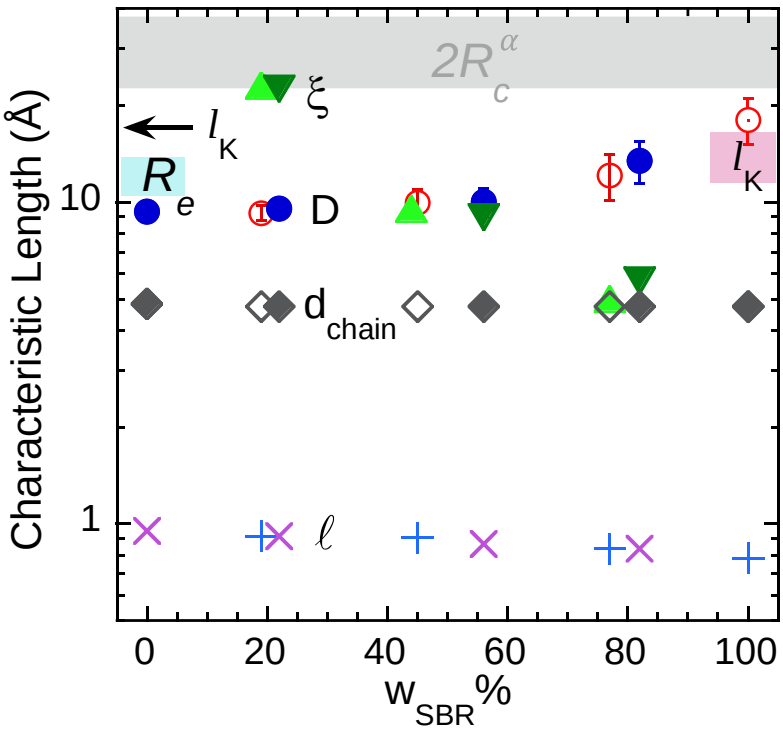

Figure 6.9: Composition dependence of the different characteristic length scales identified in this study: inter-molecular distance d_{chain} (diamonds), inter-nano-domain

distance D (circles) for $hSBR_1/dPS_1$ (filled) and $dSBR_1/hPS_1$ (empty) samples; pure SBR (with dot) corresponds to the results reported in Ref.[6]), correlation length ξ (triangles; $hSBR_1/dPS_1$ samples (up) and $dSBR_1/hPS_1$ (down)) and average displacement at about 80 ps ℓ (crosses: SBR; pluses: PS). The range of the relevant length scale for the α-process, $2R_c^{\alpha}$, is marked with the grey area. The arrow marks the Kuhn length l_K of polymeric PS and the red area the range of l_K reported for SBR. Blue region shows the estimate of the end-to-end distance of the PS500 oligomers. Data correspond to T ≈300 K.

Inherent to the presence of bulky side groups[19] (phenyl rings, in this case), structural heterogeneities arise due to nano-segregation of main-chain and side-group atoms. The nano-domain peak in PS is less pronounced than in higher molecular weight samples, but even for so short PS chains nano-segregation is clear. The results are similar to those found for the higher molecular weight (900 g/mol) oligomers. For the present neat SBR samples this peak is not resolvable, but in a previous work[6] it was reported the existence of a weak peak for SBR in the Q-range around 0.3 $Å^{-1}$. This peak seems to be resolvable only beyond a threshold content of styrene units in the copolymer. This is about 20% (weight) styrene, that was the case of the SBR in Ref.;[6] here is only 13.8 and 18%. Nano-domains persist in the blends. In the mixtures, the peak would arise from the presence of styrene phenyls from both, PS and SBR. Here it is found in fact that in the blend with 80% SBR content, having thus a global content of styrene % of about 30–34%, the peak is already visible (Fig. 6.8). Inter-nano-domain distance increases with SBR content, having more linear chain portions. For intermediate to high PS concentration, this distance remains around 1 nm, and can reach up to about 2 nm for pure SBR with high enough styrene content.[6] This is the approximate value of the Kuhn length ($l_K = 1$ Å) in PS.[20,21] The value of l_K in SBR is expected to depend on the microstructure and is not known for the present samples; from the literature we could also expect values in the 1-2 nm range ($l_K = 12$ Å, from Ref.,56 $l_K = 16$ Å, from Ref.[6]). Another structural parameter to be considered is the size of the structural units involved. For the oligomers, the end-to-end vector distance $\sqrt{\langle R_e^2 \rangle}$ is expected to be smaller than 2 nm, which is the value estimated from the 900 g/mol PS in Ref.[6] For the SBR chains involved in the

present samples, $\sqrt{\langle R_e^2 \rangle}$ would be of the order of 23 nm for $hSBR_1$ and 17 nm for $dSBR_1$, considering the reported value of 0.7 for the ratio $\sqrt{\langle R_e^2 \rangle}/M$, where M is the molecular mass.[22] This means, this length is much larger than any other of the characteristic lengths represented in Fig. 6.9.

Thermodynamic Aspects

SANS insight allows determining the relevant length scale for TCF, the correlation length ξ. This length strongly depends on concentration (see Figs. 4.8 and 6.9), but for SBR contents about or higher than 50% it remains below 1 nm in the whole T-range investigated. For high SBR concentrations, the values of ξ even approach the inter-molecular distance d_{chain}. Thus, under these conditions, the correlation length ξ is smaller than the chains' dimensions –or similar to the smallest one– implying that the chains are randomly mixed. Only for the highest PS-concentrations approaching the glass transition the correlation length can exceed the dimensions of the oligomers, being thus the mixture locally inhomogeneous.[23,24]

Dynamic Aspects

In the previous Chapter it has been shown that, from the comparison of SANS and DSC results on the width of the distributions of TCF, a relevant length scale of $2R_c^\alpha \approx 30$ Å is deduced for the α-relaxation as observed by the loss of equilibrium across T_g in the present mixtures. This value is in the same range found in blends of PS oligomers of 900 g/mol and SBR of different microstructure ($2R_c^\alpha \approx 25$ Å for the system $hSBR_2$-dPS_2 (see chapter 5), $2R_c^\alpha \approx 20$ Å)[6]. Note that in those cases, the value of $2R_c^\alpha$ was deduced from the study of the dielectric response, i. e., corresponding to the dynamics of the α-relaxation in equilibrium. The similarity of the $2R_c^\alpha$-value with the Kuhn length of the polymers was brought forward in those works, as suggested in Ref.[25] However, the present results rule out l_K to be behind this length scale. The oligomers in these blends are smaller than a Kuhn segment (containing 7 monomers), and the $2R_c$ value is the

similar or even larger than those found in the previous cases. Thus, the size $2R_c^{\alpha}$ cannot be related with any particular length scale associated with the chain size or conformation.

The size $2R_c^{\alpha}$ exceeds by a factor of about 20 the relevant length scale ℓ characteristic for the 'microscopic' glass transition, as observed from the EFWS. This may be defined as $\ell = \sqrt{\langle r^2(t_R, T_g)\rangle}$. As can be inferred from the above discussion, this characteristic length remains of the same order (around 1 Å) independently of choosing T_g or $T_{g,eff}$ for its definition. The atomic displacements at such relatively short times around the glass-transition are characteristic for the local motions within the cage imposed by the neighboring chains, while characteristic times observed close to T_g for the α-process by relaxation methods as dielectric spectroscopy are of the order of 1 s. In this case, they are $\tau_{BDS}(T_g) = 2.3$ s (hSBR$_1$), 100 s (hPS$_1$), 2.9 s (dSBR$_1$) and 41 s (dPS$_1$) (see table 3.5). In fact, the characteristic time at the calorimetric T_g is the magnitude invoked in the proposed model (chapter 5) to connect the component segmental dynamics in the blend above T_g with the way the equilibrium is lost when cooling down towards the glassy state. $2R_c^{\alpha}$-values in the nanometer scale have been reported for polymers and other glass-forming systems.[26]

6.5 Conclusions

For the homopolymers, in chapter 3 it has been demonstrated that the atomic displacements at some tens of ps are sensitive to the onset of liquid-like motions across the calorimetric glass-transition, even if the relaxation times associated to this phenomenon are of the order of tens of seconds, corroborating thereby previous findings. These displacements are of the order of 1 Å at the glass transition, supporting a Lindemann-like criterion. The microscopic insight on atomic displacements at $t_R \approx 80$ ps of a selected component in the blend has allowed determining its microscopic effective glass-transition in the mixture. The Lindemann-like criterion might also be applied for blends, where a simple mixing rule for the atomic mean squared displacements determines the condition for glass transition. The values obtained for the microscopic effective glass-transition in the mixture were compared with the macroscopic counterparts deduced from the DSC analysis with a model based on TCF and SC. For the fast SBR component, a coincidence of microscopic and microscopic effective glass transition temperatures is always found. For the slow PS component, the situation is more complex. For the sample rich in SBR, the microscopic glass transitions of both components are similar, indicating that at this microscopic level the mixture is dynamically homogeneous. This leads to a kind of paradoxical situation in the sense that PS looses its equilibrium (as deduced from DSC) at a higher temperature than that where it undergoes its microscopic glass transition. This implies that there is a temperature range where this component feels a 'liquid-like' microscopic environment but behaves 'solid like' from a macroscopic point of view. On the contrary, for intermediate and high PS contents, macroscopic and microscopic effective glass transitions of PS coincide (being thus different from those of SBR) and the system is heterogeneous at microscopic level. For high PS concentrations, the system is close to phase separation. Heterogeneities are one of the sources of the non-Gaussian effects observed in the atomic displacements.

The comparative study here presented has also allowed determining the characteristic length scale of the α-relaxation to be about 30 Å. This is similar to the values previously found for blends involving different components with different sizes. Its relation with the Kuhn length can be ruled out from this work, since the oligomers do not meet this size.

Inherent to the presence of bulky side-groups in the chains, structural heterogeneities at the nano-scale arise due to nano-segregation of main-chains and side-group atoms. They persist even though the small size of the oligomers and the dilution of phenyl rings with blending, but are not expected either to be relevant to determine the characteristic length scale of the α-relaxation, that is apparently universal for glass-forming systems.

6.6 References

(1) Colmenero, J.; Arbe, A. Segmental Dynamics in Miscible Polymer Blends: Recent Results and Open Questions. *Soft Matter* **2007**, *3* (12), 1474–1485.

(2) Gambino, T.; Alegría, A.; Arbe, A.; Colmenero, J.; Malicki, N.; Dronet, S.; Schnell, B.; Lohstroh, W.; Nemkovski, K. Applying Polymer Blend Dynamics Concepts to a Simplified Industrial System. A Combined Effort by Dielectric Spectroscopy and Neutron Scattering. *Macromolecules* **2018**, *51* (17), 6692–6706.

(3) Shafqat, N.; Alegría, A.; Malicki, N.; Dronet, S.; Mangin-Thro, L.; Frick, B.; Colmenero, J.; Arbe, A. Microscopic versus Macroscopic Glass Transition(s) in Blends of Industrial Interest. *EPJ Web Conf* **2022**, *272*, 01008.

(4) Dalle-Ferrier, C.; Simon, S.; Zheng, W.; Badrinarayanan, P.; Fennell, T.; Frick, B.; Zanotti, J. M.; Alba-Simionesco, C. Consequence of Excess Configurational Entropy on Fragility: The Case of a Polymer-Oligomer Blend. *Phys Rev Lett* **2009**, *103* (18), 185702.

(5) Gambino, T.; Alegría, A.; Arbe, A.; Colmenero, J.; Malicki, N.; Dronet, S. Modeling the High Frequency Mechanical Relaxation of Simplified Industrial Polymer Mixtures Using Dielectric Relaxation Results. *Polymer* **2020**, *187*, 122051.

(6) Gambino, T.; Shafqat, N.; Alegría, A.; Malicki, N.; Dronet, S.; Radulescu, A.; Nemkovski, K.; Arbe, A.; Colmenero, J. Concentration Fluctuations and Nanosegregation in a Simplified Industrial Blend with Large Dynamic Asymmetry. *Macromolecules* **2020**, *53* (16).

(7) Narros, A.; Alvarez, F.; Arbe, A. Hydrogen Motions in the α-Relaxation Regime of Poly(Vinyl Ethylene): A Molecular Dynamics Simulation and Neutron Scattering Study. *J. Chem. Phys* **2004**, *121*, 3282.

(8) Narros, A.; Arbe, A.; Alvarez, F. Atomic Motions in The-Merging Region of 1,4-Polybutadiene: A Molecular Dynamics Simulation Study. *J. Chem. Phys* **2008**, *128*, 224905.

(9) Colmenero, J.; Alvarez, F.; Arbe, A. Self-Motion and the α Relaxation in a Simulated Glass-Forming Polymer: Crossover from Gaussian to Non-Gaussian Dynamic Behavior. *Physical Review E* **2002**, *65* (4), 12.

(10) Kob, W.; Andersen~, H. C. Testing Made-Coupling Theory for a Supercooled Binary Lennard-Jones Mixture: The van Hove Correlation Function. *PHYSICAL REVIEW E* **1995**, *51* (5).

(11) Arbe, A.; Colmenero, J.; Alvarez, F.; Monkenbusch, M.; Richter, D.; Farago, B.; Frick, B. Experimental Evidence by Neutron Scattering of a Crossover from

Gaussian to Non-Gaussian Behavior in the Relaxation of Polyisoprene. *Physical Review E* **2003**.

(12) Caprion, D.; Schober, H. R. Structure and Relaxation in Liquid and Amorphous Selenium. *Phys Rev B* **2000**, *62* (6), 3709.

(13) Kämmerer, S.; Kob, W.; Schilling, R. Test of Mode Coupling Theory for a Supercooled Liquid of Diatomic Molecules. II. *Phys Rev E* **1998**, *58* (2), 2141.

(14) Hurley, M. M.; Harrowell, P. Non-Gaussian Behavior and the Dynamical Complexity of Particle Motion in a Dense Two-dimensional Liquid. *J Chem Phys* **1998**, *105* (23), 10521.

(15) Caprion, D.; Matsui, J.; Schober, H. R. Dynamic Heterogeneity of Relaxations in Glasses and Liquids. *Phys Rev Lett* **2000**, *85* (20), 4293.

(16) Kob, W.; Donati, C.; Plimpton, S. J.; Poole, P. H.; Glotzer, S. C. Dynamical Heterogeneities in a Supercooled Lennard-Jones Liquid. *Phys Rev Lett* **1997**, *79* (15), 2827.

(17) Frick, B.; Richter, D.; Ritter, C. Structural Changes near the Glass Transition–Neutron Diffraction on a Simple Polymer. *Europhys Lett* **1989**, *9* (6), 557.

(18) Ayyagari, C.; Bedrov, D.; Smith, G. D. Structure of Atactic Polystyrene: A Molecular Dynamics Simulation Study. *Macromolecules* **2000**, *33* (16), 6194–6199.

(19) Moreno, A. J.; Arbe, A.; Colmenero, J. Structure and Dynamics of Self-Assembled Comb Copolymers: Comparison between Simulations of a Generic Model and Neutron Scattering Experiments. *Macromolecules* **2011**, *44* (6), 1695–1706.

(20) Fetters, L. J.; Lohse, D. J.; Colby, R. H. Chain Dimensions and Entanglement Spacings. *Physical Properties of Polymers Handbook* **2007**, 447–454.

(21) Rubinstein, M.; Colby, R. H. *Polymer Physics*; Oxford university press New York, 2003; Vol. 23.

(22) Fetters, L. J.; Lohse, D. J.; Milner, S. T.; Graessley, W. W. Packing Length Influence in Linear Polymer Melts on the Entanglement, Critical, and Reptation Molecular Weights. *Macromolecules* **1999**, *32* (20), 6847–6851.

(23) Wignall, G. D.; Melnichenko, Y. B. Recent Applications of Small-Angle Neutron Scattering in Strongly Interacting Soft Condensed Matter. *Reports on Progress in Physics* **2005**, *68* (8), 1761–1810.

(24) Yun, S. I.; Melnichenko, Y. B.; Wignall, G. D. Small-Angle Neutron Scattering from Symmetric Blends of Poly(Dimethylsiloxane) and Poly(Ethylmethylsiloxane). *Polymer* **2004**, *45* (23), 7969–7977.

(25) Lodge, T. P.; McLeish, T. C. B. Self-Concentrations and Effective Glass Transition Temperatures in Polymer Blends. *Macromolecules* **2000**, *33* (14), 5278–5284.

(26) Berthier, L.; Biroli, G.; Bouchaud, J. P.; Cipelletti, L.; el Masri, D.; L'Hôte, D.; Ladieu, F.; Pierno, M. Physics: Direct Experimental Evidence of a Growing Length Scale Accompanying the Glass Transition. *Science* **2005**, *310* (5755), 1797–1800.

Chapter 7

Concluding Remarks

7.1 Conclusions and Outlook

In this thesis, a detailed study of the thermodynamic, dynamic and structural properties of polymeric blends of industrial interest composed by isotopically labelled styrene-butadiene rubber (SBR) and polystyrene (PS) oligomers has been presented. Such materials are categorized as binary mixture with dynamic asymmetry. The dynamic behaviour of these mixtures resemble that of canonical athermal polymer blend and can be interpreted on the same basis using two concepts: the self-concentration (SC) which is believed to cause the dynamic asymmetry retained by the components, and the thermally driven concentration fluctuations (TCF) which are thought to be behind the broad distribution of mobilities for each component. To complete this investigation, a combination of experimental techniques such as Broadband Dielectric Spectroscopy (BDS), Small Angle Neutron Scattering (SANS), neutron Elastic Fixed Window Scans (EFWS) and Differential Scanning Calorimetry (DSC) were used. The detailed conclusions of the work have been presented at the end of Chapter 5 and 7. In the following, the main finding if the Thesis are briefly summarized.

First, a model capturing the combined effect of the two main ingredients, the self-concentration and the thermally driven concentration fluctuations, has been invoked to successfully describe blending effects not only on the equilibrium dynamics of the α-relaxation in the miscible state as monitored by BDS, but also on the DSC manifestation of the glass transition phenomenon reflecting how thermodynamic equilibrium is lost. This was achieved by considering the mixtures composed of several regions and by using only three free parameters: the self-concentration of the components φ_{self}^{SBR} and φ_{self}^{PS} describing the local composition in each region, and the width σ of the distributions of concentration associated to the spontaneous fluctuations. This model has allowed to reproduce very well the experimental results in a wide range of temperatures and compositions. In addition, the present approach has allowed decomposing the DSC curves into the component contributions, providing the composition-dependent values of the effective glass transition temperature of each blend component.

Second, the 'macroscopic' effective glass transition temperatures $T_{g,eff}$, disentangled by the analysis of the DSC results, were compared with the 'microscopic' effective glass-transitions $T_{g,eff}^{m}$ of the components determined by the atomic displacements at some tens of ps ($t_R \approx 80\ ps$), as observed by the EFWS sensitive to the onset of liquid-like motions across the calorimetric glass transition. At the glass-transition, these displacements are ≈ 1 Å. At microscopic level, the mixtures are dynamically homogeneous for high contents of the fast SBR component and heterogeneous for blends with intermediate concentrations or rich in PS. This heterogeneity was found to be one of the sources of the non-Gaussian effects observed for the atomic displacements.

Finally, the comparison of SANS and BDS results has allowed establishing the relevant length scale for the segmental relaxation in the blends. The excellent agreement also with the DSC traces has shown that this would also be the relevant length scale for the glass-formation process. The value found $2R_c \approx 25 - 30$ Å is in the range usually assumed for the α-relaxation in many glass-forming systems. On the other hand, inherent to the presence of bulky side-groups in the chains, structural heterogeneities at the nano-scale were observed and we propose that they are due to nano-segregation of main-chains and side-group atoms. They persist even though the small size of the oligomers and the dilution of phenyl rings with blending, but are not expected to be relevant to determine the characteristic length scale of the α-relaxation, that is apparently universal for glass-forming systems.

The work here presented was applied to a very simplified industrial system composed of one elastomeric copolymer and one oligomeric component allowing to tune the dynamic properties of the tire material. Tires are generally composed of ≈200 different raw materials, which are combined with rubber compounds to create the various components of a manufactured tire. In a future work, it would be very interesting to apply the methodology described in this work to a more "realistic", and therefore more complicated system, by mixing the elastomer with a resin with larger dynamic asymmetry or adding for example to the actual system a third element like those used in the tire industry, such as oil, to improve the properties of the blend without changing the final average glass transition temperature. In relation to this, the work of the last months of this

thesis was addressed to an exploratory investigation of more complex binary and ternary systems.

7.2 List of Publications

- Gambino, T.; Shafqat, N.; Alegria, A.; Malicki, N.; Dronet, S.; Radulescu, A.; Nemkovski, K.; Arbe, A.; Colmenero, J. Concentration Fluctuations and Nanosegregation in a Simplified Industrial Blend with Large Dynamic Asymmetry. *Macromolecules* **2020**, *53*, 7150− 7160.

- Shafqat, N.; Alegria, A.; Arbe, A.; Malicki, N.; Dronet, S.; Porcar, L.; Colmenero, J. Disentangling the Calorimetric Glass-Transition Trace in Polymer/Oligomer Mixtures from the Modeling of Dielectric Relaxation and the Input of Small-Angle Neutron Scattering. *Macromolecules* **2022**, *55*, 7614–7625.

- Shafqat, N.; Alegria, A.; Malicki, N.; Dronet, S.; Mangin-Thro, L.; Frick, B.; Colmenero, J.; Arbe, A. Microscopic versus Macroscopic Glass Transition(s) in Blends of Industrial Interest. *EPJ Web Conf.* **2022**, *272*, 01008.

- Shafqat, N.; Alegria, A.; Malicki, N.; Dronet, S.; Natali, F.; Mangin-Thro, L.; Porcar, L.; Arbe, A.; Colmenero, J. Microscopic versus Macroscopic Glass Transitions and Relevant Length Scales in Mixtures of Industrial Interest. *Submitted to Macromolecules* **2022.**

Acknowledgments

The successful conclusion of this PhD thesis would not have been possible without the support and encouragement of many people.

First, I would like to thank Prof. Juan Colmenero for giving me the opportunity to join the research group "Polymers and Soft Matter" at the Materials Physics Centre, as well as sharing his experience and expertise with me during these three years. I would like to express my sincere gratitude to my supervisors Prof. Arantxa Arbe and Prof. Angel Alegria for always finding time to share their experience, their immense knowledge and their guidance during these three years, without their help this thesis wouldn't be possible. Thank you, Arantxa, for introducing me to the field of neutron scattering with patience and constant encouragement. Thank you, Angel, for your help with dielectric spectroscopy, for all the constructive remarks and support.

Second, I would like to express my honest gratitude to Dr. Severin Dronet and Dr. Nicolas Malicki for their support and encouragement throughout my thesis, and for giving me the opportunity to spend three months at Michelin, in such a friendly atmosphere. My stay in Clermont-Ferrand was a really positive experience.

Then, I would like to thank to the people of the Institut Laue-Langevin (ILL) at Grenoble in France for their expert help with the neutron scattering experiments. Thank you, Lucile, Bernhard, Francesca and Lionel.

Last but not least, I would like to thank all the people of 'Polymer and Soft Matter' group. I am grateful for the opportunity that I had to work with them, for their fantastic company and for the wonderful atmosphere in the office. Specially thanks to Silvia, for her support in the characterization lab.; to Isabel, for her guidance in the synthesis lab.; to Amaia, for her assistance throughout the X-Ray experiments and to Jon, for the fruitful time spent during neutron beamtime.